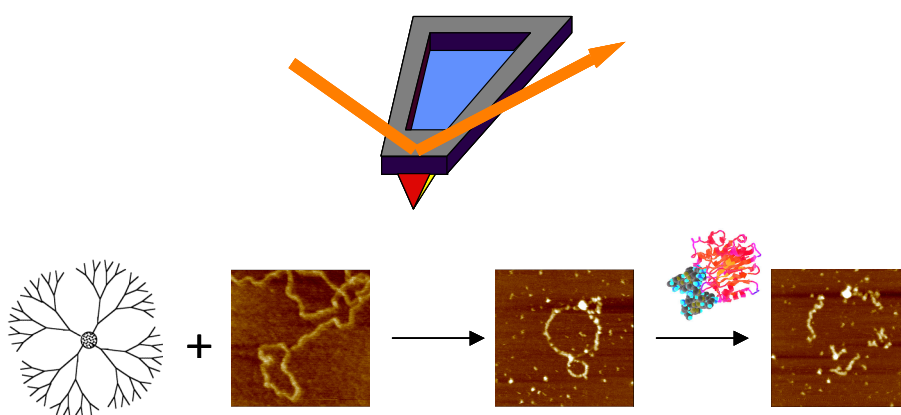

**INVESTIGATION OF POLYAMIDOAMINE
DENDRIMERS INDUCED DNA CONDENSATION
AND ENZYMATIC DEGRADATION OF THESE
COMPLEXES:**

AN ATOMIC FORCE MICROSCOPY STUDY



Hosam Gharib Abdelhady

BSc, MSc Pharmaceutical Sciences

Thesis submitted to

The University of Nottingham

for the degree of

Doctor of Philosophy

July 2004

TABLE OF CONTENTES

ABSTRACT.....	V
ABBREVIATIONS.....	VIII
LIST OF FIGURES.....	IX
LIST OF TABLES.....	XIV
CHAPTER ONE.....	1
INTRODUCTION	1
1.1 BACKGROUND	1
1.2 METHODS OF NON VIRAL GENE THERAPY.....	7
1.3 POLYAMIDOAMINE (PAMAM) DENDRIMERS.....	8
1.4 SYNTHESIS OF PAMAM DENDRIMERS.	11
1.5 MECHANISM OF DENDRIMER-MEDIATED CELL ENTRY	15
1.6 PAMAM DENDRIMERS FOR <i>IN VITRO</i> GENE TRANSFER	17
1.7 THE CONCEPT OF DNA CONDENSATION	19
1.8 MECHANISM OF CONDENSATION	20
1.9 THE NEED FOR SURFACE CHARACTERIZATION.....	21
1.10 THE ATOMIC FORCE MICROSCOPE (AFM)	22
1.10.1 Background.....	22
1.10.2 AFM Modes of Employment.....	25
1.10.2.1 Contact Mode AFM (CM-AFM).....	27
1.10.2.2 Non-Contact Mode AFM (NCM-AFM)	28
1.10.2.3 Tapping Mode/ AFM (TM-AFM)	28
1.10.2.4 Tapping Mode AFM (TM-AFM) in Liquids.....	30
1.10.3 Force-Displacement Curves (<i>f-d-c(s)</i>).....	30
1.10.4 Amplitude-Phase-Distance (<i>a-p-d</i>) Measurements.	33
1.11 AIMS OF THESIS.....	34
CHAPTER TWO.....	36
EXPERIMENTAL MATERIALS, METHODS AND INSTRUMENTATION	36
2.1 EXPERIMENTAL MATERIALS.....	36
2.1.1 Cationic Reagents.....	36
2.1.2 Model Surfaces (Alkanethiol Self-Assembled Monolayers)(SAMs).....	37
2.1.3 DNA	38
2.1.3.1 pBR322	39
2.1.3.2 pRSVLuc.....	40
2.1.4 DNase I Enzyme	40
2.2 METHODS AND INSTRUMENTATION	43
2.2.1 Substrate Preparation	43
2.2.1.1 Mica	43
2.2.1.2 Epitaxial Gold Films.....	43
2.2.1.3 Template Stripped Gold (TSG).....	44
2.2.1.4 Alkanethiol Self Assembled Monolayers (SAMs) Preparation	44

2.2.1.5	Preparation of PAMAM Dendrimer Coated Substrates for Imaging in Air.....	45
2.2.2.	<i>In situ AFM Imaging of G4 and G6 PAMAM Dendrimers on Mica</i>	45
2.2.3	<i>Surface Characterization of SAMs and Dendrimers-SAMs Complexes</i>	46
2.2.3.1	Film Morphology of SAMs Monolayers and G4 PAMAM Dendrimers on SAMs in Air.....	46
2.2.3.2	Film Morphology of SAM-COOH Monolayers and G4 PAMAM Dendrimers on SAM-COOH in Liquid.....	46
2.2.3.3	In situ Imaging of G4 PAMAM Dendrimers on SAM-COOH	47
2.2.3.4	Functionalization of AFM Tips with Alkanethiol SAMs	47
2.2.3.5	Force-Distance Curve (f-d-c) Measurements	47
2.2.3.6	Amplitude-Phase-Distance (a-p-d) Measurements.....	48
2.2.4	<i>Generic Methodology of DNA Imaging with Atomic Force Microscopy</i>	49
2.2.4.1	Preparation of DNA Plasmids for Imaging in Air.....	49
2.2.4.2	Divalent Cation Pre-treatment Method.....	49
2.2.4.3	G4 Pre-treatment Method.....	49
2.2.4.4	Preparation of Polymer-DNA Complexes	50
2.2.4.5	Imaging of DNA Condensates in Air	50
2.2.4.5.1	Using Divalent Cations	50
2.2.4.5.2	Using PAMAM Dendrimers.....	51
2.2.4.6	Preparation of DNA for Imaging in Liquid.....	51
2.2.4.6.1	Imaging in the Absence of Divalent Cations.....	51
2.2.4.6.2	Imaging in the Presence of Divalent Cations.	51
2.2.4.6.3	Imaging in the Presence of PAMAM Dendrimers.....	52
2.2.5	<i>Effect of DNase I Enzyme</i>	52
2.3	INSTRUMENTATION	53
2.3.1	<i>Atomic Force Microscopy</i>	53
2.3.1.1	AFM Cantilevers	54
2.3.1.2	AFM Data Acquisition and Analysis.....	54
2.4	<i>Gel Electrophoresis</i>	55
CHAPTER THREE.....		58
VISUALIZATION AND CHARACTERIZATION OF PAMAM DENDRIMERS ON DIFFERENT SURFACES.....		58
3.1	BACKGROUND.....	58
3.2	EXPERIMENTAL PARAMETERS	60
3.3	RESULTS AND DISCUSSION	61
3.3.1	<i>Imaging of G4 on Mica; The Effect of Drying Methods</i>	61
3.3.2	<i>In situ Imaging of G4 PAMAM Dendrimers on Mica; The Effect of Dendrimer Concentration, and Adsorption Time</i>	63
3.3.3.	<i>Imaging of G6 and G8 on Mica in Water; The Effect of Dendrimers Generation</i>	66
3.3.4	<i>Visualization of G4 Dendrimers on Gold</i>	73
3.3.4.1	Gold Film Analysis.....	73
3.3.4.2	Imaging of G4 on Gold (in Air)	75
3.3.5	<i>Film Morphology of SAMs Monolayers in Air</i>	77

3.3.6	<i>Characterization of G4 Dendrimers on SAMs</i>	78
3.3.6.1	Imaging of G4 dendrimers on SAMs in air.....	78
3.3.6.2	Film Morphology of SAM-COOH Monolayers and G4 Dendrimers on SAM-COOH in Liquid.....	80
3.3.6.3	In situ Imaging of G4 Dendrimers on SAM-COOH	81
3.3.6.4	Effect of Setpoint.....	83
3.3.6.5	Force-Distance Curve (f-d-c) Measurements.....	86
3.3.6.6	Amplitude-Phase-Distance (a-p-d) Measurements.....	92
3.4	CONCLUSIONS.....	95
CHAPTER FOUR		96
MONOVALENT COUNTERION CORRELATIONS BETWEEN LIKE-CHARGED SURFACES FACILITATE IMAGING IN REAL TIME		96
4.1	BACKGROUND.....	96
4.2	EXPERIMENTAL PARAMETERS	101
4.3	RESULTS AND DISCUSSION	101
4.3.1	<i>Imaging of DNA in the Presence of Monovalent Cations; the Theory of Fluctuation of Monovalent Cations between Two Like Charged Surfaces</i> 101	
4.3.2	<i>Imaging of DNA in 10% PBS Containing Divalent Cations, (MgCl₂ & NiCl₂)</i>	106
4.3.3	<i>Imaging of DNA in Air</i>	107
4.3.3.1	Imaging of DNA on Mica.	107
4.3.3.2	Imaging of DNA on MgCl ₂ -treated Mica.	109
4.4	CONCLUSIONS.....	110
CHAPTER FIVE		112
SURFACE VISUALIZATION OF PAMAM DENDRIMERS-INDUCED DNA CONDENSATION		112
5.1	BACKGROUND.....	112
5.2	RESULTS AND DISCUSSION	115
5.2.1	<i>Effect of Dendrimer's Loading Ratio and Generation on the DNA Condensation</i>	115
5.2.1.1	Effect of G4 Dendrimer's Loading Ratio.....	115
5.2.1.2	Effect of G6 Dendrimer's Loading Ratio.....	124
5.2.1.3	Effect of G8 Dendrimer's Loading Ratio.....	125
5.2.2	<i>Surface-influenced DNA Condensation in the Presence and Absence of Sufficient Soluble G4 Dendrimers</i>	126
5.2.2.1	In the Presence of Sufficient Soluble G4 Dendrimers.....	126
5.2.2.2	In the Absence of Sufficient Soluble G4 Dendrimers	128
5.2.3	<i>Ionic Strength Dependence</i>	129
5.2.4	<i>pH Dependence</i>	131
5.2.5	<i>Imaging of DNA on G4-treated Mica in Air</i>	134
5.2.6	<i>Imaging of DNA-Dendrimers Condensates in Air</i>	135
5.2.7	<i>Possible Condensation Mechanisms and Pathways of PAMAM-DNA Polyplexes onto Mica Surface</i>	136
5.2.7.1	Towards Toroidal Formation.....	136
5.2.7.2	Towards Flowers Formation	139
5.2.8	<i>Four Dimensions Investigations of the DNA Condensation and Condensates Disassembly in Liquid</i>	140

5.2.9	<i>Analysis of Condensate Volumes</i>	149
5.2.10	<i>Effect of Loading Ratio and Generation Type on the Complex Retardation in Gel Electrophoresis</i>	155
5.3	CONCLUSIONS	158
CHAPTER SIX		161
DIRECT REAL-TIME MOLECULAR SCALE VISUALISATION OF THE DEGRADATION OF CONDENSED DNA COMPLEXES EXPOSED TO DNASE I		161
6.1	BACKGROUND	161
6.2	RESULTS AND DISCUSSION	164
6.2.1	<i>On Substrate Experiments</i>	164
6.2.1.1	Effect of DNase I on Naked DNA Plasmids	164
6.2.1.2	Effect of Dendrimer's Loading Ratio	165
6.2.1.3	Effect of Incubation Time with Dendrimers	171
6.2.1.4	Effect of Substrate	179
6.2.1.5	Effect of Incubation Cations	182
6.2.1.6	Effect of Dendrimer's Generation	183
6.2.2	<i>In Solution Experiments</i>	184
6.2.2.1	Effect of Loading Ratio.....	184
6.2.2.2	Effect of Generation.....	186
6.2.3	<i>Gel Electrophoresis Investigations of the Effect of Loading Ratio, Generation Type and Incubation Time with DNase I on the Protection of the Obtained Complexes</i>	187
6.3	CONCLUSIONS	193
CHAPTER SEVEN		194
OVERALL CONCLUSIONS		194
BIBLIOGRAPHY		198

ABSTRACT

Extensive investigations have been made to try and understand the physical properties and structures of condensed DNA phases *in vitro* during the past decades (Bloomfield, 1991, Marquet and Houssier, 1991, Bloomfield, 1996). The packing pathways of DNA molecules are three dimensional processes, and are not yet fully understood (Yoshikawa *et al.*, 1997). Distinguishing different single DNA molecules at different locales in time in the presence of condensating or dissociating agents is crucial for understanding the mechanisms of packing and unpacking of DNA molecules. The aim of this study is to provide an increased understanding of the some of the pathways of packing and unpacking of DNA. This aim was achieved by monitoring in time and at molecular scale the interaction between the DNA and polyamidoamine dendrimers, as condensating poly cations, and by observing the dissociation of some of these condensates in time when they were exposed to DNase I enzyme, as a dissociating *in vivo* agent. The main techniques used were atomic force microscopy (AFM) and gel electrophoresis. We believe that the results could be beneficial to the understanding of the *in vivo* condensation and dissociation process of certain DNA morphologies.

Chapter 1 will focus on providing an overview of the single molecule techniques used, atomic force microscopy as a means of detecting individual biomolecules in near physiological conditions with time and its application in monitoring non-viral gene delivery systems on surfaces. Methods used for gene delivery, and the PAMAM dendrimers as one of the recently applied polymer in non-viral gene delivery are also reviewed.

The materials and methods used in this thesis were considered in chapter 2.

Chapter 3 will concentrate on the factors effecting the interactions of generation 4, 6 and 8 PAMAM dendrimers on surfaces. An understanding of these interfacial interactions is important to understand their effects on the individual DNA molecules. This aim was achieved by using AFM as an imaging and force measuring tool to visualize and characterize the adsorption of these dendrimers on mica, gold and on alkanethiol self assembled monolayers (SAMs).

Developing a deep understanding of the adsorption of DNA onto oppositely charged substrates would be of fundamental importance in understand the packing and unpacking pathways of these molecules. This philosophy is demonstrated in Chapter 4 in which the ability of the monovalent cations to facilitate imaging of DNA, and the effect of these monovalent cations in the partial condensation of DNA is explored. In addition, Chapter 4 introduces DNA imaging in the presence of divalent cations in liquid and in air.

The folding pathways of dendrimer-induced DNA condensation with time on the surface of mica in aqueous environment were the targets of Chapter 5. In addition, the surface-influenced DNA condensation in the presence and absence of sufficient soluble cations and the ionic strength dependence were also studied. Structural volume and hence information regarding the number of plasmid molecules in each condensate was explored. Furthermore, the effect of loading ratio and generation type on the complex retardation in gel electrophoresis was investigated.

Chapter 6 investigates the different mechanisms of the DNA-PAMAM dendrimer condensate relaxation and fragmentation by DNase I with time and explores the mechanisms of wrapping and unwrapping of the DNA on the larger generations of dendrimers.

The final chapter, Chapter 7, discusses the progress made towards the aims of this thesis. Interestingly, this investigation is one of the first to apply atomic force microscopy operating in liquid to visualize at the molecular scale and in real time DNA molecules in the absence of multivalent cations, to explore the formation of DNA complexes with ethylene di amine PAMAM dendrimers that have real potential as gene delivery vectors and to investigate the different condensation and dissociation pathways of individual DNA molecules.

Overall it is hoped that the work described in this thesis provides a step forward in the methods applied for AFM based nano-force biomolecular imaging with time and provides a valuable information that aid in developing a successful non-viral gene delivery system.

ABBREVIATIONS

a-p-d	- amplitude-phase-distance
AFM	- atomic force microscopy
Au	- gold
Bar	- dynes/cm ²
bp	- base pair
Da, kDa	- Dalton, kilo Dalton
DNA	- deoxyribonucleic acid
DNase I	- deoxyribonuclease I
EDA PAMAM	- ethylene diamine core polyamidoamine dendrimers
EBr	- ethidium bromide
f-d-c	- force-distance curve
G4	- generation 4 PAMAM dendrimers
G6	- generation 6 PAMAM dendrimers
G8	- generation 8 PAMAM dendrimers
kbp	- kilo base pairs
NaKE	- sodium-potassium-EDTA
PAMAM	- poly (amidoamine) dendrimers
PBS	- phosphate buffered saline
PEG	- poly (ethylene glycol)
SAMs	- self assembled monolayers
SAM-CH ₃	- SAM substrates functionalized in methyl groups
SAM-COOH	- SAM substrates functionalized in carboxyl groups
SAM-NH ₂	- SAM substrates functionalized in amine groups
SPM	- scanning probe microscopy
STM	- scanning tunnelling microscopy
TEM	- transmission electron microscopy
TESP	- tapping-mode etched silicon probe
THF	- tetrahydrofuran
Torr	- 1.33 mbar
TSG	- Template Stripped Gold
U	- enzymatic activity in units

LIST OF FIGURES

Figure 1.1: Synthesis of tetra-functional PAMAM dendrimers.	13
Figure 1.2: Schematic representation of the divergent method.	14
Figure 1.3: Schematic representation of the convergent method.	14
Figure 1.4: Schematic representation of the mechanism of dendrimer-mediated gene delivery into cells.	17
Figure 1.5: Schematic representation of The AFM and its modes of action.	26
Figure 1.6: Force-displacement curves.	32
Figure 1.7: Amplitude-phase-distance curves.	34
Figure 2.1: A space-filling model of the DNA double β -helix.	39
Figure 2.2: Proposed mechanism of action of DNase I enzyme.	42
Figure 3.1: Height images of G4 dendrimers on mica; Effect of drying methods.	62
Figure 3.2: <i>In situ</i> imaging of G4 dendrimers (10^{-14} M) on mica.	64
Figure 3.3: <i>In situ</i> imaging of G4 dendrimers ($0.1 \mu\text{gml}^{-1}$) on mica.	65
Figure 3.4: F-d-c(s) measured between a silicon nitride tip and mica before and after the adsorption of G4.	66
Figure 3.5: <i>In situ</i> imaging of the adsorption of G6 dendrimers onto mica (in 10% PBS).	67
Figure 3.6: Height images of G6 dendrimers adsorbed on mica imaged in deionized water.	68
Figure 3.7: Height images of G8 adsorbed on mica imaged in deionized water.	69
Figure 3.8(a): Relation between diameters of G4, G6 and G8 and their heights on mica.	70
Figure 3.8(b): Comparison of the mean dendrimer volume measured by AFM from particle profiles and theoretical volume of PAMAM Dendrimers.	71
Figure 3.9: Height image in air of (a) an epitaxially grown Au film on mica and (b) TSG.	75

Figure 3.10: Height images of G4 dendrimers on epitaxial gold.	76
Figure 3.11: AFM topographical images of SAMs onto epitaxially grown gold films.	78
Figure 3.12(a-c): AFM topographical images of SAMs following their exposure to a solution of G4 dendrimers in air.	79
Figure 3.12(d): Relation between the Diameter and Height of features observed on SAMs coated Surfaces.	79
Figure 3.13: AFM topographical images of SAM-COOH before and following its exposure to a solution of G4 dendrimers in deionized water.	81
Figure 3.14: In situ imaging of the adsorption of G4 PAMAM dendrimers onto a SAM-COOH surface.	83
Figure 3.15: The effect of the setpoint on imaging quality.	84
Figure 3.16: The relation ship between the R% and the height and diameter of the imaged molecules.	85
Figure 3.17: F-d-c(s) between a SAM-COOH modified tip and the different SAMs and SAMs coated substrates.	90
Figure 3.18: A-p-d curves recorded between a SAM-COOH modified TESP tip and the different SAMs and SAMs coated substrates.	93
Figure. 4.1: Top view AFM images of different DNA topologies immediately after the dilution of DNA with 10% BPS.	103
Figure. 4.2: Top view AFM images of different DNA topologies. The DNA was incubated in 10%PBS for 24 hrs before imaging.	104
Figure. 4.3: Top view AFM images of different DNA topologies on mica. The DNA was imaged immediately in the same buffer.	105
Figure. 4.4: Top view AFM images of different DNA topologies on mica. The DNA was imaged immediately in the 10% PBS containing 2mM MgCl ₂ and 1mM NiCl ₂ .	106
Figure. 4.5: Top view AFM image of uncondensed DNA plasmids in air.	108
Figure. 4.6. An AFM image of DNA on MgCl ₂ treated mica in air.	109
Figure 5.1: Representative AFM Images of DNA and G4-DNA complexes at different charge ratios.	120

Figure 5.2: Representative AFM Images of G4:DNA complexes formed at 15:1 and 20:1 ratios and imaged in deionized water.	120
Figure 5.3a: The change in the (free water/free amine ratio) relative to changes in G4:DNA ratios.	123
Figure 5.3b: The origin of charge inversion in adsorption of high generation dendrimers.	123
Figure 5.4: AFM Images of G6: DNA complexes at increasing charge Ratios imaged in deionized water.	125
Figure 5.5: AFM Images of G8: DNA complexes at increasing charge ratios imaged in deionized water.	126
Figure 5.6: AFM images of different DNA topologies on G4 treated mica without washing.	127
Figure 5.7: Images and schematic representations of toroidal and plectonemic structures.	128
Figure 5.8: AFM images of different DNA topologies on G4 treated mica after washing.	129
Figure 5.9: AFM Images of G6: DNA complexes (ionic strength dependence).	130
Figure 5.10: AFM Images of DNA: PAMAM dendrimer complexes (pH dependence).	133
Figure 5.11: AFM image of DNA plasmid on G4 treated mica in air.	134
Figure 5.12: AFM Images of DNA: PAMAM dendrimer complexes arranged in order of increasing dendrimers generation in air.	135
Figure 5.13: Schematic representations of the spool-like model and constant radius of curvature model of torus formation.	138
Figure 5.14: A schematic representation depicts a possible mechanism of formation of flowers.	140
Figure 5.15: AFM image sequences for the 1:1 G4 to DNA ratio, images, show in near in situ, the formation of toroidal complex.	142
Figure 5.16: AFM image sequences for the 1:1 G4 to DNA ratio, images show intermediates towards toroidal formation.	144
Figure 5.17: AFM image sequences for DNA on G4 treated mica without washing.	145

Figure 5.18: AFM image sequences for the 1:1 G6 to DNA ratio, Images show the DNA molecules wrapping around the G6 molecules.	146
Figure 5.19: AFM image sequences for 7.5:1 G4: DNA ratio, in which DNA and dendrimer molecules were allowed to equilibrate in 10% PBS solution for four hrs, 10:1 ratio incubated for 4.5 hrs and 10:1 ratio incubated for 1 hr.	147
Figure 5.20: Schematic representations of DNA condensates.	151
Figure 5.21: The percentage of each condensate morphology relative to the dendrimers generation and irrelative to the loading ratio.	152
Figure 5.22: The volume of PAMAM dendrimer-DNA complexes relative to dendrimers generations.	153
Figure.5.23: Gel electrophoretic retardation pattern for plasmid-PAMAM complexes.	156
Fig. 5.24: Gel electrophoretic retardation pattern for G4, G6 and G8 PAMAM dendrimers.	157
Figure 6.1: Scheme of supercoiled DNA and the formation of open circular or linear DNA as the result of nicking of one DNA strand or both strands.	163
Figure 6.2: Control AFM images of the DNase I and its effect on bare DNA adsorbed onto mica surfaces.	165
Figure 6.3(a): Effect of DNase I enzyme on G4-DNA (0.5:1) complex.	167
Figure 6.3(b): Effect of DNase I enzyme on G4-DNA (1:1) complex.	169
Figure 6.3(c): Effect of DNase I enzyme on G4-DNA (5:1) complex.	169
Figure 6.3(d): The mean starting and ending times of fragmentation within different complex's ratios with G4 dendrimers.	171
Figure 6.4a: AFM image sequences for the 1:1 G4; DNA and incubated For 15 min before the addition of the enzyme. Images show the DNA molecule relaxing to reach its maximum diameter.	173
Figure 6.4b: Changes in the measured DNA dimensions with time following the addition of DNase I.	175
Figure 6.4c: AFM image sequences for the 1:1 G4 to DNA ratio and incubated for 15 min before the addition of the enzyme. Images show a rapid relaxation of the DNA molecule.	176
Figure 6.4d: AFM image sequences for the 1:1 G4 to DNA ratio and	

incubated for 15 min before the addition of the enzyme. Images show fragmentations of the DNA molecules.	177
Figure 6.5: AFM image sequences for the 1:1 G4 to DNA ratio, in which DNA and dendrimer molecules were allowed to equilibrate in solution for 2hr prior to deposition onto mica.	179
Figure 6.6: AFM image sequences for DNA plasmid in which the DNA was adsorbed onto G4 treated mica before the introduction of DNase I.	180
Figure 6.7: AFM images of a `flower-like' complex formed at 20:1 G4: DNA ratio.	181
Figure 6.8: AFM image of a `flower-like' complex formed at 20:1 G4:DNA ratio. Fetures consistent with a densely packed layer of G4 were observed.	182
Figure 6.9: Time-lapse images showing the effect of DNase I on G4:DNA complex, 1:1 ratio. The effect of MnCl ₂ .	182
Figure 6.10: Time-lapse images showing the effect of DNase I on G6: DNA complex. Images show the unwrapping of the DNA from G6 molecules	184
Figure 6.11: Time-lapse images showing the effect of DNase I on G4: DNA complexes at different ratios in solution.	186
Figure 6.12: Time-lapse images showing the effect of DNase I on G6: DNA complexes in solution. The effect of incubation time with DNase I.	187
Figure 6.13: Typical gels showing time-dependent degradation by DNase I of DNA complexed with G4 at increasing ratios.	190
Figure 6.14: Typical gels showing time-dependent degradation by DNase I of DNA complexed with G6 at increasing ratios.	192

LIST OF TABLES

Table 1.1: The non-viral delivery methods proposed in gene therapy and their limitations.	7
Table 5.1: The percentage of each condensate morphology relative to the dendrimers generation and irrelative to the loading ratios.	152
Table 5.2: The volume of PAMAM dendrimer-DNA complexes.	153
Table 6.1: The mean starting and ending times of fragmentation within different complex's ratios with G4 dendrimers.	170
Table 6.2: The changes in the measured dimensions of the DNA with time after the addition of DNase I.	174
Table 6.3: The number of molecules that follows the SSB and DSB mechanisms after the addition of the DNase I enzyme.	178

CHAPTER ONE

INTRODUCTION

1.1 BACKGROUND

While classical molecular structural techniques normally rely on molecular ensemble experiments, which average over all possible molecular conformations and mutations, the recent advent of single molecule techniques allow the manipulation and observation of individual molecules. Experiments with single molecules have been reported with scanning tunnelling microscopy (STM) (Guckenberger *et al.*, 1994), fluorescence microscopy (Yanagida *et al.*, 1983), fluorescence correlation spectroscopy (Wennmalm *et al.*, 1997), optical tweezers (Wang *et al.*, 1997), bead techniques in magnetic fields (Smith *et al.*, 1992), optical micro fibres (Cluzel *et al.*, 1996) and atomic force microscopy (AFM) (Hansma *et al.*, 1992b). All these methods provide directly or indirectly information on molecular structure and function. They differ, however, in the molecular properties they probe, their spatial and temporal resolution, their molecular sensitivity, and working environment. The development of the atomic force microscope (AFM) (Binnig *et al.*, 1986, Binnig *et al.*, 1987) quickly after the STM was invented by Binnig and Rohrer in the early 1980s (Binnig and Rohrer, 1982) provided new opportunities to image insulators such as biomolecules. The STM, for which Binnig and Rohrer were awarded the Nobel Prize in Physics in 1986, whilst yielding atomic resolution had limited biological application up until this point due to its need for a

conducting substrate. STM, AFM and other probe microscope techniques have been actively used to search for many different signatures of the presence of atoms and molecules (Hansma *et al.*, 1988, Drake *et al.*, 1989, Bustamante *et al.*, 1992, Lyubchenko *et al.*, 1992, Vallea *et al.*, 2002, Edwardson and Henderson, 2004). A significant breakthrough came in the late 1980s with the scanning of biomolecules submerged in aqueous solutions which allowed reproducible imaging of DNA and crystals of membrane proteins (Hoh *et al.*, 1991). A variety of biological application for AFM have since been developed (Edwardson and Henderson, 2004); these include the nanometer resolution imaging of gap junctions (Hoh *et al.*, 1991), bacterial toxins (Yang *et al.*, 1994), bacterial outer membrane proteins and channels (Lal *et al.*, 1993), measuring intermolecular interaction forces (Frisbie *et al.*, 1994, Lee *et al.*, 1994, Moy *et al.*, 1994), mapping surface charges on the nanometer scale (Xu and Arnsdorf, 1995, Xu and Arnsdorf, 1997, Ellis *et al.*, 1999a) and monitoring biochemical processes (Henderson *et al.*, 1992) such as DNA packing and unpacking which is important for many natural biological processes including viral replication and cell division (Kukowska-Latallo *et al.*, 1996, Bielinska *et al.*, 1997, Hill *et al.*, 2001).

This latter application of AFM in DNA packing is the main subject of this thesis. DNA is extremely compacted (condensed) in bacteria, in cell nuclei, sperm heads and virus capsids (Livolant *et al.*, 1989). This condensation is induced spontaneously by naturally occurring cationic molecules for example, spermine, spermidine and basic proteins termed histones when electrostatic repulsion of the DNA phosphate backbone is adequately neutralized (Tabor

and Tabor, 1984). The prime example is fitting of DNA into a bacteriophage's capsid, since bacteriophages are simple systems that do not possess condensing proteins (histones) present in eukaryotic cells (Eickbush and Mondrianakis, 1978, Marx and Ruben, 1983, Stevens, 2001). The packed DNA, hence, typically occupies only 1×10^{-4} to 1×10^{-6} of the volume of an uncondensed, wormlike coil of DNA in solution (Wilson and Bloomfield, 1979, Widom and Baldwin, 1980, He *et al.*, 2000). Such packing densities aid in protecting the DNA from the nuclease enzymes that would otherwise digest the nucleic acid material by decreasing the accessibility of the DNA to nucleases (Marx and Reynolds, 1982). This decreased accessibility results in a considerable increase in the stability of plasmid and oligonucleotide DNA in biological fluids (Mahato and Kim, 2002). In addition, the ability of the endogenous polycations to induce DNA condensation has been demonstrated *in vitro* (Chattoraj *et al.*, 1978, Allison, 1981, Plum *et al.*, 1990). In this circumstance, monomolecular condensation occurs with the production of rod-like, and toroidal structures (Calladine, 1980). Theoretical evidence for a relationship between toroidal and rod-like condensates has been reported by Noguchi *et al.*, (Noguchi *et al.*, 1996). This investigation applied Monte Carlo simulations and demonstrated the existence of toroidal, rod-like, and stable fused intermediate structures. Recently, Dunlap *et al.* (Dunlap *et al.*, 1997) used AFM to examine DNA in incomplete condensates induced by polyethylenimine and found clearly, for the first time, individual DNA strands in the condensed state. In this experiment, DNA molecules were observed as being clearly arranged in parallel. Condensation of DNA into condensed structures, and dissociation of DNA condensates *in vitro* can provide useful insights into the physical factors

governing the folding, packaging, and unpacking of DNA *in vivo*. However, despite much progress in studying the mechanisms of DNA condensation and enzymatic degradation using a variety of microscopic, light scattering, fluorescence, gel electrophoresis and calorimetric techniques, the precise details of the DNA packing assembly and dissociation mechanisms are yet to be fully understood. Studying these phenomena is important to learn about the physical-chemical mechanisms that are involved in packing and unpacking DNA *in vivo*, and in view of applications of various types of DNA condensates as non-viral gene carriers for gene therapy (Vijayanathan *et al.*, 2002). The development of AFM has provided a powerful individual molecular surface analytical technique, which is beginning to make a significant contribution to the characterization of novel gene delivery systems. AFM also enables the dynamics of interfacial processes that occur when such systems are exposed to aqueous physiological conditions to be studied.

Before the application of AFM is considered, the number of well-known physiological obstacles to the development of efficient non viral gene delivery systems should be considered (Culver and Blaese, 1994, Tang *et al.*, 1996, Lehn *et al.*, 1998, Garnett, 1999, Templeton and Lasic, 2000), so as to guide experimental design. These barriers and our inability to overcome them currently cause a comparatively low efficiency and the inability to target gene expression to specific areas. These barriers (Zabner *et al.*, 1995) may be divided into extracellular barriers, where the DNA must pass through, for example, mucosal, epidermal and intestinal barriers, before it reaches the systemic circulation (Brown *et al.*, 2001), once in the blood stream the DNA

complexes are targets for elimination by the reticuloendothelial system, interactions with serum proteins, and uptake by non-target tissues, all of which can adversely affect the distribution to the target site, and intracellular barriers, such as the crossing of the cellular and endosomal membranes, cytoplasmic traffic and crossing the nuclear membrane (Farhood *et al.*, 1995). During administration, the genetic material will be exposed to the nuclease activities previously identified in serum. In addition, once inside the target cells, the complexes are exposed to nuclease activities in the endosomal and lysosomal compartments (Hill *et al.*, 2001) and references therein. However, the need to protect the DNA on its journey from initial administration site into the target cell nucleus must also be balanced with the requirement for the DNA to be released from its delivery system when it reaches its site of action. Over the last decade, research in somatic gene therapy has focused on selected approaches to deliver therapeutic genes to cells both *ex vivo* and *in vivo*. The first approved gene therapy clinical trial, to treat severe combined immune deficiency, was conducted in the USA in September 1990 (Thompson, 1993). However, after nearly 14 years, the field has yet to provide a routinely used treatment or cure for a single disease. In addition, countless experimental gene delivery trials have failed to bring therapies to the market due to inability of the gene to be delivered to the target area. Thus, suitable activity is insufficient if the formulation lacks tissue specificity, blood solubility, metabolic stability, or bioavailability. In principle, many of these limitations can be overcome through the use of an appropriate delivery system. Viral-based gene delivery is currently the most effective way to transfer genes to cells; these include retroviruses, adenoviruses, and those based on the herpes simplex virus

Chapter one: Introduction

(Robbins and Ghivizzani, 1998, Walther and Stein, 2000). In April 2002, the first successful use of viral-based gene therapy to treat severe combined immune deficiency by the replacement of genetic material in samples of 18-month-old Rhys Evans's bone marrow in the UK was successfully announced (Meikle, 2002). However, concerns with issues relating to bulk production, quality control, and the limited molecular weight of genetic material each viral particle can carry have prompted the concurrent development of synthetic gene delivery systems. The justification of these concerns has been vindicated by the recent death of a reasonably healthy 18-year-old gene therapy trial patient (Marshall, 1999, Marshall, 2000). It seems desirable thus to achieve an efficient non-viral gene delivery system. To this end a synthetic carrier appears to be the initial and possibly the critical parameter (Bielinska *et al.*, 1997, Fojta *et al.*, 1999, Brown *et al.*, 2001, Hill *et al.*, 2001). These are mentioned briefly in the next section.

1.2 METHODS OF NON VIRAL GENE THERAPY

A variety of non-viral DNA delivery modes have been proposed. These are summarized in Table 1.1.

Methods of non viral gene therapy			
Method	Examples	Limitations	References
Naked DNA	Conventional injection, high-pressure projection of DNA coated gold particles, and insertion of DNA coated catheters.	Low levels of expression are achieved	(Wolff <i>et al.</i> , 1990, Ledley, 1995, Kuriyama <i>et al.</i> , 2000)
Cationic Liposomes	Intranasal administration to target the lungs of cystic fibrosis patients	Reticuloendothelial clearance. This results in difficulties in targeting tissues other than the liver.	(Caplen <i>et al.</i> , 1995, Kitson and Alton, 2000)
	Intratumoural administration to refractory cervical and ovarian carcinoma patients		(Hui <i>et al.</i> , 1997)
Polymeric Delivery Systems	Cationic polymers like poly-L-lysine, polyethylenimine, poly(methacrylate, and poly(amidoamine) dendrimers.	According to the polymer type	(Cherng <i>et al.</i> , 1996, Dash <i>et al.</i> , 1997, Ferrari <i>et al.</i> , 1997, Van De Wetering <i>et al.</i> , 1997, Godbey <i>et al.</i> , 1999a) (Williams <i>et al.</i> , 1996, Duncan, 2003)
	Neutral polymers, for example poly(vinyl alcohol), and neutral crowding polymers. for example PEG at high concentrations and in the presence of adequate salt. These polymers could provoke DNA condensation through an excluded volume mechanism.	Cannot condense DNA but do have the ability to protect naked DNA from extracellular nuclease degradation and to aid retention of the delivered nucleic acid material at the site of injection after intramuscular administration.	

Table 1.1 show non-viral delivery methods proposed in gene therapy and their limitations.

Among the cationic polymers employed, polyamidoamine (PAMAM) dendrimers (Starburst®) have recently emerged as a novel synthetic carrier for DNA transfer (Peppas, 1995), and they will be the subjects of our study.

1.3 POLYAMIDOAMINE (PAMAM) DENDRIMERS

Poly(amidoamine), or PAMAM, dendrimers (Figure 1.1) are a class of synthetic, highly branched, spherical molecules with defined chemical functionality (Tomalia *et al.*, 1985, Tomalia *et al.*, 1986, Tomalia, 1993, Bielinska *et al.*, 1997, DeLong *et al.*, 1997, Bielinska *et al.*, 1999, Chechik *et al.*, 1999, Cagin *et al.*, 2000, Li *et al.*, 2000, Tomalia and Fréchet, 2001, Tomalia *et al.*, 2002). The “dendrimer” name reflects the ordered, branching tree-like structure of these polymers (Li *et al.*, 2000). These water-soluble macromolecules are uniform in size and constructed from various initiator cores on which each complete iterative reaction sequence results in a new dendrimer “generation”. The molecular weight of the dendrimer hence increases exponentially, the number of primary amine surface groups exactly double and the diameter increases by ~ 10 Å. These generations are covalently attached, thus yielding a three-dimensional highly ordered polymeric compounds (Ottaviani *et al.*, 1998) of 10 Å to 130 Å in diameter for generation 0 through generation 10. General nomenclature for dendrimers with an ethylenediamine (EDA) initiator core is G_x EDA, where x is the particular generation (i.e. generation 4 EDA core is G₄ EDA) and G_xNH₃ for ammonia core molecules (Eichman *et al.*, 2000). However, for simplicity, we will refer to the EDA core PAMAM dendrimers in our study by their generation number

only (i.e. G4 EDA is G4). While PAMAM dendrimers of lower generation number (G0-G4) tend to exist in a relatively open planar, elliptical shape, they adopt a spherical three-dimensional structure which very loosely resembles that of a globular protein as the successive layers are added (Zeng and Zimmerman, 1997). Since the branch numbers of the dendrimers are exponentially dependent on the generation number and grow much more rapidly than the available volume, the structure spatially saturates at a given generation number, beyond which it is impossible to grow the dendrimer to completion (Lin *et al.*, 2002). Dendrimers represent a unique type of polymer that may bridge the gap between the synthetic and biological polymer fields. Although the size of most dendrimers is large enough to mimic many protein molecules, they are substantially smaller than other biological targets such as viruses (Li *et al.*, 1999). These fundamental properties have led to the commercial use of PAMAM dendrimers as globular protein replacements for immuno-diagnostics and *in vitro* gene expression applications (Esfand and Tomalia, 2001). Although there are many similarities between dendrimers and globular proteins, it is also important to note significant differences. Whereas globular proteins have tertiary structure resulting from the intricate folding of sequenced linear structure, they are extremely fragile and susceptible to denaturing conditions, such as temperature, light and pH. By contrast, dendrimers are known to be robust, covalently fixed, three-dimensional structures possessing both solvent-filled interior hollowness (nanoscale container) properties, as well as homogenous mathematically-defined surface functionality. More importantly, PAMAM dendrimers have been determined to be non-immunogenic and exhibit low mammalian toxicity, especially when their

surface contains anionic or neutral groups, such as carboxylic or hydroxylic functionalities. The large number of surface functional groups of PAMAM dendrimers has enabled these polymers to be employed for the multivalent recognition of viruses and cell surfaces. Moreover, PAMAM dendrimers have been used to improve the solubility of sparingly soluble drugs such as Piroxicam (Wiwattanapatapee *et al.*, 1999), and have increased the amount of therapeutic radio-nuclides delivered to cancer cells (Wilbur *et al.*, 1998). When the end-groups are cationic, they may neutralize the charge of the phosphate groups of various forms of nucleic acids including short, single-stranded oligonucleotides, circular plasmid DNA, linear RNA and various sizes of double-stranded DNA thereby potentially facilitating the delivery of genes and anti-sense drugs to cells (DeLong *et al.*, 1997). The larger the nucleic acid molecule, the lower the dendrimer concentration that is required to generate high-density complexes. Dendrimers are highly efficient for *in vitro* transfection and appear to be non-cytotoxic in the concentrations relevant for gene transfer (Ranucci *et al.*, 1991, Hill *et al.*, 1999, Bielinska *et al.*, 2000). In a recent study by Malik *et al.*, (Malik *et al.*, 1999) PAMAM dendrimers (G2 , G3 , G4 , G8 and G10) were shown to cause haemolysis of rat red blood cells at concentrations of 1.0 mg.ml⁻¹ (Malik *et al.*, 2000). They have been shown to be as efficient or more efficient than either cationic liposomes or other cationic polymers (e.g. polyethylenimine, polylysine) for *in vitro* gene transfer (Eichman *et al.*, 2000). A unique property of dendrimer- DNA complexes is their ability to retain transfectional activity after drying and reconstitution *in vitro*. Additionally, experiments *in vivo* have suggested that efficient gene transfer is possible with PAMAM dendrimers without inducing

immunogenicity. Initial work with heat-degraded polymers (Tang *et al.*, 1996, Dennig and Duncan, 2002) and other research using intact PAMAM dendrimers has produced promising results within the gene delivery fields (Bielinska *et al.*, 1996, DeLong *et al.*, 1997, Yoo *et al.*, 1999, Eichman *et al.*, 2000, Rudolph *et al.*, 2000).

1.4 SYNTHESIS OF PAMAM DENDRIMERS.

The synthetic procedures developed for dendrimer preparation (e.g., divergent growth, convergent growth, and self-assembly) permit nearly complete control over the critical molecular design parameters, such as size, shape, surface/interior chemistry, flexibility, and topology (Cagin *et al.*, 2000). Since 1979 two major strategies have evolved for dendrimer synthesis when Tomalia *et al.* (Tomalia *et al.*, 1985) first reported the successful well-characterized synthesis of dendritic polymers. The divergent approach pioneered by Donald Tomalia and Newkome (Newkome *et al.*, 1985) and the convergent technique introduced by Jean Frechet (Hawker and Frechet, 1990b, Hawker and Frechet, 1990a). The first revealed was the divergent method in which growth of a dendron originates from a core site (Figure 1.2). This approach is currently the preferred commercial route used by worldwide producers. It starts with an ethylenediamine (EDA) initiator core unit that is reacted with methyl acrylate by the Michael addition reaction. This results in the formation of two new branches per amine group with ester-terminated dendrimer, which is called 'half-generation' dendrimer. Subsequent amidation of the methyl ester with ethylene diamine gives a 'full generation' amine-terminated dendrimer. Repetition of Michael addition and amidation steps gives the next-higher

'generation' dendrimer with consequent increase in the molecular weight, number of terminal functional groups and size. A second method that was pioneered by Fréchet and colleagues is the convergent growth process. Unlike the divergent method, it proceeds from what will become the dendron molecular surface inward to a reactive focal point at the root (Figure 1.3). This leads to the formation of a single reactive dendron. To obtain a dendrimer structure, several dendrons are reacted with a multi-functional core to yield such a product. Another key difference is that the number of coupling reactions needed to add each new generations usually 2 or 3, depending on branch multiplicities is constant throughout the synthesis making defective products easier to separate. On the other hand, the convergent strategy is often limited to dendrimers of lower generation numbers i.e. generations 0 - 8. The problem is that the core becomes so congested that the reaction yields drop precipitously, whereas divergent syntheses can make dendrimers with as many as 10 generations. Both the commercially available PAMAM and poly(propyleneimine) dendrimers are made by the divergent method (Zeng and Zimmerman, 1997).

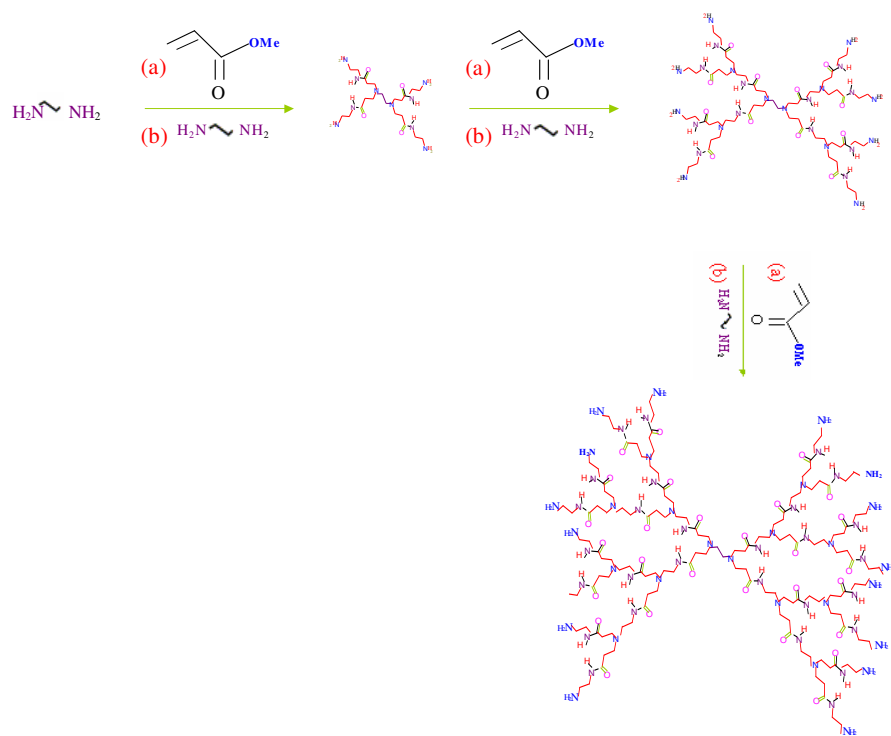


Figure 1.1. Synthesis of tetra-functional poly(amidoamine) (PAMAM) dendrimers: exhaustive Michael addition of amino groups with methyl acrylate, followed by amidation of the resulting esters with ethylenediamine

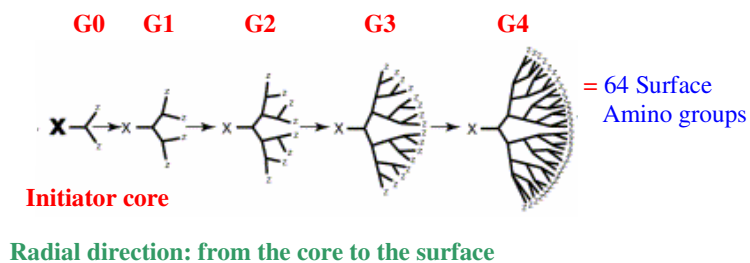


Figure 1.2. The divergent method, in which the synthesis begins from a polyfunctional core and continues radially outwards by successive stepwise activation and condensation. (Esfand and Tomalia, 2001)

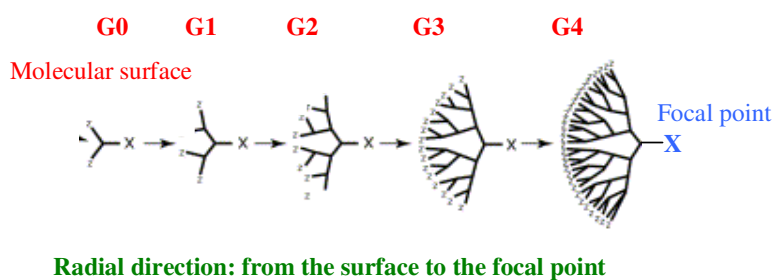


Figure 1.3. The convergent method in which the synthesis begins at what will be the periphery of the final macromolecule and proceeds inwards (Esfand and Tomalia, 2001).

1.5 MECHANISM OF DENDRIMER-MEDIATED CELL ENTRY

DNA is fundamentally a polymer of high molecular weight, typically in excess of 10^6 Da. It possesses a strong anionic charge conferred by its phosphate backbone. This combination of high molecular weight and surface charge restrict its passage across biological membranes, which consist predominantly of negatively charged lipid molecules. Thus, a key component of any delivery system is the modification of these properties in order to make the crossing of biological membranes more favourable. This can be achieved by the neutralisation of the negative charge, which results in a reduction in the size of the DNA, as well as increasing its lipophilicity. *In vitro* experiments have shown that PAMAM dendrimers can chaperone DNA through cell membranes and promote efficient gene transfection (Tang *et al.*, 1996). Figure 1.4 shows a proposed dendrimer–DNA complex pathway into cells with subsequent processing. A high dendrimer–DNA charge ratio (>5) is required for subsequent interaction with the anionic glycoproteins and phospholipids that reside on the cell membrane surface. Studies following the incorporation of radiolabeled DNA and/or dendrimer components into cells established that the uptake in most cells was primarily via an active endocytosis (Kukowska-Latallo *et al.*, 1996, Dennig and Duncan, 2002). After being in the endosome, it is essential that the complex is released into the cytosol before acidic or enzymatic DNA degradation commences within the endosomal–lysosomal cavity. It has been postulated that PAMAM dendrimers have a high buffer capacity, owing to protonatable amine groups. This characteristic enables dendrimers to act as a weak base and retard degradation caused by acidification

within the endosome–lysosome. A reduction in pH might also lead to polymeric swelling within the endosome, thus disrupting the membrane barrier of the organelle and promoting DNA and/or complex release (Richardson *et al.*, 1999). This property is believed to be the reason for their ability to produce transfection three-fold higher than that observed with poly-l-lysine (Haensler and Szoka, 1993). Dendrimers with defective branching have been synthesised and transfection efficacies superior to that of the intact polymer have been demonstrated (Tang *et al.*, 1996). After discharge from the endosome, DNA must penetrate the nuclear membrane for transcription and subsequent expression to occur. While efficient transfection has been shown to depend on mitosis, when the nuclear envelope breaks down (Brunner *et al.*, 2000) there is also evidence that the nuclear pores act as a size-exclusion barrier. Small DNA fragments enter the nucleus by passive diffusion while larger fragments are transported through the nuclear pore complex in an energy-dependent manner (Pouton, 1998). Translocation into the nucleus does occur within 30 min post-transfection. Recently, it was observed that complete separation of the polymer–DNA complex was not necessary for DNA entry into the nucleus (Godbey *et al.*, 1999b). Therefore, it might be possible that PAMAM dendrimers are also associated with DNA as it crosses into the nuclear compartment.

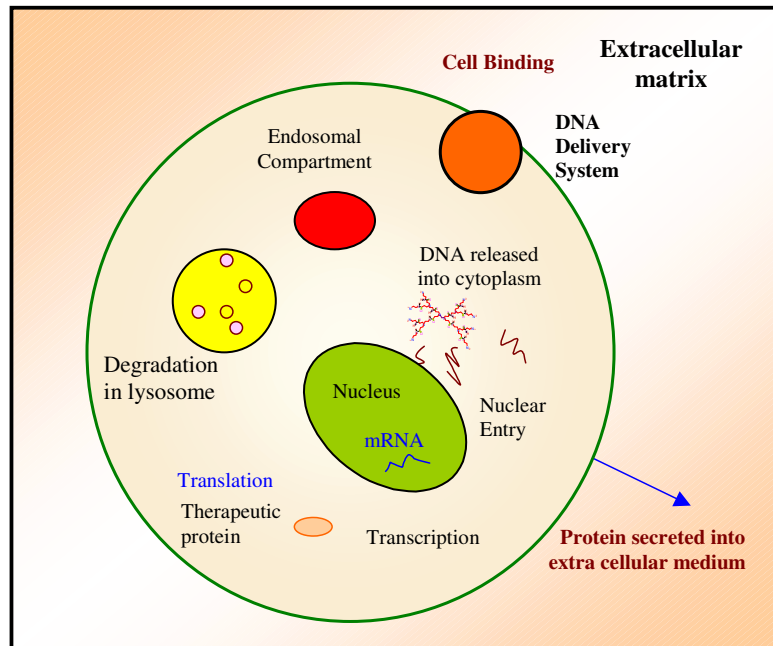


Figure 1.4. Schematic representation of the mechanism of dendrimer-mediated gene delivery into cells. The complex composed of dendrimer and plasmid DNA attach electrostatically with the negatively charged phospholipids on the exterior surface of the cell membrane stimulating complex uptake by energy-dependent endocytosis. Adapted from (Bloomfield, 1991, Eichman et al., 2000).

Field Code Changed

1.6 PAMAM DENDRIMERS FOR *IN VITRO* GENE TRANSFER

DNA and PAMAM dendrimers form complexes on the basis of the electrostatic interactions between negatively charged phosphate groups of the nucleic acid and protonated amino groups of the polymers (Kukowska-Latallo *et al.*, 1996, Bielinska *et al.*, 1997). The physicochemical properties of dendrimers are an outgrowth of their shape, as well as the presence of high positive charge density of protonated primary amine groups on their surface.

Together with high solubility in water, these characteristics have led to the use of these polyamines to mediate efficient DNA transfer into numerous cell lines *in vitro* (Bielinska *et al.*, 1999). It has been observed in studies using intact dendrimers that G5 or above show greater transfection efficiencies than G0–G4 (Haensler and Szoka, 1993). Further work from these investigators revealed that the transfection observed in these experiments was mediated by degraded dendrimers (Tang *et al.*, 1996) when compared with the intact G5 polymer. The enhanced transfection activity of the degraded polymer, Superfect® and Polyfect® (Rudolph *et al.*, 2000) (heat-activated low- and high-generation dendrimers, respectively) was attributed to increased flexibility in the structure. Independent studies by Baker and co-workers documented the efficiency of intact dendrimers as synthetic vectors for the delivery of genetic material into cells (Bielinska *et al.*, 1996, Kukowska-Latallo *et al.*, 1996). This work employed various generations of intact dendrimers to transfect plasmid DNA in a variety of cells using luciferase and β -galactosidase reporter genes to quantify efficiency. In contrast to the results obtained with degraded PAMAM dendrimers, only intact dendrimers > G5 mediated significant transfection, and this required the addition of a dispersing agent such as (diethylamino) ethyl (DEAE) dextran. The addition of other agents to the DNA–dendrimer complex alter transfection. For example, chloroquine or dextran added to dendrimer–DNA complexes significantly increase transgene expression in a number of cell lines. DEAE dextran is believed to alter the nature of the dendrimer by dispersing complex aggregates. However, it is cytotoxic and might prevent stable gene integration. Complexing DNA with dendrimers changes the molecular structure of DNA and results in condensation and aggregation of

DNA particles, but also increases DNA survival upon delivery *in vitro* and *in vivo* (Bielinska *et al.*, 1999). Complex formation analysis and characterization has been carried out on soluble– insoluble or low–high density particles by various methods such as UV light absorption, laser light scattering and measurements that use radiolabeled DNA and/or dendrimers (Bloomfield, 1996). The actual binding affinity constants of DNA and dendrimers are not easily determined, partly because of the subsequent aggregation and precipitation of the complexes (Rau and Parsegian, 1992, Bloomfield, 1996).

1.7 THE CONCEPT OF DNA CONDENSATION

DNA condensation is defined as the dramatic decrease in DNA volume to an orderly collapsed state of a finite size, ready for reversibility, in which the volume fractions of solvent and DNA are comparable. It is more common that several molecules are incorporated into the condensed structure. Therefore, condensation is difficult to distinguish clearly from aggregation or precipitation (Bloomfield, 1991, Bloomfield, 1996, Bloomfield, 1997). DNA condensation refers to *in vitro* phenomena that mimic aspects of DNA packing and unpacking; it has an intrinsic role in DNA replication, protein synthesis, and cellular reproduction. Studying these phenomena is important to learn about general physical-chemical mechanisms that are important for packing and unpacking DNA *in vivo*, and in view of applications of various types of DNA condensates as non-viral gene carriers for gene therapy. DNA condensation is a complex interplay of interactions (Bloomfield, 1991, Marquet and Houssier, 1991). These include entropy loss upon collapse of the worm-like coil, polymer stiffness that sets a limit on the radius of curvature, electrostatic

repulsions, and hydration (Bloomfield, 1996). The predominant force that must be overcome for condensation to occur is the self-electrostatic repulsion between the phosphate charges along the DNA backbone. DNA condenses in the presence of multivalent cations when 67-90% of its charge is neutralized (Wilson and Bloomfield, 1979, Bloomfield, 1997, He *et al.*, 2000). The counter-ions not only screen coulombic repulsions between the DNA phosphates, they also produce attraction through correlated fluctuations of the ion atmosphere. This idea was first put forward by Oosawa in 1970 (Bloomfield, 1996) and references therein. Experimentally, a charge of +3 or greater is required for condensation in aqueous solution at room temperature, but divalent cations will be effective if conditions are only slightly different. Detailed Monte Carlo simulation on hexagonally packed DNA predicts that divalent cations will lead to a net attraction at a separation of 5-15 Å between surfaces, depending on ion size and salt concentration (Lyubartsev and Nordenskiöld, 1995). We will show experimentally that even monovalent cations could lead to a temporary attraction between DNA double strands (ds).

1.8 MECHANISM OF CONDENSATION

Condensing agents generally work either by decreasing repulsions between DNA segments (e.g., neutralizing of phosphate charge, reorienting water dipoles near DNA surfaces, by multivalent cations), by making DNA-solvent interactions less favourable, or by causing localized bending or distortion of the DNA (Bloomfield, 1991, Bloomfield, 1996, Bloomfield, 1997, Bloomfield, 1998). There are a number of hypotheses regarding the mechanism of formation of these structures particularly with regard to toroidal condensates

(Sadoc, 2000, Shen *et al.*, 2000). These hypotheses are based on both experimental and theoretical evidence. The inner radii of the toroids are typically about 14 nm, regardless of the number of DNA molecules in the condensate (He *et al.*, 2000).

The size and morphology of condensed DNA particles are determined by the kinetics and thermodynamics of the system. Thermodynamically, a model has been proposed for the formation of toroids from DNA condensed with crowding polymer in high salt, based on a theory of the undulation enhancement of the electrostatic interaction in hexagonal arrays of semi-flexible polyions. A two-stage condensation process has been observed with an initial slow nucleation phase where the contour length of the DNA decreases at constant speed. This is followed by a fast collapse to the final condensate structure (Yoshikawa and Matsuzawa, 1995, Vasilevskaya *et al.*, 1997).

DNA condensation leads to rod like or toroidal bundles of comparable cross-sectional diameter, equivalent to about 10-15 DNA ds across. This diameter is roughly independent of the species of multivalent cation or the length or source of DNA. In rod and toroid condensates, the double-helical strands of DNA are packed almost parallel to each other in hexagonal array, with surfaces separated by 5–10 Å of solvent. These observations pose many fundamental challenges to our understanding of electrostatic interactions in solutions (Ha and Liu, 1997, Ha and Liu, 1998, Ha and Liu, 1999b, Ha and Liu, 1999a).

1.9 THE NEED FOR SURFACE CHARACTERIZATION

Much of delivery system's stability and efficacy can be attributed to the interaction of molecules with the systems surface (Davies *et al.*, 1997). For example, the surface properties of a molecule are different from the bulk

properties, since molecules at a surface are not surrounded by similar species, but are exposed to an interface. This interface significantly modifies molecular behaviour and, therefore, can generate molecular orientations and mechanical properties, which are different to the bulk material (Shakesheff *et al.*, 1996). Therefore, understanding the molecular surface interactions, which in turn are governed by its surface chemistry, we may be able to predict the system's suitability for a chosen application and hence reduce the extent of testing needed to find a new candidate for the chosen biomedical application. The AFM techniques can provide high resolution images of the topography of surfaces to sub nanometer resolution and this imaging can be performed under liquid, gas as well as vacuum conditions. In addition, AFM techniques can measure the local mechanical properties of surfaces and the forces of interactions experienced between molecules in close proximity. These attributes have resulted in the AFM techniques making a considerable impact in nanomaterial sciences.

1.10 THE ATOMIC FORCE MICROSCOPE (AFM)

1.10.1 Background

The application of the AFM has ranged from the characterisation of inorganic materials to nanolithography and continues to rapidly grow. The number of AFM articles in the Medline database has almost doubled each year since the first articles appeared in 1988 (Hansma *et al.*, 1988, Betzig and Chichester, 1993, Shao *et al.*, 1996, Diaspro and Rolandi, 1997, Kasas *et al.*, 1997, Karbach and Drechsler, 1999, Czajkowsky *et al.*, 2000, Zlatanova *et al.*, 2000, Bonnell, 2001, Reich *et al.*, 2001). A few years later, a set of articles appeared

showing the promising possibilities of the technique in the field of imaging biomolecules such as DNA in air and in liquids (Drake *et al.*, 1989, Bustamante *et al.*, 1992, Lindsay *et al.*, 1992, Lyubchenko *et al.*, 1992, Thundat *et al.*, 1992, Hansma *et al.*, 1992a, Hansma *et al.*, 1992b, Lyubchenko *et al.*, 1993, Thundat *et al.*, 1993, Yang and Shao, 1993, Shao and Yang, 1995, Hansma, 2001), providing new information about the bend angles of DNA–protein complexes (Hansma, 1996a) and ligand-induced DNA curvature. One of the main advantages of AFM over other ultra-high resolution microscopy techniques is that sample preparation is relatively simple and does not involve negative staining or shadow casting with a metal coating (as required for electron microscopy), hence AFM measurements can be made to reflect directly the natural surface of the specimen (Bezanilla *et al.*, 1994, Morris *et al.*, 1999, Henderson and Oberleithner, 2000, Jiao *et al.*, 2001, Neish *et al.*, 2002). The early dynamic visualization of fibrin polymerization (Drake *et al.*, 1989) showed the potential of the AFM for imaging processes in pseudo real time. Soon after that living cells were imaged (Haberle *et al.*, 1991) and dynamic processes occurring at the cell membrane were examined (Haberle *et al.*, 1992). To improve performance, Photonic Force Microscope, a scanning probe microscope without a mechanical connection to the tip and working with extremely small loading forces, has been developed to image inside the cell, at the European Molecular Biology Laboratory (EMBL) in Heidelberg during the last few years (Pralle *et al.*, 2000). In addition, non-imaging applications for AFM are now one of the most exciting areas for AFM, allowing investigations into intermolecular and intramolecular forces. This is done by the measurement of the interaction forces between the probe and the surface at

single specific points on that surface. For example DNA oligonucleotides covalently attached to both the tip and the sample surface have allowed histograms of unbinding forces to be recorded showing peaks in the range of 0.5–2 nN. This was attributed to the rupture of base-paired oligonucleotides of different lengths (Lee *et al.*, 1994). The unbinding force for a single biotin–avidin complex was measured from the histogram of the adhesion force for the final unbinding interaction in the force curves (Florin *et al.*, 1994a, Allen *et al.*, 1996). The tip–sample adhesive forces on the biological sample and on the surface to which it is bound were measured using force mapping. In force mapping, the tip is raster scanned while generating force curves (Frisbie *et al.*, 1994, Ellis *et al.*, 1999a, Heinz and Hoh, 1999, Ludwig *et al.*, 1999, Raab *et al.*, 1999, Allen *et al.*, 2001). With force mapping, one can also reveal the patterns of elasticity, Van der Waals forces and electrostatic interactions on the sample surface (Radmacher *et al.*, 1994). Depending on the mode of operation many types of forces and material properties can be probed, including repulsive (exchange) (Weisenhorn *et al.*, 1992), elasticity, frictional, (Sokolov, 1996), capillary (Piner *et al.*, 1999), electromagnetic, chemical, and non retarded Van der Waals forces, some times called London dispersion forces (Hartmann, 1991). There is also a broad range of non-biological AFM applications. These applications include the semiconductor industry, for example, wafer examination and studying the effects of chemical mechanical polishing.

Images are obtained by measuring changes in the magnitude of interaction between the probe and the surface. The degree to which tip shape is evident depends on the roughness of the sample. It is well known that the images generated by the AFM are influenced by the tip geometry, especially if the

samples are in the size range of the tip radius of curvature of 5-20 nm (Larmer *et al.*, 1997). The resulting image is convolutions of tip and sample geometries, and a widening of the sample structure by approximately the tip diameter is commonly observed (Fritzsche *et al.*, 1997, Rivetti and Codeluppi, 2001). A schematic representation of an AFM is shown in Figure 1.5.

1.10.2 AFM Modes of Employment

Different operating principles of AFM have been developed with the aim of reducing surface distortion (Howland and Benatar, 1996, Henderson and Oberleithner, 2000, Bonnell, 2001), (Figure 1.5) namely, contact mode AFM (CM-AFM) (Hansma *et al.*, 1988, Ikai, 1996), non-contact mode AFM (NCM-AFM) (Binnig *et al.*, 1986, Cappella and Dietler, 1999), and tapping mode AFM (TM-AFM) (Martin *et al.*, 1987, Anczykowski *et al.*, 1996). The choice of mode depends upon the nature of the sample of interest and the level of image clarity required.

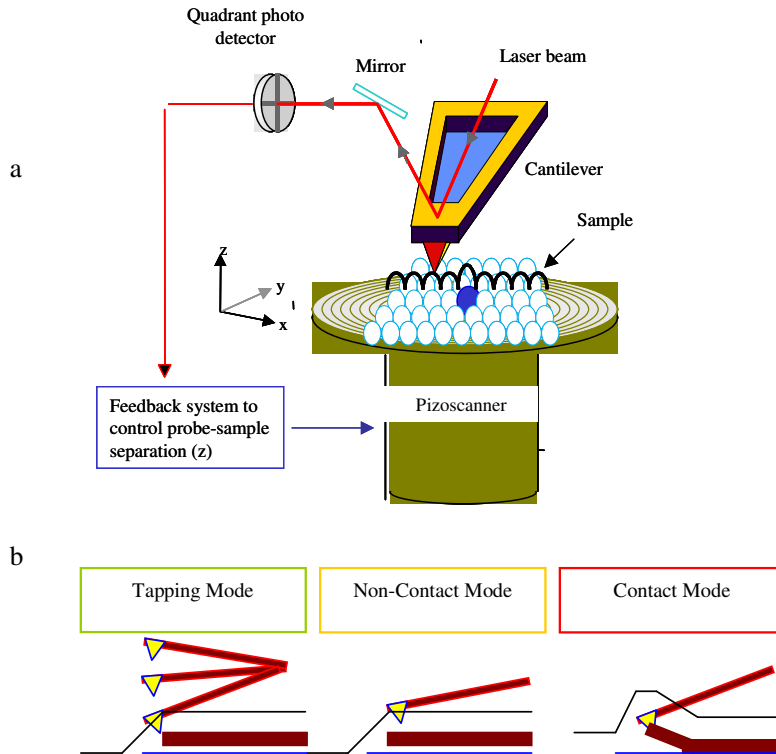


Figure 1.5. A schematic representation of an AFM. (a) A sharp probe on a flexible cantilever is raster scanning across the surface at constant force, its position monitored by reflecting a laser beam off the back of the cantilever onto a split photodiode. A piezoelectric scanner controls this scanning motion. The subsequent bending of the lever due to probe-sample interaction reveals an image at nanometer resolution, (b) Cross-sectional representations of the cantilever probe and sample in contact, non-contact and tapping mode AFM. In contact mode, the probe is damaging the imaged sample. In non-contact mode, the probe oscillates above the surface without making contact; this mode does not cause sample distortion, but generally results in poor resolution. Tapping mode is a hybrid of these two modes. Frictional forces are reduced due to the vertical oscillation of the cantilever-probe assembly, but resolution is maintained because the probe makes intermittent contact with the surface.

1.10.2.1 Contact Mode AFM (CM-AFM)

In CM-AFM (Butt *et al.*, 1990, Horber *et al.*, 1993, Le Grimellec *et al.*, 1994), the tip permanently touches the surface of the sample during scanning. Repulsive, Van der Waals, hydrophobic and electrostatic forces are exhibited when the tip and sample are in contact. Contact mode imaging is best employed on hard, non-deformable samples as the large tip-sample forces (≥ 1 nN) exhibited can cause molecular deformation of the sample (Lemoine and McLaughlin, 1999). This effect can be reduced by using a cantilever with a smaller spring constant and also by imaging in an aqueous environment. These act to decrease forces between the probe and sample. Contact mode can be conducted in air or liquid (Cappella and Dietler, 1999). The feedback mechanism is either controlled by variable deflection mode or constant deflection mode. In the variable deflection mode, the height of the cantilever remains constant, therefore as the topography of the surface goes up and down the deflection of the tip is either increased or decreased. The change in the reflection angle of the laser is recorded and converted to an image of the surface contours. In constant deflection, the deflection of the tip and hence the force between it and the sample are kept constant by moving either the tip or sample up or down. In this mode, it is these movements, which are converted into the topography image.

1.10.2.2 Non-Contact Mode AFM (NCM-AFM)

In NCM-AFM which was introduced by Martin et al (Martin *et al.*, 1987), the cantilever is oscillated at or near its resonant frequency at small amplitudes a finite (nm) distance away from the surface so that the tip and surface are never brought into contact. Images are obtained due to the change in this amplitude caused by long-range Van der Waals, and electrostatic interactions between the tip and surface. Due to the fluctuating nature of these forces the resolution of non-contact images is not always high enough to obtain definitive feature characterization (Cappella and Dietler, 1999).

1.10.2.3 Tapping Mode/ AFM (TM-AFM)

Tapping mode (TM-AFM) (Zhong *et al.*, 1993), also called intermittent contact force microscopy, embraces aspects of the other two modes: minimizing surface contacts and lateral forces by periodically touching the surface with the cantilever. The oscillating cantilever is driven to oscillate near its resonant frequency with a selected amplitude from the sample, called free amplitude, usually 10-100 nm, resulting in a short-time contact with the sample during each cycle of the oscillation (Chen *et al.*, 1998, Fain *et al.*, 2000). The vibrating tip has enough kinetic energy to escape out of the water layer, which is present on surfaces under ambient conditions. When the tip strikes the surface, part of the energy in the vibrating system is transferred to the sample leading to a reduced vibrational amplitude (called oscillation amplitude). During scanning, the feedback mechanism adjusts the distance between the sample and the base of the cantilever to maintain the oscillation amplitude of a tapping cantilever. The variation of surface topography alters the oscillation amplitude of the

cantilever. The vertical movement of the scanner, which moves to maintain the preset oscillation amplitude, then generates the topographic contrast (Hansma *et al.*, 1994, Putman *et al.*, 1994, Marth *et al.*, 1999). However, since the tip is only periodically in contact with the surface, the lateral forces, which cause deformation and sweeping of soft samples in contact mode, are reduced.

TM-AFM can also be used to generate a phase-contrast image, by monitoring the difference in phase angle (phase shift or phase-lag) between the cantilever's oscillations and the signal, which drives the piezoelectric crystal during tapping (Tamayo and Garcia, 1997, Bar *et al.*, 1999).

The simultaneously acquired phase image provides complementary information about surface properties and their lateral distribution with high spatial resolution. This is because the phase angle of cantilever oscillation lag behind the driving oscillation is sensitive to the change in tip-sample interactions due to both tip-sample separation, and the material properties of the tip and the sample (Butt *et al.*, 1995). Phase contrast cannot therefore be generated if the surface is highly uniform. Phase contrast also arises from compositional variations of the surface as well as the topographical variations caused by changes in adhesion between the tip and the specimen surface. Further surface-related information may also be obtained from selected points on a sample surface by measuring the amplitude and/or phase lag of cantilever oscillation with tip-sample distance. We refer to such data as amplitude-phase, distance (a-p,d) measurements (Chen *et al.*, 1998, Danesh *et al.*, 2000).

1.10.2.4 Tapping Mode AFM (TM-AFM) in Liquids

There are many advantages to operating an AFM with the sample and cantilever immersed in a fluid. These advantages include the elimination of capillary forces (Hansma *et al.*, 1994, Putman *et al.*, 1994, Gao, 1997), the reduction of Van der Waals forces and the ability to study technologically or biologically important processes at solid-liquid interfaces (Putman *et al.*, 1994, Henderson *et al.*, 1996). There have, however, been some disadvantages involved in working in liquids, these ranges from nuisances such as leaks to more fundamental problems such as sample damage on hydrated and vulnerable biological samples (Hansma *et al.*, 1994).

1.10.3 Force-Displacement Curves (f-d-c(s))

Force microscopy can provide a wealth of nanometer scale information critical to understanding the properties of surfaces and interfaces. However, since the tip material most commonly used in AFM is silicon or silicon nitride, AFM tips do not have much chemical variety without intentional modifications (Han *et al.*, 1995, Noy *et al.*, 1998). This was developed further in 1994 by Florin *et al.*, (Florin *et al.*, 1994b) who attached specific molecules to the tip that selectively adhere to other molecules. To study probe-sample interaction by means of force-distance curves (Burnham *et al.*, 1993), the sample (or the tip) is ramped along the vertical axis and the cantilever deflection δ_c is acquired. An AFM force-distance curve is the result of two contributions: the tip-sample interaction $F(D)$ and the elastic force of the cantilever (Figure 1.6). The tip-sample force is given by Hooke's law: $\mathbf{F} = -\mathbf{k}_c\delta_c$.

Where F is the Force in nano Newton (nN), δ_c is the cantilever deflection in nanometers (nm) and k_c is the cantilever spring constant in nN/nm. The distance controlled during the measurement is not the actual tip-sample separation distance (D), but the distance (Z) moved by the z-piezoelectric scanner. These two distances differ because of cantilever deflection δ_c and because of sample deformation δ_s . these four quantities are related as follows:

$$D = Z - (\delta_c - \delta_s).$$

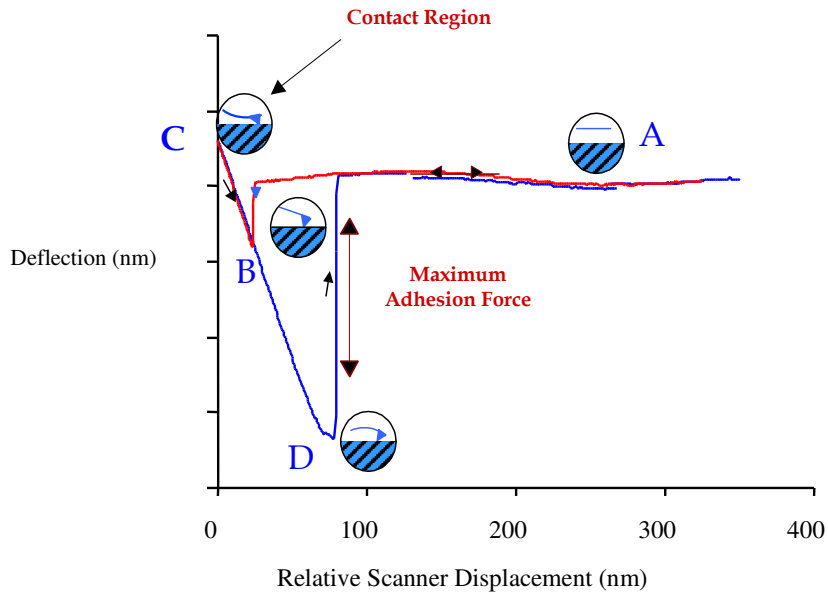


Figure 1.6. Force-displacement curves

During a force displacement cycle the probe is moved toward the surface (approach trace) at constant velocity until it is brought into contact with the sample at point (B) until a predetermined point of maximum load is reached (C). The direction of motion is then reversed, and the probe is withdrawn from the sample surface. As the probe is withdrawn from the sample (retract trace) the probe “sticks” to the surface due to interactions between the probe and the sample (D). The magnitude of this “sticking force is calculated from the difference between the maximum cantilever deflection during the withdrawal phase of the cycle and the point of zero cantilever deflection.

1.10.4 Amplitude-Phase-Distance (a-p-d) Measurements.

The a-p-d is demonstrated in Figure 1.7. At point a, the cantilever is vibrated at its resonant frequency (away from the sample surface) and is moving toward the surface at a steady rate with no observable changes in its free amplitude or phase. At point b the cantilever is close enough to the surface that it experiences both attractive and repulsive forces, such as hydrophobic, electrostatic, Van der Waals, and capillary force interactions (Israelachvili, 1991). The region between point b and point c is described as the attractive section of the a-p-d curve because the phase shift indicates the dominant forces are attractive (Chen *et al.*, 1998). In this region, the amplitude dampens and the phase lag increases (positive phase shift) as the tip moves toward the surface. At point c, the phase lag starts to decrease; indicating a change in tip-sample interactions from attractive-dominated to repulsive-dominated. The region between point c and point d is described as the repulsive section. The principle repulsive force is the elastic response of the sample to an increasing indentation by the tip and to a smaller extent of Van der Waals forces. In this region, both the amplitude and phase lag continue to decrease, (negative phase shift) as the tip continues to move forward, until point d, (oscillation amplitude). The tip is then retracted from the sample surface.

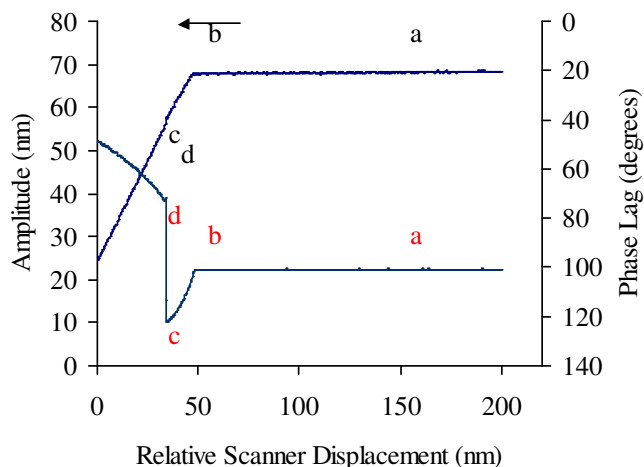


Figure 1.7.Amplitude-phase-distance curves (See text for explanation).

1.11 AIMS OF THESIS

As discussed in the previous sections, the different AFM modes can be utilized as surface analytical techniques to build up a full picture of both PAMAM dendrimers as a non-viral gene delivery carrier and biological systems (DNA and DNase I). This thesis aims to investigate in near *in situ* conditions and at the individual molecular scale the mechanisms of formation and dissociation of the different DNA-PAMAM dendrimer condensates and to further elucidate the ability of PAMAM dendrimers to protect the individual DNA molecules from the degradative enzyme (DNase I) as an example for an external and internal barrier for efficient non viral gene delivery system.

Chapter one: Introduction

The experimental chapter 2 will focus onto introducing the different materials and techniques used throughout this study. Experimental details different from those mentioned in this chapter are then mentioned with the corresponding text.

Chapter 3 will concentrate on the visualization and characterization of the individual G4 PAMAM dendrimers molecules on surfaces (mica, Au and SAMs), their aggregates and their monolayers and multilayers formation in 4D and to further investigate the behaviour of G6 and G8 on mica.

Chapter 4 will elucidate the ability to image the individual DNA molecules in liquid, in the absence and presence of divalent cations and the experimental applications of monovalent cations fluctuation in this subject.

In chapter 5, the interaction between PAMAM dendrimers and DNA are investigated in near *in situ* conditions. The effect of dendrimers loading ratios, incubation time of DNA with polymer, the effect of dendrimers generations, the effect of the presence and absence of buffer, the effect of soluble cations and the mechanisms of formation of different DNA-PAMAM dendrimers condensates are investigated.

The final experimental chapter, chapter 6 follows the different mechanisms of the DNA-PAMAM dendrimer condensates relaxation and fragmentation by DNase I in 4D and investigating the mechanisms of wrapping and unwrapping of the DNA on the larger dendrimers.

CHAPTER TWO

EXPERIMENTAL MATERIALS, METHODS AND INSTRUMENTATION

2.1 EXPERIMENTAL MATERIALS

All materials, unless otherwise stated were purchased from Sigma-Aldrich (Poole, UK) and used without further purification. Solvents utilized were of HPLC quality and obtained from Fisher (Loughborough, Leicestershire, UK). All water used was obtained from an ELGA purification system (resistivity ca 18.2 M Ω .cm, Maxima USF ELGA, High Wycombe, UK). Water and buffers were filtered through a 0.2 μ m pore size filter, (Sartorius, Göttingen, Germany) prior to use.

2.1.1 Cationic Reagents

The cationic reagents investigated fall into two categories, small molecular weight cations (Mg⁺², Mn⁺²) and cationic polymers. The cationic polymers utilized in this study are Generation 4, 6 and 8 (polyamidoamine) PAMAM dendrimers i.e., G4, G6 and G8. They were generated from amidoamine units emanating from an ethylenediamine (NH₂-CH₂-CH₂-NH₂) core, terminated with amino groups at the external surface. Calculated formula weights for the G4, G6 and G8 are 14,215, 58,047 and 233,378 Kilo Dalton respectively and contains 64, 256 and 1024 surface primary amino groups respectively

(Dendritech, Midland, MI), their ideal diameters are 4.5, 6.7 and 9.7 nm respectively (Li *et al.*, 2000). Samples were obtained as methanol solutions. To generate aqueous solutions, a portion of the methanolic stock solution from each generation was dried under a stream of argon and subsequently placed under argon in a vacuum ($p \sim 0.01$ Torr) for several hours. The dried materials were re-dissolved in water to yield $30 \mu\text{g}\cdot\text{ml}^{-1}$ aqueous stock solutions, which were stored at 4°C for a maximum of seven days. This method follows previous reported work which avoids hydrolytic degradation of PAMAM dendrimers at room temperature (Li *et al.*, 2000, Hill *et al.*, 2001). Immediately before use, a fraction of the stock solution was prepared to a concentration that allowed polymer and DNA solutions to be combined in equal volume.

2.1.2 Model Surfaces (Alkanethiol Self-Assembled Monolayers)(SAMs)

During the last decade, there has been much work on controlling the properties of surfaces through the use of organic molecular monolayer thin films. The most widely used system has been the self-assembly of alkanethiolate adsorbates onto gold (Au) surfaces (Xu *et al.*, 1998). Since 1983 they have been employed in studies of self-assembly, electron transport, and optical constants (Guo *et al.*, 1994, Liu and Salmeron, 1994, Tamada *et al.*, 1997, Woodward *et al.*, 2000), as well as for applications in surface modification, biosensors, and lithography (Barrena *et al.*, 1999). Furthermore, due to their simplicity, and molecular order, SAMs are especially suitable for understanding and modelling the organic/inorganic interface (Liu and Salmeron, 1994).

The model surfaces (alkanethiols) utilized in this work were octadecyl mercaptane, 16-mercaptohexadecanoic acid, and 11-amino-1-undecanethiol hydrochloride (Dojindo Laboratory, Japan), due to their ability to provide reproducible and well-characterized interfaces. These alkanethiols have alkyl chain lengths of ($n > 10$) and differ only in the functionality of the terminal surface carbon, to yield SAMs samples that have comparable mechanical properties, but different surface chemistry when assembled on gold (Barrena *et al.*, 1999).

2.1.3 DNA

James D. Watson is best known for his discovery of the structure of DNA (deoxyribonucleic acid), for which he shared with Francis Crick and Maurice Wilkins the 1962 Nobel Prize in Physiology or Medicine (Franklin and Gosling, 1953). In 1953, James Watson, Francis Crick, Maurice Wilson and Rosalind Franklin were the first scientists to elucidate the three dimensional DNA double helical structure using the X-ray fibre diffraction patterns (Franklin and Gosling, 1953, Watson and Crick, 1953). The structure of DNA is illustrated by a right-handed double helix, with about 10 nucleotide pairs per helical turn. Each spiral strand, composed of a sugar phosphate backbone and attached bases, is connected to a complementary strand by hydrogen bonding (non-covalent) between paired bases, adenine (A) with thymine (T) and guanine (G) with cytosine (C). The Watson-Crick model of the DNA double helix stabilized by complementary base pairing and hydrogen bonding suggested a possible copying or replication mechanism. The sequence or arrangement of bases from one strand of the helix accurately predicts the

sequence of bases from the other, complementary strand. A representation of the DNA double helix is depicted in Figure 2.1.

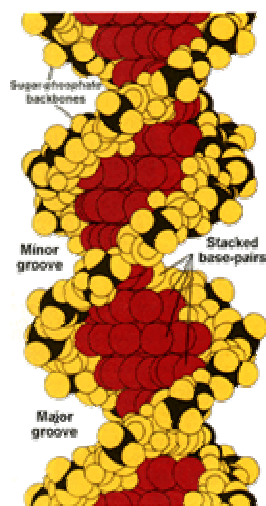


Figure 2.1. A space-filling model of the DNA double β -helix. The DNA molecule as modelled by Watson and Crick, shows how closely the bases are packed within the helix. The major and minor grooves are indicated, (Mathews and Van Holde, 1996).

Detailed information on the chemical, physical and biological properties of DNA is extensively available (Stryer, 1988, Blackburn and Gait, 1990, Neidle, 1999, Bloomfield *et al.*, 2000).

Two types of DNA have been used in this study.

2.1.3.1 pBR322

The lyophilised plasmid pBR322 is a well-characterised 4365 bp plasmid. This was diluted to a stock solution of $100 \mu\text{g}\cdot\text{ml}^{-1}$ w/v in water and further diluted before use to $3.3 \mu\text{g}\cdot\text{ml}^{-1}$ in 10% w/v (1mM) phosphate buffered saline, (PBS, 0.014 M NaCl, 0.001 M phosphate, pH 7.4) for DNA imaging in the absence of

divalent cations, in 10 % w/v PBS containing 1mM MgCl₂ and 1mM NiCl₂, if used for the imaging of bare DNA on mica in the presence of divalent cations, or in water, if used for complex formation.

2.1.3.2 pRSVLuc

A 6000 bp plasmid pRSVLuc, containing the firefly luciferase gene, was a generous gift from Cobra Therapeutics (Keele, UK). It was supplied as a 1 mg.ml⁻¹ solution in water, and was diluted to 10 µg.ml⁻¹ for gel electrophoresis experiments.

2.1.4 DNase I Enzyme

DNase I is a pancreatic endonuclease, first crystallized by Kunitz in 1950 (Kunitz, 1950), splitting phosphodiester linkages, preferentially adjacent to a pyrimidine nucleotide yielding 5'-phosphate terminated polynucleotides with a free hydroxyl group on position 3'. The proton acid-base catalysis mechanism proposed by Suck and Ofner (Suck and Ofner, 1986) was summarized in Figure 2.2. Structural analysis by X-ray crystallography shows that DNase I binds in the minor groove of B-type DNA forming contacts in and along both sides of the minor groove extending over a total of 6 base pairs plus 2 adjacent phosphates. As a consequence of DNase I binding, the minor groove opens by approximately 3 Å and the duplex bends towards the major groove by about 20° (Lahm and Suck, 1991, Suck, 1997, Paul *et al.*, 2000). In the presence of divalent metal ions, DNase I cleaves DNA at the phosphodiester bonds that link adjacent nucleotides. In the presence of Mg²⁺, DNase I hydrolyzes each strand of a duplex independently leading to random single strand breaks

(SSBs). The purine-pyrimidine bonds are subsequently preferentially cleaved leading to double strand breaks (DSBs) leading to a final product of di- and higher oligonucleotides (Weston *et al.*, 1992, Pan *et al.*, 1998, Fojta *et al.*, 1999, Pan and Lazarus, 1999). In the presence of Mn^{2+} , the enzyme cleaves both strands of DNA at approximately the same site, leading directly to DSBs. DNase I acts upon single chain DNA (Young and Sinsheimer, 1965) and upon double-stranded DNA and chromatin. In the latter case, although histones restrict susceptibility to nuclease action, over a period of time, nearly all chromatin DNA is acted upon. This could result from the looseness of histones attachment to DNA (Mirsky and Silverman, 1972). The intracellular functions of the enzyme are probably controlled by a DNase inhibitor (Lindberg and Skoog, 1970), which according to Lazarides and Lindberg (Lazarides and Lindberg, 1974) is actin. Margison and O'Connor (Margison and O'connor, 1972) report that DNase activity is greatly reduced for methylated DNA.

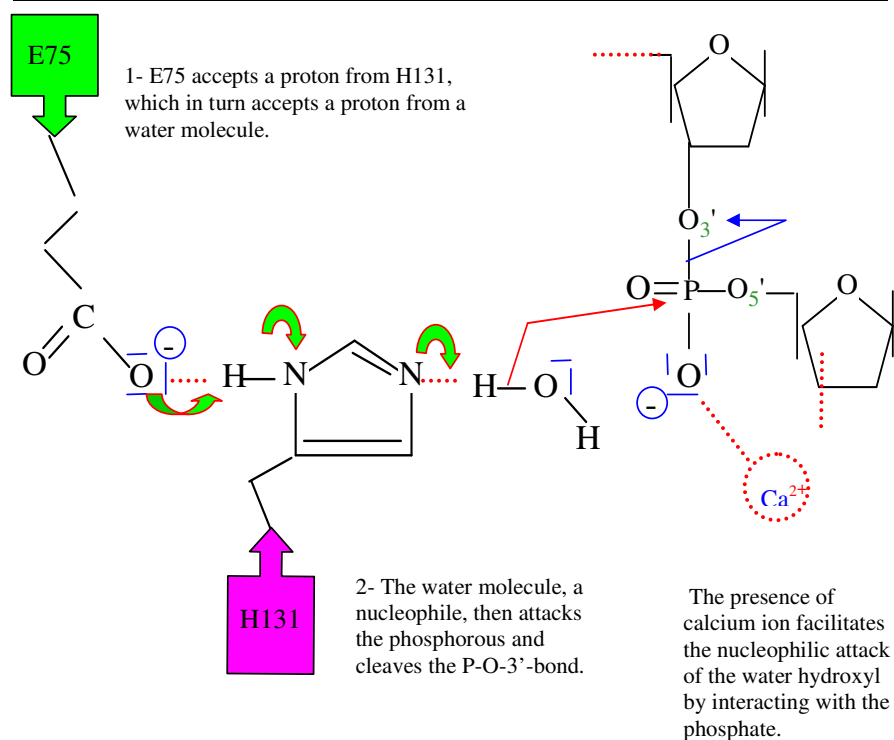


Figure 2.2. Proposed mechanism of action of DNase I enzyme. In a general acid-base catalysis (proton acceptor-donor chain Glu-His-water). In agreement with this mechanism, carbomethylation of H131 at N-3 as well as protonation by lowering the pH inactivates the enzyme.

Deoxyribonuclease I from bovine pancreas (DNase I), was obtained as a white lyophilized powder. Enzymatic activity was approximately given as 2,500 units/mg proteins. As received, it was diluted to a stock solution of 100 unit.ml⁻¹ in water and further diluted before use to 12 unit.ml⁻¹ in 1mM PBS, containing 2 mM MgCl₂ and 1mM NiCl₂, pH 7.4, except for manganese experiment, where the MgCl₂ was replaced by MnCl₂.

Unit definition: One unit completely digests 1 μg of plasmid DNA to oligonucleotides in 10 min at 37°C. One unit produces a change in A260 of 0.001 $\text{min}^{-1} \cdot \text{ml}^{-1}$ at pH 5.0 at 25 °C, using DNA, TYPE I or III as substrate.

2.2 METHODS AND INSTRUMENTATION

2.2.1 Substrate Preparation

2.2.1.1 Mica

Freshly cleaved mica (Agar Scientific, Essex, UK) was used in this study. Mica has been previously demonstrated to be a material well suited to the immobilisation and imaging of DNA (Hansma *et al.*, 1992a, Wagner, 1998). It is inert and can be easily prepared to provide a clean and atomically flat substrate by the cleaving away of surface layers. Mica sheets were cleaved using a clean scalpel or sticky backed tape.

2.2.1.2 Epitaxial Gold Films

Epitaxial gold films were prepared using the vapour deposition method of Derose *et al.*, (Derose *et al.*, 1991, Hegner *et al.*, 1993). Gold (99.9%, Birmingham Metals, UK) was first cleaned in acetone and placed into a tungsten crucible, 30 mm beneath a heating stage, in a vacuum coating system. Freshly cleaved mica was placed side down facing the Au sample. A vacuum of 10^{-6} m Bar was reached before heating the mica to 320°C for 6 hours to remove contaminants from the mica surface. Au was resistively heated and evaporated at a rate of 0.1 $\text{nm} \cdot \text{sec}^{-1}$ onto mica at 315°C. The Au film was annealed by further heating at 390°C for 24 hours. Generally, thermal annealing of Au films causes the grain boundaries to diffuse across the grains

so that they can merge to produce larger crystalline grains. The specimen was allowed to cool at its natural cooling rate. Returning the vacuum chamber to normal atmospheric pressure allowed gold film retrieval. The gold was then stored under argon prior to use.

2.2.1.3 Template Stripped Gold (TSG)

Epitaxial gold films prepared by the above method were treated using the method of Wagner *et al.*, (Wagner *et al.*, 1995). Gold films were cut into ~ 1 cm³ pieces. 10µl of EPOTEK-377 (Promatech, Cirencester, UK) was applied to the epitaxial gold surface and deposited glue side down onto a glass cover slide. The glass/epoxy/epitaxial gold assembly was cured at 150°C for 1 hour. The assembly was then soaked in a tetrahydrofuran (THF) for 10 minutes at room temperature. Mica was removed by lifting away from the gold surface with a scalpel. The newly exposed TSG was washed in THF, dried in nitrogen and tested for conductivity to ensure complete mica removal.

2.2.1.4 Alkanethiol Self Assembled Monolayers (SAMs) Preparation

1mM solutions of octadecyl mercaptane, 16-mercapto hexadecanoic acid, and 11-amino-1-undecanethiol hydrochloride were separately prepared in ethanol shortly before each experiment. Prior to SAM formation, Au/mica substrates (1cm x 1cm) were cleaned by passing 11 times through a hydrogen flame. Cleaned Au/mica substrates were then immediately immersed in the alkanethiol solutions (2.5 ml) for 24 h. Alkanethiol-coated substrates were then removed from the alkanethiol solutions, rinsed copiously with absolute ethanol to remove droplets of non-covalently bound material, before drying in a stream

of dry nitrogen. This process yielded Au substrates functionalized in methyl (SAM-CH₃), carboxyl (SAM-COOH), and amine (SAM-NH₂) groups.

2.2.1.5 Preparation of PAMAM Dendrimer Coated Substrates for Imaging in Air

Solutions of G4, G6 and G8 PAMAM dendrimers were prepared at a pre determined concentrations in water (pH 6.5-6.9). To produce dendrimer-coated mica, a 20 μ l drop of dendrimer solution was placed on freshly cleaved mica for 30 seconds, rinsed carefully with 5 (40 μ l) aliquots of water to remove loosely adsorbed dendrimer molecules before again being dried in a stream of nitrogen. Alternatively the samples were spin dried in air without washing. In case of adsorbing G4 PAMAM dendrimers onto gold, a 20 μ l drop of dendrimers was spotted onto a hydrogen-flame cleaned gold for 30 seconds, rinsed carefully with 5 (40 μ l) aliquots of water before drying in nitrogen. For the alkanethiol substrates, 40 μ l of dendrimer solution was introduced onto each nitrogen dried alkanethiol substrate and left for 15 min, rinsed with water and dried in nitrogen.

2.2.2. *In situ* AFM Imaging of G4 and G6 PAMAM Dendrimers on Mica

After stable images of freshly cleaved mica were obtained in 30 μ l of water, 15 μ l of water was exchanged with 15 μ l of predetermined concentrations of G4 or G6 PAMAM dendrimers, subsequent real time AFM images were collected at a probe scanning rate of 2.77 Hz.

2.2.3 Surface Characterization of SAMs and Dendrimers-SAMs Complexes

2.2.3.1 Film Morphology of SAMs Monolayers and G4 PAMAM Dendrimers on SAMs in Air

All AFM images were obtained within 1 day of sample preparation. Tapping mode was utilized to obtain all images. SAM substrates and dendrimer-coated samples were imaged utilizing single beam tapping-mode etched silicon probe (TESP) tips (Veeco, Santa Barbara, CA) with resonant frequencies between 278 – 300 kHz, and with ca. 50 N/m force constant. The applied force during the AFM imaging was minimized by adjusting the setpoint voltage to the lower limit suitable for stable imaging.

2.2.3.2 Film Morphology of SAM-COOH Monolayers and G4 PAMAM Dendrimers on SAM-COOH in Liquid

For liquid imaging, the SAM-COOH samples and G4 PAMAM dendrimers samples were prepared as described in section 2.2.1.5 but after washing were not allowed to dry, and were imaged in water using silicon nitride probes mounted on 100 μ m long V-shaped cantilevers, with ca. 0.32 N/m spring constant, and resonant frequencies in water of between 9-12 KHz (Veeco, Santa Barbara, CA). As imaging in liquids eliminates the capillary interaction between the AFM tip and the sample surface, imaging forces less than 0.1 nN could be used in order to yield higher resolution images than could be obtained in air.

2.2.3.3 In situ Imaging of G4 PAMAM Dendrimers on SAM-COOH

While imaging SAM-COOH surfaces, 50 μ l of dendrimer solution (0.1 μ g.ml⁻¹ in deionized water) was injected into the liquid cell. All images were taken at a scanning rate of 2.77 Hz.

2.2.3.4 Functionalization of AFM Tips with Alkanethiol SAMs

TESP tips, and V-shaped contact mode silicon nitride tips were cleaned in acetone, dried in nitrogen and placed into a Au coater (Blazers Sputter Coater, SCD 030, Blazers Union, SWISS). The Au coating was obtained for both sides of these cantilevers at 0.15 mBar, and a current of 30 mA for 45 seconds. Au-coated tips were then immersed in 1mM ethanolic solution of 16-mercapto hexadecanoic acid for 24 hr. The tips were rinsed in ethanol, and allowed to dry in nitrogen prior to use.

2.2.3.5 Force-Distance Curve (f-d-c) Measurements

Force-distance curve (f-d-c) measurements were obtained using SAM-COOH functionalized probes to determine the strength of the interaction with dendrimer-coated surfaces. Before performing such measurements, curves were recorded on the SAM surfaces so that the background level of the interaction could be determined. The slope of the force-distance curve measured on Au surface was used to convert the measured cantilever deflection from the relative units (V) to the absolute units (nm). Since small hystereses typically exist between the approach and retract curves, the average of these

two curves was employed in calibration. Using the cantilever spring constant (k_c) in (N/m), the cantilever deflection (δ_c) in (nm) was converted to force (F) in (nN) using Hooke's law (Burnham *et al.*, 1993, Cappella and Dietler, 1999). The spring constant of each cantilever was determined using the thermal noise method (Hutter and Bechhoefer, 1993). The AFM force spectroscopy plots were corrected for cantilever bending to quantification of probe-sample separation.

2.2.3.6 Amplitude-Phase-Distance (a-p-d) Measurements

Amplitude-phase-distance (a-p-d) measurements were obtained between SAM-COOH functionalized TESP probes and dendrimer coated surfaces in air. For control measurements, a-p-d curves were obtained on all SAM surfaces, again to determine the background level of the interaction. The average slope of a-p-d curves measured on Au surfaces was used to convert the measured cantilever oscillation amplitudes (RMS values) from the relative units (V) to the absolute units (nm), assuming that there was no deformation of Au surfaces and also no deflection of the cantilever during tapping. Again, since small hystereses typically exists between the approaches and retract curves, the average of these two curves was used in calibration.

It is difficult to determine the exact sample surface position in such measurements. Experimentally, however, a significant decrease in amplitude and an increase in phase from their free-status values indicate a start point of tip-sample interactions during tip approach. This can offer a reference position for all a-p-d curves measured on different samples (Chen *et al.*, 1998).

2.2.4 Generic Methodology of DNA Imaging with Atomic Force Microscopy

2.2.4.1 Preparation of DNA Plasmids for Imaging in Air

Two different immobilization procedures were used to adsorb the DNA to the mica substrate. The first method involved using divalent cations to bridge between the negatively charged mica substrate and DNA backbone (Hansma *et al.*, 1993). The second method is to use the G4 dendrimer themselves.

2.2.4.2 Divalent Cation Pre-treatment Method

Plasmid DNA samples prepared to a concentration of $100 \mu\text{g}\cdot\text{ml}^{-1}$ in water were further diluted to $3.3 \mu\text{g}\cdot\text{ml}^{-1}$ in water. One $20 \mu\text{l}$ aliquot of 10 % PBS containing 2 mM MgCl_2 , pH 7.4, was spotted onto a 1 cm^2 disc of freshly cleaved mica, incubated for 30 seconds, rinsed with four 1 ml aliquots of water and dried under a gentle stream of nitrogen before introducing the DNA. Samples were then imaged immediately to prevent drying of the mica surface and the formation of salt crystals.

2.2.4.3 G4 Pre-treatment Method

One $20 \mu\text{l}$ aliquot of $0.1 \mu\text{g}\cdot\text{ml}^{-1}$ G4 solution was deposited onto a freshly cleaved mica disc. This was incubated for 30 seconds, rinsed with five 1 ml aliquots of water, and dried under a gentle stream of nitrogen before introducing the DNA.

2.2.4.4 Preparation of Polymer-DNA Complexes

PAMAM solutions were prepared to a concentration that allowed polymer and DNA solutions to be combined in equal volumes. The quantity of polymer required to produce complexes of a given polymer to DNA ratio was calculated as the ratio between the phosphate groups of the DNA to the primary amino groups of the dendrimers. After predetermined incubation times were achieved, 30 μl of each resulting solution was spotted as a single aliquot onto 1 cm^2 freshly cleaved mica disc. For example, G4-DNA complexes (0.5:1 ratio) were prepared by adding 30 μl of polymer solution ($1.05 \mu\text{g}\cdot\text{ml}^{-1}$) to 30 μl of DNA plasmid pBR322 solution ($3.3 \mu\text{g}\cdot\text{ml}^{-1}$) in water, a 30 μl of the obtained complex then being immediately adsorbed onto mica. Different G4-DNA ratios then were prepared in the same way and incubated for the times stated, at room temperature, adsorbed onto mica, and then covered with the liquid cell. The same methods were then applied for the other two generations of dendrimers.

2.2.4.5 Imaging of DNA Condensates in Air

2.2.4.5.1 *Using Divalent Cations*

Condensates were formed by dilution of the DNA solution ($100 \mu\text{g}\cdot\text{ml}^{-1}$) in water to $3.3 \mu\text{g}\cdot\text{ml}^{-1}$ in 10 % PBS containing 2 mM MgCl_2 . 15 μl aliquot of the resulting solution was then deposited onto a 1 cm^2 freshly cleaved mica disc. After a 30-seconds incubation period, this was rinsed with four 1 ml aliquots of water and dried under a gentle stream of nitrogen. Samples were then imaged immediately.

2.2.4.5.2 *Using PAMAM Dendrimers*

G4, G6 or G8 Polymer-DNA condensates were prepared by addition of equal volumes, (30 μ l), of polymer solution to DNA solution as to make 1:1 charge ratio. After predetermined incubation times, 20 μ l of the resulting solution was spotted as a single aliquot onto a 1 cm^2 freshly cleaved mica disc, incubated for 30-seconds, rinsed with five 1 ml aliquots of water, dried under a gentle stream of nitrogen and imaged.

2.2.4.6 Preparation of DNA for Imaging in Liquid

Three different immobilization procedures were applied.

2.2.4.6.1 *Imaging in the Absence of Divalent Cations.*

The plasmid DNA pBR322 was diluted to either 3.3 μgml^{-1} or 1 μgml^{-1} in 10% w/v phosphate buffered saline. All imaging were conducted at a scan speed of approximately 2-8 Hz and at ambient conditions.

2.2.4.6.2 *Imaging in the Presence of Divalent Cations.*

DNA solution (100 μgml^{-1}) in water was diluted to 3.3 μgml^{-1} in 10 % PBS containing 2 mM MgCl_2 or 1mM MgCl_2 and 1mM NiCl_2 or 1mM MnCl_2 and 1mM NiCl_2 according to the experiment. 30 μ l aliquots of the resulting solution was then deposited onto 1 cm^2 freshly cleaved mica and imaged immediately.

2.2.4.6.3 *Imaging in the Presence of PAMAM Dendrimers.*

PAMAM dendrimers-DNA condensates were prepared by addition of equal volumes, (30 μ l), of polymer solution to DNA solution. After predetermined incubation times, 30-35 μ l of the resulting solution was spotted as a single aliquot onto a 1 cm^2 freshly cleaved mica and imaged immediately. Pre-treatment of the mica substrate was not necessary for the lower polymer ratios in our study.

2.2.5 Effect of DNase I Enzyme

DNase I was diluted with 1mM PBS, containing 2 mM MgCl_2 and 1mM NiCl_2 , pH 7.4 just before use. Polymer-DNA condensates were prepared by the addition of equal volumes of polymer solution to DNA solution. After a predetermined incubation time was achieved, 30 μ l of each resulting solution was spotted as a single aliquot onto the freshly cleaved mica and then covered with the liquid cell. In addition, the DNA was imaged in 10% PBS containing 2 mM MgCl_2 and 1mM NiCl_2 as to determine the configuration of the bare DNA in the absence of both the polymer and the enzyme. After stable imaging of DNA or complexes were obtained on freshly cleaved mica, in most cases it took less than a minute, images were recorded for a further 20 min. An aliquot of 15 μ l of the fluid in the liquid cell was then exchanged with 15 μ l of 2 U/ml DNase I (we refer to this as on substrate experiments). The time of this exchange was defined, as time equals zero. We estimated the number of DNase I molecules to be 125.32 molecules for each one plasmid DNA, i.e 0.3 molecule of DNase I for each DNA turn. Or 0.5 Unit.ml^{-1} DNase I was

introduced to the DNA-PAMAM complexes for a certain incubation times before then introducing the resulted complex to mica (we referred to as in solution experiments). Images were then captured according to the stated times and speeds. For moving features within images, we occasionally changed the x and y offsets to follow these features.

2.3 INSTRUMENTATION

2.3.1 Atomic Force Microscopy

Two AFM instruments manufactured by Digital Instruments™, Santa Barbara, CA were used in this study. The first is a Dimension 3000™ AFM. This is a cantilever-scanning instrument with an entirely open liquid cell. The second is a Multimode™ AFM, also manufactured by Digital Instruments™. In contrast with the Dimension 3000 this system laterally moves the surface beneath the AFM probe. Both systems operate with a NanoScope IIIa™ controller, version 4.23r3. The Multimode™ AFM was utilized in the imaging of DNA condensates in the liquid environment and provided the highest resolution for air and liquid imaging studies at smaller scales. A size E scanner head was used throughout.

Sample preparation for both Digital Instruments™ required the substrate to be firmly secured to a flat metal disc to prevent lateral displacement of the sample during imaging.

2.3.1.1 AFM Cantilevers

For imaging in air, silicon cantilevers, 125 μm in length, with resonant frequencies in the range of 200-300 kHz were employed (Veeco, Santa Barbara, CA). When imaging in liquid, thin armed, 100 μm in length, silicon nitride, oxide sharpened, triangular cantilevers of a nominal spring constant of 0.32 N/m were selected, operating at resonant frequencies of approximately 8-10 kHz (Veeco, Santa Barbara, CA).

2.3.1.2 AFM Data Acquisition and Analysis

All imaging was conducted in tapping mode, with 256 x 256 - 512 x 512 pixel resolution, at a scan speed of approximately 2-8 Hz and at ambient conditions. To achieve an efficient coupling between the drive amplitude and cantilever amplitude response, the cantilever was brought to the sample within a distance of 50nm. Before engaging, scan size and offset of the microscope were set to 0 to minimize sample deformation and contamination of the stylus. To engage the AFM stylus, the piezo drive amplitude was set to 300 mV, resulting in a 1-V amplitude (corresponding to 50 nm with sensitivity of 1 nm/20 mV) of the cantilever. Optimising integral and proportional gains and scan speed minimized both the noise of the topograph and the amplitude signals. Setpoints were chosen close to the free oscillation amplitude to minimize forces exerted on the interfacial species. The difference between the setpoint of jump in and the setpoint adjusted to achieve high-resolution topographs was 0.02-0.05 V, corresponding to a damping of 1-2.5 nm of the free amplitude. All post-imaging analysis, unless otherwise indicated, was carried out on NanoScope

IIIa™ software, version 4.23r3. Images were flattened using first or second order polynomial function to account for Z offsets and sample tilt. Following the flattening process and noise reduction, cross-sectional profiles through features in the image were obtained from those molecular widths and heights that could be assessed. Widths were measured at half the peak height (Schneider *et al.*, 1998) and heights were measured from the average base line to the highest point of the peak. Axial lengths of the plasmid were obtained by tracing the path of the DNA over the surface using SPIP software, Image Metrology, Denmark). This information was also required in order to calculate the volume of condensate structures. In order to measure lateral features, for example the circumference of toroidal condensates or the length of linear condensates, SPIP was used.

2.4 Gel Electrophoresis

The interaction between plasmid DNA and different generations of PAMAM dendrimers was investigated by electrophoresis on 0.8% agarose gel (Promega Corporation, Madison, USA) so as to assess the composition of PAMAM-DNA complexes and to investigate the effect of the DNase I enzyme on the obtained complexes. PAMAM-DNA complexes were prepared as detailed before. The complexes formation was ensured by vortexing briefly, and then incubating at room temperature for 2 hrs. The yield remained transparent, and no precipitation was observed over the entire range of charge ratios examined. These samples were then loaded in the wells of the agarose gel containing ethidium bromide (Ebr) ($1 \mu\text{g}\cdot\text{mL}^{-1}$). It should be noted that ethidium bromide is a carcinogen and should be handled and disposed of with appropriate

precautions. Controls for free cationic polymers were applied to the gel, while a naked DNA was included in each test as a control and to ensure that DNase I activity was effective. The gel-making and running buffer in case of PAMAM-DNA complexes was 40 mM Tris acetate (pH 7.4) and 1 mM EDTA. In case of investigating the effect of DNase I, a successful visualization of DNA requires the dissociation of the polyelectrolyte complexes prior to loading in order to allow the DNA to migrate into the gel and to allow the intercalation of ethidium bromide into the strands. Therefore, by raising the pH of the buffer above the pK_a of the PAMAM dendrimers (~ 9.5), the polymer becomes less protonated, thus allowing the complexes to disassociate under electrophoretic conditions. Therefore, the gel making and running buffer used here was sodium-potassium-EDTA buffer (NaKE buffer), pH 11.3 (4 mM sodium hydroxide, 16 mM potassium chloride, and 1 mM EDTA). While a high pH is desirable to split polymers with the most strongly alkaline pK_a , there is effectively an upper limit to this, because above approximately pH 11.6, ethidium bromide loses its affinity for DNA and fluorescence is lost (Hill *et al.*, 2001). The prepared gel was then submerged in TAE buffer for DNA-PAMAM complexes at room temperature or in NaKE buffer pre-chilled to 4°C for enzyme experiments. The NaKE buffer is also acts as a stopping buffer for the DNase I enzyme by chelating the divalent cations responsible for the enzyme activity. The loading buffer used for each 13 μ l sample (2 μ l DNA + 2 μ l polymer and + 9 μ l preparing buffer for DNA complexes or + 2 μ l DNase I + 7 μ l dissociation buffer) is 2 μ l of (40% sucrose solution + 0.25 w/v bromophenol blue). Samples were then loaded (15 μ l total volume per well) and the gel was run at a constant voltage of 70 V for 1 hr. The total amount of

DNA loaded in each well was 50ng in case of PAMAM-DNA complexes to detect the polymer being separated from the complexes during running and 10ng in case of DNase I experiments. DNA was then visualized with a UV transilluminator and photographs were taken with a Polaroid instant camera.

The staining used for polymers was a 1% brilliant blue R250 in 50:40:10 methanol: glacial acetic acid: water and subsequent washing with the destaining solution (10/10/80 v/v mixture of the staining solution without the dye).

CHAPTER THREE

VISUALIZATION AND CHARACTERIZATION OF PAMAM DENDRIMERS ON DIFFERENT SURFACES

3.1 BACKGROUND

The past several years have seen a considerable growth in the use of dendrimers at surfaces and interfaces. This results from the realization that their unique architecture can translate into unusual chemical and physical properties (Watanabe and Regen, 1994, Evenson and Badyal, 1997, Tsukruk *et al.*, 1997, Watkins *et al.*, 1997, Bliznyuk *et al.*, 1998, Hierlemann *et al.*, 1998, Tsukruk, 1998, Bielinska *et al.*, 2000, Betley *et al.*, 2001, Esfand and Tomalia, 2001, Tully and Fréchet, 2001, Müller *et al.*, 2002, Tomalia *et al.*, 2002). Crooks and co-workers reported the first example of covalent attachment of PAMAM dendrimers to a solid surface. This was accomplished by forming amide bonds between the peripheral amino-groups of the PAMAM dendrimer and the carboxylic acid groups of a self-assembled monolayer (SAM) of mercaptoundecanoic acid on gold (Wells and Crooks, 1996). Sheiko and co-workers first examined the properties of hydrophobic carbosilane dendrimers deposited onto mica and pyrolytic graphite surfaces by using AFM (Sheiko *et al.*, 1996). Li *et al.* (Li *et al.*, 2000) also used the AFM to study the molecular properties of PAMAM dendrimers, i.e., their size, shape, and rigidity after deposition on a mica surface. Hierlemann *et al.* (Hierlemann *et al.*, 1998), have

shown that dendrimers spontaneously form nearly close-packed, monolayer-thick films when exposed to gold surfaces. Examples of distorted and compressed dendritic macromolecules within monolayers and multilayers films were also presented in that study. We aimed in this chapter to understand the factors effecting the surface interactions of three selected generations of PAMAM dendrimers namely, generation 4 (as a soft molecule with a hydrodynamic diameter of 4.5 nm), and generation 6 and 8 (as rigid molecules with hydrodynamic diameters of 6.7 and 9.7 nm respectively) on surfaces. An understanding of these interfacial interactions is important to the biomedical applications of these polymers. This aim was achieved by using the AFM as an imaging and force measuring tool to visualize and characterize the adsorption of these dendrimers on mica, gold and on alkanethiol self assembled monolayers (SAMs). The formation of self-assembled monolayers of alkanethiols on gold (Au) surfaces provides an excellent way to control both surface properties and chemical functionality (Liu and Salmeron, 1994, Barrena *et al.*, 1999).

The self-assembly of alkanethiols on Au is initiated by strong chemical interactions between the sulphur end-group and the Au surface which is believed to result in chemisorption of the molecules as thiolates, forcing the molecules to pack in registry with the Au lattice (Tamada *et al.*, 1997). Although the interaction of the sulphur atoms with Au is still not well understood, the molecular assembly can be seen as the result of competition between intermolecular forces and sulphur-substrate interactions. The two forces, the balance of which determines the surface phase behaviour in SAMs, are: lateral interactions between SAM molecules (dominated by Van der Waals

forces) and vertical interactions between SAM molecules and the substrate (Lio *et al.*, 1997). A crystalline film at room temperature, however, can only be formed if the attractive tail-tail interaction is strong enough to align the tails in parallel. This is the case for sufficiently long alkyl chains, where the number of alkyl groups (n) is ≥ 10 (Schoenenberger *et al.*, 1994). Diffraction techniques suggests that the size of ordered domains in SAMs of alkanethiol is at most ~ 10 nm (Xu *et al.*, 1998). In previous studies, alkanethiols were used to study the behaviour of PAMAM dendrimers on Au, Lackowski *et al.*, (Lackowski *et al.*, 1999). A dynamic phase-segregation process was described involving dendrimer/ n -alkanethiol mixed-monolayers after the sequential immersion of Au substrates into ethanolic solutions of, first, dendrimers and then n -alkanethiols. For the smallest dendrimers (G4) used in their studies, adsorption of the hexadecanethiol was found to completely displace the dendrimers from the Au surface after 96 hrs (Lackowski *et al.*, 1999). Thus to further build on such studies done by Li *et al.*, (Li *et al.*, 2000) and by Schoenenberger *et al.*, (Schoenenberger *et al.*, 1994), we have, here, investigated the behaviour of the G4, G6 and G8 PAMAM dendrimers on mica, and we have further investigated the behaviour of the G4 PAMAM dendrimers on Au and on alkanethiol surfaces with different functionalities, namely, methyl, carboxyl, and amino terminated alkanethiol self-assembled monolayers (from hereon referred to as SAM-CH₃, SAM-COOH and SAM-NH₂ surfaces respectively).

3.2 EXPERIMENTAL PARAMETERS

Details of the experimental materials, methods & instrumentation are present in Chapter 2, sections 2.11, 2.12, 2.2.1, 2.2.2 and 2.2.3.

3.3 RESULTS AND DISCUSSION

3.3.1 Imaging of G4 on Mica; The Effect of Drying Methods

Figure 3.1 shows series of topographical tapping mode AFM images of (a) freshly cleaved mica and (b-d) G4 dendrimers adsorbed at the water-mica interface following exposure of a mica surface to aqueous solution of G4 ($1000 \mu\text{gml}^{-1}$). These samples then were dried in nitrogen, (b & c), or spin-dried in air (at 1000-rpm), (d), before imaging in air. In contrast to the essentially featureless image of mica surface (Figure 3.1(a)) with height of 0.1-0.25 nm, a consistent set of small features can be seen in Figure 3.1(b), which are attributed to adsorbed aggregates of G4 dendrimers. Detailed cross-sectional measurements on a large number of such isolated features give an average height of 3.3 ± 0.8 nm and an average diameter of 84.6 ± 20.9 nm. On some samples prepared using the same method these dendrimers were also sometimes found to make layer(s) of average height of 2.3 ± 0.20 nm in thickness, Figure 3.1(c). Within this layer(s) features of 13.2 ± 2.2 nm in diameter could often be discerned with the height of these features of 0.43 ± 0.1 nm, most likely indicating G4 molecules immersed in a dendrimer film. Some times larger aggregates were obtained as indicated by the arrow where the diameter was 32 nm while its height was 2.7 nm. In Figure 3.1(d), the image shows linear features of diameter, height and contour length of 16 ± 4.1 , 1.1 ± 0.3 nm and 70-400 nm respectively. These features most likely indicate dendrimer aggregates. Similar features were observed by Zhang *et al* (Zhang *et al.*, 2000) who used spin-drying to adsorb polyphenylene dendrimer molecules on mica. Thus we believe that the spin-drying method is the main cause for the

dendrimers to be rolled as strands comparative to the spherical features obtained from drying in a stream of nitrogen. The surface behaviour of dendrimers in Figure 3.1 (b-d) suggests compressed dendritic aggregates on an underlying film of dendrimers. We provide further evidence supporting this behaviour in section 3.2.

We and others (Bliznyuk *et al.*, 1998, Tsukruk, 1998) assume that the interaction between surface groups along with short-range Van der Waals forces and long-range capillary forces are considered to be responsible for formation of the observed compact structures.

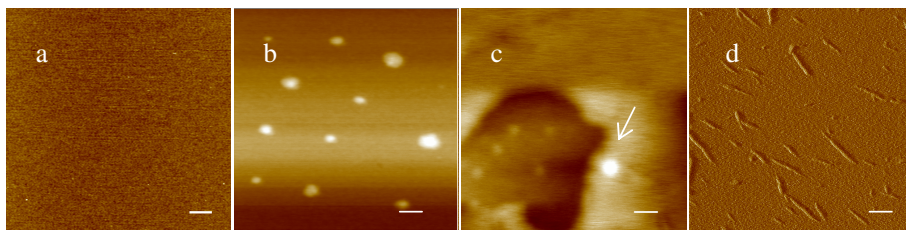


Figure 3.1. Height images of (a) mica, (b-d) G4 dendrimers on mica adsorbed from $1000 \mu\text{g.mL}^{-1}$ solution in water. This Figure shows the effect of drying methods on the behaviour of G4-PAMAM dendrimers on mica, (b) G4 PAMAM dendrimers dried under nitrogen, the image shows spherical aggregates of dendrimers on mica, (c) another image of G4 PAMAM dendrimers under the same situation of (b); the image shows a monolayer of dendrimers and dendrimer aggregates, the arrow shows larger aggregate of dendrimers. Figure 3.1(d) depicts images of G4 PAMAM dendrimers on mica using spin drying method; it shows linear aggregates of dendrimers. Scale bars =200, 170, 40 and 200 nm respectively, z scales = 4, 25, 40 and 10 nm respectively.

3.3.2 In situ Imaging of G4 PAMAM Dendrimers on Mica; The Effect of Dendrimer Concentration, and Adsorption Time

By controlling the applied dendrimer concentration, modified surfaces ranging from isolated molecules to monolayer or multilayers coverage were obtained. Figure 3.2 depicts a series of real time AFM images recorded over a period of 31 mins, which show the adsorption of G4 dendrimers at the water-mica interface following exposure of the mica surface to a $0.00014 \text{ ng.ml}^{-1}$ (10^{-14} M) aqueous solution of G4. In contrast to the essentially featureless images of mica surfaces at 0 min (before the adsorption of G4), 2 globular features can be observed after 1 min of diameters of 29 and 35 nm, and heights of 3 and 4.3 nm respectively. Such dimensions are bigger than those predicted for individual molecules and thus are most likely indicate dendrimer aggregates. After 4 min, a consistent set of small features can be seen which we also attribute to adsorbed aggregates of G4 dendrimers. Detailed cross-sectional measurements on such isolated features give an average height of $2.0 \pm 0.6 \text{ nm}$ and a diameter of $29.6 \pm 3.3 \text{ nm}$. As the exposure time increased, the observed globular features were found to increase in number. At 22 min features of average diameter of $10.5 \pm 0.9 \text{ nm}$, their average height was $1.2 \pm 0.2 \text{ nm}$ begin to appear, most likely indicating individual dendrimer molecules.

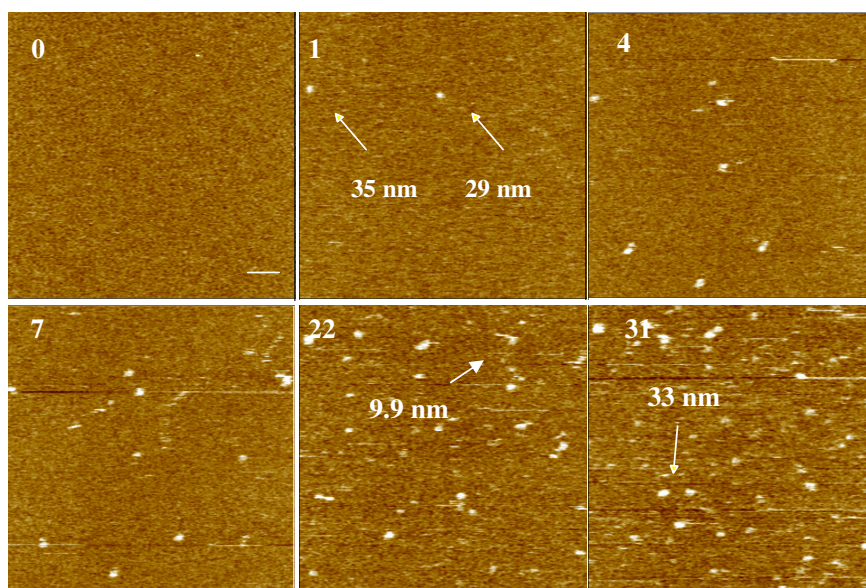


Figure 3.2. In situ imaging of the adsorption of G4 dendrimers (10^{-14} M) on mica surface (in deionized water). Numbers on the images represent time lapsed in minutes. Scale bar = 100nm, z scale = 10 nm.

Figure 3.3 depicts a second series of time lapse images recorded for the adsorption of G4 dendrimers on mica but at a higher concentration of $0.1 \mu\text{g}.\text{ml}^{-1}$, 1 min after the injection of the G4 dendrimer solution, a film of dendrimers was shown to move towards the right side of the imaging field, most properly indicating the drift of the imaged sample underneath the AFM tip. After 10 min, 2 new features (indicated by arrows) of diameters of 34 and 26.4 nm respectively and heights of 3.8 and 2.9 nm respectively were observed on the dendrimers film, most probably indicating dendrimer aggregates. These aggregates were found to disappear with the increase of the exposure time, most likely indicating the formation of new dendrimers layer(s). The formations of G4 layers were confirmed by the f-d measurements between the Silicon-Nitride tip and mica substrate before and after the adsorption of

Chapter three: Visualization and characterization of PAMAM dendrimers on different surfaces

dendrimers, labelled as mica and Mica-G₄ respectively and assuming the same contact area between the tip and the surface in each case, Figure 3.4. It is clear that the hydrophilic interaction between the silicon nitride tip and mica surface in aqueous solution (0.36 nN) is bigger than that recorded on the adsorbed dendrimer layer, (0.15 nN). We thought that in addition to the strong electrostatic interaction between the positively charged G4 dendrimers and the mica surface, these dendrimers will most likely arrange themselves as to decrease the electrostatic repulsion energy between their surfaces and due to their open structure, their branches interpenetrate each other on mica surface and establish intermolecular interaction (Naylor *et al.*, 1989) and hence the tip might face the internal less hydrophilic surface, resulting in small adhesion.

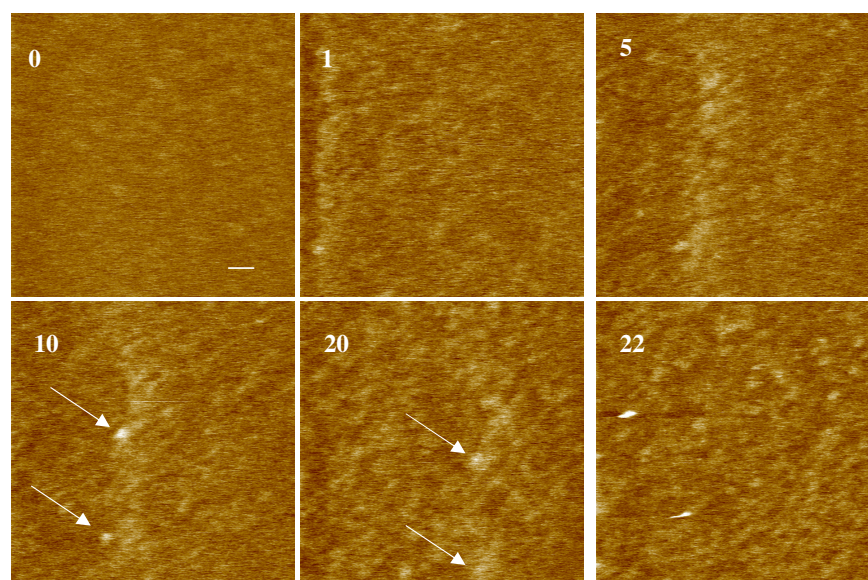


Figure 3.3. *In situ* imaging of the adsorption of G4 dendrimers ($0.1 \mu\text{g.mL}^{-1}$) on mica surface (in deionized water). Numbers on the images represent time lapsed in minutes. Arrows show the appearance and disappearance of certain dendrimer features. Scale bar = 100 nm, z scale = 10 nm.

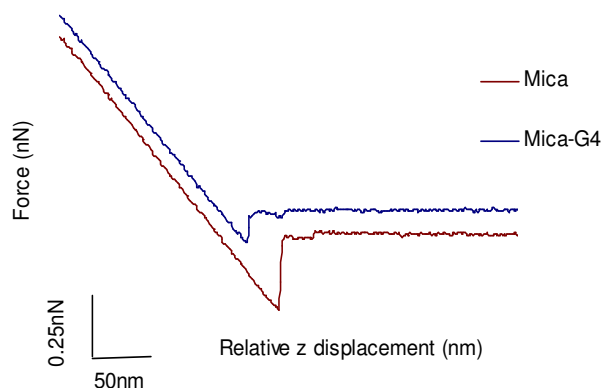


Figure 3.4. The recorded forces of F-d-c(s) measured between a silicon nitride tip and a mica substrate before (Mica) and after the adsorption of G4 in aqueous solution (Mica-G4).

3.3.3. Imaging of G6 and G8 on Mica in Water; The Effect of Dendrimers Generation

Figure 3.5 illustrates a series of images during the adsorption of G6 ($2 \mu\text{g}\cdot\text{ml}^{-1}$) on a mica surface (in 10% PBS). This time individual features consistent with the dimensions of individual molecules were found to increase in number with time. This consistency was confirmed with the volume analysis of the observed features within the images, see Figure 3.8(b). Their mean diameters and height were $18 \pm 5 \text{ nm}$ and $2.1 \pm 0.6 \text{ nm}$ respectively. The discrepancies observed through comparison of the average diameters and heights of G6 in these images with those obtained with G4 are most likely reflective of the rigidity of G6, which enable them to retain their shape on mica and appear as discrete molecules for certain time before the saturation of surface. Tsukruk *et al* (Tsukruk *et al.*, 1997) have previously reported that these dendrimers collapse

Chapter three: Visualization and characterization of PAMAM dendrimers on different surfaces

upon adsorption to surfaces by comparing the densities estimated from molecular dimensions and molecular weights of the adsorbed dendrimer images and the bulk density of dendrimer monolayers evaluated from X-ray data.

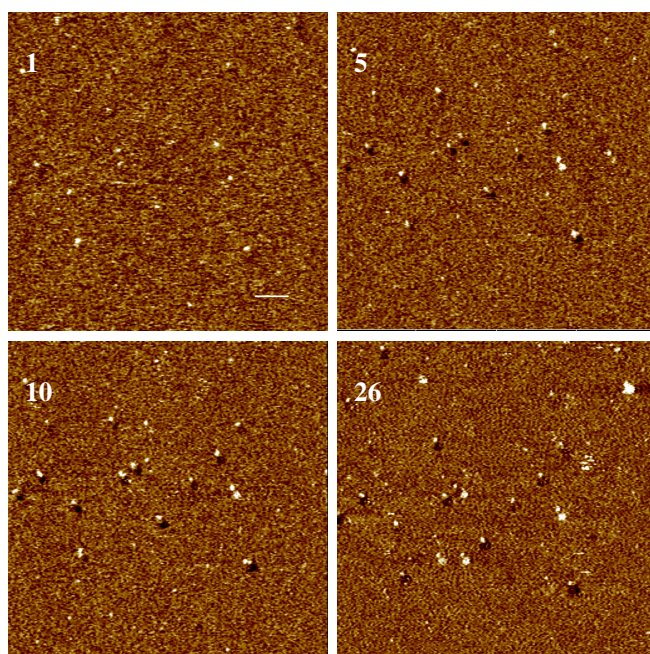


Figure 3.5. In situ imaging of the adsorption of G6 dendrimers ($2 \mu\text{g.mL}^{-1}$) onto a mica surface (in 10% PBS). Numbers on the images represent time lapsed in minutes. Scale bar = 100nm, z scale = 5 nm

Figure 3.6 shows typical images of G6 dendrimers adsorbed onto mica from $0.1 \mu\text{g.mL}^{-1}$ solution and imaged in deionized water. From our images, comparing the size of the G6 dendrimers in the dendrimer film and single molecules, the lateral dimensions of isolated dendrimers appear larger (18 ± 5 nm) than in the dendrimers film (9 ± 2 nm).

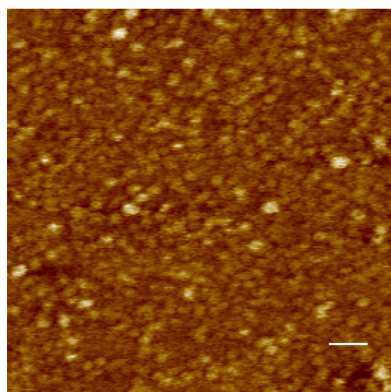


Figure 3.6. Height images of G6 dendrimers adsorbed on mica from $0.1 \mu\text{g}\cdot\text{ml}^{-1}$ solutions, imaged in deionized water. Dendrimer molecules appeared as compacted molecules within the monolayer. Scale bar = 100 nm, z scale = 10 nm.

The reason for the observed differences within the measured dimensions of the imaged individual dendrimers and dendrimers within the monolayer is that most likely the molecules within the monolayers are compacted and so the tip is not able to reach the surface of mica, most likely riding instead on the tops of the dendrimers. The result of this will be negligible addition to the lateral dimensions due to tip convolutions. In the case of isolated dendrimers however, the tip will be able to completely ride over the deformed spheres, resulting in the addition of about twice the tip radius to the actual lateral dimensions of the isolated dendrimers (Hierlemann *et al.*, 1998).

Figure 3.7 depicts typical images of G8 dendrimers adsorbed onto mica from $0.1 \mu\text{g}\cdot\text{ml}^{-1}$ solution and imaged in deionized water. Again, individual features consistent with individual dendrimers molecules were observed. Their average diameter and height were $32 \pm 5 \text{ nm}$ and $2.5 \pm 0.8 \text{ nm}$ respectively. Unlike G4, which was able to spread on mica surface to make multilayers and aggregates

due to their open structure, the G6 and G8 dendrimers appear as individual oblate features.

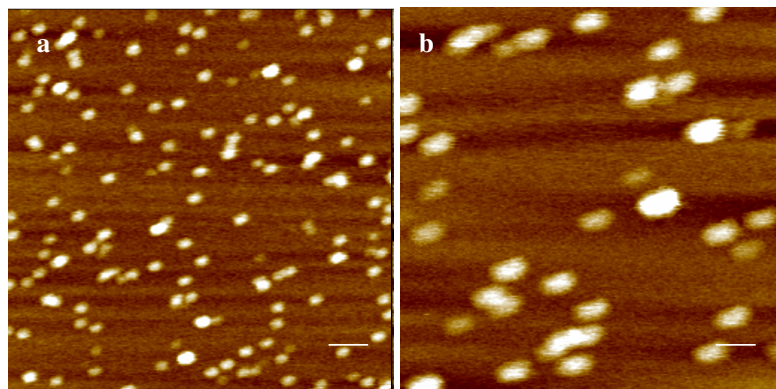


Figure 3.7. Height images of G8 adsorbed on mica from $0.1 \mu\text{g.mL}^{-1}$ solutions, imaged in deionized water. Images (a) and (b) show different scan areas for the same sample. Scale bars = 200 nm and 40 nm respectively, z scale = 25 nm.

A plot of the calculated mean diameters and heights as a function of generation was shown in Figure 3.8(a), it demonstrates that the measured diameters are always larger than heights, indicating that the dendrimer molecules are no longer spherical but instead dome-shaped when deposited on a mica surface.

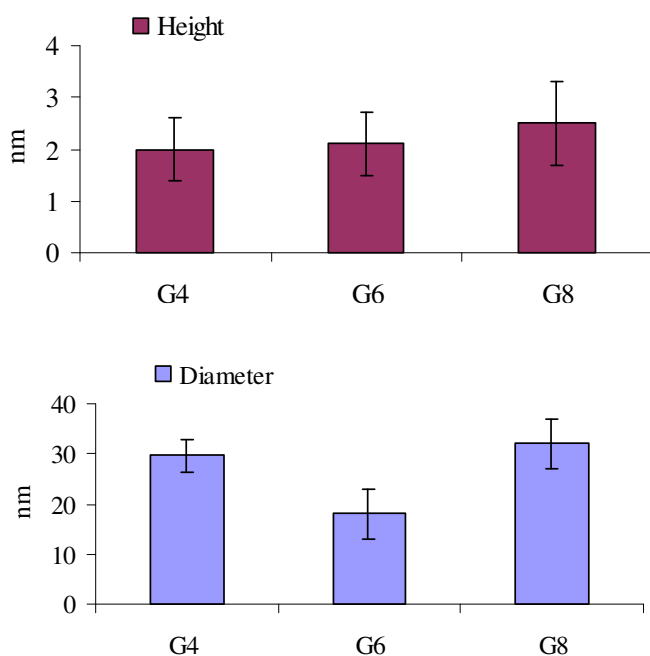


Figure 3.8(a). Relation between diameters of G4, G6 and G8 and their heights on mica.

From the observed dimensions, an approximate volume can be calculated for each particle. Figure 3.8(b) represents another histogram that relates the volume obtained from these particles to the number of molecules within the particle relative to the theoretical hydrodynamic diameter of each generation. On the basis of the dome shape predicted from our images, a molecular volume can be calculated from the following equation (Li *et al.*, 1999).

$$V = \frac{1}{6}\pi h(h^2 + 3d^2)$$

Where h is the height and d is the diameter of the cap. The number of

Chapter three: Visualization and characterization of PAMAM dendrimers on different surfaces

molecules per feature was then calculated by dividing the calculated volume by the theoretical volume of the individual molecule of the corresponding generation.

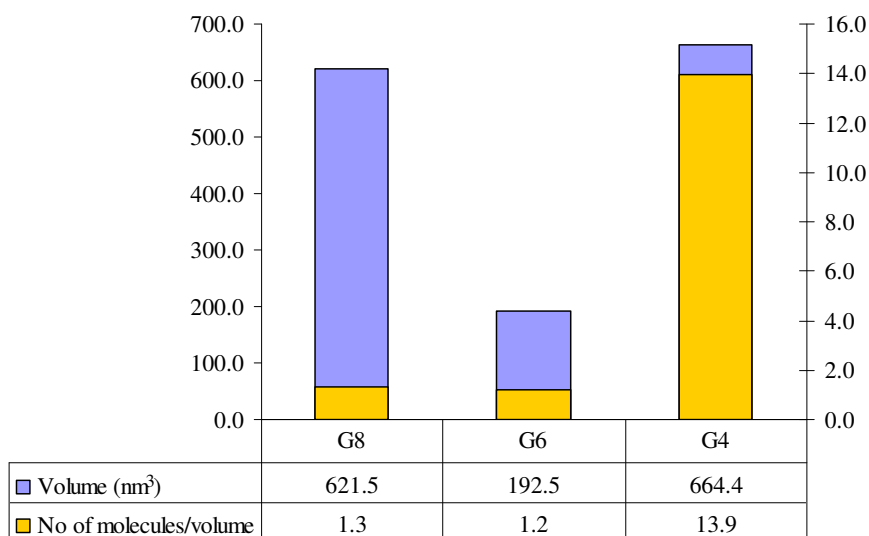


Figure 3.8(b). Comparison of the mean dendrimer volume measured by AFM from particle profiles and theoretical volume of PAMAM Dendrimers.

It is clear that data obtained from volume measurements support the previous data that G4 presents in aggregates with ~13.9 molecule/particle while G6 has only ~1.2 molecules/particle and G8 ~1.3 molecules/particle which are adsorbed in most cases as distinct individual particles. It was also found that the number of particles decreases in the imaging field as the dendrimer generation increases. This is most likely because the concentration in $\mu\text{g.ml}^{-1}$ used in the experiments was fixed for all generations and the only variable is then the molecular weight of dendrimers and hence their numbers will nearly decrease to 1/4 from G4 to G6 and another 1/4 from G6 to G8.

The observed increase in height of the individual molecules with generation, suggests that the molecular rigidity of dendrimers increases with increasing generation, most likely due to the partial swelling of the dendrimers due to the increase in their surface primary amine groups. On the other hand, due to the open structure of the G4 molecule, self-aggregation was enhanced to make the aforementioned features with diameters of 84.6 ± 20.9 nm as in Figure 3.1(b). In addition, we found it very difficult to image individual molecules of the G4 dendrimer; most of the image surfaces were found to consist of small domains of different sizes. Those discrepancies between the measured and hydrodynamic diameters of G4 may be attributed to as following. Firstly, low-generation members of a dendrimer family (i.e. G4 in our study) exist as open, plate like molecules in which the dendrimer branches can relatively easily interpenetrate each other and thus form aggregates (Naylor *et al.*, 1989). Secondly, the convolutions due to the AFM tip will broaden features, since the resulting image is always a convolution of tip and sample geometry (Fritzsche *et al.*, 1997). Finally, the frequency and vertical velocity of the vibrating tip are also most likely to be sufficiently high to cause deformations of the dendrimers. Our observations are however consistent with the AFM data presented by Hierlemann *et al* and Li *et al* (Hierlemann *et al.*, 1998, Li *et al.*, 2000). Li *et al.*, (Li *et al.*, 2000) has reported that the surface adsorption forces between the mica surface and individual dendrimers increase with increasing generation, as predicted from Mansfield's model of dendrimer surface adsorption (Mansfield, 1996). Therefore, when deposited on solid substrates, they tend to deform to different degrees as a result of the interplay between their inherent rigidity and interactions between the dendrimer molecules and

the mica surface (Li *et al.*, 2000). A computer-based simulation of dendrimer surface adsorption has recently been reported (Mansfield, 1996). It describes the dendrimer adsorption geometry and the interaction energy between the dendrimer and the surface for G1-G8 dendrimers. The results indicate that higher generation dendrimers (e.g. G4-G8) flatten and spread on the surface, while the lower generations, such as G1 and G2 dendrimers, adsorb weakly and retain their bulk-phase conformation.

3.3.4 Visualization of G4 Dendrimers on Gold

3.3.4.1 Gold Film Analysis

Figure 3.9(a) shows an AFM height image of Au coated mica prepared by epitaxial growth on freshly cleaved mica sheets. This method produces atomically flat gold islands with single crystal grains measuring 200-500 nm in diameter (Derose *et al.*, 1991). Common adhesion promoters such as chromium and titanium were avoided in this work because they can form alloys (e.g., AuCr₃) with Au, which can in principle behave differently than a pure gold film (Dishner *et al.*, 1998). During the course of these experiments, it was also noticed that a white hue sometimes developed on the Au surface, most likely indicating areas with rough morphology. It has been reported that if such areas are abundant enough it can be difficult to find a region of the surface smooth enough for use (Derose *et al.*, 1993). Here we found that Au films prepared at a temperature of 315 °C and annealed at 390 °C for 24 hours produced the smoothest surface morphologies. Average surface roughness (R_a) and root mean roughness (R_{ms}) values for each Au island (215 nm x 215 nm) was found to be $1.88 \pm 0.3 \text{ \AA}$ and $2.79 \pm 0.2 \text{ \AA}$ respectively. In contrast, Figure 3.9(b)

shows AFM height image of Template Stripped Gold (TSG) surface. The image reveals two typical topographical features; first, the gold surface exhibits atomically flat terraces extending over up to several hundred nanometers. Second, triangular areas with ca 60°, typical of epitaxial Au (111), can be recognized. Moreover, on this type of surface, Au crystal lattice structures are available for the adsorption of molecules such as alkanethiols and which should provide better packing of surface of chemisorbed molecules (Wagner *et al.*, 1995).

Average surface roughness (R_a) and root mean roughness (R_{ms}) values for these surfaces were found to be $(1.5 \pm 0.1 \text{ \AA})$ and $(3.1 \pm 0.2 \text{ \AA})$ per $1 \mu\text{m} \times 1 \mu\text{m}$, respectively). It is obvious that TSG provides superior substrate flatness. However, during preparation of TSG, since the gold/mica adhesion is comparable to the mica cohesion (Stamou *et al.*, 1997), lattice planes of mica often remained attached to areas of the gold surface and had to be removed using both mechanical and chemical treatments that could have deteriorated the quality of the gold surface. For this reason and the ability to also obtain an atomically flat gold surface from the first procedure, epitaxial gold was preferred for these studies.

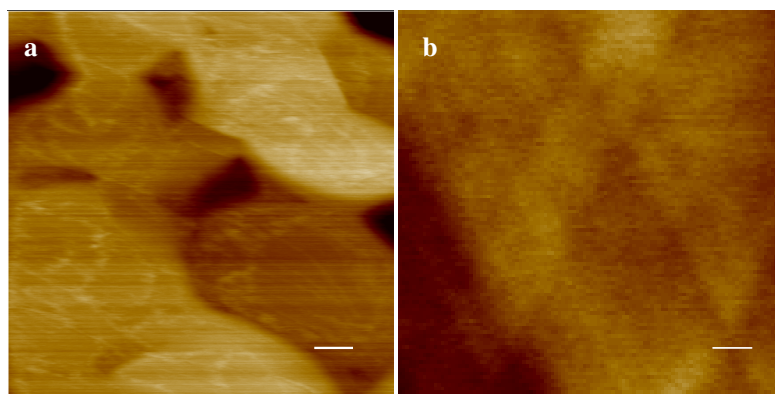


Figure 3.9. Height images recorded in air of (a) an epitaxially grown Au film on mica. The surface topography consists of large flat Au islands, (b) TSG. Flat terraces extending over up to several hundred nanometers and triangular areas with ca 60° have been seen. Scale bar = 100nm, z scales = 65 and 5 nm respectively.

3.3.4.2 Imaging of G4 on Gold (in Air)

The images presented in Figure 3.10 show epitaxially grown gold surfaces following the adsorption of G4 dendrimers from a 1000 $\mu\text{g}\cdot\text{ml}^{-1}$ solution in water, which were dried with nitrogen prior to imaging. The data in Figure 3.10(a) suggest the formation of multilayers of dendrimers. The thickness of these layers could be measured from the occasional holes observable near the edge of Figure 3.10(a), which most likely form during sample drying. The thickness was found to be 1.5-2.2 nm. The adsorption of these dendrimers on Au is most likely due to an induced electrostatic interaction between the charged dendrimers and the conducting Au surface. Because the dendrimers bear positive charge in aqueous solution under the conditions used, there exists an attractive image-charge interaction between themselves in solution and the Au surface (Rahman *et al.*, 2000). The enhanced stability of the adsorbed

dendrimers on Au can be accounted for by two factors. First, the G4 dendrimer has a high surface area and a dense exterior, which results in a strong Van der Waals interaction with the Au surface together with the image-charge interaction. Second, there are a large number of amine groups that are able to chemisorb to the Au surface, which in a process analogous to polydentate metal-ion ligand chemistry, can stabilize the amine/Au interaction (Tokuhisa *et al.*, 1998). Figure 3.10(b) depicts another image of G4 dendrimers adsorbed on Au from $0.1 \mu\text{g}\cdot\text{ml}^{-1}$ solution. G4 dendrimers were found to aggregate to form features of average diameter of $87 \pm 18 \text{ nm}$. Their average height was $4.5 \pm 1.75 \text{ nm}$. We believe that these features are aggregates of dendrimers being adsorbed on a previously adsorbed dendrimer layers on the Au surface in a similar scenario as shown in Figure 3.3.

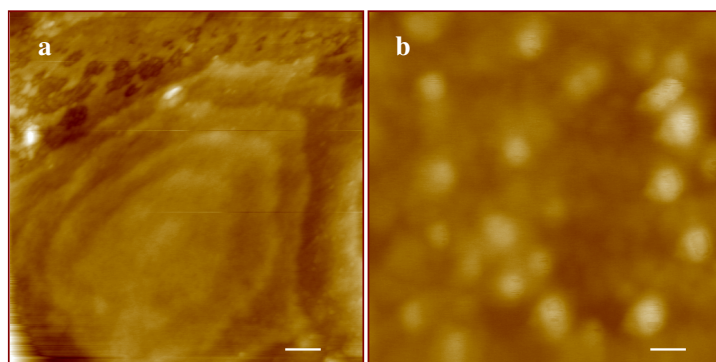


Figure 3.10. Height images of G4 dendrimers on epitaxial gold (a) prepared from $1000 \mu\text{g}\cdot\text{ml}^{-1}$ solution. The dendrimers appear as monolayers on the gold surface; and (b) prepared from $0.1 \mu\text{g}\cdot\text{ml}^{-1}$ solution. The dendrimers appear aggregated on the gold surface. Scale bars = 500 and 100 nm respectively, z scales = 35 and 25 nm respectively.

3.3.5 Film Morphology of SAMs Monolayers in Air

Figure 3.11 displays images of (a) SAM-NH₂, (b) SAM-COOH, and (c) SAM-CH₃ substrates recorded in tapping mode at a setpoint of 98 % of the free oscillation amplitude. All the images show the island features associated with the gold surface, with an overlying patchy topography that we attribute to the presence of the surface bound alkylthiols. Such features were never observed on non-functionalized gold surfaces. Here it should be noted that the conditions and timescales employed for our SAM formation, are commensurate with those well documented for the formation of ordered monolayer films (Schoenenberger *et al.*, 1994, Xu *et al.*, 1998). The brighter parts in these images thus most likely correspond to small raised islands of alkanethiols within a SAM monolayer. The diameter of these features was about 20-60 nm, but sometimes they appeared to be aggregated in clusters of up to 160-200 nm in diameter. The height of the islands above the background is uniform and equal to 1.93 ± 0.24 nm, approximately the length for one alkanethiol molecule. Similar islands have been observed in previous ultra-high vacuum scanning tunnelling microscopy studies of alkanethiol functionalised surfaces (Poirier, 1997).

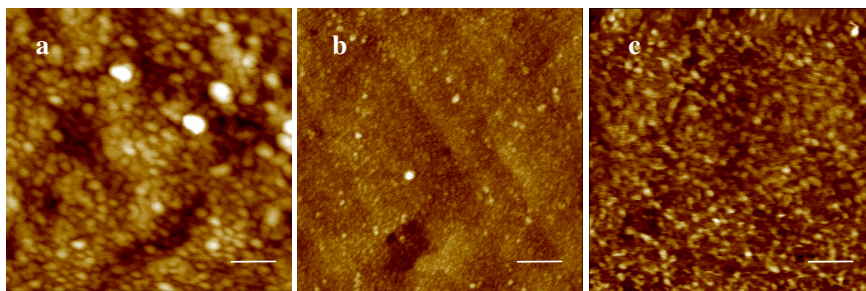


Figure 3.11. Representative topography images of the SAM surfaces formed through deposition of the alkanethiols (a) 11-amino-1-undecanethiol hydrochloride, (b) 16-mercaptohexadecanoic acid, and (c) octadecyl mercaptane onto epitaxially grown gold films. Images obtained in air, scale bar = 200 nm, z-scales = 70, 20, and 10 nm respectively.

3.3.6 Characterization of G4 Dendrimers on SAMs.

3.3.6.1 Imaging of G4 dendrimers on SAMs in air

Figure 3.12 (a-c) shows typical images of G4 dendrimers adsorbed onto (a) SAM-NH₂, (b) SAM-COOH, and (c) SAM-CH₃ substrates to form SAM-NH₂-G4, SAM-COOH-G4, and SAM-CH₃-G4 surfaces respectively. In these images, spherical features were obtained. The observed diameters of these features are (a) 22.1 ± 2.5 , (b) 20.0 ± 6.5 , and (c) 30.5 ± 1.3 nm. The heights of these features are (a) 1.5 ± 0.4 , (b) 1.8 ± 0.4 , and (c) 2.1 ± 0.3 nm. Again the values of diameter are significantly larger than the theoretical diameter value of 4.5 nm predicted for a spherical G4 dendrimer molecule, while the values of height again are significantly smaller, see Figure 3.12(d).

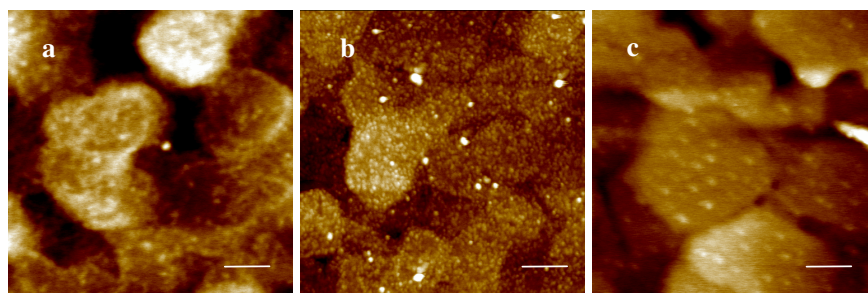


Figure 3.12(a-c). Representative topography images of (a) 11-amino-1-undecanethiol hydrochloride, (b) 16-mercaptohexadecanoic acid, and (c) octadecyl mercaptane following their exposure to a solution of G4 dendrimers ($0.1 \mu\text{g}\cdot\text{mL}^{-1}$) Images recorded in air, scale bar = 100 nm, z scale = 7 nm.

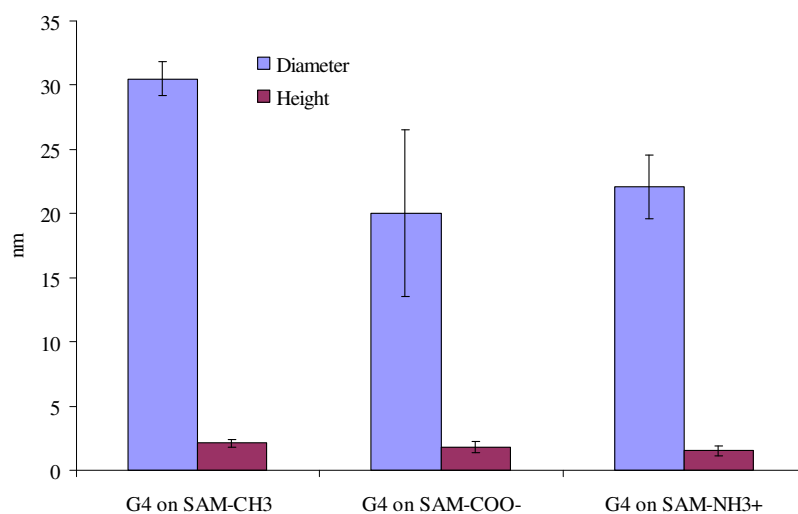


Figure 3.12(d). Relation between the Diameter and Height of features observed on SAMs coated Surfaces.

3.3.6.2 Film Morphology of SAM-COOH Monolayers and G4 Dendrimers on SAM-COOH in Liquid

Figure 3.13(a) depicts an image of SAM-COOH surface imaged in deionized water, it shows islands of 20-50 nm in diameter, these islands sometimes aggregate in clusters up to 120-150 nm in size. Figure 3.13(b) depicts an image of G4 dendrimers on SAM-COOH in deionized water. Individual dendrimer molecules are not seen, but instead the dendrimers are found to aggregate to give a patchy film with features of 40-65 nm in diameter. The height of these features is 6.4 ± 1.6 nm.

While these images agree with published data (Li *et al.*, 2000), they have features which are similar to those observed on the SAM substrates, thus making the discrimination of features related to either types of surface difficult. Two approaches were subsequently employed to solve this problem, namely; the *in situ* imaging of dendrimers adsorbing on one of the alkanethiol surfaces, (SAM-COOH), and force measurements on the SAM-COOH surface before and after the adsorption of the dendrimers.

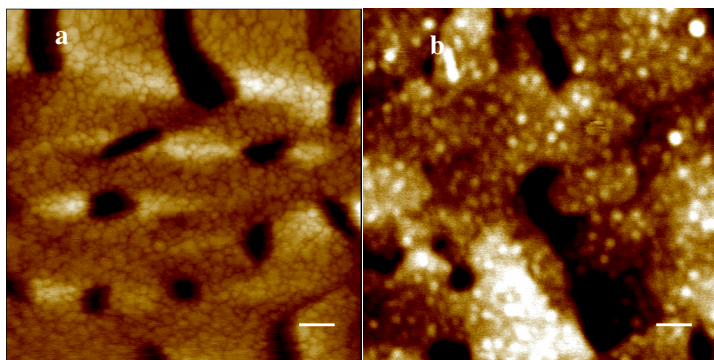


Figure 3.13. (a) A typical height image of SAM-COOH surface recorded in deionized water showing raised islands of diameter 20-150 nm, (b) A typical height image of the same surface following exposure to a $0.1 \mu\text{g.ml}^{-1}$ dendrimer solution recorded in deionized water. Here dendrimers can be seen to aggregate to give a grainy film with features of 40-65 nm in diameter, scale bar = 100 nm, z scales = 30 nm and 5 nm respectively.

3.3.6.3 In situ Imaging of G4 Dendrimers on SAM-COOH

Figure 3.14 depicts a series of images recorded at one position on a SAM-COOH surface in deionized water over a 48 minute time period, immediately before (Figure 3.14 (a)) and following the injection of a dendrimer solution ($0.1\mu\text{gml}^{-1}$), (Figures 3.14 (b-f)). 5 min after the injection of the dendrimer solution, patches (20-90 nm in diameter) were found to appear in the AFM images (Figure 3.14 (b)). Again these features are most likely to be dendrimer aggregates, as they were observed to grow in size with time to form a tightly packed layer in which individual molecules and/or aggregates could not be discriminated (Figure 3.14 (c)). Globular features, which we attribute to the presence of additional dendrimer molecules not able to be incorporated in the

previous layer, were then are seen to appear over this layer, as can be seen in the Figure 3.14 (d) (highlighted with arrows). As the exposure time increased, these globular features were also found to grow in size, and coalesce to form another densely packed layer (Figure 3.14 (e)). Finally in Figure 3.14 (f), obtained at $t = 48$ mins, features of diameter ~ 10 nm can be seen to yet again appear over this newly formed layer.

This series of images clearly reveal a time-dependent change in the sample topography, thus confirming that dendrimers are able to adsorb to SAM-COOH surfaces under the conditions employed in our experiments. The images also indicate that under our experimental conditions the dendrimer molecules first tend to form a densely packed film. Such a phenomenon has also been observed in previous studies (Li *et al.*, 2000), and arises as the dendrimers arrange themselves at the surface as to maintain their lowest energy conformation. At a certain point however, within this packing geometry additional dendrimer molecules will no longer be able to be incorporated within this layer, and will begin to form additional layers as evident in images 5(d) and 5(f). Although the formation of multilayers of similarly charged molecules may at first seem counterintuitive, we propose that such a condition can arise through the hydrogen bonding between and/or interpenetration of dendrimer molecules.

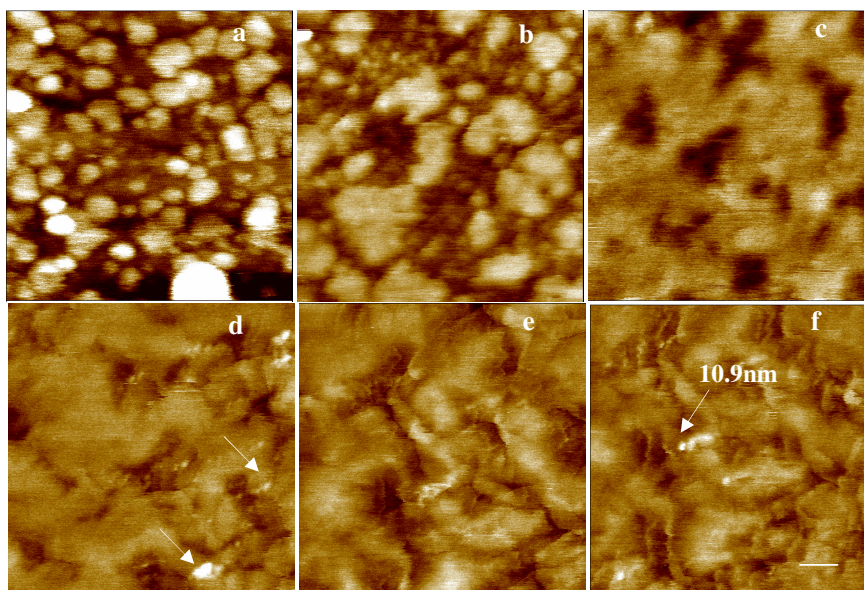


Figure 3.14.(a-f) In situ imaging of the adsorption of G4 PAMAM dendrimers (from a 0.1 μgml^{-1} solution) onto a SAM-COOH surface. Arrows on (d) show aggregates of G4 molecules on dendrimers monolayer. The arrow on (f) shows a small feature that is most likely indicates individual G4 molecule on a dendrimers monolayer. Scale bar = 35 nm, z scale = 30 nm.

3.3.6.4 Effect of Setpoint

Figure 3.15 (a-c) represents the effect of set point on imaging quality of SAM-NH₂ in deionized water. We will concentrate in our analysis on the three marked features within the image. Three set points were chosen relative to the free amplitude set point. The relative set point R% used is defined in the following equation,

$$\mathbf{R\% = A_{sp}/A_0 \times 100}$$

Where A_{sp} is the set point of tapping amplitude and A_0 is set point of free oscillation amplitude. Figure 3.16 is a histogram that summarizes the

Chapter three: Visualization and characterization of PAMAM dendrimers on different surfaces

relationship between the R% and height and diameter of the three marked molecules. At R% = 70, all features were distorted, their heights were dramatically decreased while their diameters were increased most likely due to the hard tapping. As R% becomes 85%, the distortion of these features decreased, their heights slightly increased and their diameters slightly decreased. Finally, when R% reached the value of 98%, images became more sharp and clear. Interestingly, their heights were nearly doubled and their diameters were nearly decreased to half of the first mentioned diameters. It is very important hence to choose the higher possible R% as to get real information as possible about the imaged features. This was our strategy throughout this study.

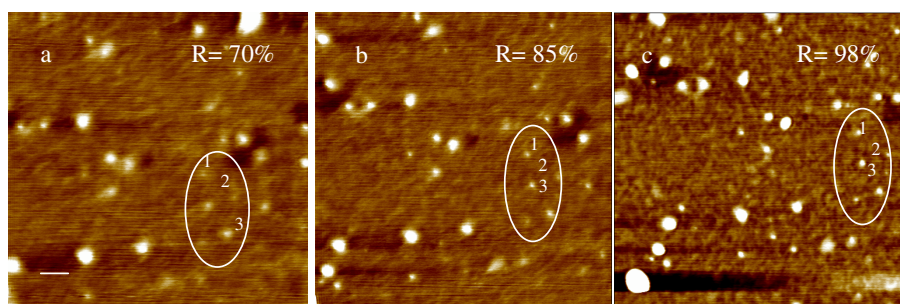


Figure 3.15 (a-c). The effect of the set point on imaging quality, as R% increases to a certain percentage, imaging quality increases. Scale bar = 100 nm, z scale = 10 nm.

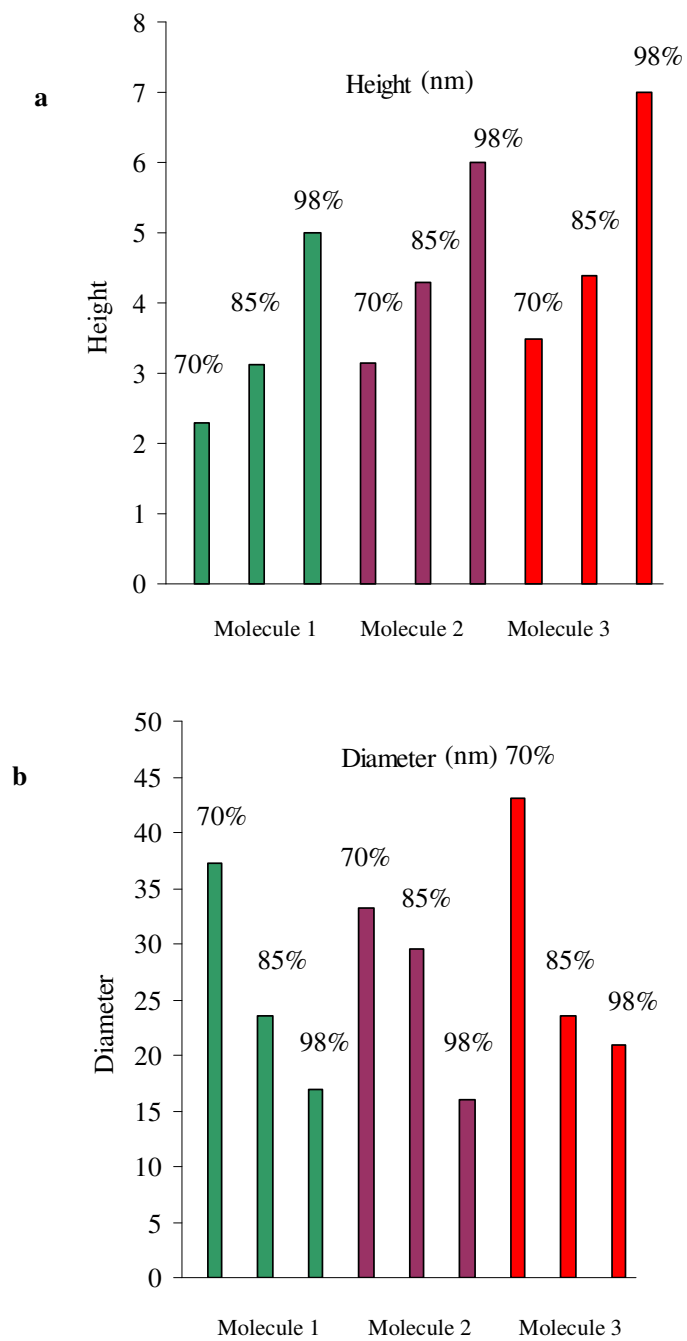


Figure 3.16. Histograms summarize the relation ship between the R% and the (a) height and (b) diameter of the three marked molecules.

3.3.6.5 Force-Distance Curve (f-d-c) Measurements

Adhesion force-distance measurements were recorded in deionized water (pH ca 6.5) between a SAM-COOH coated tip and all SAM coated surfaces, prior to and following dendrimer adsorption. Previous studies performed by ourselves and other groups have highlighted the sensitivity of adhesion force measurements (Frisbie *et al.*, 1994, Allen *et al.*, 1997b, Allen *et al.*, 1999, Giesbers *et al.*, 2002, Smith *et al.*, 2003) and a-p-d curves (Danesh *et al.*, 2000) to differences in the chemical nature of the probe-sample interface, and in this study we wished to investigate whether such measurements could be exploited for the differentiation between SAM and dendrimer coated SAM substrates.

In all experiments, to assess the reliability of probe and surface functionalization process, force measurements were first recorded between SAM-COOH functionalized probes and the three different SAM surfaces. Only those probes that demonstrated adhesive behaviour consistent with previous studies were then utilized in subsequent measurements (Frisbie *et al.*, 1994, Giesbers *et al.*, 2002, Smith *et al.*, 2003). It should also be noted that in these and subsequent dendrimer experiments we were unable to determine the radius of curvature of the functionalized probes, and thus also estimations of probe-sample contact areas. Therefore, in our experiments direct comparisons of forces were only made between those obtained within one experiment recorded with the same probe, and in which the probe-sample contact force was maintained at a constant value. Only trends in the obtained adhesive forces were compared between experiments obtained with different AFM probes.

Figure 3.17(a-f) shows representative series of force-distance measurements obtained for each tip-substrate combination. Within these series of

measurements, it can be seen that the largest adhesion forces were recorded on the SAM-NH₂ surface (7.80 ± 0.13 nN) (Figure 3.17(c)). In the other two combinations (on the SAM-COOH surface, Figure 3.17(a) and on the SAM-CH₃ surface Figure 3.17(b)), smaller adhesive forces of 1.3 ± 0.2 and 2.4 ± 0.6 nN were observed respectively. Several groups have indicated that the pKa values of acid and amine functionalities in closely packed self-assembled monolayers are markedly different from their values when free in solution (Sun *et al.*, 1993, Creager and Clarke, 1994, Smith *et al.*, 2003), attributed to intramonolayer hydrogen bonding between adjacent groups in the respective monolayers. Indeed, in recent chemical force titration experiments between carboxylic acid terminated SAMs (Smith *et al.*, 2000) the pK_{1/2} (the solution pH at which half the surface groups are ionized) was found to be around 8, under conditions of low ionic strength. This value was found to be in good agreement with surface pKa values (also approximately 8) derived from gas phase and cyclic voltammetry experiments. Similar measurements recorded between amine terminated SAMs revealed that the behaviours of such surfaces were more complex (Wallwork *et al.*, 2001), although also consistent with a model incorporating intra-monolayer hydrogen bonding (at intermediate pH values and conditions of low ionic strength).

Under the conditions employed in our experiments (i.e. deionized water, pH ca. 6.5) it is therefore likely that both the SAM-COOH and SAM-NH₂ surfaces would be composed of both non-dissociated and ionized functional groups. We thus attribute the larger adhesion forces, recorded between SAM-COOH tips and SAM-NH₂ surfaces, to electrostatic attractive interactions between any

ionized carboxyl and amine groups and also to inter-surface hydrogen bonds induced upon probe-sample contact and which can occur by virtue of the non-dissociated terminal functionalities (Smith *et al.*, 2000). The detection of adhesion forces when recorded on a SAM-COOH surface is also consistent with a model in which hydrogen bonds can form during probe-sample contact, although here such interactions will be opposed by repulsive interactions between any ionized carboxyl groups. The intermediately ranking of the forces recorded on the hydrophobic SAM-CH₃ surfaces, which is both unable to interact with the SAM-COOH tip electrostatically or via hydrogen bonding, is consistent with previous observations (Frisbie *et al.*, 1994).

Figures 3.17(d)-(f), show representative force measurements recorded on the same SAM substrates following their exposure to an aqueous solution of dendrimers. The probe utilized in these measurements was also the same as that employed to record Figure 3.17(a)-(c). The mean adhesion force obtained on the dendrimer treated SAM-COOH surface was 2.4 ± 0.9 nN, Figure 3.17(d). Adhesion forces recorded with the same probe on dendrimer treated SAM-CH₃ and SAM-NH₂ surfaces were found to be 5.2 ± 1.7 nN (Figure 3.17(e)), and 2.7 ± 0.5 nN (Figure 3.17(f)), respectively.

From these measurements it can be seen that both the magnitude and order of ranking of the adhesive forces differ markedly to those recorded with the same probe (at the same contact force) on the SAM surfaces prior to dendrimer adsorption. This observation thus indicates the ability of adhesion force measurements to detect the presence of dendrimers on the surface. Interestingly, the adhesion forces recorded on the dendrimer coated SAM surfaces were however, also found to differ. It should also be noted that

although the data displayed in Figure 3.17 was obtained using only one probe, several repeats of the experiment were actually performed. In all experiments, the trends in the recorded adhesive forces were the same as that displayed in Figure 3.17; with differences only in the absolute recorded force values i.e. due to variation in probe geometry.

We postulate that the differences in the forces recorded on the dendrimer coated surfaces may arise due to the high flexibility of the employed G4 dendrimer molecules and their subsequent ability to change their conformation upon surface adsorption (Li *et al.*, 2000). Under our experimental conditions, the surface amine groups of the dendrimers are protonated, and the polar solvent will cause their structures to be swollen. Within a dendrimer molecule the interaction between polymer branches is thus weak, leaving the surface functional groups free to interact with the different SAM substrates. When dendrimers are adsorbed onto SAM-COOH substrates, we propose that the initial layer of dendrimers may change their conformation by exposing some of their functional groups towards the small number of ionized carboxylic acid groups present on the surface, due to the electrostatic attraction.

Contrary to this, in the case of the adsorption of the dendrimers onto SAM-NH₂ substrates, they may change their conformation by exposing the majority of their functional groups away from the surface due to the repulsive electrostatic forces imposed by the small number of protonated amine groups present. This electrostatic repulsion will also most likely reduce the number of dendrimer molecules on the substrate, as compared with the previous example. Assuming however, that these molecules will also arrange themselves on the surface as to minimize such repulsion, achievable by maximising their contact area with the

surface through exposure of their interior hydrophobic branches, the molecules will be relatively elongated and the surface amine groups distributed over a large area of the elongated molecule relative to the SAM-NH₂ substrate.

Finally, if the substrate has no charge on its surface (i.e. as for SAM-CH₃), any change in dendrimer conformation upon surface adsorption will largely be driven through the hydrophobic interactions between the internal core of the dendrimers and the underlying surface. As on the SAM-NH₂ substrate, the dendrimers would arrange themselves on the surface in order to maximize the hydrophobic interactions with the substrate. However, unlike the case for that substrate, electrostatic repulsive forces will not hinder dendrimer adsorption, and thus the number of dendrimer molecules should be greater than on the SAM-NH₂ substrate. The resultant closer packing of the dendrimer molecules on the hydrophobic surface will result in a surface amine group density greater than that for the dendrimers on the oppositely charged SAM, but which is still lower than the density obtained due to the SAM-NH₂ substrate. To conclude, we thus suggest that the observed differences in adhesion forces recorded on the different dendrimer coated SAM surfaces are reflective of differences in the dendrimer surface conformation and the subsequent change in the density of protonated amine groups available for binding to the SAM-COOH tip.

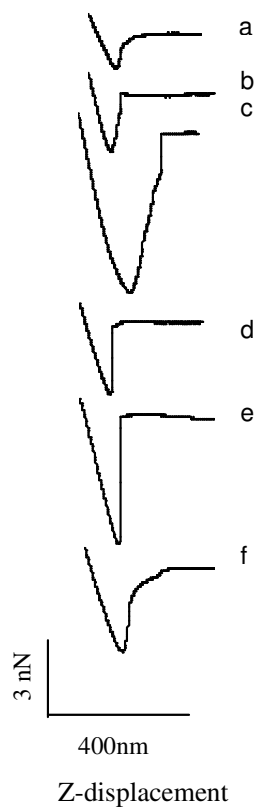


Figure 3.17. F-d-c(s) Force distance measurements recorded between a SAM-COOH modified tip and the different SAM substrates. All measurements are recorded in deionized water, and dendrimer coated SAM surface indicated in the legend by a 'G4' suffix.

3.3.6.6 Amplitude-Phase-Distance (a-p-d) Measurements

Representative a-p-d curves obtained using a SAM-COOH functionalised TESP AFM probe and the same range of substrate surfaces as employed in force distance measurements, are presented in Figures 3.18. For clarity, only the approach curves are shown. It should also be noted that these measurements were recorded in air, unlike the force-distance measurements presented in Figure 3.17. In this type of measurement, during tip-sample approach prior to any significant tip-sample interactions, both amplitude and phase signals were constant for all the samples and thus they appear as horizontal lines in the figures. At a certain distance, the cantilever becomes close enough to surface to experience both attractive and repulsive forces, including capillary force interactions, and the amplitude starts to decrease, while the phase lag starts to increase (observed as a negative phase shift), indicating the onset of tapping (Anselmetti *et al.*, 1994, Chen *et al.*, 1998, Danesh *et al.*, 2000). This change can be seen to continue during approach until a point where the phase shift suddenly switches from negative to positive, indicating a change in tip-sample interactions from attractive-dominated to repulsive-dominated as shown in Figure 3.18(b). Simultaneously, a discontinuity can be seen in the amplitude curve. We also found that in some cases, the transition of phase shift from negative to positive did not always appear as such a sudden jump, but a continuous evolution, as shown in Figures 3.18(c) and 3.18(d). Furthermore, in Figures 3.18(a) and 3.18(e) there is no phase transition due to the strong electrostatic attraction between the tip and SAM-NH₂ and the dendrimer coated SAM-CH₃ substrates respectively.

Accordingly, the amplitude curves in these measurements also show a smooth and usually non-linear decrease.

Comparing profiles of the a-p-d curves obtained from Figures 3.18(a-e), it is clear that the a-p-d measurements appear to indicate a difference in the surface chemical functionality of these different substrates. These results support the data obtained in our force-distance measurements, in that the carboxyl functionalized probe experiences different forces and behaves differently when interacting with each of the different substrates. The observed trends in the a-p-d data recorded on the dendrimer coated substrates are also consistent with the force-distance measurements, further supporting our hypothesis that the dendrimers are able to change their conformation on the different alkanethiol surfaces due to their flexibility. These results are in line with the work of Danesh *et al.*, (Danesh *et al.*, 2000) who used a-p-d curves to differentiate between different functionalised surfaces.

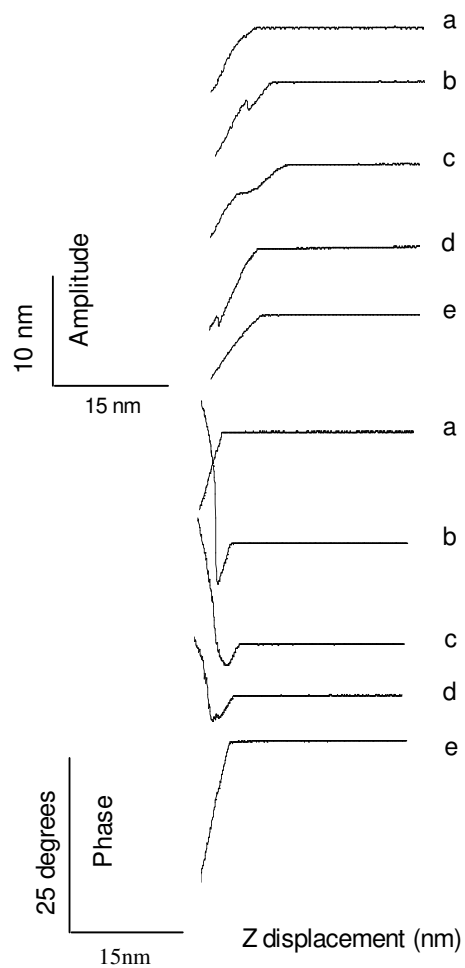


Figure 3.18. A-p-d curves recorded between a SAM-COOH modified TESP tip and the same range of surfaces as tested in Figure 3.17. All measurements are recorded in air, and again dendrimer coated SAM surfaces are indicated in the legend by a 'G4' suffix.

3.4 CONCLUSIONS

We have shown that AFM images in air and in liquid were found to provide topological information about PAMAM dendrimers and PAMAM dendrimers coated surfaces. By controlling dendrimer concentration, modified surfaces ranging from isolated molecules to monolayer or even multilayer coverage were obtained. However, we found it difficult to image individual molecules of the G4 dendrimer (the theoretical diameter is ~4.5 nm) on mica and gold. Rather, the surface behaviour appeared to produce at low concentration collapsed small aggregates of dendrimer molecules and also at higher concentrations aggregates of dendrimers on underlying dendrimer films.

For G6 and G8, individual dendrimer molecules could be clearly observed within the AFM images, which appeared as monodispersed, dome-shaped particles which were randomly distributed on the mica surface.

The diameter and height data were used to calculate the molecular volume of each particle imaged in the AFM studies. The calculated volumes for G6 and G8 were in very good agreement with theoretical values for individual molecules while that for G4 indicate the aggregation of these open molecules.

In the case of the adsorption of G4 dendrimers on different SAM surfaces, the similarity of the spherical features observed on both types of substrates (SAMs surfaces, and G4 treated SAMs) caused difficulties in their discrimination using AFM height images only. *In situ* imaging and force measurement (force-distance and amplitude-phase-distance) experiments were therefore performed to determine whether the imaged features were G4 dendrimer molecules or the

Chapter three: Visualization and characterization of PAMAM dendrimers on different surfaces

underlying functionalized substrates. *In situ* imaging of the adsorbed G4 dendrimers onto SAM-COOH surfaces in deionized water indicated the rapid formation of multilayers, most likely via electrostatic interactions and hydrogen bonding. This finding is supported by the appearance and merging of some aggregates and reappearance of new aggregates of dendrimer molecules upon such layers. Utilizing AFM probes functionalized with SAM-COOH, and applying the AFM in its force-distance and amplitude-phase distance modes, our data suggest conformational changes of the G4 dendrimers molecules on the different alkanethiol surfaces.

CHAPTER FOUR

MONOVALENT COUNTERION CORRELATIONS BETWEEN LIKE-CHARGED SURFACES FACILITATE IMAGING IN REAL TIME

4.1 BACKGROUND

DNA plays an important role in many cellular processes like replication, recombination, and transcription. Besides its genomic information, DNA exhibits very interesting biophysical and physicochemical properties, which are essential for a proper functioning of the biomolecular processes involved. Fundamental phenomena like molecular elasticity, binding to proteins and supercoiling can be investigated nowadays on a single molecular level (Anselmetti *et al.*, 2000). For example, developing a deep understanding of the adsorption of DNA onto oppositely charged substrates would be of fundamental importance to understanding many key physiological processes. It is not surprising therefore that many experimental studies have approached this problem from many different viewpoints. Much of this work has been strongly motivated by applications to gene therapy (Sens and Joanny, 2000) and references therein. Of relevance here are individual molecule techniques, which allow the addressing and observation of the conformation of individual molecules. The atomic force microscope in particular has proved its use in both the characterization and analysis of biomolecules, and has been used to observe DNA in a near natural state and observe DNA undergoing natural processes

Chapter four: Monovalent cation correlations between like-charged surfaces facilitate imaging in real time.

(Argaman *et al.*, 1997, Clausen-Schaumann *et al.*, 2000). AFM studies typically use muscovite mica as the substrate of choice in which to image DNA, this being primarily as a result of its atomically flat surface after cleavage along the basal plane of the potassium layer (Terashima, 2002). Muscovite mica consists of tetrahedral double sheets of $(\text{Si/Al})_2\text{O}_5$ electrostatically linked by K^+ ions. The K^+ are believed to dissociate in an aqueous environment where they are then replaced by protons (H_3O^+) (Campbell *et al.*, 1998), such K^+ ions are believed to give rise to a surface charge of 0.0025 C/m^2 at neutral pH, equivalent to 0.015 electronic charges per nm^2 (Pashley, 1982). In parallel, DNA carries a high negative charge in aqueous solutions, such a charge results from two electronic charges per base pair (or equivalently, per 3.4 \AA) along the length of the double helix (Ha and Liu, 2001). Such negative charge carried by the phosphates prevents stabilization to the mica, and hence reinforces the need for surface modification to enable aqueous imaging of DNA. With reference to DNA the methods most frequently utilised involve the formation of electrostatic bridges between DNA and substrate. One of the first methods for reliable AFM imaging of DNA utilized the attachment of positive amine groups to the mica surface, using aminopropyltriethoxysilane-creating APTES-mica (Lyubchenko *et al.*, 1993). This approach binds DNA very strongly to the mica, and as a result the persistent length of DNA may be lowered. Such strong binding may also be detrimental to various *in-vitro* experiments (Zuccheri *et al.*, 1998). An alternative approach is the pretreatment of mica with divalent cations. Divalent metal cations are widely presented *in vivo*, and known to be essential for living organisms to maintain regular activities (Sigel, 1989). This may take the form

of magnesium, nickel, or other divalent cation being present in the DNA solution (Hansma *et al.*, 1995, Wagner, 1998). A systematic study of the effect of the cationic radius on the adsorption of DNA onto mica led to the conclusion that stronger adsorption occurred in the presence of highly charged transition metal ions such as Ni^{2+} and Cu^{2+} , whereas the metal ions of Mg^{2+} and Mn^{2+} were produce a weaker adsorption (Hansma, 1996b). These cations will serve two effects, first the ion-exchange between protons, K^+ , and the divalent cation will result in a net-positive charge carried by the mica, (Osman M.A, 2000), second the overall charge of the DNA molecule will also be altered, this can lead to problems as a result of changing the conformation of the DNA (Chasovskikh and Dritschilo, 2002). It is important that this does not occur, or can be quantified, so that their influence is not confused with the molecule or system of interest. In addition, transition metals have a strong base-affinity. They can chelate or coordinate directly to the nucleophilic atoms of bases and thus perturb the hydrogen bonding between base pairs, resulting in a destabilization of DNA (Chasovskikh and Dritschilo, 2002). Whilst strong adsorption is desirable for high resolution imaging, it is often preferable to weakly attach DNA to a substrate. This allows a more natural conformation to be adapted, and can enable real time processes to be studied. A method exploited for modulating the ionic environment, producing sufficient attachment to mica, whilst maintaining mobility of DNA has previously been exploited, enabling “real time” imaging of DNA related processes, (Zuccheri *et al.*, 1998). Contrary to the well-established intuition by mean-field Poisson-Boltzmann theory, which predicts that like-charged rods should repel, regardless of the valency of the counterion, it now seems that like-charged

particles sometimes attract each other (Manning, 1994). Reports of this extraordinary effect and efforts to explain it have led to some debate (Grier, 1998, Diehl *et al.*, 2001). The interaction between charged objects is strongly affected by the electrolytes present in the solution. The macroions attract the counterions and repel the coions, which generate large inhomogeneities in the densities of the electrolytes. The main effect of these inhomogeneities is the screening of the Coulomb interaction between polyions. This is characterized by the Debye-Huckel screening length, which at the mean-field level would decrease Coulomb repulsion in accordance with DLVO theory (Barbosa, 2002). The ability to control adhesion forces could ultimately prove invaluable to any microscopist wishing to study DNA and other like biomolecules. If we look at a simple analogy, describing DNA as an array of negative charges that has a “rod-like characteristics” and the mica, as a planar surface with “plane-like properties” it would be possible to discuss the attraction between mica (negative plane) and DNA (negative rod) in relation to previous work by Mashl and Grønbech-Jensen (Mashl and Grønbech-Jensen, 1998). Statistical evidence for the attraction between rods and planes has been put forward where a systematic study of such like-like interactions resulted in attraction mediated by counterions that induced “counter-ion correlation”. These counterions in the solution are divided into free counterions and condensed counterions. Free counterions are allowed to roam throughout the volume, but condensed counterions are restricted to lie on the surface and reduce the local monomer charge. The condensed and free counterions are in chemical equilibrium, and so, the local monomer charge fluctuates (Nyquist *et al.*). Although the number of polyions and counterions is fixed, the number of condensed counterions per

Chapter four: Monovalent cation correlations between like-charged surfaces facilitate imaging in real time.

monomer can vary. Such observations have also been made with like-charged spheres (Grier, 1998, Grier, 2000, Messina *et al.*, 2000) and describe a columbic depletion zone. Whilst Mashl and Grønbech-Jensen suggested that such “counter-ion correlation” is more profound with an increase valency of counterions, they may also be observed with the use of monovalent cations (Diehl *et al.*, 2001). Moreover, Mash and Gronbech-Jensen (Mashl and Gronbech-Jensen, 1998) found an effective attraction between rods and a planar surface that is mediated by counter-ions at room temperature in the dilute-rod limit. They indicated that this attraction was due to counterion fluctuation and correlations (neglected in Poisson-Boltzmann theory) that overcome the inherent columbic repulsion between the two macroions. Density functional arguments also predict that like-charged plates can attract (Ha and Liu, 2001). The phenomena under contention depend on three energy scales, those set by Van der Waals attraction, by the randomizing influence of thermal energy, and by the hierarchy of electrostatic interactions among highly charged polymer particles and the singly charged simple ions around them. The balance of these three determines the properties of the system (Grier, 1998). Suggestions that the proximity of the rod and plane may dictate the probability of “counterion-correlation” mean that the rod and the plane would have to lie within sufficient proximity for such correlations to occur. This suggests the importance of Brownian motion. Besides attraction between like-charged rods and planes, attraction between rods of like-charge has also been suggested (Potemkin *et al.*, 2002).

Here we aim to

Chapter four: Monovalent cation correlations between like-charged surfaces facilitate imaging in real time.

- 1- Test the theory of fluctuation of monovalent cations between two like charged surfaces, namely DNA-DNA (rod-rod) and DNA-mica (rod-plane) surfaces in the absence of divalent cations using AFM in real time and at an individual molecular level.
- 2- Imaging of DNA in 10% PBS containing divalent cations, (MgCl₂ & NiCl₂).
- 3- Imaging of DNA in Air.
 - i. Imaging of DNA on Mica.
 - ii. Imaging of DNA on MgCl₂-treated Mica.

4.2 EXPERIMENTAL PARAMETERS

Details of the experimental materials, methods & instrumentation are present in Chapter 2, sections 2.11, 2.13, 2.2.1.1 and 2.3.

4.3 RESULTS AND DISCUSSION

4.3.1 Imaging of DNA in the Presence of Monovalent Cations; the Theory of Fluctuation of Monovalent Cations between Two Like Charged Surfaces

Figure 4.1 shows a sequence of time-laps images of 1 µg.ml⁻¹ plasmid DNA, diluted in 10% PBS and immediately adsorbed onto mica and imaged in the same buffer. DNA molecules exhibit a width of typically 11-14 nm that is more than the theoretical diameter of DNA (2 nm); a well-known phenomenon largely governed by tip convolution effects (Allen *et al.*, 1992, Thundat *et al.*, 1992, Vesenka *et al.*, 1994, Miller *et al.*, 1995, Ramirez-Aguilar and Rowlen,

Chapter four: Monovalent cation correlations between like-charged surfaces facilitate imaging in real time.

1998, Rivetti and Codeluppi, 2001). Average height observed were 1.2 ± 0.3 nm which is higher than heights previously measured with AFM (Hansma *et al.*, 1998). The mean contour length of these features were 1120 ± 70 nm, this is compatible with the theoretical contour length of one DNA plasmid molecule of 1484.1 nm. It's noteworthy that the plasmid's morphology is changing with time, representing random movement, during which the DNA molecule contracts and relaxes. This illustrates the weak adsorption of DNA to the mica substrate in 10% PBS. Within these images features of mean diameter and heights of 17 ± 2 and 2 ± 0.3 nm respectively were obtained. These are thought to result from NaCl.

Chapter four: Monovalent cation correlations between like-charged surfaces facilitate imaging in real time.

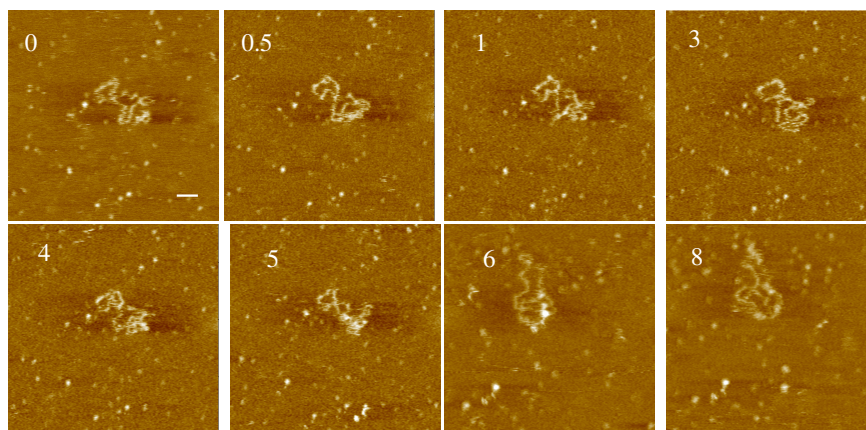


Fig. 4.1. Top view AFM images of different ds DNA topologies on mica taken in AFM tapping mode under ambient condition immediately after the dilution of DNA with 10% BPS. Numbers on the images represent time lapsed in minutes. Scale bar = 70 nm, z scale = 6 nm. My colleague, Ellis, J.S, and I obtained these images.

Figure 4.2 shows typical topographical images for $3.3 \mu\text{g}\cdot\text{ml}^{-1}$ DNA plasmid incubated in 10 % PBS for 24 hrs before imaging. All of these molecules were changing their tertiary structures with time. We will only concentrate on 3 features from these molecules, namely those denoted a, b and c in the images. Features a and b together had a contour length of 2396 nm, their thickness and heights were 12 ± 2 nm and 0.9 ± 0.1 nm respectively. These features reflect 2 DNA molecules fused together, which was confirmed with time, when these molecules were identified as two separate molecules. The first (a) has two loops of a contour length of 1435 nm, a thickness of 13 ± 2 nm and a height of 1.0 ± 0.3 nm. The other (b) was a partially condensed circle of a contour length of 961nm, thickness of 14 ± 2.5 nm and height of 1.1 ± 0.3 nm. With time, the contour length of molecule (b) decreases dramatically to 766 nm after 5 min, 690 nm after 6.5 min, 620 nm after 8.5 min and finally 520 nm after 13 min

Chapter four: Monovalent cation correlations between like-charged surfaces facilitate imaging in real time.

respectively, while its thickness and height increase to be 33 ± 1 nm, and 1.8 ± 0.3 nm respectively. Regarding molecule (c), the contour length was 1576 nm, which starts to decrease in length after 5 min to be 1200 nm when it starts to fold from one end. The thickness and height for the molecule was 12 ± 2 nm and 1 ± 0.2 nm respectively while they were 32 ± 2 nm and 1.8 ± 0.3 nm respectively at the folded end.

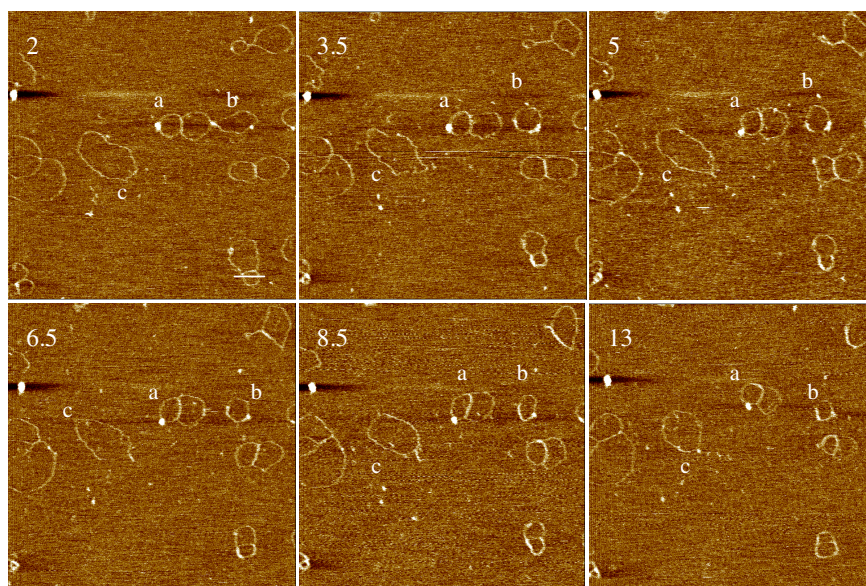


Fig. 4.2. Top view AFM images of different ds DNA topologies on mica taken in tapping mode AFM under ambient condition. The DNA was incubated in 10%PBS for 24 hrs before being imaged in the same buffer. Open relaxed DNA molecules were observed to change their conformation by time. Molecule (c) was condensed into a partially condensed toroid. Numbers on the images represent time lapsed in minutes. Scale bar = 250 nm, z scale = 5 nm.

Although DNA condensation and aggregation usually require multivalent cations, Attraction has been predicted in univalent salt solution between parallel polyelectrolyte rods, modelled as infinite linear arrays of uniformly

Chapter four: Monovalent cation correlations between like-charged surfaces facilitate imaging in real time.

spaced monovalent charge sites (Manning, 1994). Attraction results from the enhanced translation entropy of the condensed counter-ions as they share the space between the polyions. The relationship between this theoretical prediction and the experimental results remains to be clarified. Figures 4.3 depict a similar data series as above in figure 4.2 but also suggesting that aggregation between DNA strands has occurred. Observation over 14 minutes suggests the de-aggregation of DNA. These data suggest two occurrences, firstly attraction between DNA and mica leading to partial immobilization, secondly rod-rod attraction leading to aggregation of DNA, such attraction may be weak, as both desorption from the surface and de-aggregation occurs rapidly.

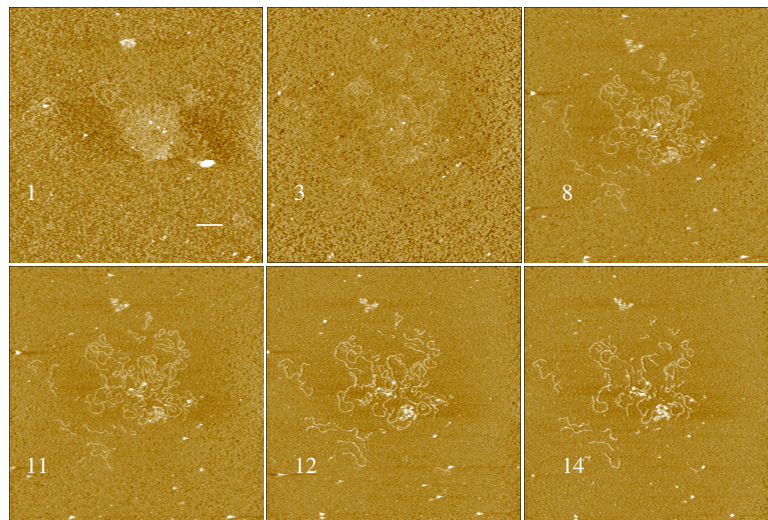


Figure 4.3. Top view AFM images of different ds DNA topologies on mica taken in tapping mode AFM under ambient condition. The DNA was imaged immediately in the same buffer. De aggregation of DNA aggregates was shown in real time. My colleague, Ellis, J.S obtained these images. Numbers on the images represent time lapsed in minutes. Scale bar = 200nm, z scale = 10nm.

Chapter four: Monovalent cation correlations between like-charged surfaces facilitate imaging in real time.

4.3.2 Imaging of DNA in 10% PBS Containing Divalent Cations, (MgCl_2 & NiCl_2).

Figure 4.4 (a-c) represents different images for $3.3 \mu\text{g}\cdot\text{ml}^{-1}$ DNA plasmid being diluted in 10% PBS containing 2mM MgCl_2 and 1mM NiCl_2 . It depicts representative tertiary structures of those observed when the bare DNA molecules adsorbed on mica surface and imaged in the aforementioned buffer.

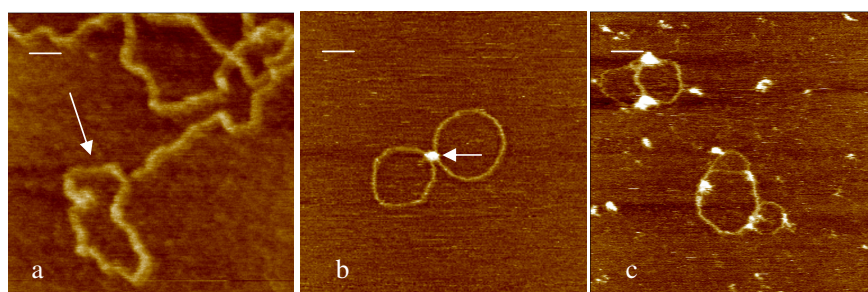


Figure. 4.4. Top view AFM images of different ds DNA topologies on mica taken in tapping mode AFM under ambient condition. The DNA was imaged immediately in the 10% PBS containing 2mM MgCl_2 and 1mM NiCl_2 , (a) shows open circular and supercoiled DNA, (b) shows one twisted DNA molecule where the height at the point of twisting, marked by an arrow, most likely represents the height of two DNA double strands over each other and (c) shows features, most probably salt particles, that located on many of the DNA stands. Scale bars = 100, 100 and 75 nm respectively, z scale = 5 nm.

In figure 4.4 (a), the mean apparent thickness of these molecules was 17 ± 1.2 nm, the height was 1.5 ± 0.5 nm. The circumference of the marked molecule was approximately 1423 nm which when compared to the theoretical contour length of the plasmid DNA refers to individual DNA molecule. Duplicate

Chapter four: Monovalent cation correlations between like-charged surfaces facilitate imaging in real time.

measurements usually differed by about 2 to 3 %. Figure 4.4 (b) shows another height image for the DNA plasmid in the same experimental condition. The diameter of the marked white feature is 47 nm, the height was 5.3 nm. The diameter of the DNA was 19 ± 4 nm and the height was 1.2 ± 0.4 nm. The contour length of these two features together was ~1562 nm. The contour length of one of them was 814 nm, these two features represent one twisted DNA molecule where the height at the point of twisting most likely represents the height of two DNA double strands over each other. In image (c), small features of solid material were located on many of the DNA stands, most probably salt particles. However if this were the case they would be expected to be found randomly across the mica surface. These deposits are predominantly found apparently attached to the nucleic acid material, suggesting an attraction or dependence on the presence of the DNA.

4.3.3 Imaging of DNA in Air.

4.3.3.1 Imaging of DNA on Mica.

Figure 4.5 shows a representative image of naked DNA plasmids being adsorbed from 10% PBS buffer containing 2mM MgCl₂ and 1mM NiCl₂ and imaged in air. These plasmids display relaxed, open structure morphology with some entanglements and fasciculation of the strands.

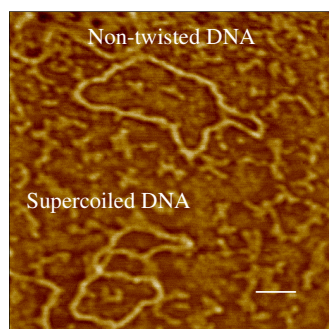


Fig. 4.5. Top view AFM image of uncondensed DNA plasmids visualized using AFM operating in air. The plasmids display relaxed open structure and supercoiled morphologies on mica. Scale bar = 100 nm, z scale = 15 nm.

In some cases however, islands and/or holes of 0.6-0.9 nm in height appear in the substrate. Since this kind of defects are not present on freshly cleaved mica, we deduce that they are due to salt layers, which cover the mica substrate when DNA is prepared from a buffer solution. After drying of the preparation, the DNA molecules appear to be trapped in this salt layer. This layer distorts the measurement of DNA height and is the main source of error; some sample deformation due to either the loading force of the tip or the interaction with the substrate is also present.

Height measurements of DNA in air using tapping mode reveal a height of 0.35 ± 0.2 nm. This value increases up to 1.5 ± 0.5 nm when the salt layer as in figure 4.4(a), in which the molecules are embedded, is removed. In addition to the salt layer that hinders the tip from reaching the surface of the substrate, the lower height of the DNA measured in air has been attributed to dehydration of the sample. The average thickness of these molecules were 23.5 ± 3.2 nm.

4.3.3.2 Imaging of DNA on MgCl_2 -treated Mica.

Figure 4.6 depicts a representative image of naked DNA plasmids being adsorbed onto MgCl_2 treated mica. The DNA appears as partially condensed long rods of a thickness and contour length of 15 ± 2 nm, 400 ± 100 nm respectively. The reason of this partial condensation of the DNA is most likely due to the release of some divalent cations from the mica to the DNA solution before the drying process. Interestingly, most of these rods were aligned in the same direction reflecting the direction of the stream of nitrogen gas during the drying process.

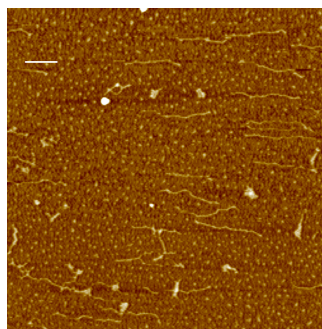


Fig. 4.6. Top view of an AFM image of ds DNA on MgCl_2 treated mica in air. Both long rods and plectonemic morphology are observed. Scale bar = 270 nm, z scale = 20 nm

4.4 CONCLUSIONS

Immobilization of DNA molecules on mica was obtained successfully in the presence of monovalent cations. This was theorized as being due to random fluctuations in condensed sodium ions leading to formation of temporary dipoles between the DNA molecules (rods) and the mica surface (planar surface). In addition, aggregation was observed, confirming the theory that monovalent cations may induce like-charged attraction. These data suggest that further research needs to be conducted into the counter-ion correlation theory. Molecular dynamics simulations of simple condensing highly charged, semiflexible polyelectrolytes such as DNA by multivalent ions are performed where all charges are explicitly treated. No condensates form or are stable for divalent counterions (Stevens, 2001). DNA condensation typically occurs for counterion valences of 3 or larger. The importance of multivalency is that it increases the magnitude of the Coulombic interactions and enables the net attraction to occur before the steric repulsion enters. For monovalent and divalent ions, the Coulombic interactions are not strong enough to counter entropic effects. Thus, condensates do not form for low valence counterions. However, regarding the situation here where molecules might condense to form toroidal like structures as in Figure 4.2, we suggest that these are unstable condensates temporarily formed as a result of the neutralization of the DNA molecule where the entropy cannot stop the volume decreasing, and the system will shrink until steric repulsions stop the contraction and reverse the condensation to form open circular molecules at the end.

Chapter four: Monovalent cation correlations between like-charged surfaces facilitate imaging in real time.

It has been observed that pre-treatment of a mica substrate with MgCl_2 and a subsequent deposition of DNA will result in the formation of partially condensed DNA molecules. The morphology of these condensates depends on the density of the cations across the substrate and the amount of soluble cations. Using these methods, it appears to be possible to visualise intermediates of the DNA condensation process. It is difficult to compare these intermediate stages to those observed when plasmid DNA is condensed in solution, however it appears that whether DNA condensation is surface-mediated or in solution, if adequate cations are present toroidal and plectonemic condensates will result.

CHAPTER FIVE

SURFACE VISUALIZATION OF PAMAM

DENDRIMERS-INDUCED DNA CONDENSATION

5.1 BACKGROUND

DNA and polyamidoamine (PAMAM) dendrimers form complexes on the basis of the electrostatic interactions between negatively charged phosphate groups of the nucleic acid and protonated amino groups of the polymers (Kabanov and Kabanov, 1995, Bielinska *et al.*, 1997, Kabanov *et al.*, 1998). The physicochemical properties of dendrimers are dependant on their shape, as well as the presence of high positive charge density of protonized primary amine groups on their surface. Together with high solubility in water, these characteristics have led to the use of these polyamines to mediate efficient DNA transfer into numerous cell lines *in vitro* (Bielinska *et al.*, 1999). Complexing DNA with dendrimers changes the molecular organisation of DNA and results in condensation and aggregation of DNA particles, but also increases DNA survival upon delivery *in vitro* and *in vivo*. DNA condensation occurs once a critical concentration of the cation is reached where the Coulombic interactions being sufficient strong that they dominate entropic interactions and can achieve a charged-ordered state that has the lowest Coulombic energy (Matulis *et al.*, 2000, Stevens, 2001). In the thermodynamic analysis of the osmotic stress-induced condensation of DNA in the presence of multivalent cations it was argued that the source for the entropy increase

accompanying DNA condensation in aqueous environment must be the change in entropy of water induced by the approaching DNA molecules, and thus that the hydration force is the source of attraction between DNA molecules (Matulis *et al.*, 2000). However, the hydration force and electrostatic mechanisms may be indistinguishable in an aqueous environment, since the orientation of the water dipoles by ions and charged surfaces also leads to a positive entropic contribution. Complex formation analysis and characterization can be carried out on soluble–insoluble or low–high density particles by various methods such as UV light absorption, laser light scattering and measurements that use radiolabeled DNA and/or dendrimers. The actual binding affinity constants of DNA and dendrimers are not easily determined, partly because of the subsequent aggregation and precipitation of the complexes (Rau and Parsegian, 1992). However, it has been observed in studies using intact dendrimers that G5 or above show greater transfection efficiencies than the lower generation G0–G4 dendrimers (Haensler and Szoka, 1993). Further work from these investigators revealed that the transfection observed in these experiments was mediated by degraded dendrimers when compared with the intact G5 polymer. The enhanced transfection activity of the degraded polymer was attributed to increased flexibility in their structure. Independent studies by Kukowska-Latallo and co workers documented the efficiency of intact dendrimers as synthetic vectors for the delivery of genetic material into cells (Kukowska-Latallo *et al.*, 1996). This work employed various generations of intact dendrimers to transfect plasmid DNA in a variety of cells using luciferase and β -galactosidase reporter genes to quantify efficiency. In contrast to the results obtained with degraded PAMAM

dendrimers, only intact dendrimers >G5 mediated significant transfection, and this required the addition of a dispersing agent such as (diethylamino) ethyl (DEAE) dextran. The addition of other agents to the DNA–dendrimer complex can alter transfection. For example, chloroquine or dextran added to dendrimer–DNA complexes significantly increase transgene expression in a number of cell lines. DEAE dextran is believed to alter the nature of the dendrimer by dispersing complex aggregates. However, it is cytotoxic and might prevent stable gene integration. Thus, an understanding of the physicochemical properties and biological function of dendrimer-DNA complexes appears to be an important issue for the development of artificial systems for gene transfer. We demonstrate this philosophy here in a study where plasmid DNA has been condensed using G4, G6 or G8 PAMAM dendrimers, and the morphology of these condensates has been visualized and compared in terms of their tertiary structures. An assessment is then made regarding the effect of the dendrimer’s loading ratio, the dendrimer’s generation, and the effect of the ionic strength and pH of the dendrimer solution on the obtained condensates. Condensates have been visualized mainly in near *in situ* conditions (in liquid) and on occasion in partially hydrated state (in air). Finally, an assessment has been made regarding the ability of a positively charged substrate to induce DNA condensation in the presence and absence of soluble cations. A comparison also is made of the tertiary structure of DNA condensates that are formed in the solution state to those which are surface mediated. There is a question of how well the composition of adsorbed structures represents the composition that is in solution. We have no readily accessible way of determining this, and hence, it

is possible that there are intermediates in solution that are missed in this study. However, this does not significantly effect the interpretation of the data, since we report only the structures that are seen and make no assumptions about ones that are not. The question of how the substrate may affect the structure of the condensates is discussed below. However it is interesting to note the similarities of our protocol to those reported by others who have utilised positively charged substrates to immobilize DNA in the study of DNA tertiary structure (Lyubchenko *et al.*, 1992, Pope *et al.*, 2000). As a parallel, a number of investigations have also been reported in which the mica substrate used has been coated with small molecular cations before deposition of DNA solution in order to intentionally induce DNA condensation (Allen *et al.*, 1997a, Fang and Hoh, 1998b, Ono and Spain, 1999). In these studies, this protocol has been proposed as a means of enabling the visualization of DNA condensates that have been formed on a surface in contrast to those formed in solution.

5.2 RESULTS AND DISCUSSION

5.2.1 Effect of Dendrimer's Loading Ratio and Generation on the DNA Condensation.

5.2.1.1 Effect of G4 Dendrimer's Loading Ratio.

The folding pathway of dendrimers-induced DNA condensation on the surface of mica in aqueous environment was examined by varying the concentration of dendrimers in a dilute DNA solution and visualizing intermediates by AFM. DNA was condensed in solution with G4 over seven primary amine charges to DNA phosphate ratios, 0.005:1, 0.5:1, 1:1, 2.5:1, 5:1, 10:1 and 15:1. These ratios were chosen to investigate the effect of G4 loading ratio on the structural

morphology of the DNA complexes taking in consideration that the theoretical point of collapse of the nucleic acid molecule is when ca 85-90 % of its anionic phosphate charge has been neutralized (Bloomfield, 1996, Matulis *et al.*, 2000). Too low a cation concentration will lead to unstable poorly condensed complexes susceptible to attack from nucleases. These complexes are also likely to have a low positive, or even a negative, surface charge reducing the potential for interaction with the negatively charged cell membrane, leading to diminished cellular uptake. Alternatively, too many cations in the system would lead to excess positive charges that would be freely available in the body resulting in high toxicity. The higher ratios mentioned above of >5:1 provide an excess of positive charge but were used to investigate the effect of a high cation concentration on full condensation of the genetic material. Figure 5.1 (a-h) depicts representative AFM Images of (a) DNA imaged in 10% PBS containing 1mM NiCl₂ and 2mM MgCl₂ and (b-h) DNA-G4 complexes at different charge ratios imaged in deionized water. In Figure 5.1 (a) characteristic morphology consistent with linear, naked-circular and supercoiled DNA were observed. This is supported by complementary agarose gel electrophoresis discussed later, Figure 5.23 (lane 1), which shows the pBR322 plasmid to consist of the three forms of DNA, linear (lower band), naked circular (middle band) and supercoiled (upper band) respectively. The mean thickness of these molecules was 17 ± 1.2 nm; the mean height was 1.5 ± 0.5 nm. In Figure 5.1 (b) the G4-DNA molecules were shown to aggregate and adhere to the mica surface at this very small ratio (0.005:1) indicating that these small open structure dendrimer molecules (G4) were able to bridge between the DNA-DNA molecules and the DNA-mica surfaces. The structures

formed at this ratio are of a non-uniform morphology. Most polyplexes consist of a dense core surrounded by a large quantity of diffuse materials. The relative quantities of dense and diffuse material vary with some structures containing solely material of the more diffuse nature. The mean apparent thickness of these molecules in the un-aggregated areas was 7 ± 2 nm; the mean height was 1.3 ± 0.3 nm. For the 0.5:1 ratio (Figure. 5.1c), features consistent with individual molecules or small aggregates of G4 molecules are observed to decorate the DNA molecule. For the DNA to be fully condensed, a high proportion of the total cationic charge present must make contact with a section of DNA. However, the theoretical cationic charges available here are not sufficient to combine with the DNA. In addition a number of cationic charges will be effectively 'lost' because they adhered to the negatively charged mica surface. The measured thickness and height of the decorated DNA strands were 22 ± 5.5 and 3.7 ± 1.4 nm, respectively, while the measured thickness and height of the undecorated parts were 11.0 ± 0.5 and 0.5 ± 0.1 nm, respectively. This is consistent with some regions of the DNA plasmids having a high density of bound G4 whilst other regions remain relatively bare. At 1:1 ratio, the observed complexes mostly appear as thickened ring-like structures or pre matured toroids (thickness ranging from 20 to 60 nm), similar to the classical DNA condensates that have been predicted theoretically (Hud *et al.*, 1995, Stevens, 2001) and observed experimentally (Plum *et al.*, 1990, Lin *et al.*, 1998). The reason of considering them as premature toroids is the ability to distinguish the low compaction of these rings. The thickened regions are made up of parallel strands of condensed DNA molecules, consistent with DNA folding as a mechanism for DNA condensation, Figure 5.13. Features

attributable to individual G4 molecules can no longer be seen to decorate the individual complexes, most likely due to their higher packing density along the DNA. As the ratio increased to 2.5: 1, DNA condensates can grow in size by means of a DNA loop from one condensate reaching into the adjacent condensate, Figure 5.1(e). Many molecules have two or more independent loops; other molecules with multiple intramolecular loops that cross at a single point can also be seen. These loops of DNA resemble the petals of a flower with the central region, the pistil. Structures like these have been observed before by my colleague Alison Martin, by Fang and Hoh (Fang and Hoh, 1998a) and Montigny *et al.* (Montigny *et al.*, 2001). Experimentally cationic charges may be present in excess to that of the anionic charges, however, for the DNA to be fully condensed a high proportion of the total cationic charges present must make contact with a section of DNA. In reality, not all the theoretical cationic charges available are practically able to combine with the DNA. A number of cationic charges may be effectively 'lost' because they are sterically unable to reach a section of the charged DNA after part of the polymer molecule has become complexed to other DNA molecules and again a number of the polymeric charges will also adhere to the negatively charged mica surface. Flowers become very prevalent as the G4 loading is further increased, Figure 5.1 (f-h). The multimolecular flowers generally have a single crossover point, which appears as a very tall structure with a height of (5-7 nm) often 5-10 times taller than an isolated DNA strand. In some larger structures there are multiple crossover points. In addition to these flower-like structures disk-like structures are also observed. The thickness of the strands within a disk (ca 30 nm) is usually greater than those in the flowers (ca 3-5 nm),

suggesting that the strands in a disk are composed of many closely associated DNA strands, Figure 5.1(f). Stabilization of strand-strand interactions is suggested by the presence of these flowers or disks. However, disks have never been seen in the absence of flowers in the same preparation, while flowers are frequently seen in the absence of disks. In addition, it appears in many images that a disk is forming from a flower. Hence it is likely that disk formation follows flower formation. At the 15:1 ratio, Figure 5.1(h), the disk-like structures are less frequently observed, rather flowers and open looped molecules were seen, most likely an indication of the start of the reverse condensation process. This was confirmed by repeating these experiments at 15:1 and 20:1 ratios, Figure 5.2 (a-d). Again all molecules appeared as open loops and relaxed circles. The average contour length of which was 1540 ± 60 nm and the average diameter was 485 ± 5 nm, which reflects individual relaxed DNA molecules. The average thickness was 17 ± 1 nm and the average height was 0.6 ± 0.1 nm. The possible reason for observing a relaxed DNA in these high dendrimers ratio is most likely due to the accommodation of many dendrimer molecules onto the DNA ds(s) leading to charge inversion. We also considered the effect of the decrease in the number of water molecules relative to the number of free amine groups available in the system at these ratios. Theoretical estimates of the number of free amine groups in the 15:1 and 20:1 ratios are ca 7.3^{16} and 9.9^{16} molecules respectively, in the $30 \mu\text{l}$ aliquot. This results in the ratio of water molecules to free amine

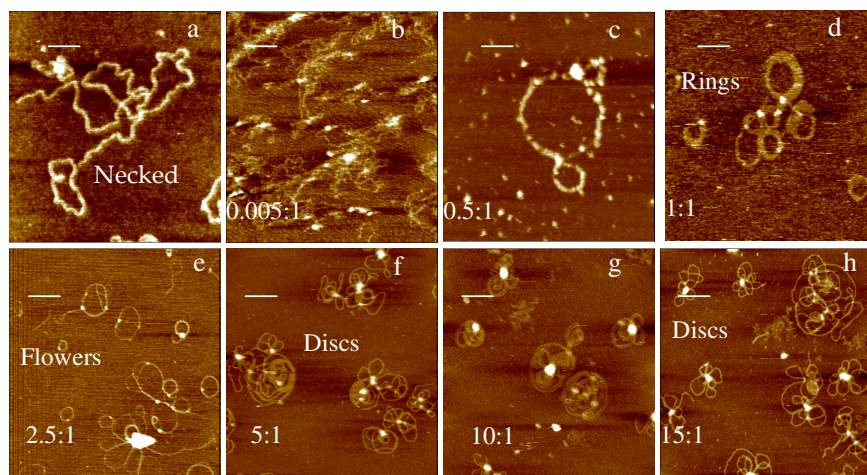


Figure 5.1. Representative AFM Images of (a) DNA and (b-h) G4-DNA complexes at different charge ratios, imaged in deionized water. Dendrimers: DNA ratios were mentioned on the images. The most interesting features are multimolecular flower-shaped structures made up of condensed rings, open loops and toroids, which all have one or few crossover points that are as much as 5-10 times taller than that of a single double stranded DNA molecule. A disc-shaped condensate also appears at 5:1-15:1 ratios. Scale bars = 180, 150, 70, 100, 370, 100, 100 and 100 nm respectively, z scale = 7 nm.

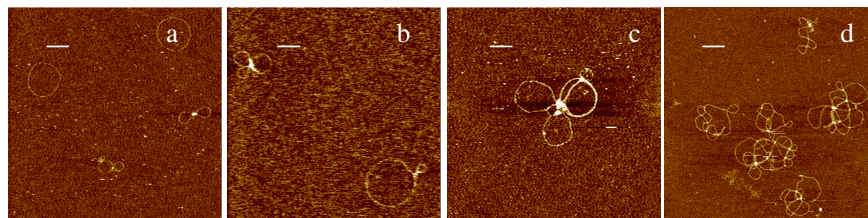


Figure 5.2. Representative AFM Images of G4:DNA complexes formed at (a-c) 15:1 and (d) 20:1 ratios and imaged in deionized water. Molecules appear as relaxed open circles and loops. Scale bars = 300, 160, 120 and 100 nm respectively, z scale = 5 nm.

groups of 11.6:1 and 8.6:1 respectively compared with 162:1 for the ratio 2:1 (Figure 5.3a). Obviously, the number of water molecules decreases linearly with the increase in the dendrimers ratios. Consider the situation in which the DNA double helix is totally covered and neutralized by dendrimers with a large number of peripheral monovalent positive charges (64 charges per molecule in our study). Due to its 3-D structure, each positive charge on the dendrimer cannot position itself directly opposite each negative charge on the DNA. As a result a fraction of the positive charge is situated some distance from the DNA phosphate backbone. Additionally, the size and shape of the dendrimer molecule forces large segments of the helix between adsorbed dendrimers to remain negatively charged. Nguyen and Shklovskii (Nguyen and Shklovskii, 2002) stated that an additional dendrimer could still be adsorbed on DNA as follows. When a new dendrimer molecule arrives at the DNA double helix, which is already neutralized by dendrimers, it creates a place for itself in the following way. One dendrimer monomer partially detaches from DNA surface, exposing some of the negative charge of the DNA. These negative “vacancies” can then join together by a shift of the adsorbed dendrimer molecules along the DNA strand. Space is then found for a new dendrimer molecule to be accommodated in the vacancy (with its positive charge closer to the DNA charge than the previous dendrimer conformation). This process is dependent on the shape, flexibility & charge density of the dendrimers, and results in an increase in the total positive charge surrounding the DNA with some of the charge now found some distance from the DNA strand. Providing the dendrimer ratio is sufficiently high, this can result in charge inversion, the outer layer of the “complexed” strand having a net positive charge. This

mechanism is driven by elimination of the repulsive self-energy of free dendrimer molecules in extended conformations, as it has in the solution. However, in this condition of charge inversion, and due to the closely spaced dendrimers, the DNA molecule extends to relaxed open circles. In contrast, loops observed at these ratios were probably due to the temporarily bridging of G4 molecules between different DNA molecules or within the DNA molecule itself. We therefore believe that these open loops may be intermediates to the fully opened circles in case of high dendrimers ratios. Figure 5:3b.

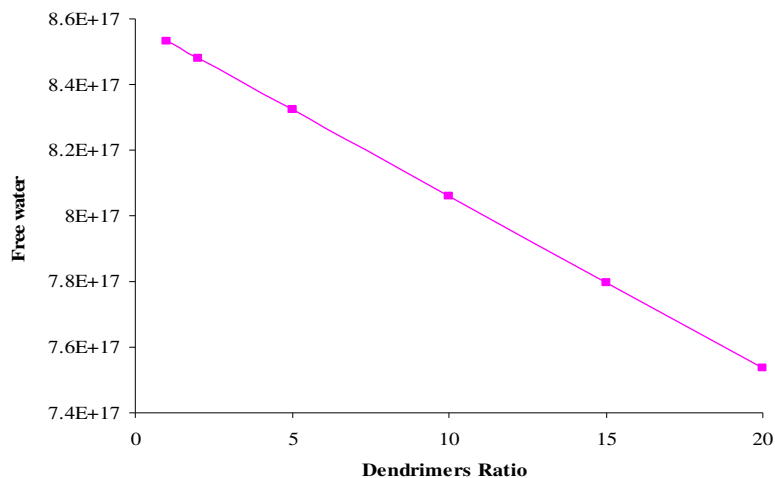


Figure 5.3a shows the change in the (free water/free amine ratio) relative to changes in G4:DNA ratios. As the polymer ratio increases the number of water molecules that can arrange themselves around the free amine groups decreases.

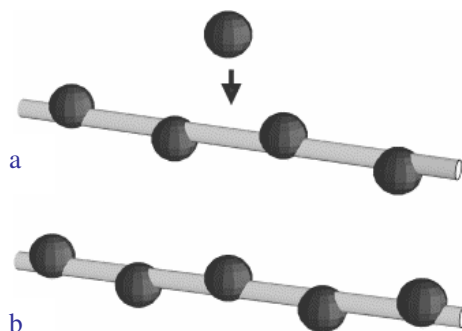


Figure 5.3b shows the origin of charge inversion in adsorption of high generation dendrimers: (a) DNA double helix (grey) neutralized by a Wigner-crystal-like liquid of a high generation dendrimers (dark spheres). A new dendrimer molecule is approaching DNA; (b) the new dendrimer molecule is integrated into Wigner-crystal-like liquid while neighbouring already adsorbed dendrimers slide away from it and smear its charge over the helix (Nguyen and Shklovskii, 2002).

5.2.12 Effect of G6 Dendrimer's Loading Ratio.

Representative G6-DNA condensates formed at the 0.5:1 ratio are depicted in Figure 5.4. A number of flower-like condensates were observed. These flower-like condensates appeared to contain less diffuse materials and petal like strands of nucleic acid, than those of the higher ratios observed with G4. The presence of partly formed condensates at this ratio was expected. This indicates that the number of G6 molecules were not sufficient to make inter and intra molecular bridges. Another feature of this ratio is that the decoration observed previously with G4 is dramatically decreased with G6, most probably due to the number of G6 molecules being decreased to one fourth of that in G4, at the same applied ratios, and that the larger size of this generation most likely enabled the DNA to wrap around the dendrimers molecules instead of the dendrimers decorating the DNA molecules. The condensates formed at the ratio of 1:1 and 5:1 were of globular, spherical, morphology. A dense central core is evident with little or no diffuse material around the circumference of these structures. The mean cross-sectional diameter of these condensates was 85.4 ± 25.3 nm. The mean height was 4.1 ± 1.3 nm. The high molecular weight and charge density of the G6 would also be expected to entrap a greater yield of DNA than the smaller G4 molecule.

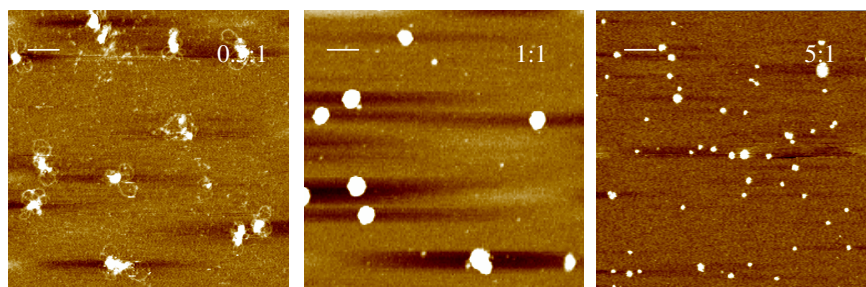


Figure 5.4. Representative AFM Images of G6:DNA complexes at 0.5:1, 1:1 and 5:1 charge ratios imaged in deionized water. Multimolecular flower-shaped structures, which all have one or few crossover points were seen at 0.5:1 ratio while spheroidal shapes were obtained with 1:1 and 5:1 ratios. Scale bars = 100, 100, and 200 nm respectively, z scales = 15, 30 and 30 nm respectively.

5.2.1.3 Effect of G8 Dendrimer's Loading Ratio.

Figure 5.5 shows condensates formed between G8 and DNA at the ratio of 0.5:1, 1:1 and 5:1 respectively. All features were of globular or spherical morphology; no flowers, relaxed molecules, or diffused materials were seen, most probably reflecting the high compaction of this generation relative to G6 and G4. The mean cross-sectional diameter of these condensates was 80.2 ± 35.5 nm. The mean height was 5.5 ± 2.3 nm.

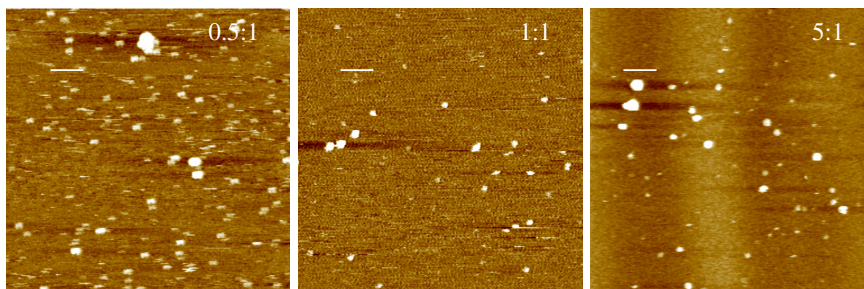


Figure 5.5. Representative AFM Images of G8: DNA complexes at 0.5:1, 1:1 and 5:1 charge ratios imaged in deionized water, spheroidal shapes were obtained with all ratios. Scale bars = 120, 120 and 260 nm respectively, z scales = 12, 7 and 35 nm respectively.

5.2.2 Surface-influenced DNA Condensation in the Presence and Absence of Sufficient Soluble G4 Dendrimers.

5.2.2.1 In the Presence of Sufficient Soluble G4 Dendrimers

The effect of soluble PAMAM molecules on the adsorbed DNA was studied as follows. One 20 μl aliquot of 0.1 $\mu\text{g}\cdot\text{ml}^{-1}$ G4 solution in 10% PBS solution was deposited onto a freshly cleaved mica disc. This was then incubated for 30 seconds. This volume then was almost replaced with a 20 μl aliquot of 3.3 $\mu\text{g}\cdot\text{ml}^{-1}$ DNA in 10% PBS without previous washing. This method leaves some free G4 on the surface of mica ready to interact with DNA plasmid. Figure 5.6 shows polyplexes of toroidal, linear, plectonemic and flower morphologies. The toroidal condensates possess a mean external diameters of 87 ± 7 nm, their internal diameters was 37 ± 8 nm and their thickness was 26 ± 2 nm. The mean length of the plectonemic and rod condensates was approximately 300 ± 20 nm. Their thickness was 25 ± 2 nm. In parallel, condensates of toroidal, plectonemic

and rod-like morphology have been frequently reported for DNA-spermine and DNA-spermidine complexes (Gosule and Schellman, 1976, Gosule and Schellman, 1978, Allison, 1981, Plum *et al.*, 1990, Bottcher *et al.*, 1998, Lin *et al.*, 1998). A schematic representation of these structures together with images obtained at 6:1 (I) and 20:1 (II) G4 : DNA ratios are shown in Figure 5.7.

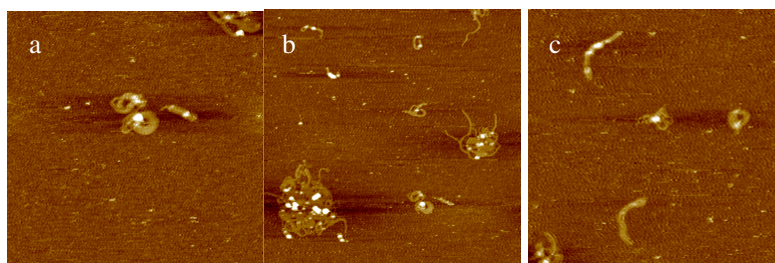


Fig. 5.6. Top view AFM images of different ds DNA topologies on G4 treated mica taken in tapping mode AFM under ambient condition without washing. The DNA was imaged immediately in the 10% PBS. This method leaves some free G4 on the surface of mica ready to interact with DNA plasmid. This method shows (a) toroidal and linear, (b-c) plectonemic and flower morphologies. Scale bars = 150, 270 and 130 nm respectively, z scale = 20 nm.

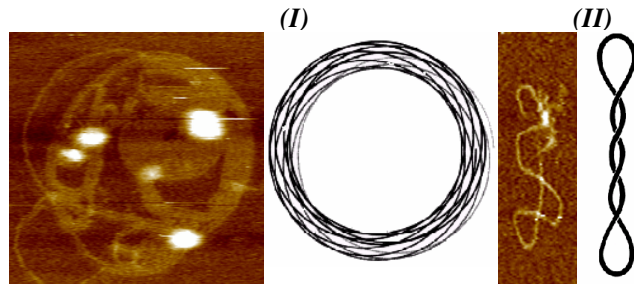


Figure 5.7. Images and schematic representations of (I) toroidal and (II) plectonemic structures. The toroidal structures are made up of multi loops. Each loop is parallel to the other loops, except in the region where it crosses over itself. The ends of the strands will continue around and eventually be parallel to the non-crossover part of the loop.

5.2.2.2 In the Absence of Sufficient Soluble G4 Dendrimers

One 20 μl aliquot of 0.1 $\mu\text{g}\cdot\text{ml}^{-1}$ G4 solution in 10% PBS was deposited onto a freshly cleaved mica disc. This was incubated for 30 seconds, rinsed with five 1 ml aliquots of water, then one 20 μl aliquot of 3.3 $\mu\text{g}\cdot\text{ml}^{-1}$ of DNA solution was introduced in 10% PBS to the surface without previous drying. This method produces a network of DNA flowers, rings and plectonemic structures. All of these forms were loosely formed, where the strands of DNA were clearly observed, Figure 5.8(a-c). The mean thickness of these strands in most cases was 3.3 ± 0.8 nm and the mean distance between these strands was ca 4.5 ± 0.5 nm, as in the marked area in (b). However, for ring-like structures, the thickness was 25 ± 2 nm, the internal diameter was 78 ± 7 nm and the external diameter was 127 ± 4 nm. We assume that some of the adsorbed dendrimers reentered the solution and complexed with DNA molecules to give these early

condensates. The washing of the G4 pre-treated substrate allows relative comparisons to be drawn with the previous protocol, however it is not possible to absolutely quantify the ‘amount’ of G4 remaining, hence it is difficult to know the cationic charge: DNA phosphate ratios.

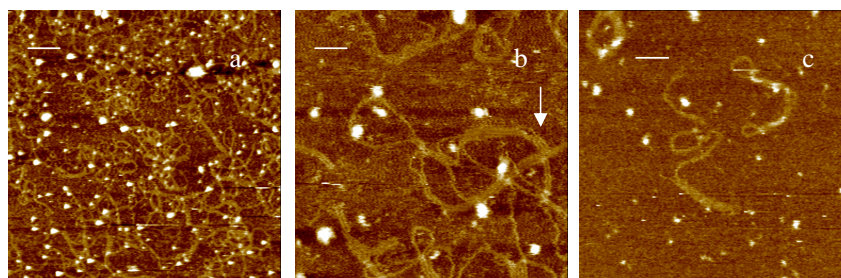


Figure. 5.8 (a-c) Top view AFM images of different ds DNA topologies on G4 treated mica taken in tapping mode AFM under ambient condition after washing. The DNA was then imaged immediately in the 10% PBS. This method leaves very little G4 on the surface of mica ready to interact with DNA plasmid. Flowers, plectonemic morphologies were observed. The arrow in (b) shows parallel-arranged DNA strands. Scale bars = 100, 30 and 60 nm respectively, z scales = 15, 15 and 6 nm respectively.

5.2.3 Ionic Strength Dependence.

Figure 5.9 (a-c) shows images of DNA-G6 complexes at 1:1, 5:1 and 7.5:1 ratios respectively prepared and imaged in 1mM (10%) PBS containing 14.7 mM NaCl (pH 7.4). For the convenience of comparison, we show the degree of changes in the tertiary morphological structures of the DNA-G6 complexes relative to those obtained in deionized water in Figure 5.4 (a-c). Plectonemic, loops, flowers morphologies and aggregates of loosely formed complexes were seen. The compact spheroids seen before at these ratios in Figure 5.4 were not seen here. The same holds true in Figure 5.9 (d-f) when we imaged these

complexes at the same ratios, in 10 mM (100%) PBS containing 147 mM NaCl (pH 7.4). Here, complexes appeared as open loops. These loops are more opened than those imaged in 10% PBS. Again no spheroids were seen even at high ratios. These observations, most likely, indicate that as ionic strength increases, the binding between DNA and dendrimer decreases, which is in agreement with electrostatic contributions to the binding. When monovalent salt is added at sufficiently high concentrations, it can reverse condensation to a certain extent, leading to isolated chains and open structural complexes.

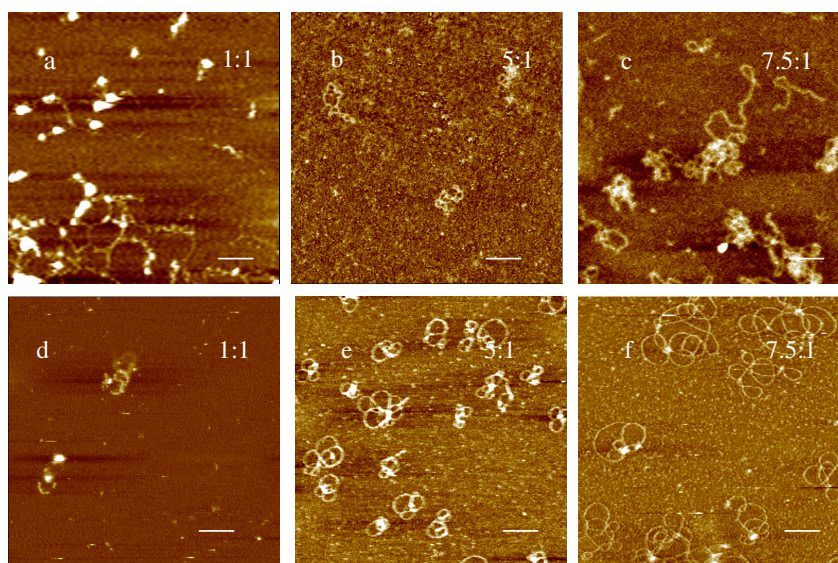


Figure 5.9 (a-f). Representative AFM Images of G6:DNA complexes arranged in order of increasing dendrimers-DNA ratios from 1:1 to 7.5:1. Ratios are stated on the images. Images from a-c were imaged in 10% PBS while images d-f were imaged in 100% PBS. Comparing these images with that in Figure 5.4, obtained in water indicate that the binding between DNA and dendrimer is poor even at ratios of 7.5:1. Scale bars = 250, 270, 120, 100, 100 and 100 nm respectively, z scales = 5, 8, 10, 7, 12 and 15 nm respectively.

These results are in general agreement with results obtained by Conwell *et al.*, (Conwell *et al.*, 2003) who studied the DNA complexes with hexamine cobalt (III) and found that the obtained condensates is a salt-dependant phenomenon and with results obtained by Burak *et al.*, (Burak *et al.*, 2003) who found that the number of condensed spermine ions at the onset of aggregation of DNA decreases with the addition of monovalent salt.

5.2.4 pH Dependence.

The ability of PAMAM dendrimers to act as a proton sponge has been widely suggested. During intracellular trafficking, their buffering capacity will not only tend to inhibit the action of the lysosomal nucleases, which operate optimally in acidic conditions, but will also alter the osmolarity of the vesicle. In the presence of PAMAM, there will be a net increase in the ionic concentration within the endosome, resulting in a swelling of the polymer by internal charge repulsion and osmotic swelling of the endosome, due to water entry. Hence, resulting in accelerating the release of the genetic material from the endosome and hence reducing their exposure to the endosomal enzymes. Here we study the effect of the acidic (5.5), physiological (7.4) and basic (11.3) pH(s), of the imaging media, on the stability of G4, G6 and G8 PAMAM-DNA complexes being formed in water. An assessment then will make on the structural integrity of such complexes at the molecular level.

Complexes were formed at 5:1 ratio in deionized water, equilibrated for some seconds before imaging in 10% PBS, pH 5.5, Figure 5.10 (a-c) or in 10% PBS, pH 7.4, Figure (d-f). At these pHs, the morphology of the observed condensates is markedly consistent with spheroidal DNA condensates

previously reported (Rackstraw *et al.*, 2001). The measured diameters and heights of these features were 85 ± 15 and 10.6 ± 5.7 nm, respectively. Both in pH 5.5 and pH 7.4, a greater portion of the dendrimer surface groups is expected to be protonated, since the pK_a of dendrimers is ca 9.5. This effect was confirmed by the spheroidal morphology obtained with these dendrimers. Manipulation of the pH of the imaging medium to 11.3 caused some of these complexes, Figure 5.10 (g and h) to rapidly disassemble, due to the neutralization of the charges on the G4 and G6 dendrimers respectively, and for free DNA molecules to be observed within 1-3 min. This confirms that the spheroids are made up of condensed plasmid molecules. However, this scenario was not true with DNA-G8 complexes, Figure 5.10 (i), where the complex retained its spheroidal morphology for more than 5 minutes, most probably due to the strong interaction with G8 relative to the G4 and G6 respectively. PAMAM dendrimers-DNA condensates appear to be stable when exposed to environmental conditions across the central part of the pH spectrum, as demonstrated by the similarity of structures elucidated at pH 5.5 and 7.4.

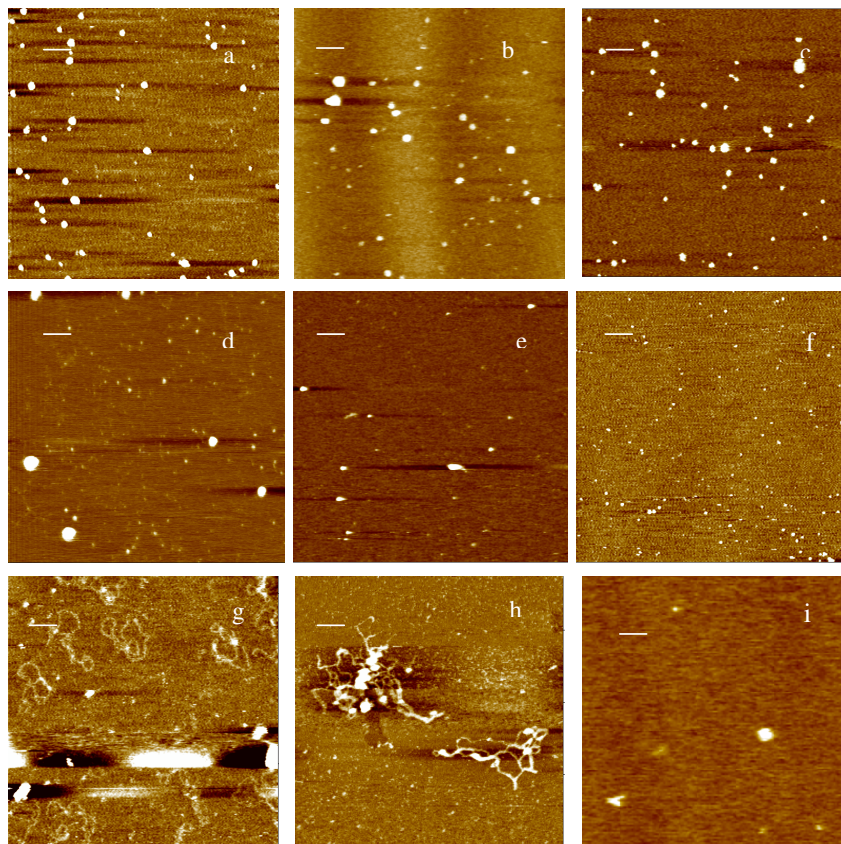


Figure 5.10. Representative AFM Images of DNA: PAMAM dendrimer complexes arranged in order of increasing dendrimers generation at 5:1ratios. Images (a-c) represent the image of complexes in pH 5.5, (d-f) represent images in pH 7.4 and images (g-i) in pH 11.3. Images a, d and g represent G4, b, e and h represent G6 and c, f and i represent G8 complexes. Scale bars = 100, 160, 200, 500, 300, 300, 100, 100 and 150 nm respectively, z scales = 7, 35, 30, 50, 8, 7, 7, 30 and 12 nm respectively.

5.2.5 Imaging of DNA on G4-treated Mica in Air.

Figure 5.11 depicts a representative image of naked DNA plasmids being adsorbed onto G4 treated mica (section 2.2.4.5). A number of plectonemic condensates were observed, where G4 molecules were found to decorate the DNA molecules. The partially condensed plectonemic ‘tangles’ of DNA observed were of similar morphology to those presented by Allen *et al* (Allen *et al.*, 1997a). The reason of forming these partially condensates in air is again due to the reentrance of G4 molecules into the DNA solution and subsequently their interaction with the DNA leading to partially neutralization, decoration, and partially condensation of DNA molecules before drying. The average thickness and height of these forms in the undecorated areas was 16 ± 4 and 0.6 ± 0.2 nm respectively, the variation of height obtained relative to the theoretical height of DNA was attributed to the dehydration of DNA molecules in air and to the surrounding molecules of polymers where the DNA molecules were embedded and perhaps due to the tip convolution. The average thickness and height in the decorated areas were 23 ± 4 and 2.5 ± 0.8 respectively.

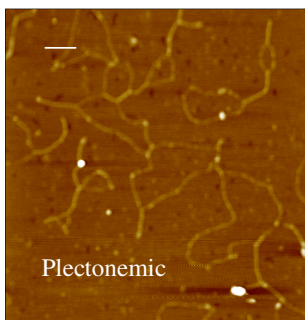


Figure 5.11. Top view AFM image of DNA plasmid on G4 treated mica taken in tapping mode AFM under ambient condition in air. G4-decorated plectonemic morphologies are observed. Scale bar = 120 nm, z scale = 10 nm.

5.2.6 Imaging of DNA-Dendrimers Condensates in Air.

AFM topographical images of polyplexes formed between DNA and each of G4, G6 and G8 respectively at 1:1 charge ratio are depicted in Figure 5.12 (a-c); details were presented in section 2.2.4.5.2 Globular structures of varying uniformity are observed. These have a mean cross-sectional diameter of 90.5 ± 34.4 nm. Some times these complexes aggregated to form big complexes as with G6 dendrimers in Figure 5.12 (b). Samples dried with compressed Nitrogen may have artifactual effects on condensation and aggregation, which will disrupt weakly, condensed and aggregated molecules and only strong condensates and aggregates will be observed after drying. We decided to work in liquid in most of our work to be as near the natural environmental conditions for the DNA molecules as possible, to eliminate the artifactual effects due to drying methods and to visualize the effect between the different generations of PAMAMs used here and the DNA in real time.

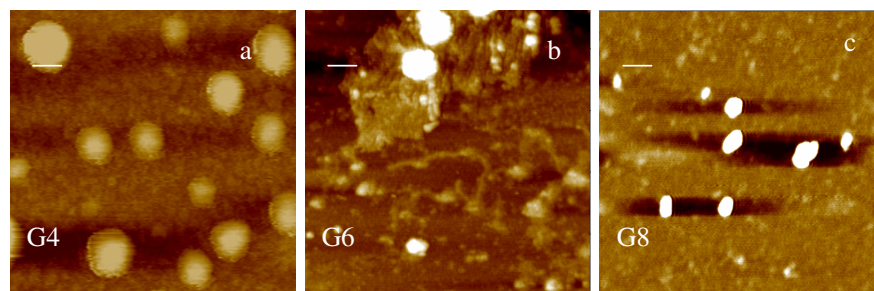


Figure 5.12 (a-c). Representative AFM Images of DNA: PAMAM dendrimer complexes arranged in order of increasing dendrimers generation at 1:1ratios, (a) G4, (b) G6 and (c) G8. All condensates have been formed in water, dried under nitrogen and imaging has been conducted in air. Scale bars = 45, 100 and 80 nm respectively, z scales = 10, 35 and 5 nm respectively.

5.2.7 Possible Condensation Mechanisms and Pathways of PAMAM-DNA Polyplexes onto Mica Surface.

In biological systems, there are many surfaces with which DNA can and does interact. One might even view the nucleosome as a surface onto which DNA “condenses”. However, thermodynamic and spectroscopic experiments have defined a major transition in the DNA condensation pathway as an abrupt collapse that occurs when a condensing agent neutralizes approximately 85-90% of the backbone charges. (Bloomfield, 1991, Bloomfield, 1996, Matulis *et al.*, 2000). The counter-ions not only screen coulombic repulsions between the DNA phosphates, they also produce attraction through correlated fluctuations of the ion atmosphere. This idea was first put forward by Oosawa in 1970 (Oosawa, 1971), and was recently applied to DNA. A more detailed model based on the Poisson-Boltzmann theory predicts that aggregates will re-dissolve as salt is added due to the screening of short-range electrostatic attractions. In the following we will explore the probable mechanism of condensation towards toroidal or flower structures.

5.2.7.1 Towards Toroidal Formation

The morphology of condensed DNA particles is most commonly that of a compact, orderly toroid for which there are two models of formation, the first being the spool-like model originally proposed by Ubbink and Odijk (Ubbink and Odijk, 1995). This model relies on the hypothesis that toroids are formed from a curved rod consisting of hexagonally packed DNA molecules. This curved rod closes on itself in order to avoid discontinuity of its ends. The

spool-like model is flawed however, in that if the strands are hexagonally packed there will be a considerable gradient in the curvature contribution to the energy of the strands, dependant on their radial position from the centre of the toroid. This mechanism has hence been revised by Hud *et al* (Hud *et al.*, 1995), who have proposed the constant radius of curvature model. In this model, the DNA is coiled with a constant radius of curvature into a series of equally sized contiguous loops that are approximately coplanar but non-concentric. Each loop of DNA is in close contact along its entirety with the loops immediately pre and succeeding it. The centres of each loop lie on a helical path around the central axis of the toroid giving the entire toroid the structure of a helix of extremely low pitch. X-ray scattering data shows that the surface-to-surface spacing between DNA helices is only about 1-2 water molecules in diameter, so that the packaging density of DNA condensed *in vitro* is entirely comparable to that of interphage DNA (Bloomfield, 1997). Schematic representations of the spool-like and constant radius of curvature models are provided in Figure 5.13 (a). Interestingly, one of our high resolution AFM images of surface-directed DNA condensation have been acquired in water and show parallel arrays of DNA strands held together at intervals in a dense disk, Figure 5.13 (b). This morphology forms at a high G4 dendrimer ratio (6:1). We believe that this morphology is an intermediate following the constant radius of curvature model represented in Figure 5.13 (a (II) towards toroidal formation. The large end loop seen in this figure may have been formed after the ring-like structure had collapsed. The formation of these structures is evidence for stabilization between DNA molecules along their lengths, which should extend in all dimensions. However, the morphology seen

is highly planar. Such a planar morphology may result from the collapse of the three-dimensional arrangements onto the surface or from the attractive interactions between the DNA and the substrate. All the arguments presented above suggest that the structures observed might be influenced by the substrate but are predominantly the result of DNA-DNA interactions and not DNA-substrate interactions.

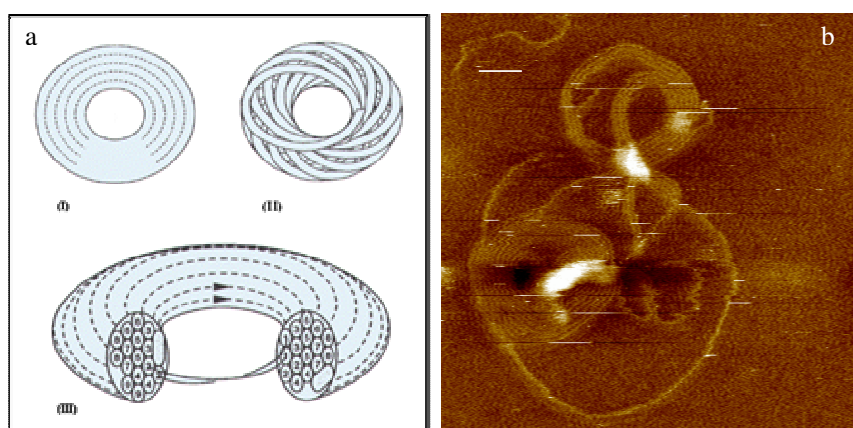


Figure 5.13. Represents top views of (a) the spool-like model (I) and constant radius of curvature models (II) of torus formation. A lateral cross-section of the spool-like model is presented in (III). The ends of the cross-sections of the DNA strands are numbered, indicating their complement on each side of the cross-section. This figure is adapted from that presented in Böttcher *et al.*, (Böttcher *et al* 1998). In (b), the hexagonal packing of the DNA strands was held together at intervals in dense disk, this morphology was formed at 6:1 ratio between the G4 and the DNA. Scale bar = 35 nm, z scale = 6 nm.

In a proposed binding model for DNA-dendrimer complexes by Chen *et al* (Chen *et al.*, 2000), the DNA wraps around larger dendrimers while the

wrapping of DNA does not occur for smaller dendrimers. Furthermore, the surface groups of small dendrimers are more mobile than those of large dendrimers, due to the open structure of the smaller generation (larger entropy). Hence, instead of DNA wrapping on G4 dendrimers, the G4 dendrimers will bind to the DNA molecule, decorating it, leading to inter and intra DNA ds interactions. We have seen such behaviour here with G4 dendrimers at different charge ratios, Figure 5.1, where these molecules were found to decorate the DNA molecules at low charge ratios and form temporarily intermediates at high charge ratios. We further confirmed these suggestions by near in situ (four dimensions) imaging of the G4 (small dendrimers) and G6 (large dendrimers) and DNA molecules as to investigate the possible pathways of toroids formation.

5.2.7.2 Towards Flowers Formation

Regarding the flowers condensates being observed with G4 dendrimers, we confirm the suggestion made by Montigny that the flower-like condensates are made due to the binding of cations with the DNA molecules leading to the DNA looping and subsequent loop condensation (Montigny *et al.*, 2001). Figure 5.14 depicts a schematic representation and four AFM images suggesting a possible mechanism of formation of these ‘flower-like’ condensates. Considering this hypothesis, it is clear that the single twisted decorated plasmid, marked in the figure, is an intermediate in the formation of these flower-like structures.

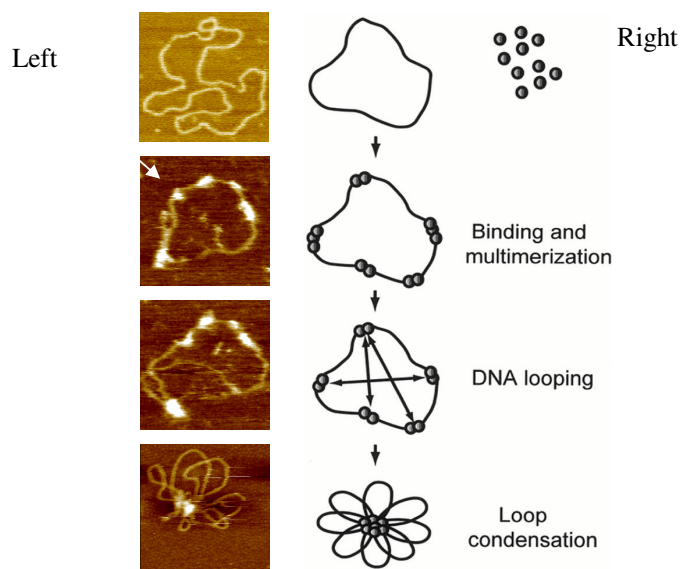


Figure 5.14. Right, a schematic representation depicts a possible mechanism of formation of DNA condensates of a flower-like morphology from plasmid DNA and small molecular cations, for example spermine or spermidine. This schematic has been adapted from a similar representation in Montigny et al (Montigny et al., 2001). Left, four AFM images taken from three different experiments with G4 PAMAM dendrimers, they show steps similar to those suggested in the scheme.

5.2.8 Four Dimensions Investigations of the DNA Condensation and Condensates Disassembly in Liquid.

Dynamic real time assembly and disassembly of flower and toroidal DNA condensates have been visualized using atomic force microscopy. Imaging was conducted in an aqueous environment allowing the visualization of hydrated, PAMAM dendrimer-DNA polyplexes undergoing dynamic structural movement and conformational change without the presence of drying artefacts. An increased understanding of the process of DNA condensation and

condensate disassembly will we believe aid the development and optimisation of gene delivery vectors. Experimentally Golan *et al* (Golan *et al.*, 1999) have utilised AFM in an attempt to image condensates at various stages of formation, concluding that linear structures are intermediates in the formation of toroids, and these toroidal structures ultimately collapse into short rigid rods. A similar investigation conducted by Fang *et al* (Fang and Hoh, 1999) concluded that plasmids follow one of two pathways when they condense either to form rods or toroids and that these structures are discrete end-points of each other. Such studies however do have the flaw that they produce snapshots of a sequential process and not the full inter-relationship of structural transition. A limited number of studies including our own, Abdelhady *et al* (Abdelhady *et al.*, 2003), have exploited AFM to visualize dynamical molecular processes involving DNA, Martin *et al* (Martin *et al.*, 2000), Pope *et al* (Pope *et al.*, 1999) and Ono *et al* (Ono and Spain, 1999). In our studies, firstly, regarding the condensation processes, Figure 5.15 displays images recorded for the 1:1 G4: DNA ratio, in which DNA and G4 molecules are allowed to equilibrate in solution for 15 min. The data displayed are noteworthy since the observed complex was treated with DNase I enzyme so as to study the effect of DNase I on G4:DNA complexes. We will concentrate on the structural changes of the complex before the clear enzymatic interaction that takes place at 71-94 min. Then we will discuss in details the effect of DNase I on this complex in the next chapter. Initially a multi-looped molecule was obtained with a contour length of 1074 nm, a measured height of 0.85 ± 0.2 nm and a maximum height at the marked white spot of 3.7 nm. The measured thickness of the remainder of the complex was 18 ± 1.2 nm. Over the

next 36.5 minutes the DNA becomes increasingly condensed, demonstrated by a reduction in diameter and an increased thickness and height of the condensed complex to 27.6 ± 2.3 and 1.8 ± 0.34 nm respectively. We confer the presence of looped molecule to the binding of G4 with the DNA molecule leading to the DNA looping and subsequent loop condensation by pulling the DNA double strands from one loop to the other in such away as to arrange the DNA double strands parallel to each other in a highly compacted ring (toroid).

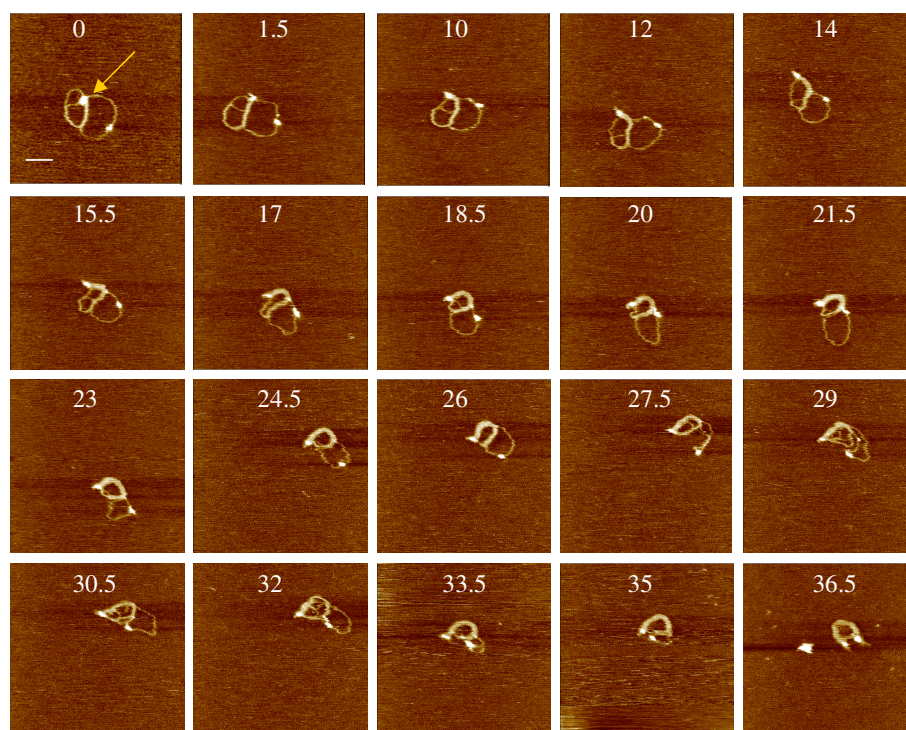


Figure 5.15. AFM image sequences for the 1:1 G4 to DNA ratio, in which DNA and dendrimer molecules were allowed to equilibrate in solution for 15 min. Images, show in near in situ, the formation of toroidal complex. Numbers on the images represent time lapsed in minutes. The arrow at $t = 0$ min shows the point of maximum height of the molecule. Scale bar = 100 nm, z scale = 3 nm.

Figure 5.16 depicts another sequence of AFM images in deionized water being formed at 1:1 ratio and allowed to equilibrate for 2 hrs before imaging. Plectonemic and double looped condensates were obtained. From this sequence, the hypothesis can be developed that when plasmids first encounter the G4 cationic polymer they begin an inward collapse and appeared as an interwound plectonemic and multi looped condensates. The initial step in the condensation after that is the increased intrinsic bending of these molecules to form ring-like condensate. This is also supported by the recent theoretical work of Rouzina and Bloomfield (Rouzina and Bloomfield, 1998) showing that small multivalent cations can induce local bends in DNA. The next identifiable step in the process is the initial intramolecular loop formation appeared as 3-looped molecule after 34 min(s) of imaging. We thought that, if this molecule aggregates with other molecular condensates, then multimeric condensates would appear, which require intermolecular contacts. One of those intermolecular contacts is the crossover points and interactions that involve the ends of DNA molecules. In the case when there are no or few free ends there must be intra or intermolecular contacts involving the ends. There are several possibilities for such a contact, including partial overlaps between molecules, end-to-end interactions, or termination of free ends at the crossover point. Figure 5.17 shows a third sequence of images where the G4 dendrimers were first adsorbed onto mica for some seconds, the aliquot was then removed carefully with tissue without washing, then the DNA was introduced and imaged in 10% PBS. Within the figure, the plectonemic structure on the left was observed to coil round and fuse to form a continuous ring-like structure, thus minimizing discontinuity of their ends, the basis of the spool-like model

towards toroid. The right structure resembles that in Figure 5.13 that appear as multimeric flower and disk-like structures.

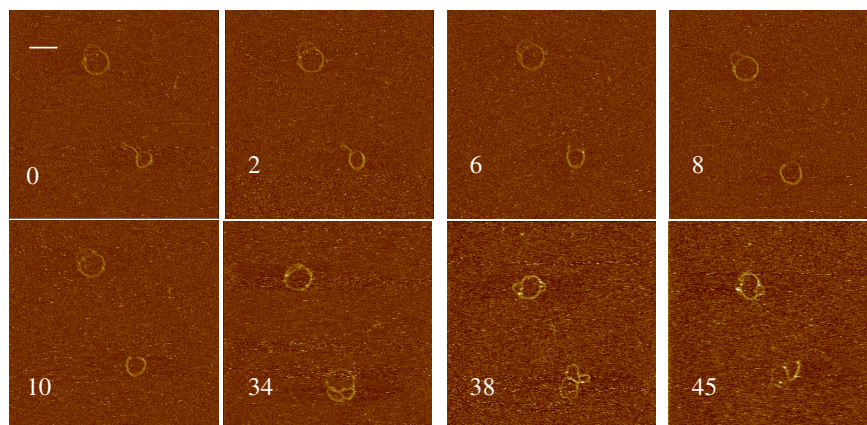


Figure 5.16. AFM image sequences for the 1:1 G4 to DNA ratio, in which DNA and dendrimer molecules were allowed to equilibrate in solution for 2 hr. Images, show in near in situ, the formation of ring-like complex. We consider this as an intermediate towards toroidal formation. Numbers on the images represent time lapsed in minutes. Scale bar = 100 nm, z scale = 5 nm.

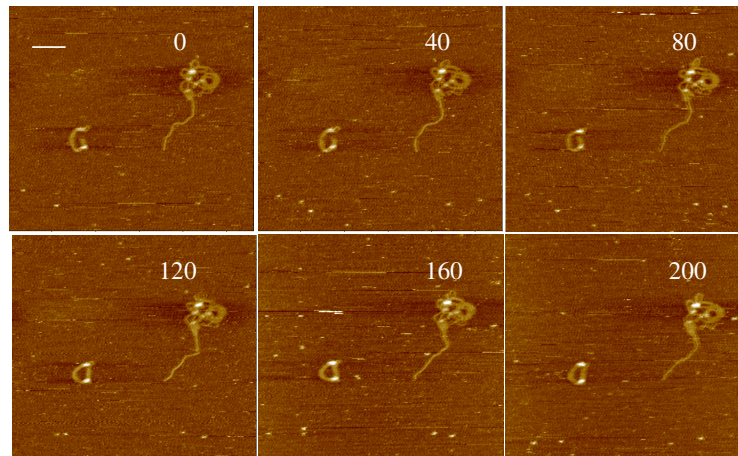


Figure 5.17. Top view AFM image sequences for ds DNA topologies on G4 treated mica taken in tapping mode AFM under ambient condition without washing. The DNA was imaged immediately in the 10% PBS. This method leaves some free G4 on the surface of mica ready to interact with DNA plasmid. This method shows, in near in situ conditions, the bending of the plectonemic structure, the molecule in the left, to make an intermediate towards the toroidal morphology. Numbers on the images represent time lapsed in seconds. Scale bar = 140 nm, z scale = 25 nm.

A fourth sequence of images showing the formation of toroidal structures when the DNA is first treated with larger dendrimers (G6) in 100% PBS at 1:1 ratio and imaged in the same buffer instantaneously is shown in Figure 5.18. It is clear from this sequence of images that these structures adopt the mechanism of wrapping of the DNA molecules around G6 molecules to form a toroidal morphology after 21 minutes. The mean external diameter of these toroids was 42 ± 1 nm, the thickness was 12 ± 2 nm and the height was 2.5 ± 0.5 nm. This results in an internal diameter of 13.5 ± 1 nm that is similar to that obtained by the use of spermine and spermidine, leading to the production of toroidal DNA

with inner radii of 140 Å (He *et al.*, 2000). These data also agree with data presented by Chen *et al* (Chen *et al.*, 2000) who found that the DNA could wrap around larger dendrimer molecules, G7 in his study, for about 1.4 turns, which is analogous to the DNA-histones complex, while it cannot wrap around the smaller G4 molecules. He also found that one dendrimer molecule can bind to two or more independent DNA pieces.

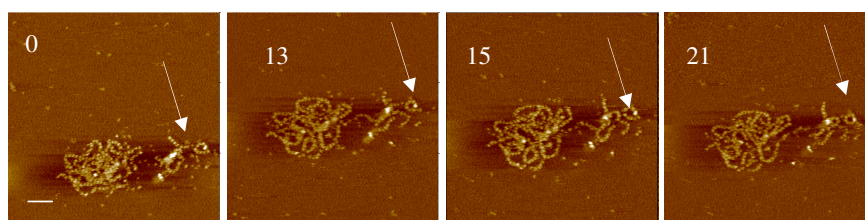


Figure 5.18. AFM image sequences for the 1:1 G6 to DNA ratio, in which DNA and dendrimer molecules were allowed to equilibrate in 100% PBS solution for few seconds. Images show the DNA molecules wrapping around the G6 molecules in near in situ conditions towards toroidal morphology. Numbers on the images represent time lapsed in minutes. Arrows on the images showing the formation of the toroidal structure. Scale bar = 60 nm, z scale = 9 nm.

Secondly, regarding the disassembly of the DNA condensates, toroids and flowers, Figure 5.19 represents three different sequences of images being taken in 10% PBS. These sequences were formed at 7.5:1 and 10:1 G4-DNA ratios and incubated for 4.5 hours before imaging as in Figure 5.19 (I) and (II) respectively and at 10:1 ratio and incubated for one hour before imaging, Figure 5.19 (III).

Chapter five: Surface Visualization of PAMAM Dendrimers-induced DNA Condensation

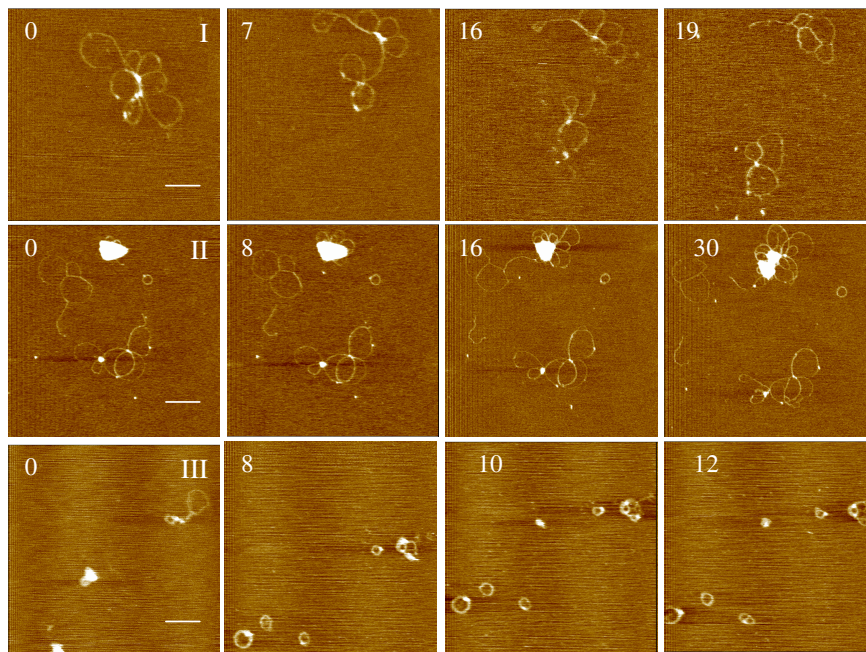


Figure 5.19. AFM image sequences for (I) 7.5:1 G4: DNA ratio, in which DNA and dendrimer molecules were allowed to equilibrate in 10% PBS solution for 4 hrs, (II) 10:1 ratio incubated for 4.5 hrs and (III) 10:1 ratio incubated for 1 hr. It's obvious that these images represent a reverse mechanism to the DNA condensation in real time. Numbers on the images represent time lapsed in minutes. Scale bars for each sequence = 200, 350 and 250 nm respectively, z scales = 7, 9 and 10 nm respectively.

In figure 5.19 (I) the flower-like structure can be seen to open after 7 minutes with the molecule then identified into two discrete parts; each of them was moving away from the other after a further time period of 16 min. After 19 min, these molecules rearrange, each displaying different multi-looped morphologies. In figure 5.19 (II) multi-looped, toroidal DNA and a large aggregate were seen. We will concentrate on the toroidal structure and the aggregate presented in this image. Interestingly, the aggregate seems as

condensed flowers, started to open after 8 min reaching a maximum relaxation after 30 min where ‘petals’ appeared to originate from multi-focal points within this flower. In addition to the flower structure seen in this image, a toroidal structure was observed, its external diameter being 185 nm and its height 2.6 nm. This diameter increased to reach 192 nm after 8 min and its height decreased to 1.8 nm. After 30 min this toroidal structure further relaxed and reached its maximum diameter of 247 nm and minimum height of 1.1 nm. A behaviour like this was also observed in Figure 5.19(III) where a multi toroidal aggregate were seen to disassemble after 8 min and a three distinct toroids were observed at the lower left end of the image. The external diameters of these toroids from the left to right were 127, 103 and 190 nm respectively. Their heights were 2, 2.6 and 1.8 nm respectively. These toroids were found to relax with time to reach a diameter of 196, 157 and 240 nm respectively after 10 min; their heights were 1.9, 2 and 1.1 nm respectively. The formation of these aggregates that are composed of loosely associated molecules suggests that there is long-range attractive interaction between DNA molecules at these ratios. Rau and Parsegian have proposed that hydration forces underlie long-range attractive interactions between parallel DNA strands in the presence of condensing agents (Rau and Parsegian, 1992). It is clear from these images that the mechanism adopted here is opposite to that adopted in the condensation processes to make either multi-lobed flowers or toroids. These images together with those obtained in real time to elucidate the mechanisms of condensation are supportive to each other in clarifying the pathways of condensations and disassembly. Furthermore images observed in Figure 5.19 (II) and (III) agree with those observed in Figure 5.9 in that the

presence of monovalent cation aids in reversing the condensation process. Moreover, data obtained in Figure 5.19 (II) and (III) represents the effect of incubation time with the 10% PBS. It's clear that as the incubation time with 10 % PBS increases the degree of complexation decreases resulting in the formation of intermediates rather than toroids and/or rods.

5.2.9 Analysis of Condensate Volumes

AFM captures topographical information in three-dimensions. Analysis of such three-dimensional information has the potential, allowing for certain considerations, to allow the assessment of the structural volume and hence to provide information regarding the number of plasmid molecules in each condensate. Figure 5.20 shows different morphological structures of PAMAM dendrimer-DNA condensates presented in three-dimensional orientations. Here, a novel assessment of condensate volume relative to structural morphology has been made. Our measurements are based on considering the DNA double strands as a long flexible cylindrical geometry. This cylinder can either loop around it self to make a flower like structure, further enterwind and compact to arrange the DNA double strands in parallel before condensation closes the structure to make rings or toroids. Other scenarios to consider are cylinders bending around themselves to make parallel cylinders (rods) or forms intermediate structures between these morphologies. All of these morphologies include cross sections of the DNA double strands. These cross sections most likely maintain a constant radius for the condensed DNA during and within the formation of toroids and we propose that this constant radius mechanism is

applicable to rod formation as well when the toroid opens onto rod or vice versa. In case of ring or toroidal morphologies, the estimation of the volume is then simply achieved using equation 5.1(a) that was extracted from the schematic representation in Figure 5.20 (j). For flowers, the volume was estimated by integrating the volume of the petals (cylinders) of these flowers and the volumes of the cross sections, equation 5.1(b). If the cross sections appeared as a spheroidal morphology, then their volume was considered as the volume of the sphere, equation 5.1(d). If the geometry of the cross sectional part is not spherical in shape, then the volume will depend on the new geometry. All measurements of these condensates were taken at half maximum height of the condensate in order to minimise tip convolution effects (Allen *et al.*, 1997a). The relative percentage occurrence of the globular, ring-like, linear and flower condensates are described in Table 5.2 and Figure 5.21.

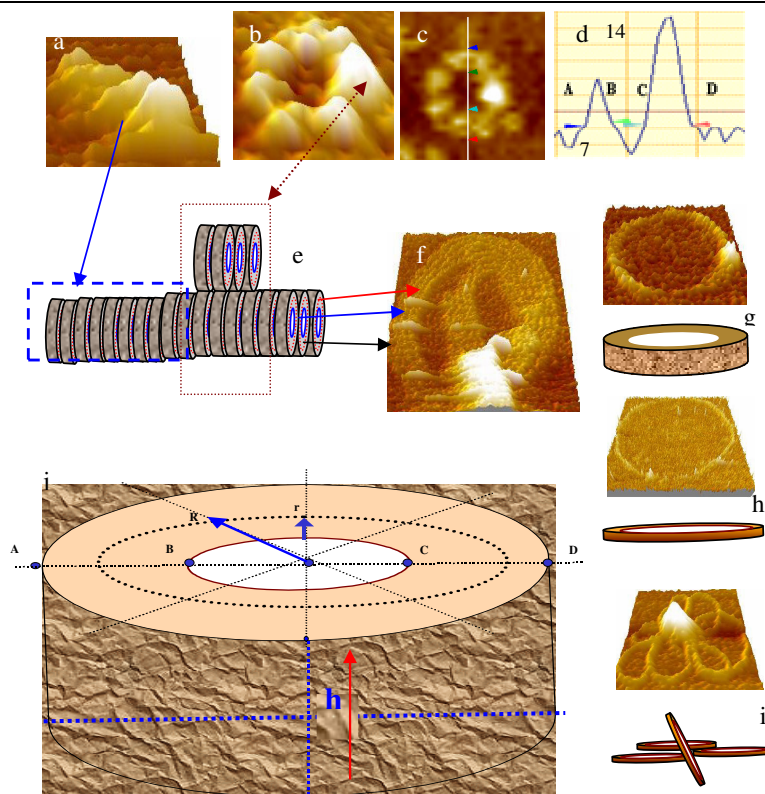


Figure 5.20. 3D representations of (a) rod, (b) toroid, (c) 2D image of the same toroid where cross-sectional measurements were taken at the positions displayed by arrows and is shown annotated with the readings taken from it in (d). Schematic representation of the possible arrangements of the DNA ds(s) were shown in (e), arrows refer to these arrangements in (a, b and f respectively), in (f), the DNA ds(s) were found to follow the constant radius mechanism of toroidal formation, the mean thickness of DNA ds was 2.4 nm and the separation distance between two DNA ds(s) was ca 2-4 nm. 3D representations of ring, open relaxed ring, flower morphologies and their schematic representations were shown in (g-i) respectively. Schematic representations of a toroid where cross-sectional measurements are taken at the positions displayed in (j) and are used to calculate toroidal and ring volumes with equation 5.1 (a).

Equation 5.1

(a): Volume of toroid or ring = $2\pi^2(r+h/2)^2R/4$ or $\pi(r+h/2)^2L$.

(b): Volume of flower = $\Sigma(\pi(r+h/2)^2L)$ for each petal + Σ Volumes of the cross points.

(c): Volume of rode = $\pi(r+h/2)^2L$

(d): Volume of spheroid = $4/3 \pi(D/2)^3$

Where: $r = ((A-D)-(B-C))/4$ for rings and toroids in Figure 5.20(j).

$R = ((B-C)/2)+r$ for rings and toroids in Figure 5.20(j).

L= contour length

D = diameter of the rod or spheroid

Generation	n	Globular %	Rings %	Linear %	Flowers %
G4	186	15.6	19.3	4.3	60.7
G6	84	66.6	7.1	3.6	22.6
G8	70	100	0	0	0

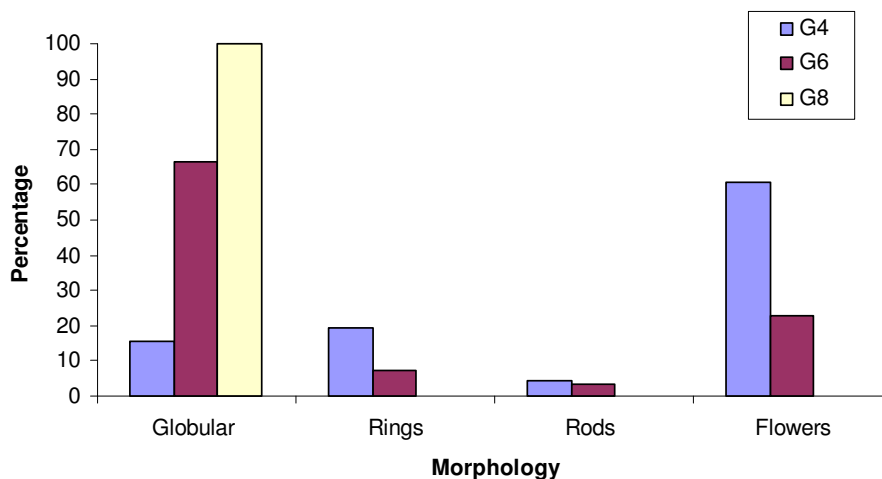


Table 5.1 and Figure 5.21 show the percentage of each condensate morphology relative to the dendrimers generation and irrelative to the loading ratio.

Chapter five: Surface Visualization of PAMAM Dendrimers-induced DNA Condensation

The estimated volumes of the aforementioned condensates are shown in table 5.3 and Figure 5.22 respectively. We did not attempt to estimate the volume of aggregated condensates.

Parameter	G4				G6		G8	Naked DNA
	Globular	Toroids	Linear	Flowers	Globular	Toroids	Globular	
n	15	7	5	9	15	5	15	11
r (nm)	30	12	11	5	45	9	41	5.5
h/2(nm)	10	1	1.2	1.5	5	0.9	6	0.7
(r+h/2)/2	20	6.5	6.1	3.25	25	4.95	23.5	3.1
Contour length (nm)		350	300	1641		150		1150
Volume (nm ³)	33493	46433	35052	54426	65417	11541	54334	34702
No of DNA molecules relative to the estimated volume of naked DNA	1.0	1.3	1.0	1.6	1.9	0.3	1.6	1.0
No of DNA molecules relative to the theoretical volume of naked DNA	7.2	10.0	7.5	11.7	14.0	2.5	11.7	7.4

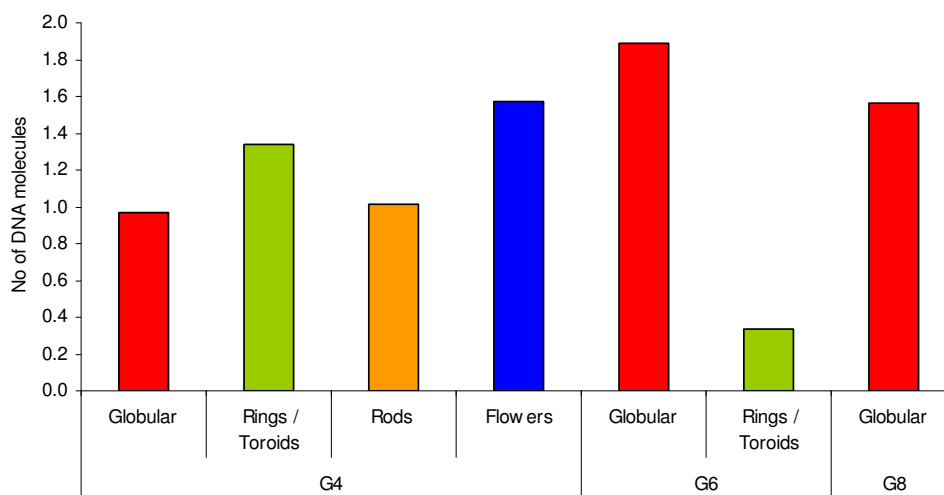


Table 5.2 and Figure 5.22 show volume of PAMAM dendrimer-DNA complexes with different dendrimer generations and a histogram depicting the volume distribution of the obtained morphologies relative to the dendrimers generation.

Analysis of the morphology and volume for all systems revealed similar magnitudes of condensate volume. G4-DNA condensates appear to contain one plasmid in most cases, relative to the estimated DNA volume, except with the flowers morphology that reveal an average of 1.6 plasmids per condensate. In case of condensates obtained with G6, the toroidal structure revealed an average volume of 0.3 plasmid relative to the estimated volume of DNA (based upon the AFM data) while it results in 2.5 plasmids relative to the theoretical volume of the plasmid DNA. Interestingly toroids obtained with G6 however produce toroids of the more classical geometry, rather than the loose structures observed with G4 system. Typical, classical toroids have reported outer radial geometries of approximately 40 nm for DNA lengths ranging from 0.4 to 48 Kbp (Marx and Ruben, 1986, Bloomfield, 1991). The values we report for the G4 system are approximately two times higher than those for classical toroids. However the globular structures observed with G6 results in a volume of 1.9 plasmids per condensate. For G8 dendrimers only globular condensates were observed. Interestingly, as the generation of the used dendrimers increases, the degree of compactness of the obtained condensates also increases, a behaviour that was clear in the obtained morphology, i.e. with G4 dendrimers, rings, rods, flowers and globular morphologies were seen while classical toroids and globules were the only structures observed with G6 and only globular structures were observed with G8 dendrimers. The discrepancy in the measured volumes is most likely due to the tip convolution and sample compression effects.

5.2.10 Effect of Loading Ratio and Generation Type on the Complex Retardation in Gel Electrophoresis

Agarose gel electrophoresis is a convenient method for monitoring the reaction between PAMAM dendrimers and DNA mixtures, and is capable of revealing much detail of the interaction. Figure 5.23 shows the pattern on the gel for G4, G6 and G8, complexed with plasmid DNA at various ratios. Although gel migration is affected by size and charge, our data suggest that charge is the primary determinant of the migration patterns in this case. Thus, by varying the dendrimers: DNA ratio a variety of cationic, neutral, or anionic complexes can be created.

Lane 1 shows the pattern of naked DNA plasmid in the absence of polymer, the DNA is separated as 2 bands. These are likely to represent different “conformations” of plasmid; the upper band represents super coiled DNA while the middle band represents the linear and open circular forms of DNA fused together in one band. We believe that if extra running time were allowed, this band will separate into two as latter confirmed in chapter 6. The lower band represents the DNA that trapped in the well. At 0.5:1 ratio, lanes 9 and 13 with G6 and G8 respectively, an excess of un-complexed DNA was present and again two bands toward the anode were seen. The upper band represent supercoiled and condensed DNA while the middle band represents linear and open circular DNA fused together. At this ratio, the complexed plasmid still has a negative net charge, as shown by its migration to the anodic edge of the loading well, the same holds true with 0.5:1 ratio with G4 (data not shown here).

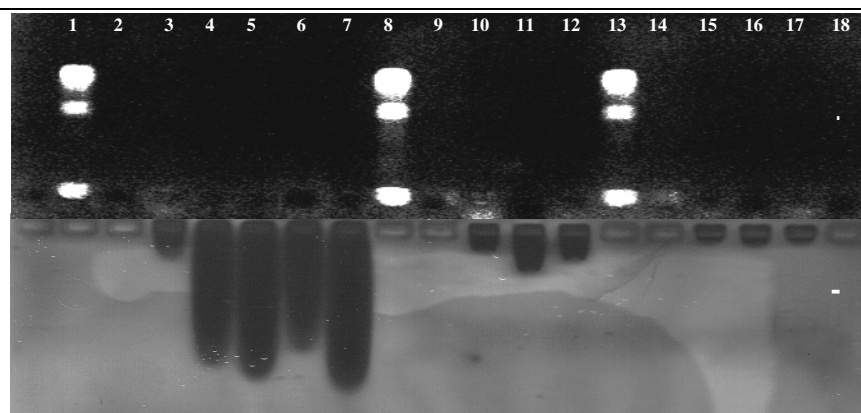


Figure.5.23. Gel electrophoretic retardation pattern for PAMAM-plasmid complexes. Upper images show fluorescently labelled plasmid migration. The lower images show the same gels following staining for polymers. The anodic and cathodic ends are marked with + and -, respectively, and the loading wells were marked with numbers. Lane 1 contains free plasmid as control. Complex ratio details for the remaining wells are as follows: lanes 3-7 contain 1, 3, 5, 7 and 10:1 G4:DNA respectively; lanes 8-12 contain 0.5,1, 3, 5 and 7:1 G6:DNA respectively and lanes 13-18 contain 0.5, 1, 3, 5 and 7:1 G8:DNA, respectively.

At 1:1 ratios or above, the gels indicate that most of the DNA is associated with the complex and DNA bands disappeared from this point onwards due to the loss of EBr fluorescence on complete complexation of DNA with polymer, demonstrating that PAMAMs were capable of binding with DNA at physiological pH. When the polymer-loading ratio increases the DNA might be expected to migrate to the cathodic side, implying a positive charge on the complex. However, this behaviour is not seen here, probably due to the loss of EBr fluorescence on complete complexation of DNA with polymer. Interestingly, inspection of the gel stained for the polymer suggests a trend of bands of free polymer running toward the cathode. This indicates that once

stoichiometric complexes are formed between dendrimers and DNA molecules there is no further association of the polymer with the complex. The rate of migration of the free polymer differs dramatically within generations, while they were quick in case of G4; they were slower in the case of G6 and very slow in case of G8. This might reflect the effect of generation size and charge on the formation of strong complex between them and the DNA. This finding was confirmed using gel electrophoresis for G4, G6 and G8 PAMAM-dendrimers in the absence of DNA, Figure 5.24. The amount of dendrimers used in each generation was the same as to make 5:1 PAMAM: DNA ratios. It was clear that as the dendrimers increased in generation (size), rates of moving towards the cathode decrease. Data obtained from gel electrophoresis supports that obtained from the AFM indicating that the reaction strength between the DNA and the PAMAM dendrimers increases with generation.

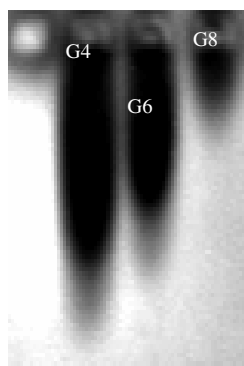


Fig. 5.24. Gel electrophoretic retardation pattern, towards the cathode, for G4, G6 and G8 PAMAM dendrimers respectively following staining. As the dendrimers increase in generation, rates of moving towards the cathode decreases.

5.3 CONCLUSIONS

Images reveal that dendrimer-induced DNA condensation involves multiple well-defined structural intermediates. The reasons for these intermediates may be due to the interruption in the folding process as a result of the immobilization of the condensates onto the mica surface, the lack of sufficient polymer cations as in case of low ratios and the presence of salt in the preparing solutions or imaging environment. The morphology of these complexes depends on the loading ratio of dendrimers, dendrimer's generation and the presence or absence of soluble dendrimers in the imaging field. As the concentration of dendrimers relative to DNA is increased, the nucleic acid takes on a more condensed morphology. Initially the DNA becomes increasingly twisted and supercoiled, a number of flower-like condensates, disks, rings, toroids and rods are observed. We observed that pre-treatment of mica with G4 and subsequent deposition of DNA will result in the formation of partially condensed DNA complexes. However it appears that whether DNA condensation is surface-mediated or in solution, if adequate cations are present rods, toroids and plectonemic condensates will result. Samples prepared and imaged in water gave better condensation than samples in saline, but samples in saline are more relevant for comparison with *in vivo* results. The binding between DNA and dendrimers became weaker at higher ionic strength and/or high pH, consistent with the importance of the electrostatic interactions in the DNA-dendrimer binding. It is evident that polyplexes formed from DNA and G4 possess an increased tendency toward aggregation than those formed from higher generations. However, the pathway observed in Figure 5.16,

plectonemic structure towards ring and finally towards multi-looped structure, together with that previously observed in Figure 5.15, towards the formation of toroids from multi looped condensates, suggested that one structure (plectonemic, ring or toroid) is an intermediate in the formation of the other, or in other words that they exist in a dynamic equilibrium. Such observation does not support the hypothesis that the plectonemic, ring-like morphologies and toroids are distinct end-points of condensation formed by contrasting folding pathways (Noguchi *et al.*, 1996). This is consistent with the hypothesis that these thicker rings of more robust appearance are formed from the concentric wrapping of an interwound condensate. From this sequence, the hypothesis can be developed that when plasmids first encounter the cationic polymer they collapse into interwound linear condensates. The number of interwound twists (loops) of these structures increases and ultimately they coil round and fuse to form a ring-like structure, thus minimizing discontinuity of their ends, the basis of the spool-like model, crossover stabilization is then formed between these structures leading to multimerization and strand-strand stabilization of these loops or rings. However, in common with all surface imaging, there is the question of how closely the composition and morphology of adsorbed structures represents that in the bulk solution. In this study, repeated imaging of the sample was possible over a number of hours. In addition, images taken in air as a result of the precipitation of all of the suspended condensates in solution did not reveal any significantly different morphology than that obtained in liquid. It would be expected that if other structures rather than those already observed were present then they would adhere to the substrate in a similar manner to the condensates observed.

CHAPTER SIX

DIRECT REAL-TIME MOLECULAR SCALE VISUALISATION OF THE DEGRADATION OF CONDENSED DNA COMPLEXES EXPOSED TO DNASE I

6.1 BACKGROUND

Despite much progress, there remain a number of well-known obstacles to the development of efficient gene delivery systems. To help overcome these challenges, it is clear that a deeper understanding of the detailed structure of proposed vector complexes and their response to environmental challenges would be of great benefit in the rational design of such systems. We demonstrate this philosophy here in a study of the effect of DNase I on the molecular structure of PAMAM dendrimer-DNA complexes. Such complexes form through electrostatic interactions between negatively charged phosphate groups of the DNA and protonated amino groups of the dendrimers (Kukowska-Latallo *et al.*, 1996, Bielinska *et al.*, 1997, Hill *et al.*, 2001). The complexes remain highly soluble, indicating that nuclease resistance may be achieved without forming insoluble complexes (Bielinska *et al.*, 1997). *In vitro* experiments have shown that such dendrimers can chaperone DNA through cell membranes and promote efficient gene transfection (Tang *et al.*, 1996). In parallel, atomic force microscopy has demonstrated potential in studying processes involving DNA (Bezanilla *et al.*, 1994, Hansma and Pietrasanta,

1998, Golan *et al.*, 1999, Umemura *et al.*, 2000). For example, work imaging static DNA condensates induced by polylysine (Hansma and Pietrasanta, 1998, Golan *et al.*, 1999) and spermidine (Fang and Hoh, 1998a) has been reported. Liu *et al.* have also visualized the end point structure of a chitosan-DNA complex after exposure to DNase I (Liu *et al.*, 2001b). In these studies resolution has been achieved by imaging fixed samples in air and therefore information on process dynamics is limited, and structural morphology may contain drying artifacts. A limited number of studies have exploited AFM to visualise dynamical molecular processes involving DNA (Bezanilla *et al.*, 1994, Ellis *et al.*, 1999b, Ono and Spain, 1999, Pope *et al.*, 1999, Berge *et al.*, 2000, Martin *et al.*, 2000). Here our studies, which build upon this work, show the effect of the DNase I enzyme on DNA following complexation with increasing ratios and incubation times of generation 4, 6 and 8 PAMAM dendrimers. DNase I is a pancreatic endonuclease, which catalyses the hydrolysis of double-stranded DNA (Pan *et al.*, 1998) and is a commonly employed biochemical probe in DNA footprinting studies. It recognizes certain sequence-dependent structural variations of the double helix and senses DNA flexibility. Structural analysis by X-ray crystallography shows that DNase I binds in the minor groove of B-type DNA (Lahm and Suck, 1991, Suck, 1997, Paul *et al.*, 2000) forming contacts in and along both sides of the minor groove extending over a total of 6 base pairs plus 2 adjacent phosphates. As a consequence of DNase I binding, the minor groove opens by approximately 3 Å and the duplex bends towards the major groove by about 20° (Lahm and Suck, 1991, Suck, 1997, Martin *et al.*, 2000). In the presence of divalent metal ions, DNase I cleaves DNA at the phosphodiester bonds that link adjacent

Chapter six: Direct real-time molecular scale visualisation of the degradation of condensed DNA complexes exposed to DNase I

nucleotides. Cleavage preferentially occurs adjacent to pyrimidine bases. In the presence of Mg_2^+ , DNase I hydrolyses each strand of a duplex independently leading to random single strand breaks (SSBs). The purine-pyrimidine bonds are subsequently preferentially cleaved leading to double strand breaks (DSBs) leading to a final product of di- and higher oligonucleotides (Weston *et al.*, 1992, Pan *et al.*, 1998, Fojta *et al.*, 1999, Pan and Lazarus, 1999). In the presence of Mn_2^+ , the enzyme cleaves both strands of DNA at approximately the same site, leading directly to DSBs, Figure 6.1.

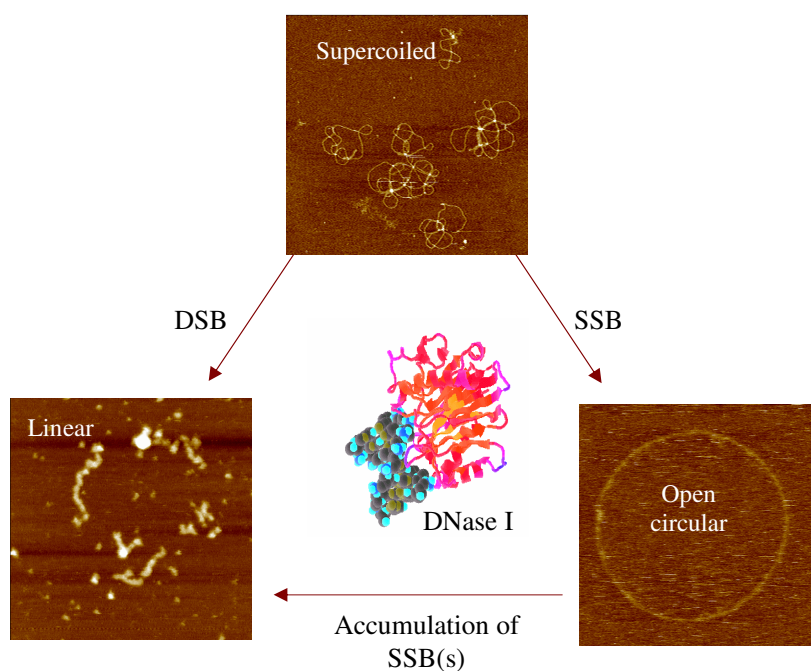


Figure 6.1. Scheme of supercoiled DNA and the formation of open circular or linear DNA as the result of nicking of one DNA strand (single-strand break (SSB)) or both strands in the same site or near to each other (double-strand break (DSB)).

6.2 RESULTS AND DISCUSSION

6.2.1 On Substrate Experiments

6.2.1.1 Effect of DNase I on Naked DNA Plasmids

Figure 6.2 (a) shows topographical image of the DNase I on mica, this reveals a mean diameter of 19 ± 2 nm and a mean height of 1.7 ± 0.3 nm. Figure 6.2 (b) depicts an example control AFM study of naked DNA adsorbed onto freshly cleaved mica and exposed to DNase I, details of samples preparation are in sections 2.2.5 and 2.4. This shows that fragmentation due to the accumulation of SSBs of the DNA molecules starts at ~9 min after the addition of DNase I with complete fragmentation within 22 min (significantly shorter than time periods subsequently observed for G4-DNA complexes, Figure (6.3)). Such data clearly demonstrate the accessibility of the DNase I to the cleavage site of the surface immobilised DNA.

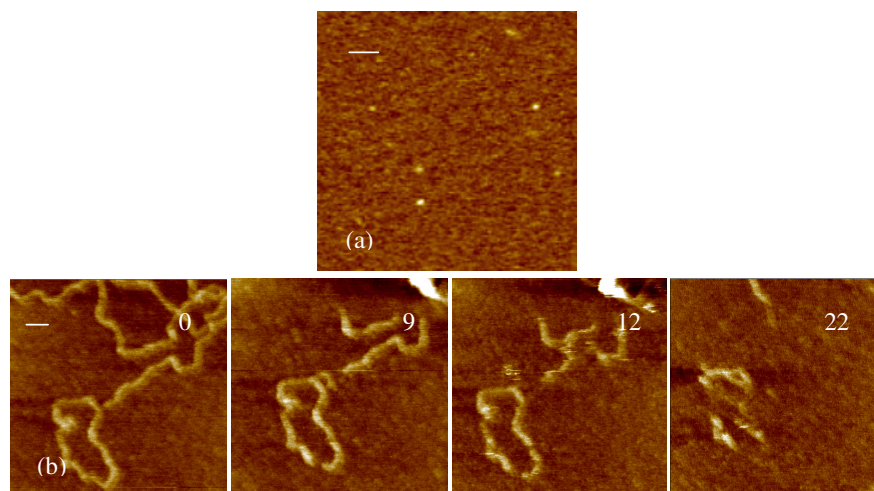


Figure 6.2. Control AFM image of (a) the DNase I adsorbed onto mica, (b) Control AFM images shows the effect of DNase I on bare DNA adsorbed onto mica surfaces. Images were taken in 1mM PBS containing 2mM MgCl₂ and 1mM NiCl₂. Numbers on the images represent time lapsed in minutes. Scale bars = 55, 100 nm respectively, z scales = 5, 7 nm respectively.

6.2.1.2 Effect of Dendrimer's Loading Ratio

Figure 6.3 shows examples of the effect of DNase I on G4-DNA complexes at (a) 0.5:1, (b) 1:1 and (c) 5:1 ratios; complexes were prepared in which DNA and G4 molecules were allowed to equilibrate in solution for a few seconds before being directly introduced to the mica and imaged for ~20 min prior to the addition of the enzyme. The images observed before and at 0 min for all ratios demonstrate the influence of G4 loading upon the morphology of the complexes. For the 0.5:1 ratio (Figure. 6.3a), features consistent with individual molecules or small aggregates of G4 molecules are observed to decorate the DNA at 0 min. During the hour after addition of DNase I, a slight

relaxation of the ring structure is initially observed via an extension in length of 66 nm to 1442 nm and eventually a fragmentation of the complex. At 0 min the measured thickness and height of the decorated DNA strands were 22 ± 5.5 and 3.7 ± 1.4 nm, respectively, while the measured thickness and height of the undecorated parts were 11.0 ± 0.5 and 0.5 ± 0.1 nm, respectively. This is consistent with some regions of the DNA plasmid having a high density of bound G4 whilst other regions remain relatively bare. Subsequent image data show this G4 coverage is in a constant state of flux. For example, the highlighted portion of the complex at 19 min, which is initially protected by G4 complexes, becomes bare after 22 min and is rapidly fragmented by 41 min.

Figure 6.3b shows the effect of DNase I on a G4-DNA complex at 1:1 ratio. Here the observed complexes mostly appear as thickened ring-like structures (thickness ranging from 20 to 60 nm), similar to those previously reported for toroidal DNA condensates and their intermediates (Liu *et al.*, 2001a).

The thickened regions are made up of parallel strands of condensed DNA molecules, consistent with DNA folding as a mechanism for DNA condensation. Features attributable to individual G4 molecules can no longer be seen to decorate the individual complexes, most likely due to their higher packing density along the DNA. The images recorded over 102 min, subsequent to enzyme addition; show dynamic changes in molecular conformation and a gradual degradation of the complexes. This fragmentation indicates that the enzyme is still able to access the DNA double helix sufficiently to allow the accumulation of SSBs, and complete strand breakage. It is also interesting to note that regions of the complexes that appear to be

composed of several laterally associated strands of DNA display more resistance to enzymatic degradation than isolated strands.

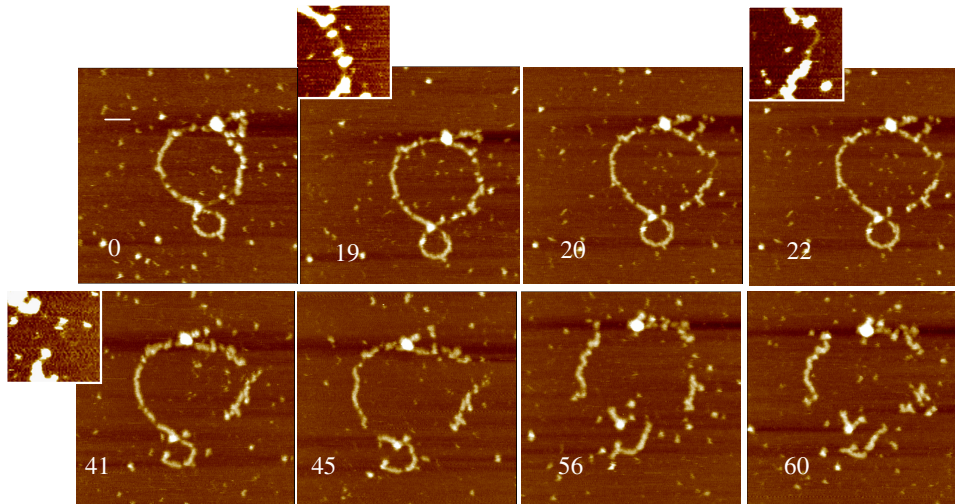


Figure 6.3(a). Effect of DNase I enzyme on G4-DNA (0.5:1) complex, the complex was immediately adsorbed onto mica and imaged in deionized water until stable images were obtained, then the DNase I was introduced. Numbers on the images represent time lapsed in minutes. Scale bar = 70 nm, z scale = 10 nm.

At the higher, 5:1 G4: DNA ratio (Figure 6.3c), the morphology of the observed condensates is markedly changed and consistent with 'spheroid' DNA condensates. Following the addition of DNase I, it can be seen that the complexes are still protected at 120 min without any significant degradation. The measured diameter and height of these features were 69 ± 15 and 10.6 ± 5.7 nm, respectively. Manipulation of the pH of the imaging medium to 11.3 in

Chapter six: Direct real-time molecular scale visualisation of the degradation of condensed DNA complexes exposed to DNase I

the absence of the enzyme, caused these complexes to rapidly disassemble, due to neutralization of the charge on the dendrimers, and for free DNA molecules to be observed within 1 min. This confirms that the spheroids are made up of condensed plasmid molecules.

Chapter six: Direct real-time molecular scale visualisation of the degradation of condensed DNA complexes exposed to DNase I

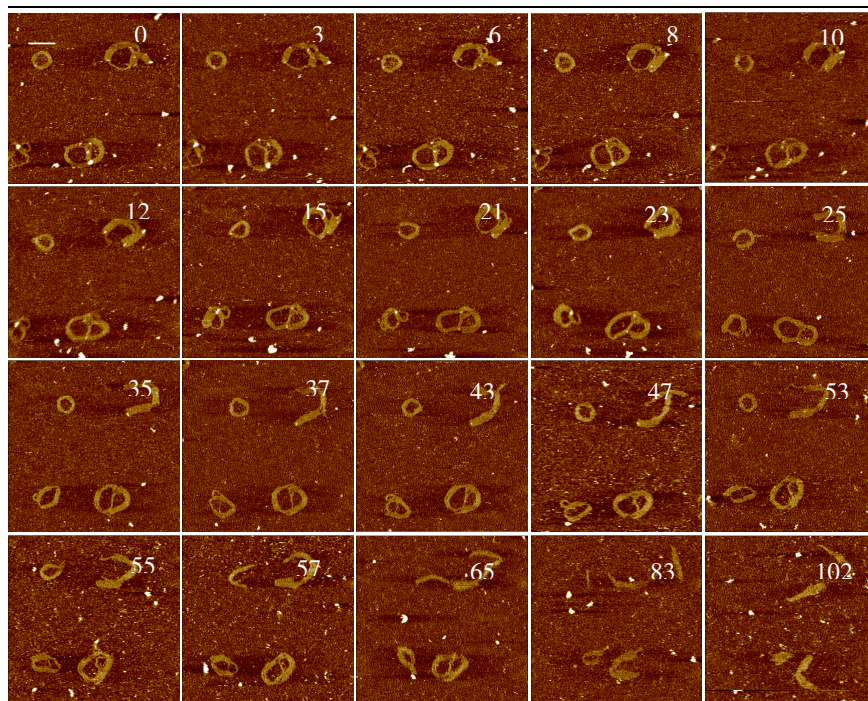


Figure 6.3(b). Effect of DNase I enzyme on G4-DNA (1:1) complex. Numbers on the images represent time lapsed in minutes. Scale bar = 100 nm, z scale = 5 nm.

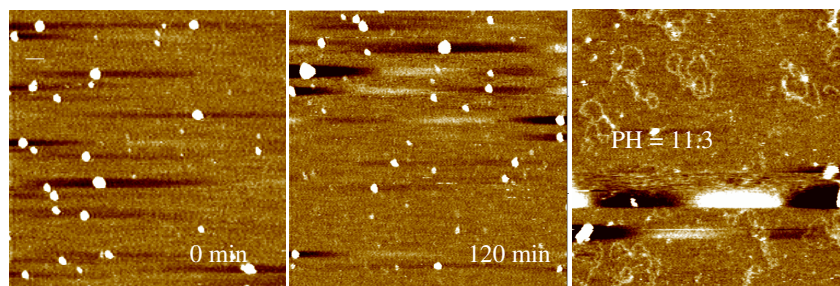


Figure 6.3(c). Effect of DNase I enzyme on G4-DNA (5:1) complex, spheroidal condensates were observed. Following the addition of DNase I, it can be seen that the complexes are still protected at 120 min without any significant degradation. Manipulation of the pH of the imaging medium to 11.3 in the absence of the enzyme caused these complexes to rapidly disassemble. Scale bar = 100 nm, z scale = 7 nm.

Chapter six: Direct real-time molecular scale visualisation of the degradation of condensed DNA complexes exposed to DNase I

The images displayed in Figure 6.3 a-c thus demonstrate that the morphology of the G4-DNA complexes varies markedly with increasing G4 loading and that the degree of protection afforded by the complex is found to rise with increasing G4 loading, at least up to 5:1. From these and other data, we estimate an average for the observed lifetime until complete degradation of the naked DNA and the complexes at different ratios as 18.5 ± 7.8 min for naked DNA ($n = 3$), 66 ± 8.4 min for 0.5:1 G4: DNA ratio ($n = 5$) and 141.5 ± 37.5 min for 1:1 G4: DNA ratio ($n = 46$). These findings are summarized in Table 6.1 and Figure 6.3 (d) respectively.

Ratio	Time (min)			Number of molecules	Morphology	Mean	SD	SE
	Starting/Ending(S/E)	Experiment						
		1	2					
0.0	S	9	15	3	Open circular	12.0	4.24	2.45
	E	13	24	3		18.5	7.78	4.49
0.5	S	22	52	5	Loops	37.0	21.21	9.49
	E	60	72	5		66.0	8.49	3.79
1	S	20	43	46	Loops and Flowers	31.5	16.26	2.40
	E	115	168	46		141.5	37.48	5.53
5	S	>115	>110	>112.5	Spheroids			
	E	Protection		35				

Table 6.1 summarizes the mean starting and ending times of fragmentation within different complex's ratios with G4 dendrimers.

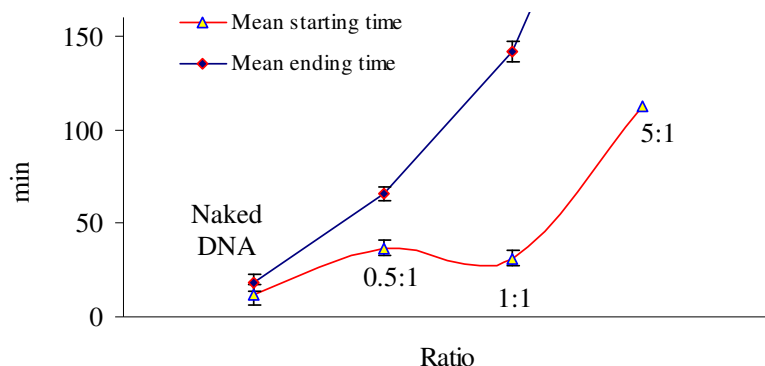


Figure 6.3(d) shows the mean starting and ending times of fragmentation within different complex's ratios with G4 dendrimers.

6.2.1.3 Effect of Incubation Time with Dendrimers

It is feasible that the complex architecture, and hence its ability to resist degradation, will also depend on the time allowed to form the system. Figure 6.4a displays images recorded for the 1:1 G4: DNA ratio, in which DNA and G4 molecules were allowed to equilibrate in solution for 15 min prior to deposition onto mica and subsequent exposure to the DNase I enzyme. By consideration of the images in Figure 6.3b (instantaneous mixing), Figure 6.5 (2hr incubation) it can be seen that for all incubations the morphology of the observed complexes is predominantly toroidal. The importance of the time allowed for complex formation is also apparent. For example, many of the features observed in Figure 6.3b appear to be composed of several loops, and may thus represent incompletely formed toroidal complexes or multimeric intermediates. In contrast, those complexes observed following longer incubation times are mostly ring-like, toroidal complexes of diameter 70 ± 130

nm. The data displayed in Figure 6.4a are noteworthy since the observed complex is still undergoing structural changes consistent with complexation before a clear enzymatic interaction takes place (79 - 99 min). Initially a multi-looped molecule is observed with a contour length of 861 ± 20 nm, a width of 18 ± 1.2 nm and a maximum height at the marked high feature of 3.7 nm. The measured height of the remainder of the complex is 0.8 ± 0.2 nm. Over the next 36 min the DNA becomes increasingly condensed, as demonstrated by an increased width and height of the condensed complex to 27 ± 2.3 nm and 1.8 ± 0.3 nm, respectively, and a reduced length of 433 nm. Within the sequence a globular feature consistent with an enzyme molecule is apparent at 36 min. At 90-94 min an abrupt relaxation of the complex is coincident with the highlighted isolated feature 'binding' to the complex. The complex shows an immediate increase in observed length of ~400 nm. The complex then opens out to a relaxed open circle morphology, reaching a maximum observed length of 1535 ± 45 nm, a thickness of 11 ± 0.3 nm and a height of 0.5 ± 0.1 nm. The contour length, thickness and height profiles of this molecule were illustrated in table 6.2 and Figure 6.4 b respectively.

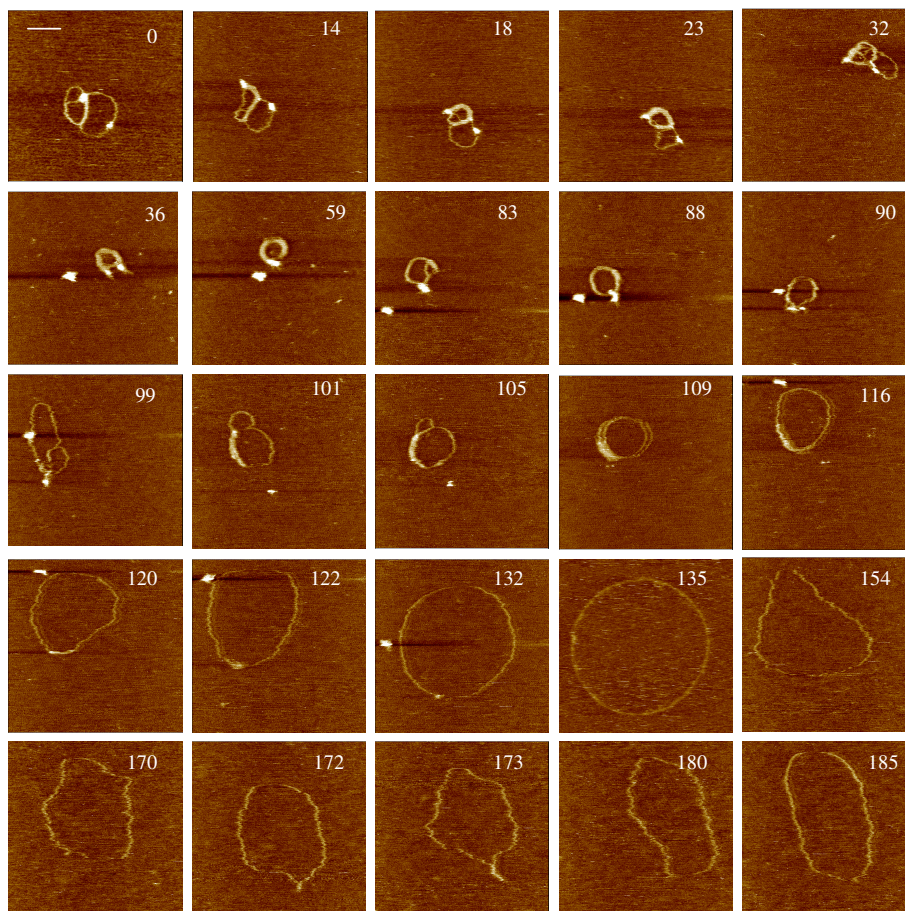


Figure 6.4a. AFM image sequences for the 1:1 G4 to DNA ratio, in which DNA and dendrimer molecules were allowed to equilibrate in solution for 15 min prior to deposition onto mica. The DNA molecule was observed to condense and reaches its smallest diameter after 36 min before a sudden relaxation commences after 99 min and the DNA reaches its maximum diameter after 132 min. Numbers on the images represent time lapsed in minutes. Scale bar = 70 nm, z scale = 3 nm.

Chapter six: Direct real-time molecular scale visualisation of the degradation of condensed DNA complexes exposed to DNase I

Time (min)	Contour Length (nm)	Thickness (nm)	Height (nm)
0	861	17.7	0.6
1.4	960	16.5	0.9
2.8	922	23.7	1.2
4.2	795	22.0	2.1
5.6	900	18.4	1.6
7	910	18.4	1.6
8.4	907	18.4	1.6
9.8	907	17.0	0.5
11.2	800	16.5	0.7
12.6	800	18.4	0.6
14	800	18.4	0.6
15.4	674	18.3	0.8
16.8	710	20.1	0.8
35	617	22.0	1.0
75.6	375	25.7	1.2
78.4	608	22.0	1.1
81.2	492	22.0	0.7
85.4	1001	14.7	0.7
86.8	415	18.3	0.8
93.8	765	18.3	0.8
100.8	681	17.7	0.8
127	1733	11.0	0.5
154	1732	11.0	0.5
173	1535	11.0	0.6
185	1462	16.5	0.5

Table 6.2. The changes in contour length, thickness and height of DNA with time after the addition of DNase I.

Other AFM sequences obtained under the same experimental conditions confirm these findings. For example consider the data in Figure 6.4b. This time the relaxation process was observed to start after 7min instead of 132 min indicating that this behaviour is not only depending on the experimental

conditions but also depends on the state of the individual molecule as well, Figure 6.4c. To support these results another repeat is shown in Figure 6.4d. This time, interestingly, the previous behaviour of the relaxation of the DNA molecules was not observed, rather, fragmentation was the only mechanism observed which commences after 45 minutes and a complete fragmentation appeared after 115 min most likely due to the accumulation of SSBs.

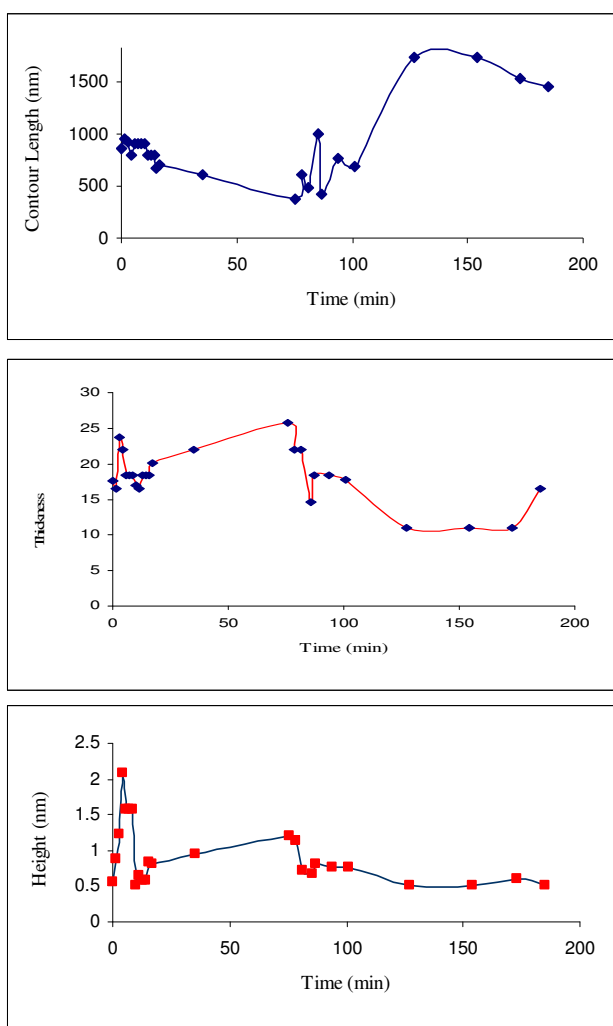


Figure 6.4b. Changes in contour length, thickness and height of the DNA molecule observed in Figure 6.4a with time following the addition of DNase I.

Chapter six: Direct real-time molecular scale visualisation of the degradation of condensed DNA complexes exposed to DNase I

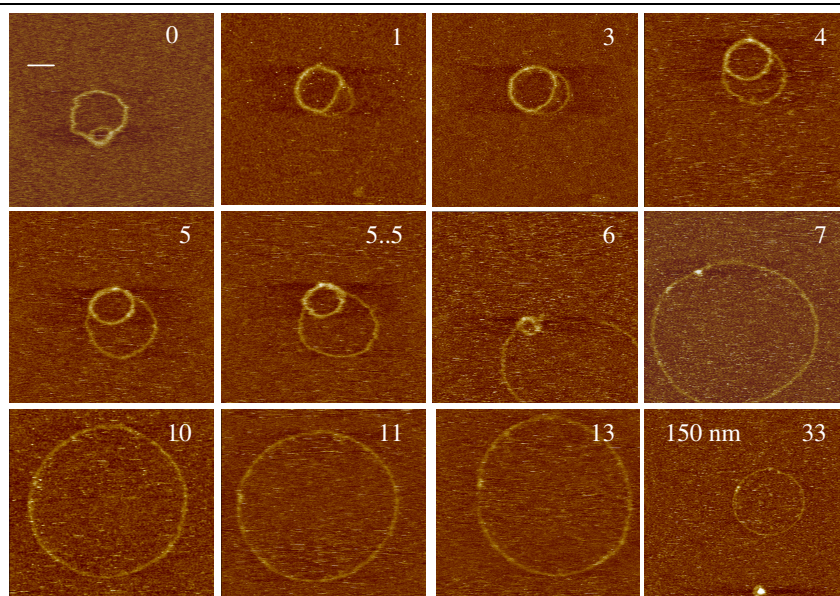


Figure 6.4c. AFM image sequences for the 1:1 G4 to DNA ratio, in which DNA and dendrimer molecules were allowed to equilibrate in solution for 15 min prior to deposition onto mica and subsequent introduction of DNase I. The relaxation of the DNA molecule was observed after 7 min. Numbers on the images represent time lapsed in minutes. Scale bar of images at times of 0-13 min = 70 nm, scale bar at 33 min = 150 nm, z scale = 5 nm.

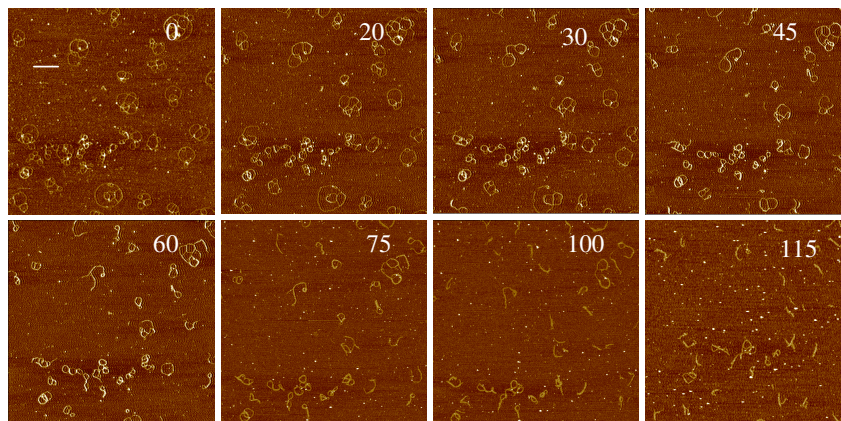


Figure 6.4d. AFM image sequences for the 1:1 G4 to DNA ratio, in which DNA and dendrimer molecules were allowed to equilibrate in solution for 15 min prior to deposition onto mica and subsequent addition of the DNase I. Fragmentation of the DNA molecules was observed due to the accumulation of the SSBs. Numbers on the images represent time lapsed in minutes. Scale bar = 300 nm, z scale = 5 nm.

An increase in the time of incubation before deposition onto mica from 15 min to 2 h produces complexes that are consistently condensed into toroidal structures (Figure 6.5) and which do not display the continuing condensation seen in Figure 6.4a. It is evident that such complexes resist degradation for longer, showing extensive fragmentation only after ~10 hr through an opening of their structure with individual strands becoming partially detached. It is not immediately apparent why, on some occasions, complexes are degraded to an open relaxed plasmid that is not fragmented as compared to the more common endpoint of complete fragmentation, although it may be related to the initial distribution in the DNA population of relaxed and supercoiled plasmids. From a total of 19 separate experiments, this former pathway was observed twice. In terms of the total number of individual complexes observed undergoing this

Chapter six: Direct real-time molecular scale visualisation of the degradation of condensed DNA complexes exposed to DNase I

degradation route, this corresponds to 2 complexes from 44, or ~5%, table 6.3.

We also note that this scenario always leads to a near perfect circular plasmid, which degrades no further, suggesting for this pathway that this is a minimum energy state of the DNA-dendrimer-substrate system, with relaxation of all writhe in the DNA. In this particular case, interactions between the plasmid and the substrate appear to dominate and that this acts to fully open the plasmid and inhibit further action of the DNase I beyond the inclusion of sufficient SSBs to relax the DNA.

Mechanism	No of experiments	No of molecules	Total experiments with G4	Total No of molecules
SSB	2	2	2	2
DSB	1	42	17	570
Total	3	44	19	572
Percentage of SSB	66.7	4.5	10.5	0.3

Table 6.3 shows number of molecules that follows the SSB and DSB mechanisms after the addition of the DNase I enzyme.

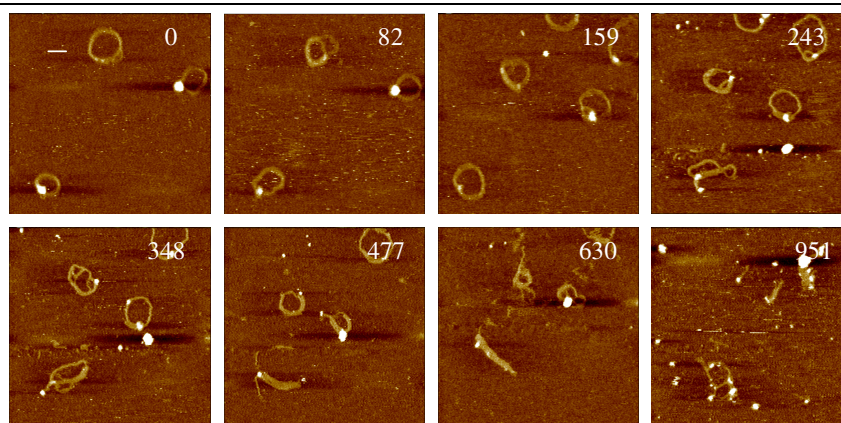


Figure 6.5: AFM image sequences for the 1:1 G4 to DNA ratio, in which DNA and dendrimer molecules were allowed to equilibrate in solution for 2hr prior to deposition onto mica. Numbers on the images represent time lapsed in minutes. Scale bar = 100 nm, z scale = 5 nm.

6.2.1.4 Effect of Substrate

Clearly, in interpreting the data, the effect of the substrate on DNA complex structure and behaviour must be considered. For example, one would expect free G4 to bind to the negatively charged mica surface and possibly play a role in condensing and protecting adsorbed DNA. However, control experiments adsorbing DNA to mica pre-treated with G4 showed no evidence of protection of DNA compared to adsorption on bare mica, Figure 6.6.

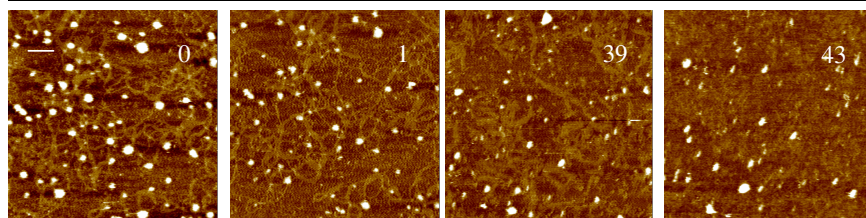


Figure 6.6. AFM image sequences for DNA plasmid in which the DNA was adsorbed onto G4 treated mica before the introduction of DNase I. Numbers on the images represent time lapsed in minutes. Scale bar = 600 nm, z scale = 15 nm.

It is worthy of note that, in experiments with a high excess of G4 to DNA, some evidence of the potential structural effects of the substrate was found. The data in Figure 6.7 show a 'flower-like' complex formed at 20:1 G4: DNA ratio following prior incubation for 2 hr before the introduction of DNase I. Under such conditions we should expect to observe highly complexed spheroid-like structures, as in Figure 5.5. We propose that here the excess of dendrimer causes an artifactual structure to form through the immobilisation of the complex at the solid-solution interface. This is supported by higher resolution images of the substrate background in Figure 6.8 that reveal features ($5.5 \pm 1\text{nm}$) consistent with a densely packed layer of the positively charged G4 molecules. In close proximity to the complex, this layer appears to order and align features within the complex, some of which now have dimensions consistent with exposed DNA ($6 \pm 2\text{ nm}$). Hence, we believe that this process is driven by a reorganisation of the surface bound complex due to the attraction of the positive G4 to exposed portions of negative DNA.

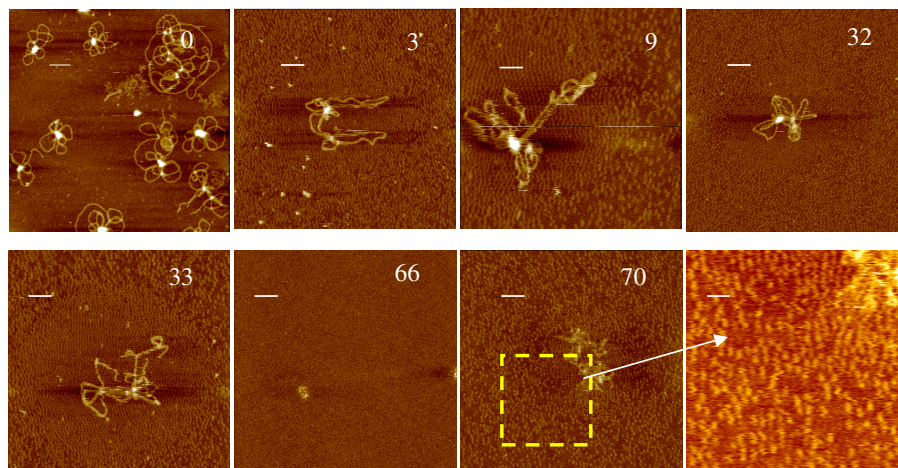


Figure 6.7. AFM images of a 'flower-like' complex formed at 20:1 G4: DNA ratio. A higher resolution image of the substrate background at 70 min shows features consistent with a densely packed layer of DNA segments. Numbers on the images represent time lapsed in minutes. Scale bars =100, 60, 33, 60, 50, 200, 50 and 15 nm respectively, z scale = 5 nm.

We propose that such exposed portions result from DNA that becomes transiently free of solution derived G4 (as observed dynamically in Figure 6.3 (a)). These free regions are then preferentially attracted to the highly packed surface adsorbed dendrimers, causing the opening and distortion of the complex structure observed. Whilst such effects were not observed at lower G4: DNA ratios, they may play a role in the formation of the open loop plasmids such as observed in Figure 6.4 a and c. Moreover, it is clear that since 'open loop' data were recorded in the presence of Mg_2^+ , the action of enzyme leads to SSBs, and hence the open circular endpoint is a possibility.

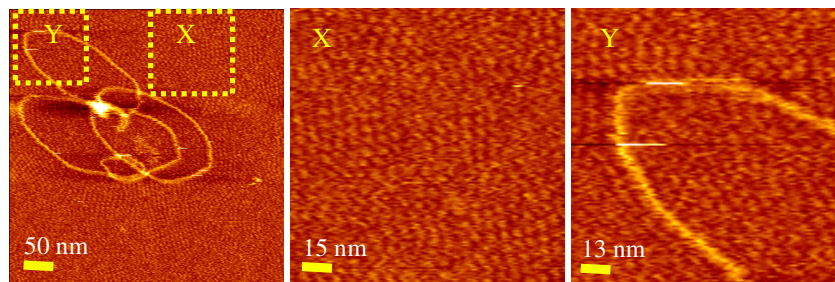


Figure 6.8. AFM image of a 'flower-like' complex formed at 20:1 G4: DNA ratio. Higher resolution images (centred on regions marked X and Y) of the substrate background show features consistent with a densely packed layer of G4.

6.2.1.5 Effect of Incubation Cations

When carrying out similar experiments in Mn_2^+ instead of Mg_2^+ , in which the enzyme cleaves both strands of DNA, only fragmentation should be observed. This was indeed the case as evidenced by the data shown in Figure 6.9.

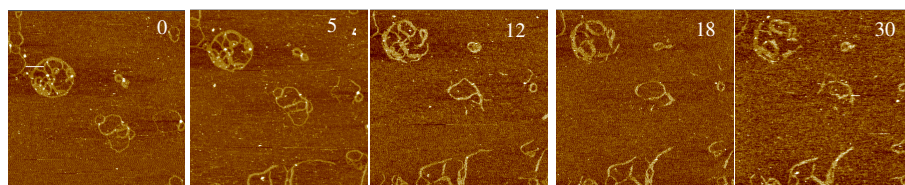


Figure 6.9. Time-lapse images showing the effect of DNase I on G4: DNA complex, 1:1 ratio, incubated for 15 min before deposition. The DNase I then was added and the system was imaged in 1 mM PBS, containing 2 mM $MnCl_2$ and 1mM $NiCl_2$. Numbers on the images represent time lapsed in minutes. Scale bar = 100 nm, z scale = 7 nm.

6.2.1.6 Effect of Dendrimer's Generation

Since the morphology of DNA condensates with both G6 and G8 was spheroidal structures, Figures 5.4 and 5.5, these morphologies were able to retain their structures against the effect of DNase I for longer time as seen with the spheroidal structures formed with G4 complexes at 5:1 ratio, Figure 6.3c. To help assess the impact of the substrate we latter show studies of these complexes using the Gel electrophoresis.

To assess the effect of dendrimer generations we have also studied the effect of DNase I on G6: DNA complexes being formed at 1:1 ratio, incubated for 2 hr, and imaged in 10% PBS, Figure 6.10. It's obvious from these data that the obtained complexes were of globular structures and displayed aggregation, for simplicity we will focus on the marked spherical molecule. This molecule had a diameter and height of 80 nm and 6 nm respectively. No obvious changes were observed after the addition of DNase I until 65 min when a small rod like structure was found to emanate from the spheroidal structure accompanied with a decrease in the diameter and height of this feature. This rod like structure then started to increase in length with time and reaches its maximum length of 400 nm after 105 min, its diameter was 40 nm and its height was 1.2 nm. We propose that the DNA molecule was unwrapped from the G6 molecules and then fragmented after 125 min. This behaviour is opposite to the previous one observed in Figure 5.18 where the DNA molecules were found to wrap around the G6 dendrimers.

Chapter six: Direct real-time molecular scale visualisation of the degradation of condensed DNA complexes exposed to DNase I

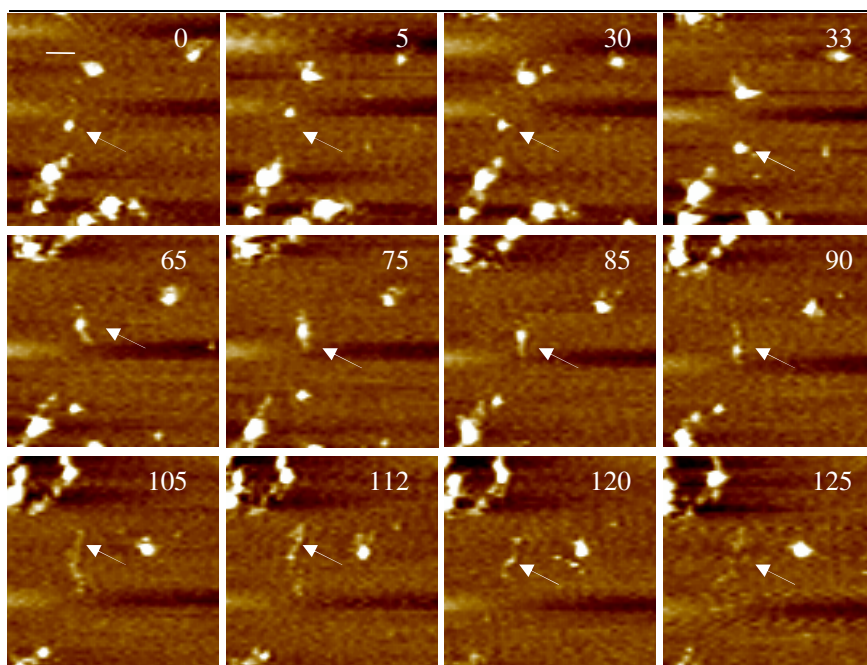


Figure 6.10. Time-lapse images showing the effect of DNase I on G6: DNA complex, 1:1 ratio, incubated for 2hr before deposition and imaged in 10% PBS, containing 2 mM MgCl₂ and 1mM NiCl₂, pH 7.4. Numbers on the images represent time lapsed in minutes. Arrows show the unwrapping of DNA from G6 molecules. Scale bar = 100 nm, z scale = 5 nm.

6.2.2 In Solution Experiments

6.2.2.1 Effect of Loading Ratio

Figure 6.11 shows examples of the effect of DNase I on G4-DNA complexes at (a) 1:1 and (b) 5:1 ratios. Complexes were prepared in which DNA and G4 molecules were allowed to equilibrate in solution for 2hr and then incubated with DNase I for 1 min prior to deposition onto mica. In both ratios, the morphology of the observed condensates is markedly consistent with ‘flower’-

like DNA condensates. The displayed complexes also appear to be composed of several plasmid molecules. Images at 1 min represents the first images directly after incubation with enzyme. For the 1:1 ratio the data in Figure 6.11a, show complexes completely fragmented after 5 min and traces of the fragmented molecules starting to disappear from the imaging field after 7 min. In Figure 6.11b, at 5:1 ratio, it can be seen that even for this higher ratio the complexes are completely fragmented by 58 min. Indeed, by consideration of the complexes at 41 min, it can be seen that DNA strands located towards the complex perimeter, and thus presumably more accessible to enzyme, become fragmented at much earlier exposure times. The images displayed in Figure 6.11 thus demonstrate that the morphology of the G4-DNA complexes did not vary markedly with increasing dendrimer: DNA ratio. Note that these morphologies were observed after 1 min of incubation with DNase I. However, the degree of protection afforded by the complex is found to rise with increasing dendrimer loading. Since we did not stop the reactivity of the enzyme after adsorption onto mica, the enzyme was still active and even at the highest loading ratio employed, the molecule could still be degraded relatively quickly if compared to the same ratios studied on substrate where a complete fragmentation was observed after ca. 1 hr with 1:1 ratio and was protected for more than 120 min with 5:1 ratio. This confirmed the restricted accessibility of DNase I on surface and that 1 min incubation of the aforementioned ratios with DNase I in liquid before depositing onto the surface was enough to enhance the accessibility of the enzyme.

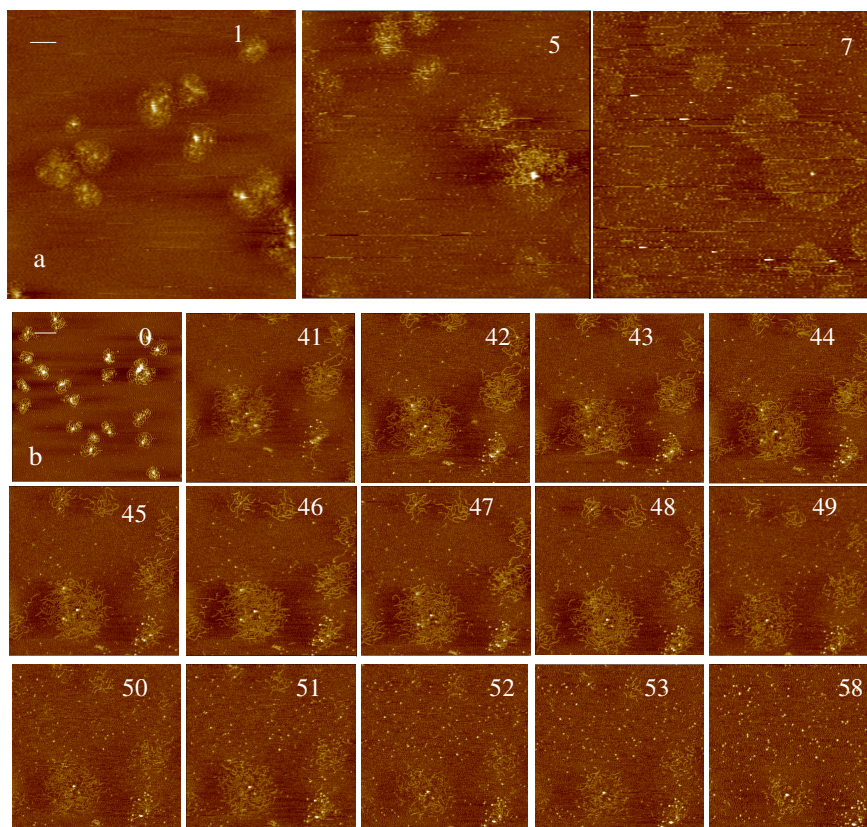


Figure 6.11. Time-lapse images showing the effect of DNase I on G4: DNA complexes at (a) 1:1 and (b) at 5:1 ratios incubated for 2hr before then incubated for 1 min with the enzyme and subsequent deposition onto mica. Numbers on the images represent time lapsed in minutes. Scale bars = 175 and 100 nm respectively, z scale = 6 nm.

6.2.2.2 Effect of Generation

The data from a preliminary experiment at a 1:1 ratio of G6: DNA and incubated for 2 hr before being incubated with DNase I for 30 min are shown in Figure 6.12. It is clear that most of the condensates were stable up to 30 min

and appeared as spheroidal structures as previously observed (Figure 5.4). After 60 min, these spheroidal molecules were opened to make open looped structures. We thus consider these molecules to be stable for more than 30 min up to less than 60 min.

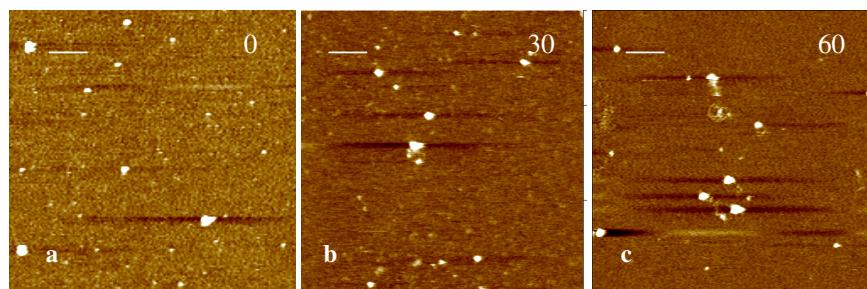


Figure 6.12. Time-lapse images showing the effect of DNase I on G6: DNA complexes at 1:1 ratio following incubation with the DNase I for 30 and 60 min respectively. Complexes were found to be stable against the enzyme action for 30 min and less than 60 min. Numbers on the images represent time lapsed in minutes. Scale bars = 200, 300 and 300 nm respectively, z scales = 15, 5 and 4 nm respectively.

6.2.3 Gel Electrophoresis Investigations of the Effect of Loading Ratio, Generation Type and Incubation Time with DNase I on the Protection of the Obtained Complexes.

The morphology, size, and aggregation state of the complexes are affected by the polymer used and by the formulation conditions. The ratio of polymer to DNA, order of addition, and salt concentration of the medium are some of the important factors involved. It would be expected that any of these factors might influence the ability of these complexes to protect DNA from degradation by

nucleases, depending on how well the DNA is sequestered from the nucleases. The choice of conditions is also important for assessing nuclease degradation. Here we show results according to the experimental conditions detailed in section 2.4. Gel electrophoresis data for the time course degradation of G4: DNA polyelectrolyte complexes at different ratios are shown in Figure 6.13. Lane 1 and 16 show the pattern of naked DNA plasmid in the absence of DNase I, the DNA is separated as 2 bands as mentioned before in Figure 5.23. We believe if extra running time were used the lower band would split into two bands as in lanes 8 and 22 that represent linear and open circular DNA respectively. Lanes 3-6 represents intact DNA in their complexes at 0.5, 1, 3 and 5: 1 ratios respectively in the absence of DNase I and we refer to their time as zero time. These ratios was then loaded in the same order onto the gel after incubation with the DNase I for 30 min (lanes 8-11), 1 hr (lanes 12-15), 2 hr (lanes 18-21), 3 hr (lanes 22-25) and 5 hr (lanes 26-29). Lanes 2 and 17 show the effect of DNase I on naked DNA. Bands corresponding to the full-size plasmid have disappeared by 10 min, and have been replaced in most cases by more mobile, less dense bands representing degradation products which may include either nucleotides or oligo-nucleotide fragments, neither of which binds EBr to the same extent as double-stranded DNA. To provide a more realistic test of protection we have to compare our data with data obtained with serum. Interestingly, a cationic peptide, (N-(2-aminoethyl) glycine)₃₆, has been shown to protect DNA from degradation in 50% (v/v) serum but not in the presence of DNase I (1 IU/mg DNA) (Murphy *et al.*, 1998). However, our results compare favourably with *in vivo* studies in mice where plasmid DNA has been seen to be linearized and largely degraded within 5 min and completely degraded

within 15 min of administration (Kawabata *et al.*, 1995). Moreover, it agrees with results obtained by performing time-course studies that reported plasmid DNA to be largely degraded by DNase I within 5 min (Xu and Szoka, 1996), within less than 10 min with 50% newborn calf serum (Hill et al 2001) and within 15 min when exposed to 100% rat serum (Chiou *et al.*, 1994).

At 0.5:1 ratio, after 30 min incubation with DNase I, lane 8, degradation started almost immediately but occurred relatively slowly compared to naked DNA. Two bands representing linear and open circular DNA are shown. The density of these bands together (by naked eye) is lower than that of intact DNA in lane 3. After 1 hr of incubation with DNase I, lane 12, all bands have disappeared and no intact plasmid is apparent, rather a smear of digested materials was seen. However, at 2-5 hours of incubation, lanes 18, 22 and 26 respectively, again, the two bands were observed in linear and open circular regions, this time they were very faint than those obtained in lane 8. We refer this discrepancy to differences within the gel environment, where any small differences in the experimental conditions, like gel volumes, volume of the running buffer, degree of steering of the running buffer etc, could lead to the observed differences within the gels. On the other hand, complexes formed at ratios greater than 0.5:1 show that intact plasmid DNA can be recovered after up to 5 h of exposure to DNase I enzyme showing increased nuclease protection against degradation. However, it's clear that, after 1 hr, degradation commenced and increased with the incubation time with enzyme. It is noteworthy, however, that the intensity of the bands concerned suggests that incubation with DNase I converts the more mobile bands (supercoiled or

condensed) into the less mobile bands (open circular and linear) in all ratios, and finally the intensity of both bands decreases with further incubation times.

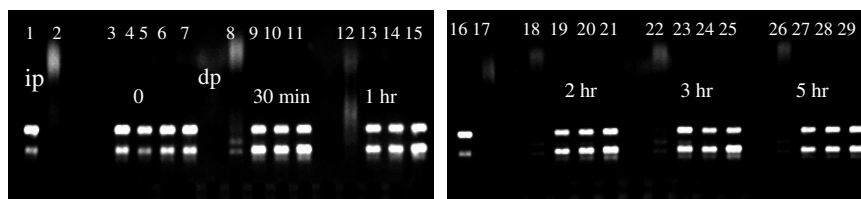


Figure 6.13. Typical gels showing time-dependent degradation by DNase I of plasmid DNA complexed with G4 at increasing ratios. The time of incubation with DNase I is noted in the gel. ip, intact plasmid; dp, degraded plasmid. Lane 1 and 16 contain free plasmid as control. Lane 2 and 17 contain DNase I treated plasmid. Complex ratio details for the remaining wells are as follows: lanes 3-6 contain 0.5, 1, 3, and 5 G4: DNA ratios respectively before treating with the DNase I. lanes 8-11 contain the same complex's after 30 min incubation with DNase I and then the same complexes were incubated with the enzyme for 1 hr as in lanes 12-15, 2 hrs, lanes 18-21, 3 hrs as in lanes 23-25 and for 5 hrs, lanes 26-29.

The same finding was observed with DNA complexed with G6 (Figure 6.14). Lane 1 and 15 show the pattern of naked DNA plasmid in the absence of DNase I, the same finding as those in the previous figure was true. Lanes 3-6 represents intact DNA in their complexes at 0.5, 1, 3 and 5:1 ratios respectively at zero time. These ratios were then loaded as mentioned with G4 dendrimers. Lanes 2 and 16 show the effect of DNase I on naked DNA. Bands corresponding to full-size plasmids have faintly appeared in the first gel (left) as three distinct bands together with less dense bands representing degradation

products which may include either nucleotides or oligo-nucleotide fragments while it was fully disappeared from the second gel (right) by 10 min.

At 0.5:1 ratio, after 30 min incubation with DNase I, lane 7, again two bands represent linear and open circular DNA were shown. After 1 hr of incubation with DNase I, lane 11, the lower band increases in size and brightness while the upper one decreases in both, indicating that some of the supercoiled and/or highly condensed DNA transformed to open relaxed molecules. This behaviour holds true for 2-3 hours, lanes 17, 21 respectively. After 5 hr, however both bands have loosed the most of their brightness and their sizes were decreased indicating that most of the DNA was degraded. Surprisingly, no bands were fully disappeared indicating that even at this very small ratio, at our experimental conditions, some of the DNA molecules still protected from the enzyme. This finding couldn't be obtained from the AFM, which indicated that complexes at ratios larger than this were completely degraded after 1 hr. However, complexes formed at ratios greater than 0.5:1 show that intact plasmid DNA were recovered as two bands up to 5 hr of exposure to DNase I enzyme. At a 1:1 ratio, lanes 4, 8, 12, 18, 22 and 26, the degree of protection was clearly higher than that obtained with 0.5:1 ratio. Then again, the same behaviour of transforming the more mobile DNA to less mobile forms before then disappears from the gel indicates their complete fragmentation. In view of these observations ratios greater than 1:1 are shown in lanes 9,10, 13, 14, 19, 20, 23, 24, 27 and 28. The same behaviour was seen as with 1:1 ratio but in this time the amount of intact DNA showed in the regions of supercoiled/condensed DNA were more than those for 1:1 ratios indicating more protection against the enzyme.

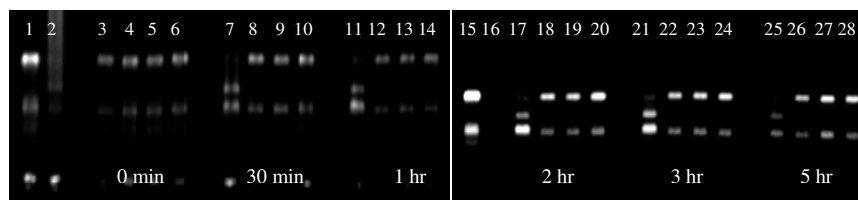


Figure 6.14. Typical gels showing time-dependent degradation by DNase I of plasmid DNA complexed with G6 at increasing ratios. The time of incubation with DNase I is noted in the gel. Lanes 1 and 15 contain free plasmid as control. Lane 2 and 16 contain DNase I treated plasmids. Complex ratio details for the remaining wells are as follows: lanes 3-6 contain 0.5, 1, 3, and 5 G6: DNA ratios respectively before treating with the DNase I. lanes 7-10 contain the same complexes after 30 min incubation with DNase I and then the same complexes were incubated with the enzyme for 1 hr as in lanes 11-14, 2 hrs lanes 17-20, 3 hrs as in lanes 21-24 and for 5 hrs, lanes 25-28.

6.3 CONCLUSIONS

Clearly there are many factors that delineate the ability of a DNA condensing agent to form stable condensates capable of resisting enzymatic degradation for a sufficient period to facilitate transfection. We have demonstrated an approach based upon direct molecular observation that reveals the effect of structural factors and the process of degradation itself. In the example of a G4 and G6 system, we have shown that increasing polymer loading, polymer generation and incubation time can facilitate increased DNA protection. In addition, we report here a simple electrophoretic assay to determine degradation of DNA molecules in their complexes (Hill *et al.*, 2001). The assay is based on a high pH buffer, which can dissociate the complexes under standard electrophoretic conditions. This assay was used qualitatively to determine the time taken for degradation to occur using different polymer loading ratios, polymer generations and time of incubation with DNase I. Alternatively, a standard gel analysis program can be used quantitatively to investigate rates of DNA degradation from complexes in the presence of DNase I. Yet, this is beyond the target of my thesis.

CHAPTER SEVEN

OVERALL CONCLUSIONS

This investigation is one of the first to apply real time AFM, in aqueous conditions and at an individual molecular scale, to the visualisation and characterisation of DNA in the absence of multivalent cations, and to the condensation and dissociation of DNA with fourth, sixth, and eighth generation of ethylenediamine core dendrimers. Such complexes were also investigated using real time AFM imaging to evaluate the degree of protection obtained against the DNase I enzyme. In addition the molecular properties of these PAMAM dendrimers as imaged by AFM, i.e., their size, shape, and rigidity after deposition on surfaces, in air and in liquid have been studied.

By controlling dendrimer concentration, modified surfaces with coverage ranging from isolated molecules to multilayers were obtained. These observations were confirmed by the *in situ* imaging of dendrimers on mica and alkanethiol SAMs surfaces in deionized water.

The calculated volumes for G6 and G8 from the AFM data were in very good agreement with theoretical values for individual ‘relatively rigid’ molecules while that for G4 indicated aggregation of these more ‘relatively open’ molecules.

The behaviour of G4 was also investigated by applying the AFM in its force-distance and amplitude-phase distance modes. It was shown that both modes

suggest conformational changes of the G4 dendrimer molecules on the different alkanethiol surfaces.

Routine imaging of DNA is a major advance towards the useful biological applications of AFM. The ability to control adhesion forces could ultimately prove invaluable to any microscopist wishing to study DNA and other like biomolecules. Towards that, we investigated the ability of monovalent cations (particularly Na^+) to facilitate AFM imaging of DNA. Immobilization of individual DNA molecules and DNA aggregates to mica was successfully shown in the presence of monovalent cations and imaged with the AFM for the first time. This was theorized as being due to random fluctuations in condensed sodium ions leading to formation of temporary di-poles between the DNA-DNA molecules (rod-rod), DNA-mica (rod-planar). These data show that further research needs to be conducted into the application of current counterion correlation theory. Despite the fact that DNA condensation typically occurs for counterion valences of 3 or more, monovalent cations were found in our experimental conditions to be capable of condensing the DNA molecules to form temporarily toroidal like structures.

With regard to the mechanism of DNA condensation, we applied the approach of condensing the nucleic acid material by a stepwise addition of the PAMAM dendrimers. The genetic material was then examined at each stage and a data collected showing the DNA progressing from a random coil to a fully formed condensate structure. The morphology of these complexes depends on the loading ratio of dendrimers, the dendrimer generation and the presence or

absence of soluble dendrimers in the imaging field. We hypothesized that when plasmids first encounter the cationic polymer they collapse into interwound linear condensates. The number of interwound twists of these structures increases and ultimately they coil round and fuse to form a ring-like structure. Crossover stabilization is then formed between these structures leading to multimerization and strand-strand stabilization of these loops or rings.

Moreover, we have demonstrated a novel assessment of condensates volumes relative to structural morphology based on considering the DNA double strands as a long flexible cylindrical geometry. These cylinders can either form flower like structure, rings, toroids, rods or intermediate structures between these morphologies. All of these morphologies include cross sections of the DNA double strands. These cross sections most likely maintain a constant radius for the condensed DNA.

In addition, in relation to the study of the effect of DNase I on the aforementioned complexes with PAMAM dendrimers, we have demonstrated an approach based upon direct molecular observation that reveals the effect of structural factors and the process of degradation itself. In the example of a G4 and G6 system, we have shown that increasing polymer loading, polymer generation and incubation time can facilitate increased DNA protection. The data reveal the dynamic motion associated with latter stages of condensation and structural changes thereafter, and the effect of introducing DNase I into the environment. As yet it is difficult to completely separate these two processes as even at equilibrium dynamic changes are seen in the complex structure (Martin *et al.*, 2000), and indeed such conformational shifts in complex structure may

facilitate the degradation caused by the enzyme. Nevertheless, this approach offers an accessible means of studying a range of complex biomolecular processes at interfaces such as, for example, would occur in membrane environments. In this context, a future combination of dynamic imaging with molecular scale sample manipulation and single molecule force spectroscopy (Scheuring *et al.*, 2002) would represent a significant step.

BIBLIOGRAPHY

- Abdelhady, H. G., Allen, S., Davies, M. C., Roberts, C. J., Tendler, S. J. B. and Williams, P. M. (2003) Direct Real-Time Molecular Scale Visualisation of the Degradation of Condensed DNA Complexes Exposed to Dnase I. *Nucleic Acids Research*. **31**, 4001-4005.
- Allen, M. J., Bradbury, E. M. and Balhorn, R. (1997a) Afm Analysis of DNA-Protamine Complexes Bound to Mica. *Nucleic Acids Research*. **25**, 2221-2226.
- Allen, M. J., Hud, N. V., Balooch, M., Tench, R. J., Siekhaus, W. J. and Balhorn, R. (1992) Tip-Radius-Induced Artifacts in Afm Images of Protamine-Complexed DNA Fibers. *Ultramicroscopy*. **42**, 1095-1100.
- Allen, S., Chen, X., Davies, J., Davies, M. C., Dawkes, A. C., Edwards, J. C., Roberts, C. J., Sefton, J., Tendler, S. J. B. and Williams, P. M. (1997b) Detection of Antigen-Antibody Binding Events with the Atomic Force Microscope. *Biochemistry*. **36**, 7457-7463.
- Allen, S., Connell, S. D. A., Chen, X., Davies, J., Davies, M. C., Dawkes, A. C., Roberts, C. J., Tendler, S. J. B. and Williams, P. M. (2001) Mapping the Surface Characteristics of Polystyrene Microtiter Wells by a Multimode Scanning Force Microscopy Approach. *Journal of Colloid and Interface Science*. **242**, 470-476.
- Allen, S., Davies, J., Davies, M. C., Dawkes, A. C., Roberts, C. J., Tendler, S. J. B. and Williams, P. M. (1999) The Influence of Epitope Availability on Afm Studies of Antigen-Antibody Interactions. *Biochemical Journal*. **341**, 173-178.
- Allen, S., Davies, J., Dawkes, A. C., Davies, M. C., Edwards, J. C., Parker, M. C., Roberts, C. J., Sefton, J., Tendler, S. J. B. and Williams, P. M. (1996) In Situ Observation of Streptavidin-Biotin Binding on an Immunoassay Well Surface Using an Atomic Force Microscope. *Federation of European Biochemical Societies Letters*. **390**, 161-164.
- Allison, S. A. (1981) Structure of Viral J29 DNA Condensed by Simple Triamines: A Light-Scattering and Electron Microscopy Study. *Biopolymers*. **20**, 469-488.
- Anczykowski, B., Krüger, D., Babcock, K. L. and Fuchs, H. (1996) Basic Properties of Dynamic Force Spectroscopy with the Scanning Force Microscope in Experiment and Simulation. *Ultramicroscopy*. **66**, 251-259.
- Anselmetti, D., Fritz, J., Smith, B. and Fernandez-Busquets, X. (2000) Single Molecule DNA Biophysics with Atomic Force Microscopy. *Single Molecules*. **1**, 53-58.
-

Bibliography

- Anselmetti, D., Luthi, D., Meyert, E., Richmond, T., Dreier, M., Frommer, J. E. and Guntherodt, H. J. (1994) Attractive-Mode Imaging of Biological I Materials with Dynamic Force I Microscopy. *Nanotechnology*. **5**, 87-94.
- Argaman, M., Golan, R., Thomson, N. H. and Hansma, H. G. (1997) Phase Imaging of Moving DNA Molecules and DNA Molecules Replicated in the Atomic Force Microscope. *Nucleic Acids Research*. **25**, 4379-4384.
- Bar, G., Brandsch, R. and Whangbo, M.-H. (1999) Correlation between Frequency-Sweep Hysteresis and Phase Imaging Instability in Tapping Mode Atomic Force Microscopy. *Surface Science*. **436**, L715-L723.
- Barbosa, M. C. (2002) The Density-Functional Approach for Charged Systems. *Journal of Physics:Condensed Matter*. **14**, 2461-2465.
- Barrena, E., Ocal, C. and Salmeron, M. (1999) Evolution of the Structure and Mechanical Stability of Self-Assembled Alkanethiol Islands on Au(111) Due to Diffusion and Ripening. *The Journal of Chemical Physics*. **111**, 9797-9802.
- Berge, T., Ellis, D. J., Dryden, D. T. F., Edwardson, J. M. and Henderson, R. M. (2000) Translocation-Independent Dimerization of the Ecoki Endonuclease Visualized by Atomic Force Microscopy. *Biophysical Journal*. **79**, 479-484.
- Betley, T. A., Banaszak Holl, M. M. B., Orr, B. G., Swanson, D. R., Tomalia, D. A. and Baker, J. R. (2001) Tapping Mode Atomic Force Microscopy Investigation of Poly (Amidoamine) Dendrimers: Effects of Substrate and Ph on Dendrimer Deformation. *Langmuir*. **17**, 2768-2773.
- Betzig, E. and Chichester, R. J. (1993) Single Molecules Observed by near-Field Scanning Optical Microscopy. *Science*. **262**, 1422-1425.
- Bezanilla, M., Drake, B., Nudler, E., Kashlev, M., Hansma, P. K. and Hansma, H. G. (1994) Motion and Enzymatic Degradation of DNA in the Atomic Force Microscope. *Biophysical Journal*. **67**, 2454-2459.
- Bielinska, A. U., Chen, C., J., J. and Baker, J. (1999) DNA Complexing with Polyamidoamine Dendrimers: Implications for Transfection. *Bioconjugate Chemistry*. **10**, 843-850.
- Bielinska, A. U., Kukowska-Latallo, J., Johnson, J., Tomalia, D. A. and Baker, J. R. (1996) Regulation of in Vitro Gene Expression Using Antisense Oligonucleotides or Antisense Expression Plasmids Transfected Using Starburst Pamam Dendrimers. *Nucleic Acids Research*. **24**, 2176-2182.
- Bielinska, A. U., Kukowska-Latallo, J. F. and Baker Jr, J. R. (1997) The Interaction of Plasmide DNA with Polyamidoamine Dendrimers:
-

Bibliography

- Mechanism of Complex Formation and Analysis of Alteration Induced in Nuclease Sensitivity and Transcriptional Activity of the Complexed DNA. *Biochimica et Biophysica Acta*. **1353**, 180-190.
- Bielinska, A. U., Yen, A., Wu, H. L., Zahos, K. M., Sun, R., Weiner, N. D., Baker Jr, J. R. and Roessler, B. J. (2000) Application of Membrane-Based Dendrimer/DNA Complexes for Solid Phase Transfection in Vitro and in Vivo. *Biomaterials*. **21**, 877-887.
- Binnig, G., Gerber, C., Stoll, E., Albrecht, T. R. and Quate, C. F. (1987) Atomic Resolution with Atomic Force Microscopy. *Europhysics Letters*. **3**, 1281-1286.
- Binnig, G., Quate, C. F. and Gerber, C. (1986) Atomic Force Microscope. *Physical Review Letters*. **56**, 930-933.
- Binnig, G. and Rohrer, H. (1982) Scanning Tunnelling Microscopy. *Helvetica Physica Acta*. **55**, 726-735.
- Blackburn, G. M. and Gait, M. J. (1990) *Nucleic Acids in Chemistry and Biology*, Oxford:IRL Press at Oxford University Press, Oxford.
- Bliznyuk, V. N., Rinderspacher, F. and Tsukruk, V. V. (1998) On the Structure of Polyamidoamine Dendrimers Monolayers. *Polymer*. **21**, 5249-5252.
- Bloomfield, V. A. (1991) Condensation of DNA by Multivalent Cations: Considerations on Mechanism. *Biopolymers*. **31**, 1471-1481.
- Bloomfield, V. A. (1996) DNA Condensation. *Current Opinion in Structural Biology*. **6**, 334-341.
- Bloomfield, V. A. (1997) DNA Condensation by Multivalent Cations. *Biopolymers*. **44**, 269-282.
- Bloomfield, V. A. (1998) DNA Condensation by Multivalent Cations. *Biopolymers*. **53**, 329-341.
- Bloomfield, V. A., Crothers, D. M. and Tinoco, I. (2000) In *Nucleic Acids : Structures, Properties, and Functions*. University Science Books, Sausalito, California.
- Bonnell, D. A. (Ed.) (2001) *Scanning Probe Microscopy and Spectroscopy: Theory, Techniques, and Applications.*, Wiley - VCH, New York.
- Bottcher, C., Endisch, C., Fuhrhop, J., Catterall, C. and Eaton, M. (1998) High-Yield Preparation of Oligomeric C-Type DNA Toroids and Their Characterization by Cryoelectron Microscopy. *Journal of the American Chemical Society*. **120**, 11-17.
-

Bibliography

- Brown, M. D., Schatzlein, A. G. and Uchegbu, J. F. (2001) Gene Delivery with Synthetic (Non Viral) Carriers. *International Journal of Pharmaceutics*. **229**, 1-21.
- Brunner, S., Sauer, T., Carotta, S., Cotten, M., Saltik, M. and Wagner, E. (2000) Cell Cycle Dependence of Gene Transfer by Lipoplex, Polyplex and Recombinant Adenovirus. *Gene Therapy*. **7**, 401–407.
- Burak, Y., Ariel, G. and Andelman, D. (2003) Onset of DNA Aggregation in Presence of Monovalent and Multivalent Counterions. *Biophysical Journal*. **85**, 2100–2110.
- Burnham, N. A., Colton, R. J. and Pollock, H. M. (1993) Interpretation of Force Curves in Force Microscopy. *Nanotechnology*. **4**, 64-80.
- Bustamante, C., Vesenka, J., Tang, C. L., Rees, W., Guthold, M. and Keller, R. (1992) Circular DNA-Molecules Imaged in Air by Scanning Force Microscopy. *Biochemistry*. **31**, 22-26.
- Butt, H. J., Jaschke, M. and Ducker, W. (1995) Measuring Surface Forces in Aqueous Electrolyte Solution with Atomic Force Microscope. *Bioelectrochemistry and bioenergetics*. **38**, 191-201.
- Butt, H.-J., Wolff, E. K., Gould, S. A. C., Dixon Northern, B., Peterson, C. M. and Hansma, P. K. (1990) Imaging Cells with Theatomic Force Microscope. *Journal of Structural Biology*. **105**, 54-61.
- Cagin, T., Wang, G., Martin, R., Breen, N. and Goddard, W. A. (2000) Molecular Modelling of Dendrimers for Nanoscale Applications. *Nanotechnology*. **11**, 77-84.
- Calladine, C. R. (1980) Toroidal Elastic Supercoiling of DNA. *Biopolymers*. **19**, 1705-1713.
- Campbell, P. A., Sinnamon, L. J., Thompson, C. and Walmsley, D. G. (1998) Atomic Force Microscopy Evidence for K⁺ Domains on Freshly Cleaved Mica. *Surface Science Letters*. **410**, L768-772.
- Caplen, N. J., Alton, E., Middleton, P. G., Dorin, J. R., Stevenson, B. J. and Gao, X., Et Al. (1995) Liposome-Mediated C_{ft}r Gene-Transfer to the Nasal Epithelium of Patients with Cystic-Fibrosis. *Nature Medicine*. **1**, 39-46.
- Cappella, B. and Dietler, G. (1999) Force-Distance Curves by Atomic Force Microscopy. *Surface Science Reports*. **34**, 1-104.
- Chasovskikh, S. and Dritschilo, A. (2002) Magnesium Concentration Effects on Cruciform Extrusion in Supercoiled DNA Examined by Atomic Force Microscopy. *Applied Surface Science*. **188**, 481-485.
-

Bibliography

- Chattoraj, D. K., Gosule, L. C. and Schellman, J. A. (1978) DNA Condensation with Polyamines. Ii Electron Microscope Studies. *Journal of Molecular Biology*. **121**, 327-337.
- Chechik, V., Zhao, M. and Crooks, R. M. (1999) Self-Assembled Inverted Micelles Prepared from a Dendrimer Template: Phase Transfer of Encapsulated Guests. *Journal of the American Chemical Society*. **121**, 4910 - 4911.
- Chen, W., Turro, N. J. and Tomalia, D. A. (2000) Using Ethidium Bromide to Probe the Interactions between DNA and Dendrimers. *Langmuir*. **16**, 15-19.
- Chen, X., Davies, M. C., Roberts, C. J., Tendler, S. J. B., Williams, P. M., Davies, J., Dawkes, A. C. and Edwards, J. C. (1998) Interpretation of Tapping Mode Atomic Force Microscopy Data Using Amplitude-Phase-Distance Measurements. *Ultramicroscopy*. **75**, 171-181.
- Cherng, J.-Y., Vandewetering, P., Talsma, H., Crommelin, D. J. A. and Hennink, W. E. (1996) Effect of Size and Serum Proteins on Transfection Efficiency of Poly(2-(Dimethylamino)Ethyl Methacrylate)-Plasmid Nanoparticles. *Pharmaceutical Research*. **13**, 1038-1042.
- Chiou, H. C., Tangco, M. V., Levine, S. M., Robertson, D., Kormis, K., Wu, C. H. and Wu, G. Y. (1994) Enhanced Resistance to Nuclease Degradation of Nucleic Acids Complexed to Asialoglycoprotein-Polylysine Carriers. *Nucleic Acids Research*. **22**, 5439-5446.
- Clausen-Schaumann, H., Rief, M., Tolksdorf, C. and Gaub, H. E. (2000) Mechanical Stability of Single DNA Molecules. *Biophysical Journal*. **78**, 1997-2007.
- Cluzel, P. H., Lebrun, A., Heller, C. H., Lavery, R., Viovy, J.-L. C., D. and Caron, F. (1996) DNA: An Extensible Molecule. *Science*. **271**, 792-794.
- Conwell, C. C., Vilfan, I. D. and Hud, N. V. (2003) Controlling the Size of Nanoscale Toroidal DNA Condensates with Static Curvature and Ionic Strength. *Proceedings of the National Academy of Sciences. USA*. **100**, 9296-9301.
- Creager, S. E. and Clarke, J. (1994) Contact-Angle Titrations of Mixed Omega-Mercaptoalkanoic Acid / Alkanethiol Monolayers on Gold. Reactive Vs. Nonreactive Spreading, and Chain Length Effects on Surface Pka Values. *Langmuir*. **10**, 3675-3683.
- Culver, K. W. and Blaese, R. M. (1994) In *Gene Therapeutics: Methods and Applications for Direct Gene Transfer*.(Ed, Wolff, J. A.) Boston, Birkhauser, pp. 263-280.
-

Bibliography

- Czajkowsky, D. M., Iwamoto, H. and Shao, Z. F. (2000) Atomic Force Microscopy in Structural Biology: From the Subcellular to the Submolecular. *Journal of Electron Microscopy*. **49**, 395-406.
- Danesh, A., Davies, M. C., Hinder, S. J., Roberts, C. J., Tendler, S. J. B., Williams, P. M. and Wilkins, M. J. (2000) Surface Characterization of Aspirin Crystal Planes by Dynamic Chemical Force Microscopy. *Analytical Chemistry*. **72**, 3419-3422.
- Dash, P. R., Toncheva, V., Schacht, E. and Seymour, L. W. (1997) Synthetic Polymers for Vectorial Delivery of DNA: Characterisation of Polymer-DNA Complexes by Photon Correlation Spectroscopy and Stability to Nuclease Degradation and Disruption by Polyanions in Vitro. *Journal of Controlled Release*. **48**, 269-276.
- Davies, M. C., Roberts, C. J., Tendler, S. J. B. and Williams, P. M. (1997) In *Biocompatibility: Assessment of Medical Devices and Materials*(Ed, Braybrook, J.) John Wiley & Sons, Chichester, pp. 65-100.
- Delong, R., Stephenson, K., Loftus, T., Fisher, M., Alahari, S., Nolting, A. and Juliano, R. L. (1997) Characterization of Complexes of Oligonucleotides with Polyamidoamine Starburst Dendrimers and Effects on Intracellular Delivery. *Journal of Pharmaceutical Sciences*. **86**, 762 -764.
- Dennig, J. and Duncan, E. (2002) Gene Transfer into Eukaryotic Cells Using Activated Polyamidoamine Dendrimers. *Reviews in Molecular Biotechnology*. **90**, 339-347.
- Derose, J. A., Lampner, D. B., Lindsay, S. M. and Tao, N. J. (1993) Comparative Scanning Probe Microscopy Study of the Surface Morphology of Au Films Grown from the Vapor onto Glass, Fused Silica, and Muscovite Mica. *Journal of Vacuum Science & Technology. A*. **11**, 776-780.
- Derose, J. A., Thundat, T., Nagahara, L. A. and Lindsay, S. M. (1991) Gold Grown Epitaxially on Mica: Conditions for Large Area Flat Surfaces. *Surface Science*. **257**, 102 - 108.
- Diaspro, A. and Rolandi, R. (1997) Atomic Force Microscopy. *IEEE Engineering in Medicine and Biology*. **March/April**.
- Diehl, A., Carmona, H. A. and Levin, Y. (2001) Counterion Correlations and Attraction between Like-Charged Macromolecules. *Physical Review E*. **6401**, 1804-1809.
- Dishner, M. H., Ivey, M. M., Gorer, S., Hemminger, J. C. and Feher, F. J. (1998) Preparation of Gold Thin Films by Epitaxial Growth on Mica and the Effect of Flame Annealing. *Journal of Vacuum Science & Technology. A*. **16**, 3295-3300.
-

Bibliography

- Drake, B., Prater, C. B., Weisenhorn, A. L., Gould, S. A. C., Albrecht, T. R., Quate, C. F., Cannell, D. S., Hansma, H. G. and Hansma, P. K. (1989) Imaging Crystals, Polymers, and Processes in Water with the Atomic Force Microscope. *Science*. **243**, 1586-1589.
- Duncan, R. (2003) The Dawning Era of Polymer Therapeutics. *Nature Reviews Drug Discovery*. **2**, 347-360.
- Dunlap, D. D., Maggi, A., Soria, M. R. and Monaco, L. (1997) Nanoscopic Structure of DNA Condensed for Gene Delivery. *Nucleic Acids Research*. **25**, 3095-3101.
- Edwardson, J. M. and Henderson, R. M. (2004) Atomic Force Microscopy and Drug Discovery. *Drug Discovery Today*. **9**, 64-71.
- Eichman, J. D., Bielinska, A. U., Kukowska-Latallo, J. F. and Baker, J. R. (2000) The Use of Pamam Dendrimers in the Efficient Transfer of Genetic Material into Cells. *Pharmaceutical Science & Technology Today*. **3**, 232-245.
- Eickbush, T. H. and Mondrianakis, E. N. (1978) The Compaction of DNA Helices into Either Continuous Supercoils or Folded-Fiber Rods and Toroids. *Cell*. **13**, 295-306.
- Ellis, D. J., Berge, T., Edwardson, J. M. and Henderson, R. M. (1999a) Investigation of Protein Partnerships Using Atomic Force Microscopy. *Microscopy research and technique*. **44**, 368-377.
- Ellis, D. J., Dryden, D. T. F., Berge, T., Edwardson, I. M. and Henderson, R. M. (1999b) Direct Observation of DNA Translocation and Cleavage by the Ecoli Endonuclease Using Atomic Force Microscopy. *Nature Structural Biology*. **6**, 15-17.
- Esfand, R. and Tomalia, D. A. (2001) Poly (Amidoamine) (Pamam) Dendrimers: From Biomimicry to Drug Delivery and Biomedical Applications. *Drug Discov Today*. **6**, 427-436.
- Evenson, A. and Badyal, J. P. S. (1997) Self-Assembled Pamam Dendrimer Films. *Advanced Materials*. **9**, 1097-1099.
- Fain, S. C., Barry, K. A., Bush, M. G., Pittenger, B. and Louie, R. N. (2000) Measuring Average Tip-Sample Forces in Intermittent-Contact (Tapping) Force Microscopy in Air. *Applied Physics Letters*. **76**, 930-932.
- Fang, Y. and Hoh, J. (1999) Cationic Silanes Stabilize Intermediates in DNA Condensation. *Federation of European Biochemical Societies Letters*. **459**, 173-176.

Bibliography

- Fang, Y. and Hoh, J. H. (1998a) Early Intermediates in Spermidine-Induced DNA Condensation on the Surface of Mica. *Journal of the American Chemical Society*. **120**, 8903-8909.
- Fang, Y. and Hoh, J. H. (1998b) Surface-Directed DNA Condensation in the Absence of Soluble Multivalent Cations. *Nucleic Acids Research*. **26**, 588-593.
- Farhood, H., Serbina, N. and Huang, L. (1995) The Role of Dioleoyl Phosphatidylethanolamine in Cationic Liposome Mediated Gene Transfer. *Biochimica et Biophysica Acta*. **1235**, 289-295.
- Ferrari, S., Moro, E., Pettenazzo, A., Behr, J. P., Zacchello, M. and Scarpa, M. (1997) Exgen 500 Is an Efficient Vector for Gene Delivery to Lung Epithelial Cells in Vitro and in Vivo. *Gene Therapy*. **4**, 1100-1106.
- Florin, E. L., Moy, V. T. and Gaub, H. E. (1994a) Adhesion Forces between Individual Ligand-Receptor Pairs. *Science*. **264**, 415-417.
- Florin, E. L., Moy, V. T. and Gaub, H. E. (1994b) Adhesion Forces between Individual Ligand-Receptor Pairs. *Science*. **264**.
- Fojta, M., Kubicǎroǎ, T. and Palecek. (1999) Cleavage of Supercoiled DNA by Deoxyribonuclease I in Solution and at the Electrode Surface. *Electroanalysis*. **11**, 1005-1012.
- Franklin, R. E. and Gosling, R. (1953) Molecular Configuration in Sodium Thymonucleate. *Nature*. **171**, 740-741.
- Frisbie, C. D., Rozsnyai, L. F., Noy, A., Wrighton, M. S. and Lieber, C. M. (1994) Functional Group Imaging by Chemical Force Microscopy. *Science*. **265**, 2071-2074.
- Fritzsche, W., Takac, L. and Henderson, E. (1997) Application of Atomic Force Microscopy to Visualization of DNA, Chromatin, and Chromosomes. *Critical Reviews in Eukaryotic Gene Expression*. **7**, 231-240.
- Gao, C. (1997) Theory of Menisci and Its Application. *Applied Physics Letters*. **71**, 1801-1803.
- Garnett, M. C. (1999) Gene-Delivery Systems Using Cationic Polymers. *Critical reviews in therapeutic Drug carrier systems*. **16**, 147-207.
- Giesbers, M., Kleijn, J. M. and Stuart, C. M. A. (2002) Interactions between Acid- and Base-Functionalized Surfaces. *Journal of Colloid and Interface Science*. **252**, 138-148.
- Godbey, W. T., Wu, K. K. and Mikos, A. G. (1999a) Poly(Ethylenimine) and Its Role in Gene Delivery. *Journal of Controlled Release*. **60**, 149-160.
-

Bibliography

- Godbey, W. T., Wu, K. K. and Mikos, A. G. (1999b) Tracking the Intracellular Path of Poly(Ethylenimine)/DNA Complexes for Gene Delivery. *Proceedings of the National Academy of Sciences. USA.* **96**, 5177-5181.
- Golan, R., Pietrasanta, L. I., Hsieh, W. and Hansma, H. G. (1999) DNA Toroids: Stages in Condensation. *Biochemistry.* **38**, 14069-14076.
- Gosule, L. C. and Schellman, J. A. (1976) Compact Form of DNA Induced by Spermidine. *Nature.* **259**, 333-335.
- Gosule, L. C. and Schellman, J. A. (1978) DNA Condensation with Polyamines I. Spectroscopic Studies. *Journal of Molecular Biology.* **121**, 311-326.
- Grier, D. G. (1998) Colloids: A Surprisingly Attractive Couple. *Nature Medicine.* **393**, 621.
- Grier, D. G. (2000) When Like Charges Attract: Interactions and Dynamics in Charge-Stabilized Colloidal Suspensions. *Journal of Physics: Condensed Matter.* **12**, A85-A94.
- Guckenberger, R., Heim, M., Cevc, G., Knapp, H. F., Wiegrübe, W. and Hillebrand, A. (1994) Stm of Insulators and Biological Specimens, Based on Lateral Conductivity of Ultrathin Water Films. *Science.* **266**, 1538-1540.
- Guo, L.-H., Facci, S., Mclendon, G. and Mosher, R. (1994) Effect of Gold Topography and Surface Pretreatment on the Self-Assembly of Alkanethiol Monolayers. *Langmuir.* **10**, 4588 - 4593.
- Ha, B. Y. and Liu, A. J. (1997) Counterion-Mediated Attraction between Two Like-Charged Rods. *Physical Review Letters.* **79**, 1289-1292.
- Ha, B. Y. and Liu, A. J. (1998) Charge Oscillations and Many-Body Effects in Bundles of Like-Charged Rods. *Physical Review E.* **58**, 6281-6286.
- Ha, B. Y. and Liu, A. J. (1999a) Counterion-Mediated, Non-Pairwise-Additive Attractions in Bundles of Like-Charged Rods. *Physical Review E.* **60**, 803-813.
- Ha, B. Y. and Liu, A. J. (1999b) The Nature of Attraction between Like-Charged Rods. *Physical Review Letters.* **83**, 2681-2681.
- Ha, B.-Y. and Liu, A. J. (2001) In *Physical Chemistry of Polyelectrolytes*(Ed, Radeva, T.) Marcel Dekker, NY, pp. 163-180.

Bibliography

- Haberle, W., Hrber, J. K. H. and Binnig, G. (1991) Force Microscopy on Living Cells. *Journal of Vacuum Science & Technology. B.* **9**, 1210-1213.
- Haberle, W., Hrber, J. K. H., Ohnesorge, F., Smith, D. P. and Binnig, G. (1992) In Situ Investigations of Single Living Cells Infected by Viruses. *Ultramicroscopy.* **42**, 1161-1167.
- Haensler, J. and Szoka, F. C. (1993) Polyamidoamine Cascade Polymers Mediate Efficient Transfection of Cells in Culture. *Bioconjugate Chemistry.* **4**, 372-379.
- Han, T., Williams, J. M. and Beebe, T. P. (1995) Chemical Bonds Studied with Functionalized Atomic Force Microscopy Tips. *Analytica Chimica Acta.* **307**, 365 - 376.
- Hansma, H. G. (1996a) Atomic Force Microscopy of Biomolecules. *Journal of Vacuum Science & Technology. B.* **B 14**, 1390-1394.
- Hansma, H. G. (2001) Surface Biology of DNA by Atomic Force Microscopy. *Annual Review of Physical Chemistry.* **52**, 71-92.
- Hansma, H. G., and Laney, D.E. (1996b) DNA Binding to Mica Correlates with Cationic Radius: Assay by Atomic Force Microscopy. *Biophysical Journal.* **70**, 1933-1939.
- Hansma, H. G., Bezanilla, M., Zenhausern, F., Adrian, M. and Sinsheimer, R. L. (1993) Atomic Force Microscopy of DNA in Aqueous-Solutions. *Nucleic Acids Research.* **21**, 505-512.
- Hansma, H. G., Golan, R., Hsieh, W., Lollo, C. P., Mullen-Ley, P. and Kwoh, D. (1998) DNA Condensation for Gene Therapy as Monitored by Atomic Force Microscopy. *Nucleic Acids Research.* **26**, 2481-2487.
- Hansma, H. G., Laney, D. E., Bezanilla, M., Sinsheimer, R. L. and Hansma, P. K. (1995) Applications for Atomic Force Microscopy of DNA. *Biophysical Journal.* **68**, 1672-1677.
- Hansma, H. G. and Pietrasanta, L. (1998) Atomic Force Microscopy and Other Scanning Probe Microscopies. *Current Opinion in Chemical Biology.* **2**, 579-584.
- Hansma, H. G., Sinsheimer, R. L., Li, M. Q. and Hansma, P. K. (1992a) Atomic Force Microscopy of Single-Stranded and Double-Stranded DNA. *Nucleic Acids Research.* **20**, 3585-3590.
- Hansma, H. G., Sinsheimer, R. L., Li, M. Q. and Hansma, P. K. (1992a) Atomic Force Microscopy of Single-Stranded and Double-Stranded DNA. *Nucleic Acids Research.* **20**, 3585-3590.
-

Bibliography

- Hansma, H. G., Vesenka, J., Siegerist, C., Kelderman, G., Morrett, H., Sinsheimer, R. L., Elings, V., Bustamante, C. and Hansma, P. K. (1992b) Reproducible Imaging and Dissection of Plasmid DNA under Liquid with the Atomic Force Microscope. *Science*. **256**, 1180-1184.
- Hansma, H. G., Vesenka, J., Siegerist, C., Kelderman, G., Morrett, H. and Sinsheimer, R. L., Et Al. (1992b) Reproducible Imaging and Dissection of Plasmid DNA under Liquid with the Atomic Force Microscope. *Science*. **256**, 1180-1184.
- Hansma, P. K., Cleveland, J. P., Radmacher, M., Walters, D. A., Hillner, P. E., Bezanilla, M., Fritz, M., Vie, D., Hansma, H. G., Prater, C. B., Massie, J., Fukunaga, L., Gurley, J. and Elings, V. (1994) Tapping Mode Atomic-Force Microscopy in Liquids. *Applied Physics Letters*. **64**, 1738-1740.
- Hansma, P. K., Elings, V. B., Marti, O. and Bracker, C. E. (1988) Scanning Tunneling Microscopy and Atomic Force Microscopy: Application to Biology and Technology. *Science*. **242**, 209 -216.
- Hartmann, U. (1991) Van Der Waals Interactions between Sharp Probes and Flat Sample Surfaces. *Physical Review B*. **43**, 2404 -2407.
- Hawker, C. J. and Frechet, J. M. (1990a) Control of Surface Functionality in the Synthesis of Dendritic Macromolecules Using the Convergent-Growth Approach. *Macromolecules*. **23**, 4726-4729.
- Hawker, C. J. and Frechet, J. M. (1990b) Preparation of Polymers with Controlled Molecular Architecture. A New Convergent Approach to Dendritic Macromolecules. *Journal of the American Chemical Society*. **112**, 7638-7647.
- He, S. Q., Arscott, P. G. and Bloomfield, V. A. (2000) Condensation of DNA by Multivalent Cations: Experiment Studies of Condensation Kinetics. *Biopolymers*. **53**, 329-341.
- Hegner, M., Wagner, P. and Semenza, G. (1993) Ultralarge Atomically Flat Template-Stripped Au Surfaces for Scanning Probe Microscopy. *Surface Science*. **291**, 39-46.
- Heinz, W. F. and Hoh, J. H. (1999) Spatially Resolved Force Spectroscopy of Biological Surfaces Using the Atomic Force Microscope. *Trends in Biotechnology*. **17**, 143-150.
- Henderson, E., Haydon, P. G. and Sakaguchi, D. A. (1992) Actin Filaments Dynamics in Living Glial Cells Imaged by Atomic Force Microscopy. *Science*. **257**, 1944-1946.
-

Bibliography

- Henderson, R. M. and Oberleithner, H. (2000) Pushing, Pulling, Dragging, and Vibrating Renal Epithelia by Using Atomic Force Microscopy. *American Journal of Physiology: Renal Physiology*. **278**, F689-F701.
- Henderson, R. M., Schneider, S., Li, Q., Hornby, D., White, S. J. and Oberleithner, H. (1996) Imaging Romk1 Inwardly Rectifying Atp-Sensitive K1 Channelprotein Using Atomic Force Microscopy. *Proceedings of the National Academy of Science. USA*. **93**, 8756-8760.
- Hierlemann, A., Cambell, J. K., Baker, L. A., Crooks, R. M. and Ricco, A. J. (1998) Structural Distortion of Dendrimers on Gold Surfaces: A Tapping-Mode Afm Investigation. *Journal of the American Chemical Society*. **120**, 5323-5324.
- Hill, I. R. C., Garnett, M. C., Bignotti, F. and Davis, S. S. (1999) In Vitro Cytotoxicity of Poly(Amidoamine)S: Relevance to DNA Delivery. *Biochimica Et Biophysica Acta-General Subjects*. **1427**, 161-174.
- Hill, I. R. C., Garnett, M. C., Bignotti, F. and Davis, S. S. (2001) Determination of Protection from Serum Nuclease Activity by DNA-Polyelectrolyte Complexes Using an Electrophoretic Method. *Analytical Biochemistry*. **291**, 62-68.
- Hoh, J., Lal, R., John, S. A., Revel, J.-P. and Arnsdorf, M. F. (1991) Atomic Force Microscopy and Dissection of Gap Junctions. *Science*. **253**, 1405-1408.
- Horber, J. K. H., Haberle, W., Ohnesorge, F., Binnig, G., Liebich, H. G. and Czerny, C. P. (1993) In *Stm and Sfm in Biology*(Ed, Amrein, O. M. a. M.) Academic Press, San Diego.
- Howland, R. and Benatar, L. (1996) In *Park Scientific Instruments*.
- Hud, N. V., Downing, K. H. and Balhorn, R. (1995) A Constant Radius of Curvature Model for the Organization of DNA in Toroidal Condensates. *Proceedings of the National Academy of Sciences. USA*. **92**, 3581-3585.
- Hui, K. M., Ang, P. T., Huang, L. and Tay, S. K. (1997) Phase I Study of Immunotherapy of Cutaneous Metastases of Human Carcinoma Using Allogeneic and Xenogeneic Mhc DNA-Liposome Complexes. *Gene Therapy*. **4**, 783-790.
- Hutter, J. L. and Bechhoefer, J. (1993) Calibration of Atomic-Force Microscope Tips. *Reviews of Scientific Instruments*. **64**, 1868-1873.
- Ikai, A. (1996) Stm and Afm of Bio/Organic Molecules and Structures. *Surface sciences Reports*. **26**, 261 - 332.
-

Bibliography

- Israelachvili, J. N. (1991) *Intermolecular and Surface Forces*, Academic Press, London.
- Jiao, Y. K., Cherny, D. I., Heim, G., Jovin, T. M. and Schaffer, T. E. (2001) Dynamic Interactions of P53 with DNA in Solution by Time-Lapse Atomic Force Microscopy. *Journal of Molecular Biology*. **314**, 233-243.
- Kabanov, A. V. and Kabanov, V. A. (1995) DNA Complexes with Polycations for the Delivery of Genetic Material into Cells. *Bioconjugate Chemistry*. **6**, 7-20.
- Kabanov, A. V., Szoka, F. and Seymour, L. W. (1998) Interpolyelectrolyte Complexes for Gene Delivery: Polymer Aspects of Transfection Activity. In *Self-Assembling Complexes for Gene Delivery. From Laboratory to Clinical Trial*. Kabanov, A.V., Seymour, L.W., and Felgner, P.L. (eds.) New York: John Wiley., pp. 197-218.
- Karbach, A. and Drechsler, D. (1999) Atomic Force Microscopy-a Powerful Tool for Industrial Applications. *Surface and Interface Analysis*. **27**, 401-409.
- Kasas, S., Thomson, N. H., Smith, B. L., Hansma, P. K., Miklossy, J. and Hansma, H. G. (1997) Biological Applications of the Afm: From Single Molecules to Organs. *International Journal of Imaging Systems and Technology*. **8**, 151-161.
- Kawabata, K., Takakura, Y. and Hashida, M. (1995) The Fate of Plasmid DNA after Intravenous Injection in Mice: Involvement of Scavenger Receptors in Its Hepatic Uptake. *Pharmaceutical Research*. **12**, 825-830.
- Kitson, C. and Alton, E. (2000) Gene Therapy for Cystic Fibrosis. *Expert Opinion on Investigational Drugs*. **9**, 1523-1535.
- Kukowska-Latallo, J. F., Bielinska, A. U., Johnson, J., Spindler, R., Tomalia, D. A. and Baker, J. R. (1996) Efficient Transfer of Genetic Material into Mammalian Cells Using Starburst Polyamidoamine Dendrimers. *Proceedings of the National Academy of Science. USA*. **93**, 4897-4902.
- Kunitz, M. (1950) Crystalline Desoxyribonuclease: Isolation and General Properties - Spectrophotometric Method for the Measurement of Desoxyribonuclease Activity. *The Journal of General Physiology*. **33**, 349-362.
- Kuriyama, S., Mitoro, A., Tsujinoue, H., Nakatani, T., Yoshiji, H. and Tsujimoto, T. (2000) Particle-Mediated Gene Transfer into Murine Livers Using a Newly Developed Gene Gun. *Gene Therapy*. **7**, 1132-1136.

Bibliography

- Lackowski, W. M., Campbell, J. K., Edwards, G., Chechik, V. and Crooks, R. M. (1999) Time Dependent Phase-Segregation of Dendrimer/N-Alkylthiol Mixed-Monolayers on Au(111): An Atomic Force Microscopy Study. *Langmuir*. **15**, 7632-7638.
- Lahm, A. and Suck, D. J. (1991) Dnase I-Induced DNA Conformation 2 ? Structure of a Dnase I-Octamer Complex. *Molecular Biology*. **221**, 645-667.
- Lal, R., Kim, H., Garavito, R. M. and Arnsdorf, M. F. (1993) Imaging of Reconstituted Biological Channels at Molecular Resolution by Atomic Force Microscopy. *American Journal of Physiology. Cell Physiology*. **265**, C851-C856.
- Larmer, J., Schneider, S. W., Danker, T., Schwab, A. and Oberleithner, H. (1997) Imaging Excised Apical Plasma Membrane Patches of Mdkc Cells in Physiological Conditions with Atomic Force Microscopy. *Pfluger's archiv*. **434**, 254-260.
- Lazarides, E. and Lindberg, U. (1974) Actin Is the Naturally Occurring Inhibitor of Deoxyribonuclease I. *Proceedings of the National Academy of Science. USA*. **71**, 4742-4746.
- Le Grimellec, C., Lesniewska, E., Cachia, C., Schreiber, J. P., De Fornel, F. and Goudonnet, J. P. (1994) Imaging of the Membrane Surface of Mdkc Cells by Atomic Force Microscopy. *Biophysical Journal*. **67**, 36-41.
- Ledley, F. D. (1995) Nonviral Gene-Therapy - the Promise of Genes as Pharmaceutical Products. *Human Gene Therapy*. **6**, 1129-1144.
- Lee, G. U., Chrisey, L. A. and Colton, R. J. (1994) Direct Measurement of the Forces between Complementary Strands of DNA. *Science*. **266**, 771-773.
- Lehn, P., Fabrega, S., Oudrhiri, N. and Navarro, J. (1998) Gene Delivery Systems: Bridging the Gap between Recombinant Viruses and Artificial Vectors. *Advanced Drug Delivery Reviews*. **30**, 5-11.
- Lemoine, P. and McLaughlin, J. A. (1999) Nanomechanical Measurements on Polymers Using Contact Mode Atomic Force Microscopy. *Thin Solid Films*. **339**, 258-264.
- Li, J., Piehler, T., Qin, D., Baker, J. R. and Tomalia, D. A. (2000) Visualization and Characterization of Poly(Amidoamine) Dendrimers by Atomic Force Microscopy. *Langmuir*. **13**, A-D.
- Li, J., Swanson, R., Qin, D., Brothers, H. M., Piehler, L. T., Tomalia, D. A. and Meier, D. J. (1999) Characterizations of Core-Shell Tecto-(Dendrimer)
-

Bibliography

- Molecules by Tapping Mode Atomic Force Microscopy. *Langmuir*. **15**, 7347 - 7350.
- Lin, C., Wu, K., Sa, R., Mang, C., Liu, P. and Zhuang, B. (2002) Density Functional Theory Studies on the Potential Energy Surface and Hyperpolarizability of Polyamidoamide Dendrimer. *Chemical Physics Letters*. **363**, 343-348.
- Lin, Z., Wang, C., Feng, X. Z., Liu, M. Z., Li, J. W. and Bai, C. L. (1998) The Observation of the Local Ordering Characteristics of Spermidine-Condensed DNA: Atomic Force Microscopy and Polarizing Microscopy Studies. *Nucleic Acids Research*. **26**, 3228-3234.
- Lindberg, M. and Skoog, L. (1970) Purification from Calf Thymus of an Inhibitor of Deoxyribonuclease I. *European Journal of Biochemistry*. **13**, 326-335.
- Lindsay, S. M., Tao, N. J., Derose, J. A., Oden, P. I., Lyubchenko, Y. L., Harrington, R. E. and Shlyakhtenko, L. (1992) Potentiostatic Deposition of DNA for Scanning Probe Microscopy. *Biophysical Journal*. **61**, 1570-1584.
- Lio, A., Charych, D. H. and Salmeron, M. (1997) Comparative Atomic Force Microscopy Study of the Chain Length Dependence of Frictional Properties of Alkanethiols on Gold and Alkylsilanes on Mica. *The Journal of Physical Chemistry*. **101**, 3800 - 3805.
- Liu, D., Wang, C., Lin, Z., Li, J., Xu, B., Wei, Z., Wang, Z. G. and Bai, C. L. (2001a) Visualization of the Intermediates in a Uniform DNA Condensation System by Tapping Mode Atomic Force Microscopy. *Surface and Interface Analysis*. **32**, 15-19.
- Liu, G. Y. and Salmeron, M. B. (1994) Reversible Displacement of Chemisorbed N-Alkanethiol Molecules on Au (111) Surface: An Atomic Force Microscopy Study. *Langmuir*. **10**, 360-370.
- Liu, W. G., Yao, K. D. and Liu, Q. G. (2001b) Formation of a DNA/ N-Dodecylated Chitosan Complex and Salt-Induced Gene Delivery. *Journal of Applied Polymer Science*. **82**, 3391-3395.
- Livolant, F., Levelut, A. M., Doucet, J. and Benoit, J. P. (1989) The Highly Concentrated Liquid-Crystalline Phase of DNA Is Columnar Hexagonal. *Nature*. **339**, 724-726.
- Ludwig, M., Rief, M., Schmidt, L., Li, H., Oesterhelt, F., Gautel, M. and Gaub, H. E. (1999) Afm, a Tool for Single-Molecule Experiments. *Applied Physics a-Materials Science & Processing*. **68**, 173-176.
-

Bibliography

- Lyubartsev, A. P. and Nordenskiold, L. (1995) A Monte Carlo Simulation Study of Ion Distribution and Osmotic Pressure in Hexagonally Oriented DNA. *Journal of Physical Chemistry*. **99**, 10373-10782.
- Lyubchenko, Y. L., Gall, A. A., Shlyakhtenko, L. S., Harrington, R. E., Jacobs, B. L., Oden, P. I. and Lindsay, S. M. (1992) Atomic Force Microscopy Imaging of Double-Stranded DNA and Rna. *Journal of Biomolecular Structure & Dynamics*. **10**, 589-606.
- Lyubchenko, Y. L., Shlyakhtenko, L. S., Harrington, R. E., Oden, P. I. and Lindsay, S. M. (1993) Atomic Force Microscopy of Long DNA: Imaging in Air and under Water. *Proceedings of the National Academy of Sciences, USA*. **90**, 2137-2140.
- Mahato, R. I. and Kim, S. W. (2002) In *Pharmaceutical Perspectives of Nucleic Acid-Based Therapeutics*. Francis and Taylor, London, pp. 178-179.
- Malik, N., Evagorou, E. G. and Duncan, R. (1999) Dendrimer-Platinate: A Novel Approach to Cancer Chemotherapy. *Anti-Cancer Drugs*. **10**, 767-776.
- Malik, N., Wiwattanapatapee, R., Klopsch, R., Lorenz, K., Frey, H., Weener, J. W., Meijer, E. W., Paulus, W. and Duncan, R. (2000) Dendrimers: Relationship between Structure and Biocompatibility in Vitro, and Preliminary Studies on the Biodistribution of ¹²⁵I-Labelled Polyamidoamine Dendrimers in Vivo. *Journal of Controlled Release*. **65**, 133-148.
- Manning, R. J. (1994) Attractive Force between Two Rodlike Polylons Mediated by the Sharing of Condensed Counterions. *Langmuir*. **10**, 2450-2461.
- Mansfield, M. L. (1996) Surface Adsorption of Model Dendrimers. *Polymer*. **37**, 3835-3841.
- Margison, G. and O'connor, P. (1972) Resistance of Alkylated Deoxyribonucleic Acid to Nuclease Attack. *Biochemical Journal*. **128**, 138P.
- Marquet, R. and Houssier, C. (1991) Thermodynamics of Cation-Induced DNA Condensation. *Journal of Biomolecular Structure and Dynamics*. **9**, 159-167.
- Marshall, E. (1999) Clinical Trials - Gene Therapy Death Prompts Review of Adenovirus Vector. *Science*. **286**, 2244-2245.
- Marshall, E. (2000) Biomedicine - Gene Therapy on Trial. *Science*. **288**, 951.
-

Bibliography

- Marth, M., Maier, D., Honerkamp, J., Brandsch, R. and Bar, G. (1999) A Unifying View on Some Experimental Effects in Tapping-Mode Atomic Force Microscopy. *Journal of Applied Physics*. **85**, 7030 - 7036.
- Martin, A. L., Davies, M. C., Rackstraw, B. J., Roberts, C. J., Stolnik, S., Tendler, S. J. B. and Williams, P. M. (2000) Observation of DNA-Polymer Condensate Formation in Real Time at a Molecular Level. *Federation of European Biochemical Societies Letters*. **480**, 106-112.
- Martin, Y., Williams, C. C. and Wickramasinghe, H. K. (1987) Atomic Force Microscope-Force Mapping and Profiling on a Sub 100-? Scale. *Journal of Applied Physics*. **61**, 4723-4729.
- Marx, K. A. and Reynolds, T. C. (1982) Spermidine-Condensed Fx174 DNA Cleavage by Micrococcal Nuclease: Torus Cleavage Model and Evidence for Unidirectional Circumferential DNA Wrapping. *Proceedings of the National Academy of Science. USA*. **79**, 6484-6488.
- Marx, K. A. and Ruben, G. C. (1983) Evidence for Hydrated Spermidine Calf Thymus DNA Toruses Organized by Circumferential DNA Wrapping. *Nucleic Acids Research*. **11**, 1839-1854.
- Marx, K. A. and Ruben, G. C. (1986) A Study of Phi-X-174 DNA Torus and Lambda-DNA Torus Tertiary Structure and the Implications for DNA Self-Assembly. *Journal of Biomolecular Structure & Dynamics*. **4**, 23-29.
- Mashl, R. J. and Gronbech-Jensen, N. (1998) Effective Interactions between Rigid Polyelectrolytes and Like-Charged Planar Surfaces. *Journal of Chemical Physics*. **109**, 4617.
- Mathews, C. K. and Van Holde, K. E. (1996) *Biochemistry*, The Benjamin/Cummings publishing company, INC, California.
- Matulis, D., Rouzina, I. and Bloomfield, V. A. (2000) Thermodynamics of DNA Binding and Condensation: Isothermal Titration Calorimetry and Electrostatic Mechanism. *Journal of Molecular Biology*. **296**, 1053-1063.
- Meikle, J. (2002) In *The Guardian London*.
- Messina, R., Holm, C. and Kremer, K. (2000) Strong Attraction between Charged Spheres Due to Metastable Ionized States. *Physical Review Letters*. **85**, 872-875.
- Miller, R., Vesenska, J. and Henderson, E. (1995) Tip Reconstruction for the Atomic Force Microscope. *SIAM Journal on Applied Mathematics*. **55**, 1362 -1371.
-

Bibliography

- Mirsky, A. and Silverman, B. (1972) Blocking by Histones of Accessibility to DNA in Chromatin. *Proceedings of the National Academy of Science. USA.* **69**, 2115.
- Montigny, W. J., Houchens, C. R., Illenye, S., Gilbert, J., Coonrod, E., Chang, Y. C. and Heintz, N. H. (2001) Condensation by DNA Looping Facilitates Transfer of Large DNA Molecules into Mammalian Cells. *Nucleic Acids Research.* **29**, 1982-1988.
- Morris, V. J., Kirby, A. R. and Gunning, A. P. (1999) *Atomic Force Microscopy for Biologists.* London: Icp.
- Moy, V. T., Florin, E. L. and Gaub, H. E. (1994) Adhesive Forces between Ligand and Receptor Measured by Afm. *Colloids and Surfaces a-Physicochemical and Engineering Aspects.* **93**, 343-348.
- Müller, T., Yablon, D. G., Karchner, R., Knapp, D., Kleinman, M. H., Fang, H., Durning, C. J., Tomalia, D. A., Turro, N. J. and Flynn, G. W. (2002) Afm Studies of High-Generation Pamam Dendrimers at the Liquid/Solid Interface. *Langmuir.* **18**, 7452-7455.
- Mumper, R. J. and Rolland, A. J. (1998) Plasmid Delivery to Muscle: Recent Advances in Polymer Delivery Systems. *Advanced Drug Delivery Reviews.* **30**, 151-172.
- Murphy, J. E., Uno, T., Hamer, J. D., Cohen, F. E., Dwarki, V. and Zuckermann, R. N. (1998) A Combinatorial Approach to the Discovery of Efficient Cationic Peptoid Reagents for Gene Delivery. *Proceedings of the National Academy of Science. USA.* **95**, 1517-1522.
- Naylor, A. M., Goddard Iii, W. A., Kiefer, G. E. and Tomalia, D. A. (1989) Starburst Dendrimers 5: Molecular Shape Control. *Journal of the American Chemical Society.* **111**, 2339-2341.
- Neidle, S. (1999) *Oxford Handbook of Nucleic Acid Structure.* Oxford, Uk: Oxford University Press.
- Neish, C. S., Martin, I. L., Henderson, R. M. and Edwardson, J. M. (2002) Direct Visualization of Ligand-Protein Interactions Using Atomic Force Microscopy. *British Journal of Pharmacology.* **135**, 1943-1950.
- Newkome, G. R., Yao, Z., Baker, G. R. and Gupta, V. K. (1985) Cascade Molecules: A New Approach to Micelles. A [27]-Arborol. *Journal of Organic Chemistry.* **50**, 2003-2004.
- Nguyen, T. T. and Shklovskii, B. I. (2002) Inversion of DNA Charge by a Positive Polymer Via Fractionalization of the Polymer Charge. *Physica A.* **310**, 197-211.
-

Bibliography

- Noguchi, H., Saito, S., Kidoaki, S. and Yoshikawa, K. (1996) Self-Organized Nanostructures Constructed with a Single Polymer Chain. *Chemical Physics Letters*. **261**, 527-533.
- Noy, A., Sanders, C. H., Vezenov, D. V., Wong, S. and Lieber, C. M. (1998) Chemically-Sensitive Imaging in Tapping Mode by Chemical Force Microscopy: Relationship between Phase Lag and Adhesion. *Langmuir*. **14**, 1508 - 1511.
- Nyquist, R. M., Ha, B.-Y. and Liu, A. J. (1999) Counterion Condensation in Solutions of Rigid Polyelectrolytes. *Macromolecules*. **32**, 3481-3487.
- Ono, M. Y. and Spain, E. M. (1999) Dynamics of DNA Condensates at the Solid-Liquid Interface by Atomic Force Microscopy. *Journal of the American Chemical Society*. **121**, 7330-7334.
- Oosawa, F. (1971) *Polyelectrolytes*., Marcel Dekker, New York.
- Osman M.A, S. U. W. (2000) Determination of the Cation-Exchange Capacity of Muscovite Mica. *Journal of Colloid and Interface Science*. **224**, 112-115.
- Ottaviani, M. F., Matteini, P., M., B., Turro, N. J., Jockusch, S. and Tomalia, D. A. (1998) Characterization of Starburst Dendrimers and Vesicle Solutions and Their Interactions by Cw- and Pulsed-Epr, Tem, and Dynamic Light Scattering. *The Journal of Physical Chemistry. B*. **102**, 6029-6039.
- Pan, C. Q., Ulmer, J. S., Herzka, A. and Lazarus, R. A. (1998) Mutational Analysis of Human Dnase I at the DNA Binding Interface: Implications for DNA Recognition, Catalysis, and Metal Ion Dependence. *Protein Science*. **7**, 628-636.
- Pan, Q. C. and Lazarus, R. A. (1999) Ca²⁺-Dependent Activity of Human Dnase I and Its Hyperactive Variants. *Protein Science*. **8**, 1780-1788.
- Pashley, R. H. (1982) Hydration Forces between Mica Surfaces in Electrolyte Solutions. *Advances in Colloid and Interface Science*. **16**, 57-62.
- Paul, T., Young, M. J., Hill, I. E. and Ingold, K. U. (2000) Strand Cleavage of Supercoiled DNA by Water-Soluble Peroxyl Radicals. The Overlooked Importance of Peroxyl Radical Charge. *Biochemistry*. **39**, 4129-4135.
- Peppas, N. A. (1995) Star Polymers and Dendrimers: Prospects of Their Use in Drug Delivery and Pharmaceutical Applications. *Controlled Release Society Newsletters*. **12**, 12-13.
- Piner, R. D., Ong, S. H. and Mirkin, C. A. (1999) Improved Imaging of Soft Materials with Modified Afm Tips. *Langmuir*. **15**, 5457-5460.
-

Bibliography

- Plum, G. E., Arscott, P. G. and Bloomfield, V. A. (1990) Condensation of DNA by Trivalent Cations .2. Effects of Cation Structure. *Biopolymers*. **30**, 631-643.
- Poirier, G. E. (1997) Mechanism of Formation of Au Vacancy Islands in Alkanethiol Monolayers on Au (111). *Langmuir*. **13**, 2019-2026.
- Pope, L. H., Davies, M. C., Laughton, C. A., Roberts, C. J., Tendler, S. J. B. and Williams, P. M. (1999) Intercalation-Induced Changes in DNA Supercoiling Observed in Real-Time by Atomic Force Microscopy. *Analytica chimica acta*. **400**, 27-32.
- Pope, L. H., Davies, M. C., Laughton, C. A., Roberts, C. J., Tendler, S. J. B. and Williams, P. M. (2000) Atomic Force Microscopy Studies of Intercalation-Induced Changes in Plasmid DNA Tertiary Structure. *Journal of Microscopy-Oxford*. **199**, 68-78.
- Potemkin, I. I., Limberger, R. E., Kudlay, A. N. and Khokhlov, A. R. (2002) Rodlike Polyelectrolyte Solutions: Effect of the Many-Body Coulomb Attraction of Similarly Charged Molecules Favoring Weak Nematic Ordering at Very Small Polymer Concentration. *Physical Review E*. **66**, 011802-011812.
- Pouton, C. W. (1998) Nuclear Import of Polypeptides, Polynucleotides and Supramolecular Complexes. *Advanced Drug Delivery Review*. **34**, 51-64.
- Pralle, A., Florin, E.-L., Stelzer, E. H. K. and Hrber, J. K. H. (2000) Photonic Force Microscopy: A New Tool Providing New Methods to Study Membranes at the Molecular Level. *Single Molecules*. **2**, 129-133.
- Putman, C. A. J., Van Der Werf K, O., De Grooth, B. G., Van Hulst, N. F. and Greve, J. (1994) Tapping Mode Atomic Force Microscopy in Liquids. *Applied Physics Letters*. **64**, 2454-2456.
- Raab, A., Han, W. H., Badt, D., Smithgill, S. J., Lindsay, S. M., Schindler, H. and Hinterdorfer, P. (1999) Antibody Recognition Imaging by Force Microscopy. *Nature Biotechnology*. **17**, 902-905.
- Rackstraw, B. J., Martin, A. L., Stolnik, S., Roberts, C. J., Garnett, M. C., Davies, M. C. and Tendler, S. J. B. (2001) Microscopic Investigations into Peg-Cationic Polymer-Induced DNA Condensation. *Langmuir*. **17**, 3185-3193.
- Radmacher, M., Cleveland, J. P., Fritz, M., Hansma, H. G. and Hansma, P. K. (1994) Mapping Interaction Forces with the Atomic Force Microscope. *Biophysical Journal*. **66**, 2159-2165.
-

Bibliography

- Rahman, K. M. A., Durning, C. J., Turro, N. J. and Tomalia, D. A. (2000) Adsorption of Poly(Amidoamine) Dendrimers on Gold. *Langmuir*. **16**, 10154-10160.
- Ramirez-Aguilar, K. A. and Rowlen, K. L. (1998) Tip Characterization from Afm Images of Nanometric Spherical Particles. *Langmuir*. **14**, 2562-2566.
- Ranucci, E., Spagnoli, G., Ferruti, P., Sgouras, D. and Duncan, R. (1991) Poly(Amidoamine)S with Potential as Drug Carriers: Degradation and Cellular Toxicity. *Journal of Biomaterials Science. Polymer*. **Ed 2**, 313-315.
- Rau, D. C. and Parsegian, V. A. (1992) Direct Measurement of the Intermolecular Forces between Counterion-Condensed DNA Double Helices. Evidence for Long Range Attractive Hydration Forces. *Biophysical Journal*. **61**, 246-259.
- Reich, Z., Kapon, R., Nevo, R., Pilpel, Y., Zmora, S. and Scolnik, Y. (2001) Scanning Force Microscopy in the Applied Biological Sciences. *Biotechnology Advances*. **19**, 451-485.
- Richardson, S., Ferruti, P. and Duncan, R. (1999) Poly(Amidoamine)S as Potential Endosomolytic Polymers: Evaluation in Vitro and Body Distribution in Normal and Tumour- Bearing Animals. *Journal of Drug Targeting*. **6**, 391-404.
- Rivetti, C. and Codeluppi, S. (2001) Accurate Length Determination of DNA Molecules Visualized by Atomic Force Microscopy: Evidence for a Partial B- to a-Form Transition on Mica. *Ultramicroscopy*. **87**, 55-66.
- Robbins, P. D. and Ghivizzani, S. C. (1998) Viral Vectors for Gene Therapy. *Pharmacology & Therapeutics*. **80**, 35-47.
- Rouzina, I. and Bloomfield, V. A. (1998) DNA Bending by Small, Mobile Multivalent Cations. *Biophysical Journal*. **74**, 3152-3164.
- Rudolph, C., Lausier, J., Naundorf, S., Muller, R. H. and Rosenecker, J. (2000) In Vivo Gene Delivery to the Lung Using Polyethylenimine and Fractured Polyamidoamine Dendrimers. *The Journal of Gene Medicine*. **2**, 269-278.
- Sadoc, J. F. (2000) Toroidal DNA: Topology, Geometry and Electrostatics. *International Journal of Modern Physics B*. **14**, 737-749.
- Scheuring, S., Stahlberg, H., Chami, M., Houssin, C., Rigaud, J. L. and Engel, A. (2002) Charting and Unzipping the Surface Layer of *Corynebacterium Glutamicum* with the Atomic Force Microscope. *Molecular Microbiology*. **44**, 675-684.
-

Bibliography

- Schneider, S. W., Larmer, J., Henderson, R. M. and Oberleithner, H. (1998) Molecular Weights of Individual Proteins Correlate with Molecular Volumes Measured by Atomic Force Microscopy. *Pfluger's archiv.* **435**, 362-367.
- Schoenenberger, C., Sondag-Huethorst, J. A. M., Jorritsma, J. and Fokkink, L. G. J. (1994) What Are the "Holes" in Self-Assembled Monolayers of Alkanethiols on Gold? *Langmuir.* **10**, 611-614.
- Sens, P. and Joanny, J. (2000) Counterion Release and Electrostatic Adsorption. *Physical Review Letters.* **84**.
- Shakesheff, K. M., Davies, M. C., Roberts, C. J., Tendler, S. J. B. and Williams, P. M. (1996) The Role of Scanning Probe Microscopy in Drug Delivery Research. *Critical Reviews in Therapeutic Drug Carrier Systems.* **13**, 185-223.
- Shao, Z., Mou, J., Czajkowsky, D. M., Yang, J. and Yuan, J. Y. (1996) Biological Atomic Force Microscopy: What Is Achieved and What Is Needed. *Advances in Physics.* **45**, 1-86.
- Shao, Z. and Yang, J. (1995) Progress in High Resolution Atomic Force Microscopy in Biology. *Quarterly Reviews of Biophysics.* **28**, 195-251.
- Sheiko, S. S., Eckert, G., Ignateva, G., Muzafarov, A. M., Pickermann, J., Rader, H. J. and Moller, M. (1996) Solid-Like States of Dendrimer Liquid Displayed by Scanning Force Microscopy. *Macromolecular Rapid Communications.* **17**, 283-297.
- Shen, M. R., Downing, K. H., Balhorn, R. and Hud, N. V. (2000) Nucleation of DNA Condensation by Static Loops: Formation of DNA Toroids with Reduced Dimensions. *Journal of the American Chemical Society.* **122**, 4833-4834.
- Sigel, H. (1989) In *Metal-DNA Chemistry*, Vol. 402 (Ed, Tullius, T. D.) The American Chemical Society, Washington, D.C.; ACS Symp., pp. 159-204.
- Smith, D. A., Connell, S. D., Robinson, C. and Kirkham, J. (2003) Chemical Force Microscopy: Applications in Surface Characterisation of Natural Hydroxyapatite. *Analytica Chimica Acta.* **479**, 39-57.
- Smith, D. A., Wallwork, M. L., Zhang, J., Kirkham, J., Robinson, C., Wong, M. and Marsh, A. (2000) The Effect of Ionic Strength on the Chemical Force Titration Behaviour of W-Functionalised Sams : Evidence for the Formation of Strong Ionic Hydrogen Bonds. *Journal of physical Chemistry b.* **104**, 8862-8870.
-

Bibliography

- Smith, S. B., Finzi, L. and Bustamante, C. (1992) Direct Mechanical Measurements of the Elasticity of Single DNA Molecules by Using Magnetic Beads. *Science*. **258**, 1122-1126.
- Sokolov, I. Y. (1996) On the Recovery of the Spectroscopic Image in Atomic Force Microscopy. *Journal of Vacuum Science & Technology. A*. **14**, 2901-2904.
- Stamou, D., Gourdon, D., Liley, M., Burnham, N. A., Kulik, A., Vogel, H. and Duschl, C. (1997) Uniformly Flat Gold Surfaces: Imaging the Domain Structure of Organic Monolayers Using Scanning Force Microscopy. *Langmuir*. **13**, 25-24.
- Stevens, M. J. (2001) Simple Simulations of DNA Condensation. *Biophysical Journal*. **80**, 130-139.
- Stryer, L. (1988) *Biochemistry*. New York: Freeman.
- Suck, D. (1997) DNA Recognition by Structure-Selective Nucleases. *Biopolymers*. **44**, 405-421.
- Suck, D. and Ofner, C. (1986) Structure of Dnase I at 2.0 Å Resolution Suggests a Mechanism for Binding to and Cutting DNA. *Nature*,. **321**, 620-625.
- Sun, L., Crooks, R. M. and Ricco, A. J. (1993) Molecular Interactions between Organized, Surface-Confined Monolayers and Vapor-Phase Probe Molecules. 5. Acid-Base Interactions. *Langmuir*. **9**, 1775-1780.
- Tabor, C. W. and Tabor, H. (1984) Polyamines. *Annual Review of Biochemistry*. **53**, 749-790.
- Tamada, K., Hara, M., Sasabe, H. and Knoll, W. (1997) Surface Phase Behaviour of N-Alkanethiol Self-Assembled Monolayers Adsorbed on Au (111): Atomic Force Microscope Study. *Langmuir*. **13**, 1558 -1566.
- Tamayo, J. and Garcia, R. (1997) Effects of Elastic and Inelastic Interactions on Phase Contrast Images in Tapping-Mode Scanning Force Microscopy. *Applied Physics Letters*. **71**, 2394 -2396.
- Tang, M. X., Redemann, C. T. and Szoka, F. C. (1996) In Vitro Gene Delivery by Degraded Polyamidoamine Dendrimers. *Bioconjugate Chemistry*. **7**, 703-714.
- Templeton, N. S. and Lasic, D. D. (2000) Gene Therapy Therapeutic Mechanisms and Strategies. Marcel Dekker Inc., pp.1-16.
- Terashima, H. (2002) A Direct Measurement of the Ion-Exchange Capacity of Muscovite Mica Using a Mettler Ultramicrobalance. *Journal of Colloid and Interface Science*. **245**, 81-85.
-

Bibliography

- Thompson, L. (1993) The First Kids with New Genes. In *Time*. pp. 50-53.
- Thundat, T., Allison, D. P., Warmack, R. J., Brown, G. M., Jacobson, K. B., Schrick, J. J. and Ferrell, T. L. (1992) Atomic Force Microscopy of DNA on Mica and Chemically Modified Mica. *Scanning Microscopy*. **6**, 911-918.
- Thundat, T., Allison, D. P., Warmack, R. J., Doktycz, M. J., Jacobson, K. B. and Brown, G. M. (1993) Atomic Force Microscopy of Single-Stranded and Double-Stranded Deoxyribonucleic Acid. *Journal of Vacuum Science & Technology a-Vacuum Surfaces and Films*. **11**, 824-828.
- Tokuhisa, H., Zhao, M., Baker, L. A., Phan, V. T., Dermody, D. L., Garcia, M. E., Peez, R. F., R.M., C. and D.E., B. (1998) Preparation and Characterization of Dendrimer Monolayers and Dendrimer-Alkylthiol Mixed Monolayers Adsorbed to Gold. *Journal of the American Chemical Society*. **120**, 4492-4501.
- Tomalia, D. A. (1993) Starburst Tm/Cascade Dendrimers: Fundamentalbuilding Blocks for a New Nanoscopic Chemistry Set. *Aldrichim.Acta*. **26**, 91-101.
- Tomalia, D. A., Baker, H., Dewald, J., Hall, M., Kallos, G., Mar-Tin, S., Roeck, J., Ryder, J. and P., S. (1986) Dendritic Macromolecules:Synthesis of Starburst Dendrimers. *Macromolecules*. **19**, 2466-2468.
- Tomalia, D. A., Baker, H., Dewald, J., Hall, M., Kallos, G., Martin, S., Roeck, J., Ryder, J. and Smith, P. (1985) A New Class of Polymers: Starburst-Dendritic Macromolecules. *Polymer Journal*. **17**, 117-132.
- Tomalia, D. A., Esfand, R., Mardel, K., Henderson, S. A. and Holan, G. (2002) In *Handbook of Nanoscience, Engineering and Technology*, Vol. Chapter 20 (Ed, W.A. Goddard III, D. W. B., S.E. Lyshevski, G.J. Irafrate,) CRC Press, Boca Raton, pp. 1-20.
- Tomalia, D. A. and Fréchet, J. M. J. (2001) *Dendrimers and Other Dendritic Polymers*, J. Wiley & Sons Ltd., West Sussex.
- Tsukruk, V. V. (1998) Dendritic Macromolecules at Interfaces. *Advanced Materials*. **10**, 253-257.
- Tsukruk, V. V., Rinderspacher, F. and Bliznyuk, V. N. (1997) Self-Assembled Multilayer Films from Dendrimers. *Langmuire*. **13**, 2171-2176.
- Tully, D. C. and Fréchet, J. M. J. (2001) Dendrimers at Surfaces and Interfaces: Chemistry and Applications. *Chemical Communications*. **1**, 1229-1239.
- Ubbink, J. and Odijk, T. (1995) Polymer-Induced and Salt-Induced Toroids of Hexagonal DNA. *Biophysical Journal*. **68**, 54-61.
-

Bibliography

- Umamura, K., Nagami, F., Okada, T. and Kuroda, R. (2000) Afm Characterization of Single Strand-Specific Endonuclease Activity on Linear DNA. *Nucleic Acids Research*. **28**, E39-e39.
- Vallea, F., Derosea, J. A., Dietlera, G., Kaweb, M., Pl.Uckthunb, A. and Semenzac, G. (2002) Afm Structural Study of the Molecular Chaperone Groeland Its Two-Dimensional Crystals: An Ideal "Living"Calibration Sample. *Ultramicroscopy*. **93**, 83-89.
- Van De Wetering, P., Cherng, J.-Y., Talsma, H. and Hennink, W. E. (1997) Relation between Transfection Efficiency and Cytotoxicity of Poly(2-(Dimethylamino)Ethyl Methacrylate)/ Plasmid Complexes. *Journal of Controlled Release*. **49**, 59-69.
- Vasilevskaya, V. V., Khokhlov, A. R., Kidoaki, S. and Yoshikawa, K. (1997) Structure of Collapsed Persistent Macromolecules: Toroid Vs. Spherical Globule. *Biopolymers*. **41**, 51-60.
- Vesenka, J., Miller, R. and Henderson, E. (1994) Three-Dimensional Probe Reconstruction for Atomic Force Microscopy. *Review of Scientific Instruments*. **65**, 1-3.
- Vijayanathan, V., Thomas, T. and Thomas, T. J. (2002) DNA Nanoparticles and Development of DNA Delivery Vehicles for Gene Therapy. *American Chemical Society*. **41**, 14086-14094.
- Wagner, P. (1998) Immobilisation Strategies for Biological Scanning Probe Microscopy. *Federation of European Biochemical Societies Letters*. **430**, 112-115.
- Wagner, P., Heyner, M., Guntherodt, H. J. and Semenza, G. (1995) Formation and in-Situ Modification of Monolayers Cheisorbed on Ultraflat Template Stripped Gold Surfaces. *Langmuir*. **11**, 3867-3875.
- Wallwork, M. L., Smith, D. A., Zhang, J., Robinson, C. and Kirkham, J. (2001) Complex Chemical Force Titration of Amine Functionalised Alkyl Thiol Self-Assembled Monolayers. *Langmuir*. **17**, 1126-1131.
- Walther, W. and Stein, U. (2000) Viral Vectors for Gene Transfer - a Review of Their Use in the Treatment of Human Diseases. *Drugs*. **60**, 249-271.
- Wang, D. W., Yin, H., Landick, R., Gelles, J. and Block, S. M. (1997) Stretching DNA with Optical Tweezers. *Biophysical Journal*. **71**, 1335-1346.
- Watanabe, S. and Regen, S. L. (1994) Dendrimers as Building Blocks for Multilayer Construction. *Journal of the American Chemical Society*. **116**, 8855-8856.

Bibliography

- Watkins, D. M., Sweet, Y. S., Klimash, J., Turro, N. J. and Tomalia, D. A. (1997) Dendrimers with Hydrophobic Cores and the Formation of Supramolecular Dendrimer-Surfactant Assemblies. *Langmuir*. **13**, 3136-3141.
- Watson, J. D. and Crick, F. H. C. (1953) Molecular Structure of Nucleic Acids. A Structure for Deoxyribose Nucleic Acid. *Nature*. **171**, 737-738.
- Weisenhorn, A. L., Maivald, P., Butt, H.-J. and Hansma, P. K. (1992) Measuring Adhesion, Attraction, and Repulsion between Surfaces in Liquids with an Atomic-Force Microscope. *Physical Review B*. **45**, 11226 -11232.
- Wells, M. and Crooks, R. M. (1996) Interactions between Organized, Surface-Confined Monolayers and Vapor-Phase Probe Molecules. 10. Preparation and Properties of Chemically Sensitive Dendrimer Surfaces. *Journal of the American Chemical Society*. **118**, 3988-3989.
- Wennmalm, S., Edman, L. and Rigler, R. (1997) Conformational Fluctuations in Single DNA Molecules. *Proceedings of the National Academy of Science. USA*. **94**, 10641-10646.
- Weston, S. A., Lahm, A. and Suck, D. J. (1992) X-Ray Structure of the Dnase I-D(Ggtatacc)₂ Complex at 2.3 Å Resolution. *Journal of Molecular Biology*. **226**, 1237-1256.
- Widom, J. and Baldwin, R. L. (1980) Cation-Induced Toroidal Condensation of DNA. Studies with Co³⁺(NH₃)₆. *Journal of Molecular Biology*. **144**, 431-453.
- Wilbur, D. S., Pathare, P. M., Hamlin, D. K., Buhler, K. R. and Vessella, R. L. (1998) Biotin Reagents for Antibody Pretargeting. Synthesis, Radioiodination, and Evaluation of Biotinylated Starburst Dendrimers. *Bioconjugate Chemistry*. **9**, 813-825.
- Williams, P. M., Shakesheff, K. M., Davies, M. C., Jackson, D. E. and Roberts, C. J. (1996) Blind Reconstruction of Scanning Probe Image Data. *The Journal of Vacuum Science and Technology B*. **14**, 1557-1562.
- Wilson, R. W. and Bloomfield, V. A. (1979) Counterion - Induced Condensation of Deoxyribonucleic Acid. A Light Scattering Study. *Biochemistry*. **18**, 2192-2196.
- Wiwattanapatapee, R., Jee, R. D. and Duncan, R. (1999) In *Controlled Release of Bioactive Materials*. Boston, MA, pp. 145-146.
- Wolff, J. A., Malone, R. W., Williams, P., Chong, W., Acsadi, G. J. and Felgner, P. L. (1990) Direct Gene Transfer into Mouse in Vivo. *Science*. **247**, 1465-1468.
-

Bibliography

- Woodward, J. T., Walker, M. L., Meuse, C. W., Vanderah, D. J., Poirier, G. E. and Plant, A. L. (2000) Effect of an Oxidized Gold Substrate on Alkanethiol Self-Assembly. *Langmuir*. **16**, 5347 - 5353.
- Xu, S. and Arnsdorf, M. F. (1995) Electrostatic Force Microscope for Probing Surface Charges in Aqueous Solutions. *Proceedings of the National Academy of Science. USA*. **92**, 10384-10388.
- Xu, S. and Arnsdorf, M. F. (1997) Scanning (Atomic) Force Microscopy Imaging of Earthworm Haemoglobin Calibrated with Spherical Colloidal Gold Particles. *Journal of Microscopy*. **187**, 43-53.
- Xu, S., Cruchon-Dupeyrat, S. J. N., Garno, J. C., Liu, G.-Y., Jennings, G. K., Yong, T.-H. and Laibinis, P. E. (1998) In Situ Studies of Thiol Self-Assembly on Gold from Solution Using Atomic Force Microscopy. *Journal of Chemical Physics*. **108**, 5000-5012.
- Xu, Y. and Szoka, F. C. (1996) Mechanism of DNA Release from Cationic Liposome/DNA Complexes Used in Cell Transfection. *Biochemistry*. **35**, 5616-5623.
- Yanagida, M., Hiraoka, Y. and Katsura, I. (1983) In *Cold Spring Harbor Symposium on Quantitative Biology*, Vol. 47, pp. 177-187.
- Yang, J., Mou, J.-X. and Shao, Z. (1994) Structure and Stability of Pertussis Toxin Studied by in Situ Atomic Force Microscopy. *Federation of European Biochemical Societies Letters*. **338**, 89-92.
- Yang, J. and Shao, Z. (1993) The Effect of Probe Force on Resolution in Atomic Force Microscopy of DNA. *Ultramicroscopy*. **50**, 157-170.
- Yoo, H., Peter, S. and Juliano, R. L. (1999) Pamam Dendrimers as Delivery Agents for Antisense Oligonucleotides. *Pharmaceutical Research*. **16**, 1799-1804.
- Yoshikawa, K. and Matsuzawa, Y. (1995) Discrete Phase-Transition of Giant DNA Dynamics of Globule Formation from a Single Molecular Chain. *Physica D*. **84**, 220-227.
- Yoshikawa, K., Yoshikawa, Y., Koyama, Y. and Kanbe, T. (1997) Highly Effective Compaction of Long Duplex DNA Induced by Polyethylene Glycol with Pendant Amino Groups. *Journal of the American Chemical Society*. **119**, 6473-6477.
- Young, E. and Sinsheimer, R. (1965) A Comparison of the Initial Actions of Spleen Deoxyribonuclease and Pancreatic Deoxyribonuclease. *Journal of Biological Chemistry*. **240**, 1274-1280.
-

Bibliography

- Zabner, J., Fasbender, A. J., Moninger, T., Poellinger, K. A. and Welsh, M. J. (1995) Cellular and Molecular Barriers to Gene-Transfer by a Cationic Lipid. *Journal of Biological Chemistry*. **270**, 18997–19007.
- Zeng, F. and Zimmerman, S. C. (1997) Dendrimers in Supramolecular Chemistry: From Molecular Recognition to Self-Assembly. *Chemical Reviews*. **97**, 1681-1712.
- Zhang, H., Grim, P. C. M., Foubert, P., Vosch, T., Vanoppen, P., Wiesler, U.-M., Berresheim, A. J., Mullen, K. and De Schryver, F. C. (2000) Properties of Single Dendrimer Molecules Studied by Atomic Force Microscopy. *Langmuir*. **16**, 9009-9014.
- Zhong, Q., Inness, D., Kjoller, K. and Elings, V. B. (1993) Fractured Polymer/Silica Fiber Surface Studied by Tapping Mode Atomic Force Microscopy. *Surface Science Letters*. **290**, L688-L692.
- Zlatanova, J., Lindsay, S. M. and Leuba, S. H. (2000) Single Molecule Force Spectroscopy in Biology Using the Atomic Force Microscopy. *Progress in Biophysics & Molecular Biology*. **74**, 37-61.
- Zuccheri, G., Dame, G., Aquila, M., Muzzalupo, I. and Samori, B. (1998) Conformational Fluctuations of Supercoiled DNA Molecules Observed in Real Time with a Scanning Force Microscope. *Applied Physics A*. **66**, S585-S589.